Event topology and multiplicity dependence of $\mathrm{K}^{*}(892)^{\pm}$ meson production in proton+proton collisions with ALICE at the LHC and exploring the possibility of a thermalized medium formation in small systems

A THESIS

Submitted in partial fulfilment of the requirements
for the award of the degree
of

DOCTOR OF PHILOSOPHY

by

Suman Deb

DEPARTMENT OF PHYSICS
INDIAN INSTITUTE OF TECHNOLOGY INDORE
July 2022

Event topology and multiplicity dependence of $\mathrm{K}^*(892)^{\pm}$ meson production in proton+proton collisions with ALICE at the LHC and exploring the possibility of a thermalized medium formation in small systems

A THESIS

Submitted in partial fulfilment of the requirements

for the award of the degree

of

DOCTOR OF PHILOSOPHY

by

Suman Deb

DEPARTMENT OF PHYSICS

INDIAN INSTITUTE OF TECHNOLOGY INDORE

July 2022

INDIAN INSTITUTE OF TECHNOLOGY INDORE

I hereby certify that the work which is being presented in the thesis entitled **"Event topology and multiplicity dependence of** $\mathrm{K}^{*}(892)^{\pm}$ **meson production in proton+proton collisions with ALICE at the LHC and exploring the possibility of a thermalized medium formation in small systems"** in the partial fulfilment of the requirements for the award of the degree of **DOCTOR OF PHILOSOPHY** and submitted in the **DEPARTMENT OF PHYSICS, Indian Institute of Technology Indore**, is an authentic record of my own work carried out during the time period from July 2017 to July 2022 under the supervision of Prof. Raghunath Sahoo, Professor, Department of Physics, Indian Institute of Technology Indore, Indore, M.P., India.

The matter presented in this thesis has not been submitted by me for the award of any other degree of this or any other institute.

19.10.22

Signature of the student with date
(Suman Deb)

This is to certify that the above statement made by the candidate is correct to the best of my knowledge.

19.10.22

Signature of Thesis Supervisor with date
(Prof. Raghunath Sahoo)

Mr. SUMAN DEB has successfully given his Ph.D. Oral Examination held on 19.10.2022

19.10.2022

Signature of Thesis Supervisor with date
(Prof. Raghunath Sahoo)

To, My father, Late Mr. Sodesh Deb

"Thank you for your love, sacrifices and guidance"
This thesis is proudly dedicated to my father.

(SUMAN DEB)

ACKNOWLEDGEMENTS

This thesis would not have seen the daylight unless many well-wishers had shown me the path. I am thankful to all of them. PhD is a long road; on this road, I learned many invaluable things from my teachers, collaborators, and friends, contributing to fulfilling this dream. Even though I tried to recall everyone's contribution during my Ph.D. days, please accept my apologies if I missed someone who deserved to be on this list.

First and foremost, I would like to express my deepest and most sincere gratitude to my thesis supervisor, Prof. Raghunath Sahoo, for his precious guidance throughout my PhD. I enjoyed every moment of my PhD, primarily due to his constant support in and beyond academics. This thesis would not have been possible without his dedicated supervision, advice, and constructive criticism. He was always available to help, whether on weekends or holidays. I recall several times when he was available for physics discussions, even late at night. I am thankful to him for giving me all the necessary resources and opportunities for my research work. I am sure my words are not enough to describe his impact on me during my PhD, and his inspiring piece of advice will stay with me forever. His approach to handling any problem inspires me, and his critical remarks in physics or apart from physics are very prudent. His sense of humor, friendly behavior toward his students, and strictness at a time all make an invaluable mix from which I benefited greatly. I am very grateful to have such a dynamic person and successful physicist as my supervisor.

I feel privileged to participate in one of the experiments (ALICE) at the Large Hadron Collider (LHC), the current most powerful and largest particle accelerator in the world. This is like a dream come true. I want to thank Dr. Luciano Musa (Spokesperson, ALICE), Dr. Barbara Erazmus (Deputy spokesperson, ALICE), Dr. Mateusz Ploskon (Deputy spokesperson, ALICE), Dr. Federico Antinori (former spokesperson, ALICE), Prof. Tapan Kumar Nayak (former deputy spokesperson, ALICE), Prof. Subhasis Chattopadhyay (former ALICE-India spokesperson) and Prof. Bedangadas Mohanty (ALICE-India spokesperson) for their support in various matters despite their busy schedule. I want to extend my gratitude to my ALICE collaboration Physics Working group - Light Flavour Spectra (PWG-LF) members, especially Dr. Alberto Caliva and Dr. Ramona Lea and conveners in Physics Analysis group (PWG) - Resonances, Dr. Alexander Philipp Kalweit, Dr. Stefania Bufalino, Dr. Anders Garritt Knospe, Dr. Livio Bianchi, Dr. Viktor Riabov, Dr. Enrico Fragiacomo, Dr. Jihye Song, Dr. Chiara Oppedisano, Dr. Bong-Hwi Lim and Dr. Sourav Kundu for their beneficial suggestions and compelling exposition. Thanks to Dr. Markus Fasel's guidance, I feel privileged to complete service tasks in the ALICE EMCAL group. I want to extend my special acknowledgment to Dr. Sushanta Tripathy (or Sushant bhai) for his constant support throughtout the course of data anlaysis. I will be forever indept of him.

I am also thankful to the Lego-train operators, Dr. Neelema Agrawal and Bong-Hwi Lim, for running my jobs in the train and providing data that supports me in performing the data analysis on time. Without their help, my analysis work would never have been completed in time.

The acknowledgment would not be complete without expressing my gratitude to Prof. Jane-Alam. His dedication to research has always been a source of motivation for me. I will always cherish the Physics discussion I had with him both online and offline. He was always a phone call away for a discussion. He taught me to be a good and dedicated Physicist. Also, I enjoyed my stay at the VECC. I want to extend my appreciation to Prof. Stefen Schumann, advisor, during my Marie Sk?odowska-Curie Early Stage Researcher position at the Institute of Theoretical Physics, Georg August University of Göttingen. Prof. Schumann introduced me to the theoretical aspects of the Monte-Carlo generator called SHERPA. I appreciate the kind hospitality, fruitful Physics discussion, and his support during my stay at Göttingen. I will continue to cherish this lifelong collaboration.

I am also thankful to my colleagues Shreyasi Acharya, Pranjal Sharma, Baidyanath Sahoo, and Dukhishyam Mallick, with whom I share vivid memories during my term as ALICE-India Junior Representative and ALICE-India Junior Ambassador. Working in the ALICE-India Junior committee along with them was an elixir experience.

I would like to extend my gratitude to my PSPC committee members, Dr. Pankaj R. Sagdeo and Dr. Amod C. Umarikar, for their constant support and motivation throughout my PhD. I would like to thank all the faculty and staff members of the IIT Indore for their support. I am very grateful to the Department of Physics, IIT Indore, for providing me with all the required resources.

My sincere acknowledgment goes to my fellow lab-mates of the Experimental High Energy Physics lab at IIT Indore for constructive physics discussions and all amusements throughout the last five years. It has been truly a privilege to work with Aditya Bhaiya, Pooja Didi, Pragati Didi, Dhananjaya Bhai, Sushanta bhai, Arvind Bhai, Sudipan Bhaiya, Swatantra Bhaiya, Younus Bhaiya, Bhaswar Bhaiya, Golam Bhaiya, Captain bhaiya, Jayanta, Rutuparna, Dushmanta, Neelkamal, Girija, Ronald, Suraj, Debadatta, Kshitish, Bhagyarathi, Kamaljeet, Kangkan, Aswathy, Pavish, Bendangkokba Jamir. I could not have reached this phase without their best wishes and support.

I sincerely thank Dr. Gayatri Sahu for her help and support during my stay at IIT Indore. I will always cherish the beautiful moments with Mamun and Papun.

I am thankful to my school, college, and university teachers for their guidance, and it is because of them that I could reach at this stage. Here, I want to mention the name of Dr. Radhendu Das, who has motivated me to take Physics as my career. I would be indebted to him forever.

My journey would not have come this far without the love and support of

my mother, brother, and sister. I thank my family and friends for their constant love, support, encouragement, and faith in me. Also, I want to thank Dr. Sabina Gurung, for being a constant source of inspiration and motivation. I have learned a lot from everyone during my PhD, which has helped me and will encourage me to cherish it for the rest of my career.

(Suman Deb)

ABSTRACT

The main goal of ultra-relativistic heavy-ion collisions is to create and characterize quark-gluon plasma (QGP). It is a deconfined state of quarks and gluons that can be realized at high density and temperature. The existence of QGP was predicted by quantum chromodynamics. Such a state of matter is expected to exist microseconds after the Big Bang. Thus the study of its properties and evolution could give a better understanding of the existence of matter in the present universe. In the laboratory, QGP is expected to be formed by the collisions of heavy ions using particle colliders. Relativistic Heavy Ion Collider (RHIC) and Large Hadron Collider (LHC) are the dedicated state-of-the-art experimental facilities to this end and are focussed on understanding the properties of QGP. In central heavy-ion collisions, a large number of particles are produced through the multiple interactions of participants in the overlap region. Although most of the observed particles produced in such collisions are results of the fragmentations of pieces of the colliding nuclei, a considerable amount of particle creation occurs by high incident energies ($\approx$ TeV). While the particles created are mostly pions, the production of relatively heavy particles than pions and heavy flavor (strange and charm) quark matter also takes place. However, in pp collisions, it was expected that the final state particles are only the result of the fragmentations of pieces of the two protons. And hence, historically, the proton on proton (pp) collisions were considered a baseline for forming QGP in heavy-ion collisions due to their significantly smaller size compared to the studying later. Recent observation of heavy-ion-like features in a small systems like pp collisions from the experiment at the LHC has generated considerable interest in the scientific community. For example, the discovery of collective-like phenomena, strangeness enhancement are a few among them. These developments have significant consequences on the results obtained from heavy-ion collisions, as pp collisions have been used as a benchmark for heavy-ion collisions to understand a possible medium formation.

These open up entirely new directions for theoretical and experimental studies of characterizing QGP-like properties and understanding the origin of such observations in small collisions systems. Although hydrodynamics calculations describe data qualitatively, other approaches suggest that these can be initial state effects. To understand the recent measurements in high-multiplicity pp collisions, it is important to perform multi-differential studies with event shape observables and charged-particle multiplicity. One of the event-shape techniques called transverse spherocity (S_0) can disentangle events dominated by soft/hard-QCD processes based on their geometrical structure. Soft-QCD and hard-QCD processes could govern particle production in small system collisions like pp. While the study of bulk properties of the system would give an understanding of the underlying mechanism of the soft-QCD process, the study of jets could reveal the physics of hard-QCD processes. The detailed study in the light of transverse spherocity and multiplicity could provide deeper insight into understanding the underlying production dynamics of a particle in high multiplicity pp collisions; moreover, it could also help in tuning various models.

Recent results reported by ALICE have observed enhanced production of strange and multi-strange particles in high-multiplicity proton+proton (pp collisions and observation of evidence of collectivity in pp collisions by CMS, which was traditionally considered as one of the signatures of QGP formation. These observations compel one to ask whether high-multiplicity pp collisions create QGP-droplets? Extensive investigation using resonance particles containing strange quarks could provide hints towards the possible formation of QGP-like medium in pp collisions (specifically high-multiplicity events). Resonances are commonly known as the hadrons, which are more massive than their ground state particle and have different excited quantum states but identical quark content. These particles usually have a short lifetime (τ) as they decay strongly, and it is in the order of a few fm/c, a typical proton diameter. Because of its short lifetime, reconstructed hadronic resonances through their decay products in a detector can be used to study the hadronic medium between the chemical and the kinetic freeze-out. Experimentally measured typical lifetime of hadronic resonances ranges for 1.3 fm/c to 46.3 fm/c. As hadronic resonances of varying masses (770 - 1019 MeV/c^2), hadron class (meson and baryon), strangeness (0 - 2), and lifetimes are available, they can be used to study the properties of the hadronic phase and its different stages of evolution. A comprehensive study of hadronic resonances plays a vital role in understanding ultra-relativistic heavy-ion collisions. In such collisions, expansion of the produced fireball can be probed by the hadronic resonances, as their lifetime is comparable to the lifetime of the fireball ($\tau \approx 10$ fm/c at LHC energies) created in the heavy-ion collisions. This helps to understand in-medium phenomena like rescattering (interaction of decay daughters with other in-medium particles, results in suppression of resonances when reconstructed, as the invariant mass of the daughter particles mismatches with the parent particle) and regeneration (enhancement of resonances because of pseudo-elastic collisions in the hadronic phase). Resonance particle-like $\phi(1020)$ having $\tau \approx 46.3$ fm/c might not go through the above mentioned processes. However, resonance particle like $\mathrm{K}^*(892)^{\pm}$ meson has a lifetime ($\tau \approx 3.6$ fm/c) which is comparable to the hadronic phase lifetime. This allows one to explore the hadronic phase. The sensitivity of hadronic resonances to rescattering and regeneration processes in the hadronic phases is depicted in Figure 3.1.

The major objectives of this thesis are to understand the interplay of various processes in the hadronic phase with event shape and high-multiplicity dependence study of $\mathrm{K}^{*\pm}$ meson production using ALICE detectors at the LHC (CERN). To have a complete birds-eye view of the dynamics of particle production in pp collisions, we have also studied the event topology dependence of heavy-flavored hadrons using a pQCD-inspired model. This work revealed the importance of events topology in the production of charmed-flavored and strange-flavored hadrons. Also, we phenomenologically attempt to explore the possibility of a thermalized medium formation in pp collisions through geometric, statistical, and Monte-Carlo approach. In the case of the geometric approach, we have tried to explain the experimental results taking the proton structure as consisting of three valence quarks connected by gluons. We describe the densities of quarks and gluons as a Gaussian type assuming a spherically symmetric distribution of quark densities from their respective centers and cylindrically symmetric gluon densities about the line joining two adjacent quarks. With this consideration, we could explain charged-particle multiplicity distribution and elliptic-flow obtained in *pp* collisions at $\sqrt{s} = 7$ and 13 TeV respectively using a Glauber approach. In another work, considering final state multiplicity as a proxy of the number of constituents particles involved in the collisions, we have studied the thermodynamical quantities like heat capacity, trace anomaly, speed of sound, etc., using experimental inputs from ALICE and contrasted these results with those obtained from PYTHIA8 (devoid of thermalization). This work gives a hint of the possible onset of thermalization in a small system like pp after a certain threshold in the final state charged multiplicity. We further extended these studies to include the event topology, thereby linking to the analysis part of the thesis and motivating future potential measurements.

This thesis is divided into five chapters. The organisation of thesis is as follows:

- **Chapter 1** gives a brief and general introduction on standard model of particle physics and Quantum chromodynamics(QCD). This is followed by a short discussion on quark-gluon plasma (QGP),its formation in ultra-relativistic collisions and signatures. Then, a discussion on recent experimental observations of possible thermalized medium formation in pp collisions,which forms the motivation of this thesis. A brief motivation of various works included in this thesis is discussed, making a stage for their use in subsequent chapters.

- **Chapter 2** gives a brief introduction on the ALICE detectors used for K*(892)$^{\pm}$ identifications in this thesis. In addition, this chapter provides a short description of all other detectors used in ALICE. We also discuss about the ALICE framework: online/offline computing system, reconstruction system based on the GRID framework briefly.

- **Chapter 3** is devoted to the detailed methodology of K*(892)$^{\pm}$ meson production in pp collision as a function of event shape and multiplicity with ALICE at the LHC energies. And to have contrast with heavy flavor particles, we have also shown the event shape dependence of J/ψ, Λ_c^+, and D_0 meson in pp collisions at the LHC energies using PYTHIA8 Monte-Carlo generator. This chapter is mainly based on our analysis note and a published article mention below:

  (1). Event shape and multiplicity dependence of $K^{*}(892)^{\pm}$ production in pp collisions at $\sqrt{s}$ = 13 TeV with ALICE at the LHC, https://alice-notes.web.cern.ch/node/946,

  (2). Journal of Physics G: Nuclear and Particle Physics 48, 095104 (2021)

- In **Chapter 4**, we have presented the phenomenological studies to understand the possibility of thermalized medium formation in the pp system. We begin by designing a geometric structure of the proton, considering three valence quarks and gluons connecting them to explain experimental results. We then adopted a thermodynamical approach taking the Tsallis distribution function to investigate further the pp system using experimental data. We also studied the event shape dependence of thermodynamical quantities of produced particles in pp collisions at LHC energies using the PYTHIA8 event generator. This chapter is mainly based on our published articles:

(1). Phys. Rev. D 101, 014004 (2020),

(2). Eur. Phys. J. A 56, 252 (2020), and

(3). Eur. Phys. J. A 57, 195 (2021)

- Finally, **Chapter 5** gives the conclusion drawn from current studies.

ACRONYMS

- ALICE: A Large Ion Collider Experiment
- A side: ATLAS side
- AOD: Analysis Oriented Data
- ATLAS: A Toroidal Large ApparatuS
- BR: Branching Ratio
- C side: CMS side
- CBM: Compressed Baryonic Matter
- CGC: Color Glass Condensate
- CERN: European Organization for Nuclear Research
- CMS: Compact Muon Solenoid
- CP: Charge-Parity
- CR: Colour Reconnection
- DAQ: Data AQuisition
- DCA: Distance of Closest Approach
- DPG: Data Preparation Group
- EMCal: Electromagnetic Calorimeter
- LHC: Large Hadron Collider
- LHCb: LHC beauty
- MB: Minimum Bias

- MC: Monte Carlo
- MPI: Multi Parton Interaction
- MRPC: Multi-gap Resistive-Plate Chamber
- MWPC: Multi-Wire Proportional Chamber
- NICA: Nuclotron-based Ion Collider fAcility
- PHENIX: Pioneering High Energy Nuclear Interaction eXperiment
- HMPID: High-Momentum Particle IDentification detector
- HRG: Hadron Resonance Gas
- ITS: Inner Tracking System
- LEP: Large Electron-Positron collider
- EPOS: Energy-conserving quantum mechanical multiple scattering approach, based on Partons (parton ladders), O?-shell remnants, and Splitting of parton ladders
- ESD: Event Summary Data
- FAIR: Facility for Antiproton and Ion Research
- GEANT: GEometry ANd Tracking
- NICA: Nuclotron-based Ion Collider fAcility
- PHENIX: Pioneering High Energy Nuclear Interaction eXperiment
- PID: Particle IDentification
- pp collisions: Proton+Proton collisions
- TOF: Time-Of-Flight

- TPC: Time Projection Chamber
- TRD: Transition Radiation Detector
- VZERO/V0: Vertex 0 detector
- RHIC: Relativistic Heavy-Ion Collider
- T0: Time 0 detector

PUBLICATIONS

List of publications: **(Publication marked with [*] are included in this thesis)**

1. [*] **“Glauber model for a small system using the anisotropic and inhomogeneous density profile of a proton”**
   Suman Deb, Golam Sarwar, Dhananjaya Thakur, Pavish S., Raghunath Sahoo, and Jan-e Alam,
   Phys. Rev. D 101, 014004 (2020): **(SCI-indexed, Impact factor: 5.296)**

2. [*] **“Deciphering QCD dynamics in small collision systems using event shape and final state multiplicity at the Large Hadron Collider”**
   Suman Deb, Sushanta Tripathy, Golam Sarwar, Raghunath Sahoo, and Jan-e Alam,
   Eur. Phys. J. A 56, 252 (2020): **(SCI-indexed, Impact factor: 3.131)**

3. [*] **“Study of QCD dynamics using small systems”**
   Suman Deb, Golam Sarwar, Raghunath Sahoo, and Jan-e Alam,
   Eur. Phys. J. A 57, 195 (2021): **(SCI-indexed, Impact factor: 3.131)**

4. [*] **“Investigating Heavy-flavor vs. Light-flavor Puzzle with Event Topology and Multiplicity in Proton+Proton Collisions at $\sqrt{s}$ = 13 TeV using PYTHIA8”**
   Suman Deb, Raghunath Sahoo, Dhananjaya Thakur, Sushanta Tripathy, and Arvind Khuntia,
   Journal of Physics G: Nuclear and Particle Physics 48, 095104 (2021): **(SCI-indexed, Impact factor: 3.519)**

5. [*] **“Event shape and multiplicity dependence of $K^*(892)^{\pm}$ production in pp collisions at $\sqrt{s} = 13$ TeV with ALICE at the LHC”**
   Suman Deb and Raghunath Sahoo,
   https://alice-notes.web.cern.ch/node/946 (Analysis Note)

6. **“Event shape and multiplicity dependence of $K^*(892)^{\pm}$ production in pp collisions at $\sqrt{s} = 5.02$ and 13 TeV with ALICE at the LHC”**
   Suman Deb, Sushanta Tripathy and Raghunath Sahoo,
   https://alice-notes.web.cern.ch/node/946 (Analysis Note)

7. **“Multiplicity Dependence of J/ψ Production and QCD Dynamics in p+p Collisions at $\sqrt{s} = 13$ TeV”**
   Suman Deb, Dhananjaya Thakur, Sudipan De, and Raghunath Sahoo,
   Eur. Phys. J A 56, 134 (2020): **(SCI-indexed, Impact factor: 3.131)**

8. **“J/ψ Production Dynamics: Event shape, Multiplicity and Rapidity dependence Proton+Proton Collisions at LHC energies using PYTHIA8”**
   Anisa Khatun, Dhananjaya Thakur, **Suman Deb**, and Raghunath Sahoo,
   Journal of Physics G: Nuclear and Particle Physics 47, 055110 (2020): **(SCI-indexed, Impact factor: 3.519)**

9. **“Bose-Einstein Condensation of pions in Proton-Proton collisions at the Large Hadron Collider using non-extensive Tsallis statistics”**
   Suman Deb, Dushmanta Sahu, Raghunath Sahoo, and Anil Kumar Pradhan,
   Eur. Phys. J. A 57, 158 (2021): **(SCI-indexed, Impact factor: 3.131)**

10. **“Estimation of Impact Parameter and Transverse Spherocity in heavy-ion collisions at the LHC energies using Machine Learning”**

Neelkamal Mallick, Sushanta Tripathy, Aditya Nath Mishra, **Suman Deb**, and Raghunath Sahoo,
Phys. Rev. D 103, 094031 (2021): **(SCI-indexed, Impact factor: 5.296)**

11. **"Charmonium suppression in ultra-relativistic Proton-Proton collisions at LHC energies: A hint for QGP in small systems"**
Captain R. Singh, **Suman Deb**, Raghunath Sahoo and Jan-e Alam,
Eur. Phys. J. C 82, 542 (2022): **(SCI-indexed, Impact factor: 5.172)**

12. **"Hadron gas in the presence of a magnetic field using non-extensive statistics: A transition from diamagnetic to paramagnetic system"**
Girija Sankar Pradhan, Dushmanta Sahu, **Suman Deb**, and Raghunath Sahoo,
arXiv: 2106.14297 [hep-ph].

13. S. Acharya *et al.* [ALICE], "**"Prompt and non-prompt J/ψ production cross sections at midrapidity in proton-proton collisions at $\sqrt{\mathrm{s}}$ = 5.02 and 13 TeV",**
JHEP **03**, 190 (2022).

14. S. Acharya *et al.* [ALICE], **"Inclusive J/ψ production at midrapidity in pp collisions at $\sqrt{s} = 13$ TeV",**
Eur. Phys. J. C **81**, 1121 (2021).

15. S. Acharya *et al.* [ALICE], **"Measurement of the groomed jet radius and momentum splitting fraction in pp and Pb−Pb collisions at $\sqrt{s_{NN}} = 5.02$ TeV",**
Phys. Rev. Lett. **128**, 102001 (2022).

16. S. Acharya *et al.* [ALICE], "$\mathrm{K_S}^0$**- and (anti-)Λ-hadron correlations in**

pp collisions at $\sqrt{s} = 13$ TeV”,
Eur. Phys. J. C **81**, 945 (2021).

17. S. Acharya *et al.* [ALICE], “$\mathrm{K_S}^0$**- and (anti-)**Λ**-hadron correlations in pp collisions at $\sqrt{s} = 13$ TeV”,**
    Eur. Phys. J. C **81**, 945 (2021).

18. S. Acharya *et al.* [ALICE], **“Measurements of the groomed and ungroomed jet angularities in pp collisions at $\sqrt{s}$ = 5.02 TeV”,**
    JHEP **05**, 061 (2022).

19. S. Acharya *et al.* [ALICE], **“Polarization of Λ and $\bar{\Lambda}$ Hyperons along the Beam Direction in Pb-Pb Collisions at $\sqrt{s_{NN}}$=5.02 TeV”,**
    Phys. Rev. Lett. **128**, 172005 (2022).

20. S. Acharya *et al.* [ALICE], **“Measurement of very forward energy and particle production at midrapidity in pp and p-Pb collisions at the LHC”,**
    arXiv:2107.10757 [nucl-ex].

21. S. Acharya *et al.* [ALICE], **“Anisotropic flow of identified hadrons in Xe-Xe collisions at $\sqrt{s_{\mathrm{NN}}}$ = 5.44 TeV”,**
    JHEP **10**, 152 (2021).

22. S. Acharya *et al.* [ALICE], **“Hypertriton Production in p-Pb Collisions at $\sqrt{s_{NN}}$=5.02 TeV”,**
    Phys. Rev. Lett. **128**, 252003 (2022).

23. S. Acharya *et al.* [ALICE], **“Production of $\mathrm{K}^*(892)^0$ and $\phi(1020)$ in pp and Pb-Pb collisions at $\sqrt{s_{\mathrm{NN}}} = 5.02$ TeV”,**
    arXiv:2106.13113 [nucl-ex].

24. S. Acharya *et al.* [ALICE], **“Direct observation of the dead-cone effect in quantum chromodynamics”.**
    Nature **605**, 440 (2022).

25. S. Acharya *et al.* [ALICE], **“Measurement of Prompt $\mathbf{D^0}$, Λ_c^+, and $\Sigma_c^{0,++}$(2455) Production in Proton–Proton Collisions at $\sqrt{s} = \mathbf{13}$ TeV”,**
    Phys. Rev. Lett. **128**, 012001 (2022).

26. S. Acharya *et al.* [ALICE], **“Charm-quark fragmentation fractions and production cross section at midrapidity in pp collisions at the LHC”,**
    Phys. Rev. D **105**, L011103 (2022).

27. S. Acharya *et al.* [ALICE], **“Kaon–proton strong interaction at low relative momentum via femtoscopy in Pb–Pb collisions at the LHC”,**
    Phys. Lett. B **822**, 136708 (2021)

28. S. Acharya *et al.* [ALICE], **“Charged-particle multiplicity fluctuations in Pb–Pb collisions at $\sqrt{s_{\mathrm{NN}}} = \mathbf{2.76}$ TeV”,**
    Eur. Phys. J. C **81**, 1012 (2021).

29. S. Acharya *et al.* [ALICE], **“Experimental Evidence for an Attractive p-ϕ Interaction”,**
    Phys. Rev. Lett. **127**, 172301 (2021).

30. S. Acharya *et al.* [ALICE], **“Measurement of the production cross section of prompt Ξ_{c}^0 baryons at midrapidity in pp collisions at $\sqrt{s} = \mathbf{5.02}$ TeV”,**
    JHEP **10**, 159 (2021).

31. S. Acharya *et al.* [ALICE], **“Measurement of $\mathbf{K^*(892)^\pm}$ production in inelastic pp collisions at the LHC”,**

Phys. Lett. B **828**, 137013 (2022).

32. S. Acharya *et al.* [ALICE], **"Investigating the role of strangeness in baryon–antibaryon annihilation at the LHC"**,
    Phys. Lett. B **829**, 137060 (2022).

33. S. Acharya *et al.* [ALICE], **"Inclusive, prompt and non-prompt J/ψ production at midrapidity in p-Pb collisions at $\sqrt{s_{\mathrm{NN}}} = 5.02$ TeV"**,
    JHEP **06**, 011 (2022).

34. S. Acharya *et al.* [ALICE], **"First measurements of N-subjettiness in central Pb-Pb collisions at $\sqrt{s_{\mathrm{NN}}} = 2.76$ TeV"**,
    JHEP **10**, 003 (2021).

35. S. Acharya *et al.* [ALICE], **"Measurement of the Cross Sections of Ξ_c^0 and Ξ_c^+ Baryons and of the Branching-Fraction Ratio BR($\Xi_c^0 \to \Xi^- e^+ \nu_e$)/BR($\Xi_c^0 \to \Xi^- \pi^+$) in pp collisions at 13 TeV"**,
    Phys. Rev. Lett. **127**, 272001 (2021).

36. S. Acharya *et al.* [ALICE], **"Production of Λ and K_s^0 in jets in p–Pb collisions at $\sqrt{s_{NN}}$=5.02 TeV and pp collisions at $\sqrt{s}$=7 TeV"**,
    Phys. Lett. B **827**, 136984 (2022).

37. S. Acharya *et al.* [ALICE], **"Energy dependence of ϕ meson production at forward rapidity in pp collisions at the LHC"**,
    Eur. Phys. J. C **81**, 772 (2021).

38. S. Acharya *et al.* [ALICE], **"Exploring the NΛ-NΣ coupled system with high precision correlation techniques at the LHC"**,
    Phys. Lett. B **833**, 137272 (2022).

39. S. Acharya *et al.* [ALICE], **"Nuclear modification factor of light neutral-meson spectra up to high transverse momentum in p–Pb**

collisions at sNN=8.16 TeV”,
Phys. Lett. B **827**, 136943 (2022).

40. S. Acharya *et al.* [ALICE], **“Measurement of beauty and charm production in pp collisions at $\sqrt{s}$ = 5.02 TeV via non-prompt and prompt D mesons”,**
JHEP **05**, 220 (2021).

41. S. Acharya *et al.* [ALICE], **“Measurements of mixed harmonic cumulants in Pb–Pb collisions at $\sqrt{s_{NN}} = 5.02$ TeV”,**
Phys. Lett. B **818**, 136354 (2021).

42. S. Acharya *et al.* [ALICE], **“First measurement of the $|t|$-dependence of coherent J/ψ photonuclear production”,**
Phys. Lett. B **817**, 136280 (2021).

43. S. Acharya *et al.* [ALICE], **“Coherent** J/ψ **and** ψ' **photoproduction at midrapidity in ultra-peripheral Pb-Pb collisions at** $\sqrt{s_{\mathrm{NN}}} = 5.02$ **TeV”,**
Eur. Phys. J. C **81**, 712 (2021).

44. S. Acharya *et al.* [ALICE], **“Production of pions, kaons, (anti-)protons and ϕ mesons in Xe–Xe collisions at $\sqrt{s_{\mathrm{NN}}} = 5.44$ TeV”,**
Eur. Phys. J. C **81**, 584 (2021).

45. S. Acharya *et al.* [ALICE], **“Long- and short-range correlations and their event-scale dependence in high-multiplicity pp collisions at** $\sqrt{s} = 13$ **TeV”,**
JHEP **05**, 290 (2021).

46. S. Acharya *et al.* [ALICE], **“First measurement of coherent ρ0 photoproduction in ultra-peripheral Xe–Xe collisions at $\sqrt{s_{\mathrm{NN}}}$=5.44**

TeV",
Phys. Lett. B **820**, 136481 (2021).

47. S. Acharya *et al.* [ALICE], **Multiharmonic Correlations of Different Flow Amplitudes in Pb-Pb Collisions at** $\sqrt{s_{_{NN}}} = 2.76$ **TeV",**
Phys. Rev. Lett. **127**, 092302 (2021).

48. S. Acharya *et al.* [ALICE],S. Acharya *et al.* [ALICE], **"Inclusive heavy-flavour production at central and forward rapidity in Xe-Xe collisions at** $\sqrt{s_{NN}}$**=5.44 TeV",**
Phys. Lett. B **819**, 136437 (2021).

49. S. Acharya *et al.* [ALICE], **"Jet fragmentation transverse momentum distributions in pp and p-Pb collisions at** $\sqrt{s}$, $\sqrt{s_{\mathrm{NN}}}$ **= 5.02 TeV",**
JHEP **09**, 211 (2021).

50. S. Acharya *et al.* [ALICE], **"Production of muons from heavy-flavour hadron decays at high transverse momentum in Pb–Pb collisions at** $\sqrt{s_{\mathrm{NN}}}$**=5.02 and 2.76 TeV",**
Phys. Lett. B **820**, 136558 (2021).

51. S. Acharya *et al.* [ALICE], **"Jet-associated deuteron production in pp collisions at** $\sqrt{s}$ **= 13 TeV",**
Phys. Lett. B **819**, 136440 (2021).

52. S. Acharya *et al.* [ALICE], **"**Λ_c^+ **Production and Baryon-to-Meson Ratios in pp and p-Pb Collisions at** $\sqrt{s_{NN}}$**=5.02 TeV at the LHC",**
Phys. Rev. Lett. **127**, 202301 (2021).

53. S. Acharya *et al.* [ALICE], **"**Υ **production and nuclear modification at forward rapidity in Pb–Pb collisions at** $\sqrt{s_{NN}}$**=5.02TeV",**
Phys. Lett. B **822**, 136579 (2021).

54. S. Acharya *et al.* [ALICE], **‘Λ_c^+ production in pp and in p-Pb collisions at $\sqrt{s_{NN}}$=5.02 TeV”,**
    Phys. Rev. C **104**, 054905 (2021).

55. S. Acharya *et al.* [ALICE], **‘Pseudorapidity distributions of charged particles as a function of mid- and forward rapidity multiplicities in pp collisions at $\sqrt{s}$ =5.02, 7 and 13 TeV”,**
    Eur. Phys. J. C **81**, 630 (2021).

56. S. Acharya *et al.* [ALICE], **“Centrality dependence of J/ψ and ψ(2S) production and nuclear modification in p-Pb collisions at $\sqrt{s_{\mathrm{NN}}}$ = 8.16 TeV”,**
    JHEP **02**, 002 (2021).

57. S. Acharya *et al.* [ALICE], **“Pion-kaon femtoscopy and the lifetime of the hadronic phase in Pb−Pb collisions at $\sqrt{s_{\mathrm{NN}}}$ = 2.76 TeV”,**
    Phys. Lett. B **813**, 136030 (2021).

58. S. Acharya *et al.* [ALICE], **“Production of ω mesons in pp collisions at $\sqrt{\mathrm{s}} = 7\,\mathrm{TeV}$”,**
    Eur. Phys. J. C **80**, 1130 (2020).

59. S. Acharya *et al.* [ALICE], **“J/ψ elliptic and triangular flow in Pb-Pb collisions at $\sqrt{s_{\mathrm{NN}}}$ = 5.02 TeV”,**
    JHEP **10**, 141 (2020).

60. S. Acharya *et al.* [ALICE], **“Elliptic and triangular flow of (anti)deuterons in Pb-Pb collisions at $\sqrt{s_{\mathrm{NN}}}$ = 5.02 TeV”,**
    Phys. Rev. C **102**, 055203 (2020).

61. S. Acharya *et al.* [ALICE], **“Measurement of isolated photon-hadron correlations in $\sqrt{s_{\mathrm{NN}}}$ = 5.02 TeV pp and p-Pb collisions”,**
    Phys. Rev. C **102**, 044908 (2020).

62. S. Acharya *et al.* [ALICE], **“Constraining the Chiral Magnetic Effect with charge-dependent azimuthal correlations in Pb-Pb collisions at $\sqrt{s_{\mathrm{NN}}}$ = 2.76 and 5.02 TeV”,**
JHEP **09**, 160 (2020).

63. S. Acharya *et al.* [ALICE], **“Soft-Dielectron Excess in Proton-Proton Collisions at $\sqrt{s}$ = 13 TeV”,**
Phys. Rev. Lett. **127**, 042302 (2021).

64. S. Acharya *et al.* [ALICE], **“Dielectron production in proton-proton and proton-lead collisions at $\sqrt{s_{NN}}$ = 5.02 TeV”,**
Phys. Rev. C **102**, 055204 (2020).

65. S. Acharya *et al.* [ALICE], **“Unveiling the strong interaction among hadrons at the LHC”,**
Nature **588**, 232 (2020).

66. S. Acharya *et al.* [ALICE], **“Production of light-flavor hadrons in pp collisions at** $\sqrt{s} = 7$ **and** $\sqrt{s} = 13$ **TeV”,**
Eur. Phys. J. C **81**, 256 (2021).

67. S. Acharya *et al.* [ALICE], **“‘Z-boson production in p-Pb collisions at** $\sqrt{s_{\mathrm{NN}}} = 8.16$ **TeV and Pb-Pb collisions at** $\sqrt{s_{\mathrm{NN}}} = 5.02$ **TeV”,**
JHEP **09**, 076 (2020).

68. S. Acharya *et al.* [ALICE], **“Transverse-momentum and event-shape dependence of D-meson flow harmonics in Pb–Pb collisions at $\sqrt{s_{NN}}$ = 5.02 TeV”,**
Phys. Lett. B **813**, 136054 (2021).

69. S. Acharya *et al.* [ALICE], **“Elliptic Flow of Electrons from Beauty-Hadron Decays in Pb-Pb Collisions at $\sqrt{s_{NN}}$ = 5.02 TeV”,**
Phys. Rev. Lett. **126**, 162001 (2021).

70. S. Acharya *et al.* [ALICE], **“First measurement of quarkonium polarization in nuclear collisions at the LHC”,**
    Phys. Lett. B **815**, 136146 (2021).

71. S. Acharya *et al.* [ALICE], **“Multiplicity dependence of J/ψ production at midrapidity in pp collisions at $\sqrt{s}$ = 13 TeV”,**
    Phys. Lett. B **810**, 135758 (2020).

72. S. Acharya *et al.* [ALICE], **“Measurement of the low-energy antideuteron inelastic cross section”,**
    Phys. Rev. Lett. **125**, 162001 (2020).

73. S. Acharya *et al.* [ALICE], “ΛK **femtoscopy in Pb-Pb collisions at $\sqrt{s_{\rm NN}}$ = 2.76 TeV”,**
    Phys. Rev. C **103**, 055201 (2021).

74. S. Acharya *et al.* [ALICE], **“J/ψ production as a function of charged-particle multiplicity in p-Pb collisions at $\sqrt{s_{\rm NN}}$** = 8.16 **TeV”,**
    JHEP **09**, 162 (2020)

75. S. Acharya *et al.* [ALICE], **“Search for a common baryon source in high-multiplicity pp collisions at the LHC”,**
    Phys. Lett. B **811**, 135849 (2020).

76. S. Acharya *et al.* [ALICE], **“Measurement of nuclear effects on** ψ(2S) **production in p-Pb collisions at $\sqrt{s_{\rm NN}}$** = 8.16 **TeV”,**
    JHEP **07**, 237 (2020).

77. S. Acharya *et al.* [ALICE], **“(Anti-)deuteron production in pp collisions at** $\sqrt{s}$ = 13 **TeV”,**
    Eur. Phys. J. C **80**, 889 (2020).

78. S. Acharya *et al.* [ALICE], **"Multiplicity dependence of π, K, and p production in pp collisions at $\sqrt{s} = 13$ TeV"**,
Eur. Phys. J. C **80**, 693 (2020).

79. S. Acharya *et al.* [ALICE], **"Coherent photoproduction of ρ^0 vector mesons in ultra-peripheral Pb-Pb collisions at $\sqrt{s_{\mathrm{NN}}} = 5.02$ TeV"**,
JHEP **06**, 035 (2020).

80. S. Acharya *et al.* [ALICE], **"Higher harmonic non-linear flow modes of charged hadrons in Pb-Pb collisions at $\sqrt{s_{\mathrm{NN}}} = 5.02$ TeV"**,
JHEP **05**, 085 (2020).

81. S. Acharya *et al.* [ALICE], **"Non-linear flow modes of identified particles in Pb-Pb collisions at $\sqrt{s_{\mathrm{NN}}} = 5.02$ TeV"**,
JHEP **06**, 147 (2020).

82. S. Acharya *et al.* [ALICE], **"Investigation of the p–Σ0 interaction via femtoscopy in pp collisions"**,
Phys. Lett. B **805**, 135419 (2020).

83. S. Acharya *et al.* [ALICE], **"Evidence of rescattering effect in Pb-Pb collisions at the LHC through production of $\mathrm{K}^*(892)^0$ and $\phi(1020)$ mesons"**,
Phys. Lett. B **802**, 135225 (2020).

84. S. Acharya *et al.* [ALICE], **"Production of (anti-)^{3}He and (anti-)^{3}H in p-Pb collisions at $\sqrt{s_{\mathrm{NN}}} = 5.02$ TeV"**,
Phys. Rev. C **101**, 044906 (2020).

85. S. Acharya *et al.* [ALICE], **"Longitudinal and azimuthal evolution of two-particle transverse momentum correlations in Pb-Pb collisions at $\sqrt{s_{\mathrm{NN}}} = 2.76$ TeV"**,
Phys. Lett. B **804**, 135375 (2020).

86. S. Acharya *et al.* [ALICE], **“Underlying Event properties in pp collisions at $\sqrt{s}$ = 13 TeV”,**
JHEP **04**, 192 (2020).

87. S. Acharya *et al.* [ALICE], **“Centrality and transverse momentum dependence of inclusive J/ψ production at midrapidity in Pb–Pb collisions at sNN=5.02 TeV”,**
Phys. Lett. B **805**, 135434 (2020).

88. S. Acharya *et al.* [ALICE], **“Probing the effects of strong electromagnetic fields with charge-dependent directed flow in Pb-Pb collisions at the LHC”,**
Phys. Rev. Lett. **125**, 022301 (2020).

89. S. Acharya *et al.* [ALICE], **“Measurement of electrons from heavy-flavour hadron decays as a function of multiplicity in p-Pb collisions at $\sqrt{s_{\mathrm{NN}}}$ = 5.02 TeV”,**
JHEP **02**, 077 (2020).

90. S. Acharya *et al.* [ALICE], **“Multiplicity dependence of K*(892)^0 and ϕ(1020) production in pp collisions at $\sqrt{s}$ =13 TeV”** Phys. Lett. B **807**, 135501 (2020).

91. S. Acharya *et al.* [ALICE], **“Jet-hadron correlations measured relative to the second order event plane in Pb-Pb collisions at $\sqrt{s_{\mathrm{NN}}}$ = 2.76 TeV”**
Phys. Rev. C **101**, 064901 (2020).

92. S. Acharya *et al.* [ALICE], **“Azimuthal correlations of prompt D mesons with charged particles in pp and p–Pb collisions at $\sqrt{s_{NN}}$ = 5.02 TeV”**
Eur. Phys. J. C **80**, 979 (2020).

93. S. Acharya *et al.* [ALICE], **“? production in p–Pb collisions at $\sqrt{s_{NN}}$=8.16 TeV”**
Phys. Lett. B **806**, 135486 (2020).

94. S. Acharya *et al.* [ALICE], **“Evidence of Spin-Orbital Angular Momentum Interactions in Relativistic Heavy-Ion Collisions”**
Phys. Rev. Lett. **125**, 012301 (2020).

95. S. Acharya *et al.* [ALICE], **“Global baryon number conservation encoded in net-proton fluctuations measured in Pb-Pb collisions at $\sqrt{s_{\mathrm{NN}}} = 2.76$ TeV”**
Phys. Lett. B **807**, 135564 (2020).

96. S. Acharya *et al.* [ALICE], “$\mathrm{K}^{*}(892)^{0}$ **and** $\phi(1020)$ **production at midrapidity in pp collisions at $\sqrt{s} = 8$ TeV”**
Phys. Rev. C **102**, 024912 (2020).

97. S. Acharya *et al.* [ALICE], **“Measurement of electrons from semileptonic heavy-flavour hadron decays at midrapidity in pp and Pb-Pb collisions at $\sqrt{s_{\mathrm{NN}}} = 5.02$ TeV”**
Phys. Lett. B **804**, 135377 (2020).

98. S. Acharya *et al.* [ALICE], **“Measurement of the (anti-)3He elliptic flow in Pb–Pb collisions at sNN=5.02TeV”**
Phys. Lett. B **805**, 135414 (2020).

99. S. Acharya *et al.* [ALICE], **“Production of charged pions, kaons, and (anti-)protons in Pb-Pb and inelastic** *pp* **collisions at $\sqrt{s_{NN}} = 5.02$ TeV”**
Phys. Rev. C **101**, 044907 (2020).

100. S. Acharya *et al.* [ALICE], **“Measurements of inclusive jet spectra in pp and central Pb-Pb collisions at $\sqrt{s_{\mathrm{NN}}} = 5.02$ TeV”**

Phys. Rev. C **101**, 034911 (2020).

101. S. Acharya *et al.* [ALICE], **“Studies of J/ψ production at forward rapidity in Pb-Pb collisions at $\sqrt{s_{\mathrm{NN}}} = 5.02$ TeV”**,
JHEP **02**, 041 (2020).

102. S. Acharya *et al.* [ALICE], **“Global polarization of $\Lambda\bar{\Lambda}$ hyperons in Pb-Pb collisions at $\sqrt{s_{NN}} = 2.76$ and 5.02 TeV”**,
Phys. Rev. C **101**, 044611 (2020).

103. S. Acharya *et al.* [ALICE], **“Measurement of $\Lambda(1520)$ production in pp collisions at $\sqrt{s} = 7$ TeV and p-Pb collisions at $\sqrt{s_{\mathrm{NN}}} = 5.02$ TeV”**,
Eur. Phys. J. C **80**, 160 (2020).

104. S. Acharya *et al.* [ALICE], **“Multiplicity dependence of (multi-)strange hadron production in proton-proton collisions at $\sqrt{s} = 13$ TeV”**,
Eur. Phys. J. C **80**, 167 (2020).

105. S. Acharya *et al.* [ALICE], **“${}^{3}_{\Lambda}\mathrm{H}$ and ${}^{3}_{\bar{\Lambda}}\overline{\mathrm{H}}$ lifetime measurement in Pb-Pb collisions at $\sqrt{s_{\mathrm{NN}}} = 5.02$ TeV via two-body decay”**,
Phys. Lett. B **797**, 134905 (2019).

106. S. Acharya *et al.* [ALICE], **“Measurement of Υ(1S) elliptic flow at forward rapidity in Pb-Pb collisions at $\sqrt{s_{\mathrm{NN}}} = 5.02$ TeV”**,
Phys. Rev. Lett. **123**, 192301 (2019).

107. S. Acharya *et al.* [ALICE], **“Measurement of prompt D^0, D^+, D^{*+}, and $\mathrm{D}_{\mathrm{S}}^{+}$ production in p–Pb collisions at $\sqrt{s_{\mathrm{NN}}} = 5.02$ TeV”**,
JHEP **12**, 092 (2019).

108. S. Acharya *et al.* [ALICE], **“Multiplicity dependence of light (anti-)nuclei production in p-Pb collisions at $\sqrt{s_{\mathrm{NN}}} = 5.02$ TeV”**,
Phys. Lett. B **800**, 135043 (2020).

109. S. Acharya *et al.* [ALICE], **"Measurement of the inclusive isolated photon production cross section in pp collisions at $\sqrt{s} = 7$ TeV"**, Eur. Phys. J. C **79**, 896 (2019).

110. S. Acharya *et al.* [ALICE], **"Scattering studies with low-energy kaon-proton femtoscopy in proton-proton collisions at the LHC"**, Phys. Rev. Lett. **124**, 092301 (2020).

111. S. Acharya *et al.* [ALICE], **"Inclusive J/ψ production at mid-rapidity in pp collisions at $\sqrt{s}$ = 5.02 TeV"**, JHEP **10**, 084 (2019).

112. S. Acharya *et al.* [ALICE], **"Charged-particle production as a function of multiplicity and transverse spherocity in pp collisions at $\sqrt{s} = 5.02$ and 13 TeV"**, Eur. Phys. J. C **79**, no.10, 857 (2019).

113. S. Acharya *et al.* [ALICE], **"Study of the Λ-Λ interaction with femtoscopy correlations in pp and p-Pb collisions at the LHC"**, Phys. Lett. B **797**, 134822 (2019).

114. S. Acharya *et al.* [ALICE], **"Production of muons from heavy-flavour hadron decays in pp collisions at $\sqrt{s}$ = 5.02 TeV"**, JHEP **09**, 008 (2019).

115. S. Acharya *et al.* [ALICE], **"Measurement of the production of charm jets tagged with D^0 mesons in pp collisions at $\sqrt{\mathrm{s}} = 7$ TeV"**, JHEP **08**, 133 (2019).

116. S. Acharya *et al.* [ALICE], **"Exploration of jet substructure using iterative declustering in pp and Pb–Pb collisions at LHC energies"**, Phys. Lett. B **802**, 135227 (2020).

117. S. Acharya *et al.* [ALICE], **“Measurement of charged jet cross section in pp collisions at $\sqrt{s} = 5.02$ TeV”,**
     Phys. Rev. D **100**, 092004 (2019).

118. S. Acharya *et al.* [ALICE], **“Measurement of jet radial profiles in Pb?Pb collisions at $\sqrt{s_{\rm NN}} = \mathbf{2.76}$ TeV”,**
     Phys. Lett. B **796**, 204 (2019).

119. S. Acharya *et al.* [ALICE], **“First Observation of an Attractive Interaction between a Proton and a Cascade Baryon”,**
     Phys. Rev. Lett. **123**, 112002 (2019).

120. S. Acharya *et al.* [ALICE], **“Coherent J/ψ photoproduction at forward rapidity in ultra-peripheral Pb-Pb collisions at $\sqrt{s_{\rm NN}} = 5.02$ TeV”,**
     Phys. Lett. B **798**, 134926 (2019).

121. S. Acharya *et al.* [ALICE], **“One-dimensional charged kaon femtoscopy in p-Pb collisions at $\sqrt{s_{\rm NN}} = \mathbf{5.02}$ TeV”,**
     Phys. Rev. C **100**, 024002 (2019)

122. S. Acharya *et al.* [ALICE], **“Measurement of strange baryon–antibaryon interactions with femtoscopic correlations”,**
     Phys. Lett. B **802**, 135223 (2020).

123. S. Acharya *et al.* [ALICE], **“Investigations of Anisotropic Flow Using Multiparticle Azimuthal Correlations in pp, p-Pb, Xe-Xe, and Pb-Pb Collisions at the LHC”,**
     Phys. Rev. Lett. **123**, 142301 (2019).

124. S. Acharya *et al.* [ALICE], **“Multiplicity dependence of (anti-)deuteron production in pp collisions at $\sqrt{s} = \mathbf{7}$ TeV”,**
     Phys. Lett. B **794**, 50 (2019).

125. S. Acharya *et al.* [ALICE], **“Calibration of the photon spectrometer PHOS of the ALICE experiment,**
JINST **14**, P05025 (2019).

126. S. Acharya *et al.* [ALICE], **“Measurement of** D^0 **,** D^+ **,** D^{*+} **and** D_s^+ **production in pp collisions at** $\sqrt{s} = 5.02$ **TeV with ALICE,**
Eur. Phys. J. C **79**, 388 (2019).

127. S. Acharya *et al.* [ALICE], **“Event-shape and multiplicity dependence of freeze-out radii in pp collisions at** $\sqrt{s} = \mathbf{7}$ **TeV,**
JHEP **09**, 108 (2019).

128. S. Acharya *et al.* [ALICE], **“Real-time data processing in the ALICE High Level Trigger at the LHC,**
Comput. Phys. Commun. **242**, 25 (2019).

129. S. Acharya *et al.* [ALICE], **“Charged-particle pseudorapidity density at mid-rapidity in p-Pb collisions at** $\sqrt{s_{\mathrm{NN}}} = \mathbf{8.16}$ **TeV,**
Eur. Phys. J. C **79**, 307 (2019).

130. S. Acharya *et al.* [ALICE], **“Study of J/**ψ **azimuthal anisotropy at forward rapidity in Pb-Pb collisions at** $\sqrt{s_{\mathrm{NN}}} = 5.02$ **TeV,**
JHEP **02**, 012 (2019).

131. S. Acharya *et al.* [ALICE], **“Jet fragmentation transverse momentum measurements from di-hadron correlations in** $\sqrt{s} = \mathbf{7}$ **TeV pp and** $\sqrt{s_{\mathrm{NN}}} = \mathbf{5.02}$ **TeV p-Pb collisions,**
JHEP **03**, 169 (2019).

132. S. Acharya *et al.* [ALICE], **“**Λ_c^+ **production in Pb-Pb collisions at** $\sqrt{s_{\mathrm{NN}}} = 5.02$ **TeV,**
Phys. Lett. B **793**, 212 (2019).

133. S. Acharya *et al.* [ALICE], **“Event-shape engineering for the D-meson elliptic flow in mid-central Pb-Pb collisions at $\sqrt{s_{\rm NN}} = 5.02$ TeV,**
JHEP **02**, 150 (2019).

134. S. Acharya *et al.* [ALICE], **“Measuring $\mathbf{K^0_S K^\pm}$ interactions using pp collisions at $\sqrt{s} = 7$ TeV,**
Phys. Lett. B **790**, 22 (2019).

135. S. Acharya *et al.* [ALICE], **“Energy dependence of exclusive J/ψ photoproduction off protons in ultra-peripheral p–Pb collisions at $\sqrt{s_{\rm NN}} = 5.02$ TeV,**
Eur. Phys. J. C **79**, 402 (2019).

136. S. Acharya *et al.* [ALICE], **“Charged jet cross section and fragmentation in proton-proton collisions at $\sqrt{s}$ = 7 TeV,**
Phys. Rev. D **99**, 012016 (2019).

137. S. Acharya *et al.* [ALICE], **“Multiplicity dependence of light-flavor hadron production in pp collisions at $\sqrt{s}$ = 7 TeV,**
Phys. Rev. C **99**, 024906 (2019).

138. S. Acharya *et al.* [ALICE], **“Medium modification of the shape of small-radius jets in central Pb-Pb collisions at $\sqrt{s_{\rm NN}} = 2.76\,{\rm TeV}$,**
JHEP **10**, 139 (2018).

139. S. Acharya *et al.* [ALICE], **“Measurement of dielectron production in central Pb-Pb collisions at $\sqrt{s_{\rm NN}}$ = 2.76 TeV,**
Phys. Rev. C **99**, 024002 (2019).

140. S. Acharya *et al.* [ALICE], **“p-p, p-Λ and Λ-Λ correlations studied via femtoscopy in pp reactions at $\sqrt{s}$ = 7 TeV,**
Phys. Rev. C **99**, 024001 (2019).

141. S. Acharya *et al.* [ALICE], “$\mathrm{f}_0(980)$ **production in inelastic pp collisions at** $\sqrt{s} = 5.02$ **TeV”,**
arXiv:2206.06216 nucl-ex].

142. S. Acharya *et al.* [ALICE], **“Anisotropic flow and flow fluctuations of identified hadrons in Pb−Pb collisions at** $\sqrt{s_{\mathrm{NN}}} = 5.02$ **TeV”,**
arXiv:2206.04587 nucl-ex].

143. S. Acharya *et al.* [ALICE], **“Observation of flow angle and flow magnitude fluctuations in Pb-Pb collisions at** $\sqrt{s_{\mathrm{NN}}} = 5.02$ **TeV at the LHC”,**
arXiv:2206.04574 [nucl-ex].

144. S. Acharya *et al.* [ALICE], **“Closing in on critical net-baryon fluctuations at LHC energies: cumulants up to third order in Pb−Pb collisions”,**
arXiv:2206.03343 [nucl-ex].

145. S. Acharya *et al.* [ALICE], **“Towards the understanding of the genuine three-body interaction for p−p−p and p−p−**Λ**”,**
arXiv:2206.03344 [nucl-ex].

146. S. Acharya *et al.* [ALICE], **“Constraining the** $\overline{\mathrm{K}}\mathrm{N}$ **coupled channel dynamics using femtoscopic correlations at the LHC”**
arXiv:2205.15176 [nucl-ex].

147. S. Acharya *et al.* [ALICE], “$\Sigma(1385)^{\pm}$ **resonance production in Pb-Pb collisions at** $\sqrt{s_{\mathrm{NN}}} = 5.02$ **TeV”**
arXiv:2205.13998 [nucl-ex].

148. S. Acharya *et al.* [ALICE], **“First measurement of** Ω_{c}^{0} **production in pp collisions at** $\sqrt{s} = 13$ **TeV”,**
arXiv:2205.13993 [nucl-ex].

Conference proceedings: ,

1. **"Insight into J/ψ production with hard-QCD and RAA like factor in high multiplicity p+p collisions at $\sqrt{s}$ = 13 TeV"**
   Suman Deb, Dhananjaya Thakur, Sudipan De, and Raghunath Sahoo,
   DAE Symp.Nucl.Phys. 63, (2018) 918-919.

2. **"Energy and rapidity dependence of J/ψ production as function of charged-particle multiplicity in different event shapes"**
   Anisa Khatun, Dhananjaya Thakur, **Suman Deb**, and Raghunath Sahoo,
   DAE Symp.Nucl.Phys. 64, (2019) 768-769.

3. **"Understanding Medium formation in Small system using heat capacity at the Large Hadron Collider Energies"**
   Suman Deb, Golam Sarwar, Raghunath Sahoo, and Jan-e Alam,
   DAE Symp.Nucl.Phys. 64, (2020) 714-715.

4. **"Modeling Initial condition for Proton-Proton Collisions at the LHC energies"**
   Suman Deb, Golam Sarwar, Dhananjaya Thakur, Pavish S., Raghunath Sahoo, and Jan-e Alam,
   DAE Symp.Nucl.Phys. 64, (2020) 786-787.

5. **"Extension of Glauber-like model for Proton-Proton collisions using anisotropic and inhomogeneous density profile"**
   Suman Deb, Golam Sarwar, Dhananjaya Thakur, Pavish S., Raghunath Sahoo, and Jan-e Alam,
   PoS LHCP2021, 225 (2021).

6. **"Implementation of machine learning techniques to predict impact parameter and transverse spherocity in heavy-ion collisions**

at the LHC"
Aditya Nath Mishra, Neelkamal Mallick, Sushanta Tripathy, **Suman Deb** and Raghunath Sahoo,
PoS LHCP2021, 265 (2021) .

7. **"Multiplicity Dependence of Charmonia Suppression in pp Collisions at the LHC Energies"**
   Captain R. Singh, **Suman Deb**, Raghunath Sahoo, and Jan-e Alam,
   DAE Symp.Nucl.Phys. 65, (2022) 670-671.

8. **"Estimation of impact parameter and transverse spherocity in heavy-ion collisions at the LHC using machine learning techniques"**
   Neelkamal Mallick, Sushanta Tripathy, Aditya Nath Mishra, **Suman Deb** and Raghunath Sahoo,
   DAE Symp.Nucl.Phys. 65, (2022) 642-643.

Contents

List of Figures

Tables

Chapter 1

Introduction

"Understanding the history of matter and searching for its most interesting forms, such as galaxies, stars, planets and life, seems a suitable use for our intelligence."

- Robert Kirshner

With its unprecedented available energies, the Large Hadron Collider (LHC) at CERN, Geneva, has provided an opportunity to study the deconfined colored medium known to exist microseconds after the Big Bang called quark-gluon plasma (QGP) [1]. Although, till now, a complete theoretical understanding of the formation and evolution of such a medium is not known, a phenomenological framework called the "standard model of heavy-ion physics" has been considered by the scientific community. This framework assumes that energy densities required to form QGP are only accessible by the ultra-relativistic heavy-ion collisions. Since 2010 and 2015, QGP at LHC is produced by lead on lead (Pb-Pb) collisions at a center-of-mass energy ($\sqrt{s_{NN}}$) 2.76 TeV and 5.02 TeV respectively. In the year between 2012 and 2013, to study Cold nuclear matter (CNM) effects like hadronic reabsorption, LHC made proton on lead (p-Pb) collisions at $\sqrt{s_{NN}} = 5.02$ TeV. But to utter surprise, studies like correlations and multiplicity-dependent particle production also show hints of thermalized medium formation in p-Pb collisions. This observation forms the main motivation of this thesis to explore the presence of QGP-droplets in even smaller systems like proton on proton (pp).

In this chapter, to form the stage for the works presented in this thesis, we briefly introduce the Standard Model of particle physics in the section 1.1 and the theory of strong interaction known as quantum chromodynamics (QCD) in the section 1.2. Section 1.3 is devoted to quark-gluon plasma, its formation in ultra-relativistic collisions and signatures. We have presented a brief description of recent experimental observations of possible medium formation in pp collisions, which forms the motivation of this thesis in section 1.4. Finally, the last section 1.5 gives the motivation of the thesis.

1.1 The Standard Model of Particle Physics

"What are the basic constituents of matter or what are the elementary particles?", has been one of the fundamental questions since the dawn of human civilization. Through experiments, several thinkers of various generations tried to answer this question. The answer to this question had a fascinating journey from the atom to partons (quarks and gluons) through nucleons (protons and neutrons). Quarks occur in various flavors and generations, out of which up (u) and down (d) quarks are the most abundant in the Universe. A set of two u and a d quarks bounded together by gluons form a proton (positively charged), while a neutron (electrically neutral) is composed of a set of two d quarks and a u quarks. This bound state is called hadrons. A hadron consisting of a pair of quark and antiquark is known as meson, while the combination of three quarks to form a hadron is known as baryon. To date, no experimental evidence of the internal structure of quarks or gluons has been found, and thus they are thought to be elementary particles. As a consequence, only hadrons are experimentally observed. Given the dimension of these hadrons ($\sim$ femtometers), this quest took us to the realm of high-energy particle accelerators. Over time, a huge number of particles were proposed (theoretically) and subsequently discovered in experiments. To classify, understand the matter and their interaction, the Standard Model (SM) of particle physics is developed mainly by Glashow, Salam, and Wienberg in the 1970s [2–4]. This model was celebrated for its high precision explanation of experimental results. In the SM framework, all visible matter in the Universe comprises twelve elementary particles (namely quarks and leptons), four gauge bosons, and a Higgs boson. This classification is depicted in Fig. 1.1. All particles within the frame of SM are categorized into fermions and bosons based on their spin, a quantum number that describes the intrinsic angular momentum of the particle. It can be either half or unity (zero). Moreover, each of the fermions has a distinct antiparticle, having the same mass but opposite electrical charge. Interaction among fermions occurs with the exchange of bosons. All fermions (quarks and leptons) are further grouped into three generations: up, down quarks, electron, and electron neutrino, belong to the first generation. All other generations are shown in Fig. 1.1. It is worth noting that the lightest (heaviest) known particles belong to the first (third) generation of the Standard model. This fact is seen in the timeline of their experimental discoveries, as heavier particles are produced at higher energies. In spite of the massive success of SM, the existence of dark matter, neutrino masses, and matter-antimatter asymmetry in the Universe indicate that there is physics beyond the Standard model.

The Standard model has further described the three fundamental forces in nature: electromagnetic, weak, and strong. In 1979, the Noble Prize in Physics was given for the unification of electromagnetic and weak forces into electroweak forces. This force mediates through the exchange of massive W, Z bosons, and massless photons. And the strong forces are mediated via the exchange of gluons, massless colored objects. To understand the various interactions prescribed in SM, there are versions of quantum field theories (QFT), like Quantum electrodynamics (QED) governs the electromagnetic interaction while strong interaction is governed by quantum chromodynamics (QCD). Since this thesis deals with the study of dynamics of particles produced in collider physics where relevant forces are strong in nature, QCD forms the foundation of the philosophy. And hence QCD will be briefly discussed in the next section.

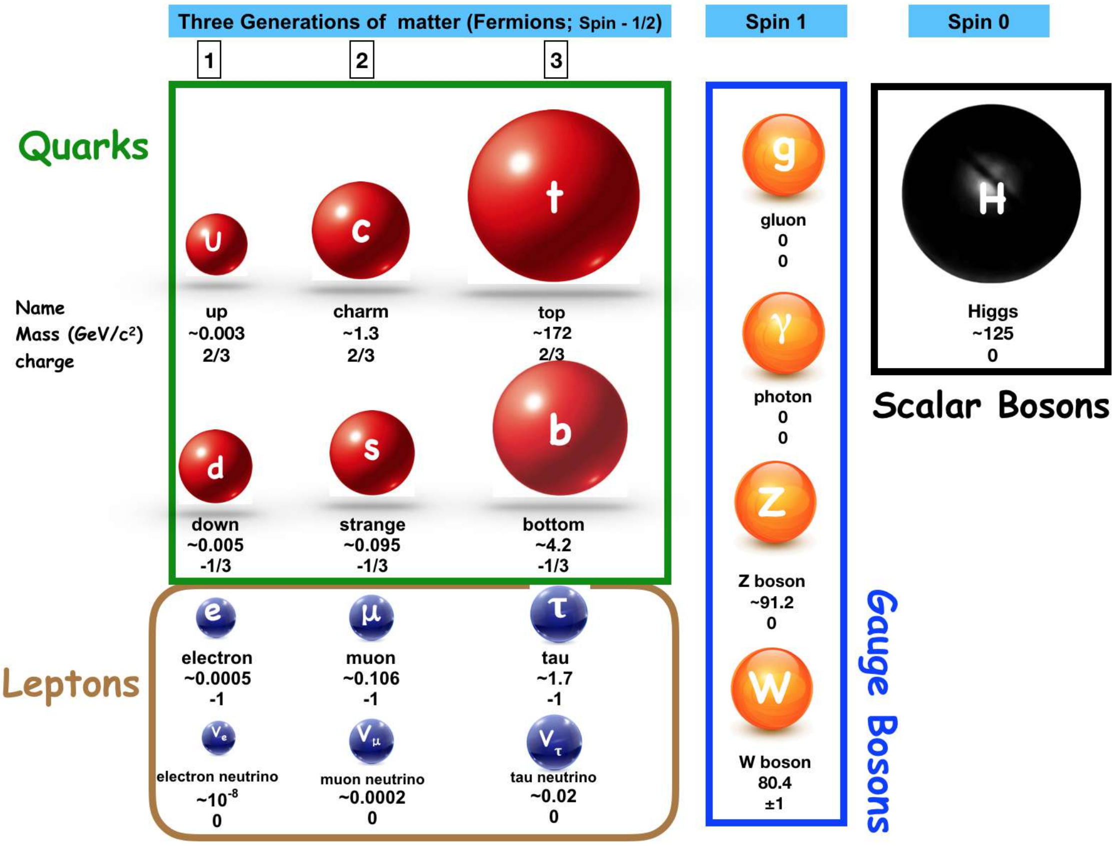

Figure 1.1: All fundamental particles within the Standard Model.

1.2 Quantum Chromodynamics (QCD): the theory of strong interaction

QCD is responsible for describing the interaction between quarks and gluons, having the color quantum numbers. Unlike QED, the gauge boson of QCD can interact with each other and binds quarks into color-neutral hadrons. At low energy scales, quantum chromodynamics can be studied on a lattice where each point in the grid represents a certain point in space-time. This approach is known as lattice QCD (LQCD) [5]. It gives the potential between two colored charges as,

$$V_{QCD}(r) \approx -\frac{\alpha_S}{r} + \kappa r, \tag{1.1}$$

where α_S is the strong coupling constant, also known as the running coupling constant. κ is the color string tension constant and found to be around 1 GeV fm^{-1} [6], and r is the separation distance between two colored charges. Since gluons can self-interact, the scale dependence of α_S differs from the coupling constant in QED. This implies that two one-loop diagram (virtual gluon and virtual quark loop) in QCD couplings has to be considered. It is found that with a decrease in energy scale, α_S increases because of the larger contribution of the virtual gluon loop than the quark loop. This can be understood from the antiscreening effect. The massless gluon radiated from the quark, which has spontaneously changed its color, can either form a quark loop or a gluon loop. In the case of a quark loop, because of the presence of quark and antiquark, a negative contribution will lead to an overall weakening of the color field. Meanwhile, in the case of the gluon loop, there will be a strong color field between the two gluons, resulting in a stronger field. This is called the antiscreening effect, where a colored particle far away from such an environment will see a stronger field created by a cloud of gluons and a quark rather than a field created by a single initial quark. However, in 1973, WilcZek, Gross, and Politzer observed that α_S at large energies becomes weaker as a highly energetic parton can penetrate the gluon cloud and sees fewer color charges accumulated at the origin. This behavior is called asymptotic freedom, and they were awarded a Noble Prize in Physics for their explanation.

Further, the QCD running coupling constant as a function of momentum transfer (Q^2) is given as,

$$\alpha_s(Q^2) = \frac{12\pi}{(33 - 2n_f)ln(\frac{Q^2}{\Lambda^2_{QCD}})}, \tag{1.2}$$

Where n_f is the quark flavors accessible at Q^2 and Λ_{QCD} is the QCD scale. For $\Lambda_{QCD} \lesssim 200$ MeV, the non-perturbative QCD is in action. Its magnitude is interpreted as a scale disentangling the regime of QCD where α_s is small from that where α_s is large. For example, at Q $\gtrsim \Lambda_{QCD}$, Eq. 1.2 gives $\alpha_s < 1$, this implies color charges approach towards asymptotic freedom and perturbative QCD is used to study strong interactions. This domain is referred to as a hard QCD regime because of the involvement of large momentum transfer. Similarly, at Q $\lesssim \Lambda_{QCD}$, Eq. 1.2 gives $\alpha_s > 1$, implies a dominance of strong force. This domain is referred to as soft QCD because of the association of low momentum transfer. In the soft QCD regime, due to the high value of the QCD coupling constant, quarks are confined within hadrons, and this is known as color confinement. Thus QCD is characterized by these two properties, namely, asymptotic freedom and color confinement. The behavior of QCD running coupling constant as a function of momentum transfer (Q) obtained by various experiments is shown in Fig. 1.2.

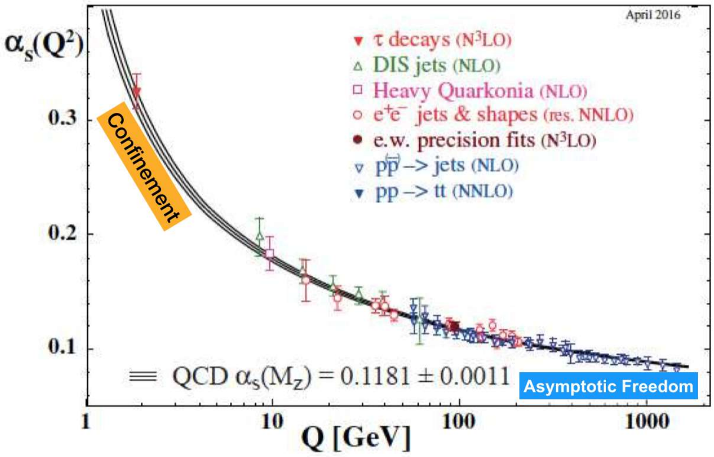

Figure 1.2: QCD coupling constant as a function of momentum transfer [7]. Lines represents the scaling predications [8].

1.2.1 Thermodynamics of QCD matter

Lattice QCD calculates the temperature dependence of energy density (ϵ) and pressure (P) in the QCD medium. The result of this calculation is shown in Fig. 1.3 [9]. In the temperature range between 150 to 200 MeV, the abrupt rise of ϵ/T^4 is observed, followed by a slow saturation towards high temperature below the Stefan-Boltzmann limits. This indicates a rapid change in thermodynamical properties in this temperature range. This can be understood by linking an increase in the partonic number of degrees of freedom (Ndof) from hadronic Ndof, which results in a phase transition. This modification in the number of degrees of freedom suggests that the QCD medium had undergone a phase transition in going from hadronic to partonic medium, which led to a change in its entire thermodynamical properties.

1.2.2 The Conjectured QCD phase diagram

The best way to understand this change in the behavior of the QCD matter is through a conjectured QCD phase diagram. This phase diagram illustrates the different states of QCD matter at its temperature (T) and net baryon density (μ_B), also known as chemical potential. It is the energy required to increase the total number of baryons and anti-baryons in a system by unity. At the microscopic level, due to particle creation and annihilation, the baryon number in a system may not be conserved at the relativistic energies. Hence μ_B was introduced. Figure 1.4 shows this conjectured QCD phase diagram. It can be seen that at low chemical potential and temperature, QCD matter consists of bound hadrons and as μ_B increases at a constant low temperature, the wave function associated with the hadrons begins to overlap. At some coordinates of T and μ_B, this overlap becomes so large that quarks no longer see the nucleonic density; it is initially bounded into and can interact with quarks from other nucleons in the system. In this transition, the thermodynamic of the system begin to alter drastically,

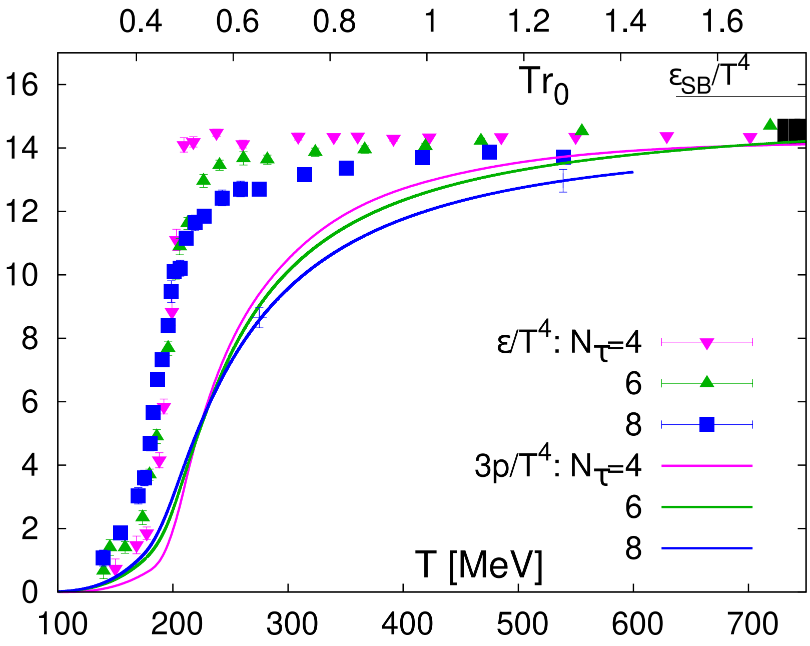

Figure 1.3: Lattice QCD predictions of energy density (points) and pressure (curves) of the QCD medium as a function of temperature and normalised by the critical temperature (T_C). ϵ_{SB}/T^4 is the Stefan-Boltzmann limit. Different colors are for different lattice constants [9].

and a new state of matter is created, called the quark-gluon plasma [1]. This phase transition at low temperature from hadron gas to QGP is a first-order transition, and it occurs spontaneously. However, towards the low μ_B domain, this transition from hadronic matter to QGP can be achieved by simply increasing the temperature of the hadronic matter itself. But, here, the thermodynamical parameters begin to alter continuously rather than instantaneously, as observed in the high chemical potential in low-temperature regions. This region is known as "cross-over". In fact, this is the same scenario predicated to exist in the early universe. Due to the presence of these two kinds of phase transitions in the QCD phase diagram, it is highly expected the existence of a critical point. It is a point of second-order phase transition. In a nutshell, as shown in Fig. 1.4, as one move towards the low μ_B region from the high μ_B region, the QCD phase transition between hadronic matter and QGP is the first order in nature until the critical point is reached. This point is a second-order phase transition, and then the transition is simply thermal breakdown (called as cross-over). The next section 1.2 will briefly describe QGP in large systems, its formation in ultra-relativistic heavy-ion collisions, followed by its evolution in space and time, and its signature with relevant experimental shreds of evidence.

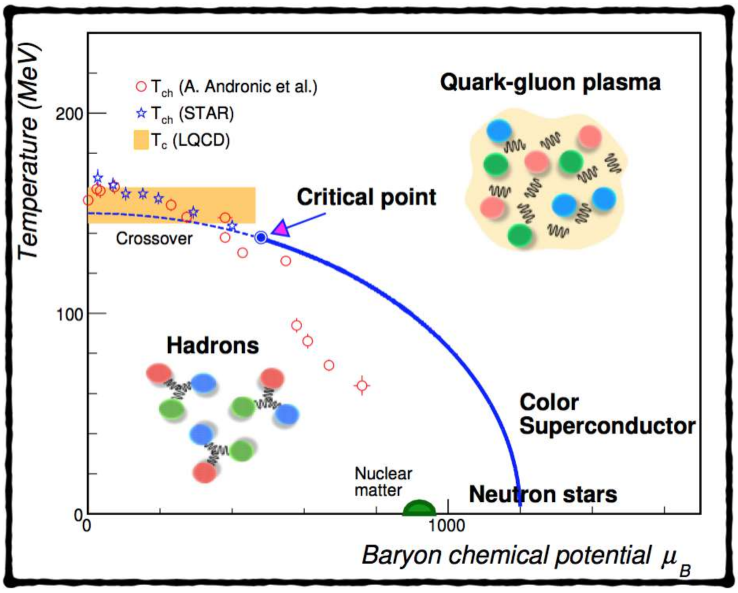

Figure 1.4: Conjectured phase diagram of the QCD matter [10].

1.3 Quark-gluon Plasma (QGP) in Large system

As discussed in earlier section 1.2.2, lattice QCD, along with thermodynamical considerations, predicts that the strong force of interaction would show unique characteristics under extreme conditions. For instance, at high temperature (T $\gtrsim$ 200 MeV), the boundary of hadrons disintegrates into a deconfined state of quarks and gluons, forming a hot and dense state of matter with dramatically different thermodynamic parameters than hadron gas. And this state of matter is called the QGP [1]. This unique state of matter can be created experimentally by the ultra-relativistic collisions of heavy ions (HIC). Once formed, QGP expands quickly due to high-pressure gradients. It subsequently cools down as it expands in volume, where because of color confinement, the colored quarks bind back to hadrons. It is estimated that the lifetime of the QGP phase is $\sim 10^{-22}s$.

1.3.1 Ultra-relativistic collisions of heavy ions

To create and study the evolution of QGP, the first heavy-ion collision was performed in Alternating Gradient Synchrotron (AGS) at Relativistic Heavy Ion Collider (RHIC), Brookhaven National Laboratory (BNL), USA, which is followed by Super Proton Synchrotron (SPS) at the Large Hadron Collider (LHC). In these colliders, two Lorentz contracted nuclei (due to acceleration at ultra-relativistic velocities) traveling in opposite directions along the beam axis are made to collide. This is depicted in Fig. 1.5. The part of nuclei taking part in the actual collisions is called the overlap region, which depends on the impact parameter (b). It is a perpendicular separation between the centers of the colliding nuclei. The nucleons participating in the collisions and residing inside the overlap region are called participants. In contrast, those who do not participate and are outside the overlap region are called spectators.

1.3.2 Formation of strongly interacting medium in relativistic heavy-ion collisions

The least understood aspect of relativistic heavy-ion collisions is the formation of QGP. Most of the models only consider the evolution of QGP, assuming its formation. At present, the collisions of color glass condensates (CGC) are considered the most viable mechanism for forming the QGP. This model is based on the fact that there is a rapid increase in gluon density with decreasing Bjorken scale (x_T). x_T is the fraction of transverse momentum of a hadron carried by a

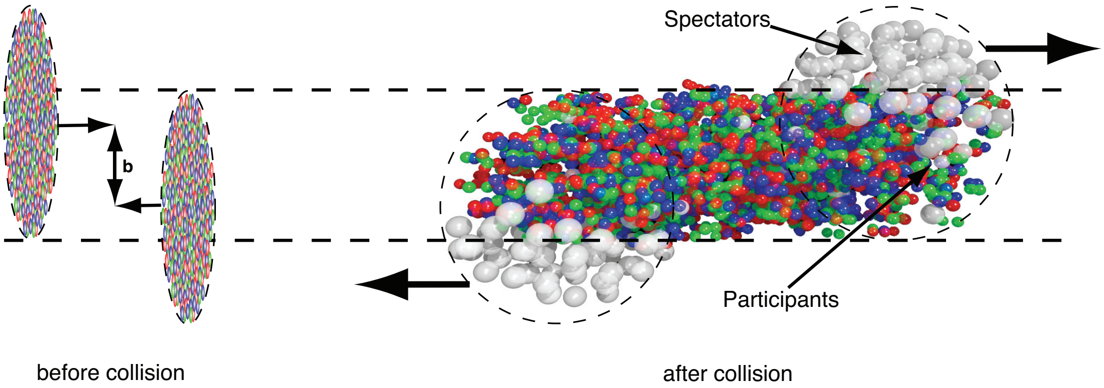

Figure 1.5: Ultra-relativistic heavy-ion collisions of two Lorentz contracted nuclei with an impact parameter [11].

parton. This scenario is shown in Fig. 1.6. At some energy scale (Q), because of limited volume, the number of low x_T gluons will saturate, forming very dense gluonic fields. With respect to the lab frame, these gluonic clouds will appear to be squeezed because of the Lorentz contraction, which will cause a weak coupling strength among the low x_T gluons. Moreover, the ultra-relativistic velocities would subject the lifetime of the gluons to time dilation leading to their slow evolution compared to the time scales involved. Thus, a weakly coupled and a very high energy density of gluons is inherited in a hadron moving with a relativistic velocities even before the collisions. Now during the collision, these two gluon densities passing each other will produce strong electric and magnetic fields. The medium of these fields is called glasma. By decaying into gluons, this glasma equilibrates and forms the quark-gluon plasma.

1.3.3 Space-time evolution of ultra-relativistic collisions

A labeled schematic diagram of the space-time evolution of ultra-relativistic nucleus-nucleus collision with the possibility of QGP formation is presented in Fig. 1.7. Let us consider a heavy ion collision occuring at the coordinate (z,τ) = (0,0), where z and τ are the space and time coordinates, respectively. A hot and

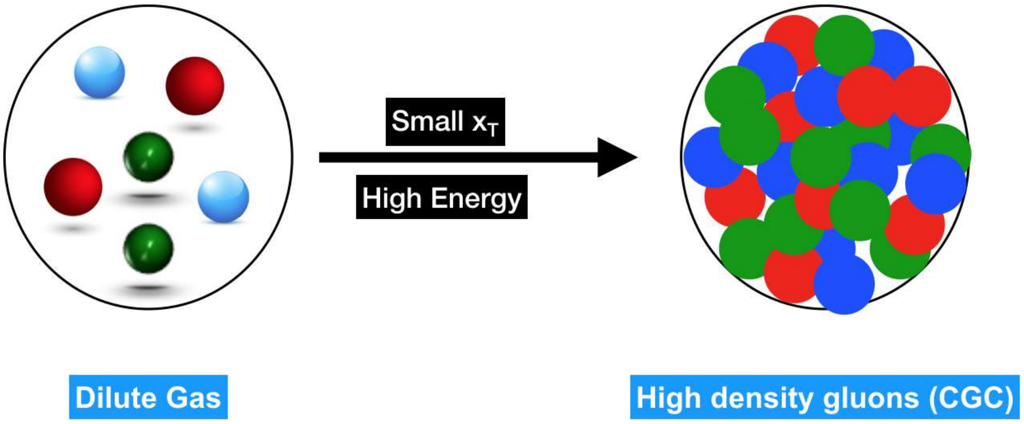

Figure 1.6: Depiction of Color Glass Condensate (CGC) model.

dense matter is expected to be produced in the central heavy-ion collision (characterized by zero impact parameter), and its evolution is depicted in Fig. 1.7. A brief discussion of each stage of the evolution is given below.

- **Pre-equilibrium phase:** This phase seems to exist for evolution time $(\tau) \leq 1\ fm/c$. During this time, partons undergo inelastic interaction to produce numerous deconfined quarks and gluons. Since it is an initial stage of the evolution of collisions, most of the particles produced in this stage are via hard QCD processes and carry high transverse momentum. At this stage, the matter consists of a non-equilibrium state of partons.

- **Formation and hydrodynamical evolution of QGP:** The non-equilibrium partons from the previous stage can evolve to the final stage by interacting (both elastic and inelastic) with each other. This interaction becomes significant for the central collisions, where the energy density is so high that the produced partons are far from independent. Eventually, it approaches thermal equilibrium with thermalization time $\sim 1\ fm/c$. At this stage, a high-temperature QCD matter is formed called quark-gluon plasma. A hydrodynamical description can very well explain the evolution of a locally thermalized QGP. This suggests that the medium formed in heavy ion collisions behaves like a strongly coupled liquid rather than a weekly interacting gas [12]. The hydrodynamical expansion of the system is caused by the high internal pressure gradients, which are in turn caused by the inhomogeneities in the medium densities within the QGP. As the system expands rapidly, it cools down until the phase transition, beyond which the colored partons start to form a colorless hadronic states. At this point, a hadronic description of the system is required. This phase is also known as the mixed phase.

- **Chemical freeze-out:** After the mixed phase, the system continues to maintain inelastic hadronic interaction/scatterings. This is supposed to maintain some kind of chemical equilibrium. As the system cools downs, these scatterings ceases, and left-out hadrons now interact elastically. Chemical freeze-out is the transition from inelastic scatterings to an elastic interaction of hadronic gas. It is quantified by a chemical freeze-out temperature (T_{ch}). At this stage, the relative abundance of the stable particle becomes fixed. According to thermal model, the current estimated value of $T_{ch} \sim$ 145-166 MeV [13].

- **Kinetic freeze-out:** The expansion and cooling of the system continue after the chemical freeze-out, but now hadrons interact only elastically. During this phase, the resonance particle (both light and heavy) decays into long-lived stable states. Even this elastic scattering ceases to exist at some temperature (T_{kin}) when the mean free path (λ) of a hadron is of the same order as the system size (r). Beyond this, the transverse momentum (p_{T}) distribution of the hadrons is fixed, and T_{kin} is known as kinetic freeze-out temperature. When the λ becomes much greater than r, all the final state particles start to stream freely and are eventually detected in the detectors.

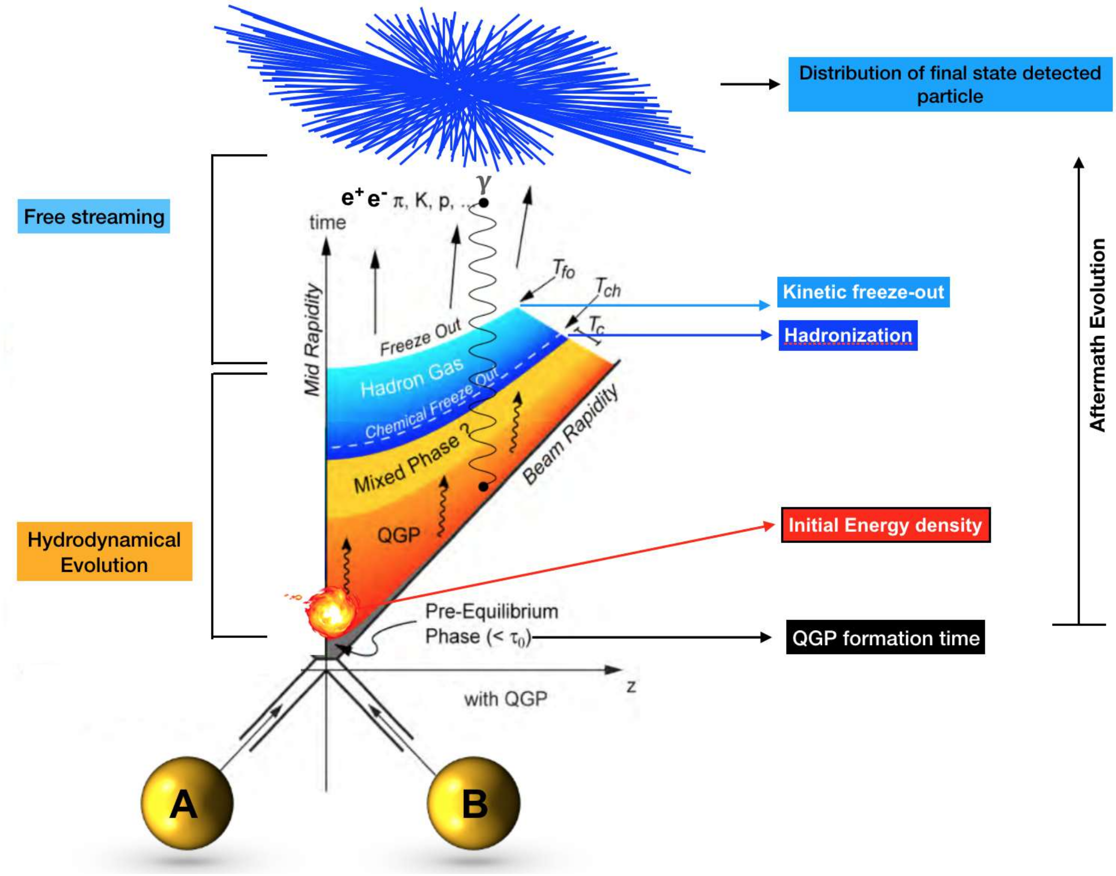

Figure 1.7: Space-time evolution of relativistic heavy-ion collisions.

Alternatively, suppose the QCD matter forms in the heavy-ion collisions and does not meet the condition of high energy density/temperature. In that case, the system has only a hadronic degree of freedom. A pre-hadronic phase is created after collisions, followed by nucleon recombines to form new hadrons. After the hadronic freeze-out, the produced hadrons are detected in the detectors. This is depicted in Fig. 1.8. This picture of space-time evolution is believed to occur in hadronic collisions. However, in recent time, the scientific community has started considering the space-time evolution of heavy-ion for small systems like pp collisions as well. This has opened a new direction toward the study of hadronic physics, which is further discussed in section 1.3 of the chapter.

Experiments measure the position and momentum of the final-state detected particles in the detectors to better study the space-time evolution of relativistic collisions and other global observables to probe the formation of a strongly interacting matter. Thus one must have a sound knowledge of kinematic variables involved in the relativistic collisions, which could be found in the ref. [14].

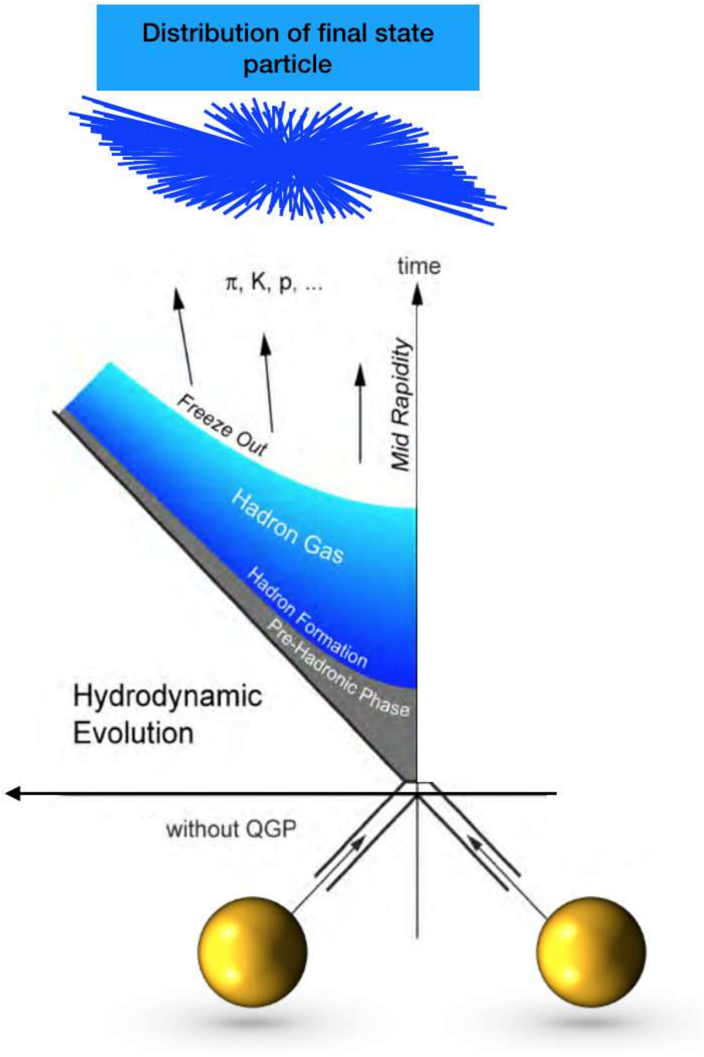

Figure 1.8: Space-time evolution of relativistic heavy-ion collisions with a no QGP scenario.

1.3.4 QGP signatures and corresponding experimental evidences

Unlike ordinary electromagnetic plasma, QGP is not observed directly due to its short lifetime of $\sim 10^{-23}$ sec or $\sim 3\ fm/c$. However, the formation of a QGP medium can be confirmed by various indirect signatures or measurements. One can infer these indirect signatures of QGP from the measurement of final-state quantities like charged-particle pseudorapidity densities, energy and transverse momentum spectra of particles, anisotropic flow, etc. It is worth mentioning that these signatures in heavy-ion collisions are probed by assuming pp collisions as a baseline. Some of the signatures of QGP formation in heavy-ion collisions are enhancement of strangeness, the observation of high-temperature matter, high energy density, azimuthal anisotropy, elliptic flow, J/ψ suppression, collective radial expansion, etc [15]. A brief discussion on some of these signatures is given below.

- **J/ψ suppression:** J/ψ is a bound state of charm and anti-charm quark ($c\bar{c}$). Since J/ψ (because of its mass) is expected to be produced at the early stages of the hadronic or nuclear collisions, it serves as an excellent tool to understand the dynamics of the medium formed in the heavy-ion collisions. Color Debye screening in the QGP medium, due to the presence of quarks and gluons, resists a charm quark to combine with an anti-charm quark to form a bound state. This screening reduces the production of J/ψ in heavy-ion collisions, and it is marked by the increase in the production of open charm hadrons like D^0, $D^{\pm}$, which are composed of charm and a light quark. Thus, J/ψ suppression serves as a signature of QGP. Experimentally, this suppression was first reported in SPS [16] and then in RHIC [17], which confirms the formation of QGP. The nuclear modification factor (R$_{AA}$) of J/ψ as a function of centrality at RHIC and LHC energies is shown in

Fig. 1.9. It is observed that the J/ψ is more suppressed in the RHIC heavy-ion collision than at the LHC. This is because of the relatively high collision energy at the LHC, where the competition between suppression and regeneration/recombination arises. At the LHC, J/ψ could also be produced from the decay of higher quarkonia states, hence compensating for the suppressed J/ψ production in the final state than in the RHIC.

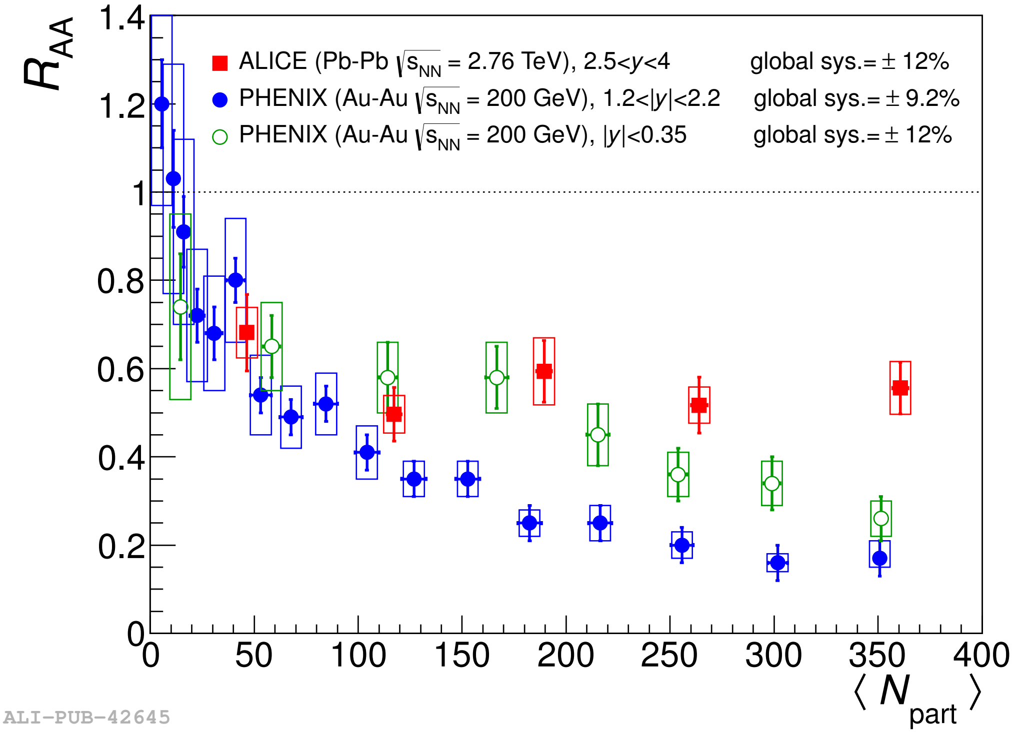

Figure 1.9: R_{AA} of J/ψ as a function of average number of participant nuceons in Pb+Pb (Au+Au) collisions at $\sqrt{s_{NN}} = 2.76$ TeV (200 GeV) [18].

- **Jet quenching:** In relativistic hadronic or heavy-ion collisions, partons interact through typical scattering processes like $g+g \to g+g$, $q+q \to q+q$, $g+g \to q+\bar{q}$, to produce a large number of partons with high transverse momentum at a very early time. This produced partons spread out in all possible directions from the collision point and eventually fragment into a narrow cone of correlated hadrons. This cone is known as “jets”. When interacting with a thermalized QGP medium, these partons lose their energy before hadronizing. The degree of energy loss is expected to be more for the jet produced inside the bulk of the medium than that produced near the periphery of the QGP medium. Thus, jet quenching is the suppression of jets composed of high-p_{T} particles. This results in the suppression of the number of high-p_{T} particle. Experimentally, the degree of suppression is studied by constructing a observable called a nuclear modification factor (R_{AA}), and it is defined as,

$$R_{AA}(p_T) = \frac{1}{\langle T_{AA} \rangle} \frac{\mathrm{Yield_{AA}}}{\mathrm{Yield_{pp}}}, \tag{1.3}$$

where, $\langle T_{AA} \rangle$ is the mean nuclear overlap function, and it is the ratio of the mean number of binary collisions and inelastic pp cross-section. A unit value of R_{AA} infers that the heavy-ion collisions are just a linear superposition of pp collisions, and there is no medium effect (no QGP formation). However, it is observed that $\mathrm{R}_{AA} < 1$ for identified particles in Pb+Pb or Au+Au collisions [19]. This observation indicates that the QGP medium caused the high-p_{T} particles to lose their energy via multiple interactions when transverse through it. Figure 1.10 shows the results of R_{AA} for charged particles and neutral pions as measured by various experiments. A clear suppression of hadrons both at LHC and RHIC is observed.

- **Enhancement of strange particle:** Enhanced production of the strange particle in the heavy-ion collision has been proposed as the most viable signature of QGP, as the colliding matter has no strange quantum number [20]. The production rate and mechanism of strange particles in the QGP medium are very different from a hadron gas. The study of the abundance of strange particle production between the hadronic and QGP phases will give an idea about the strangeness enhancement. In QGP medium, be-

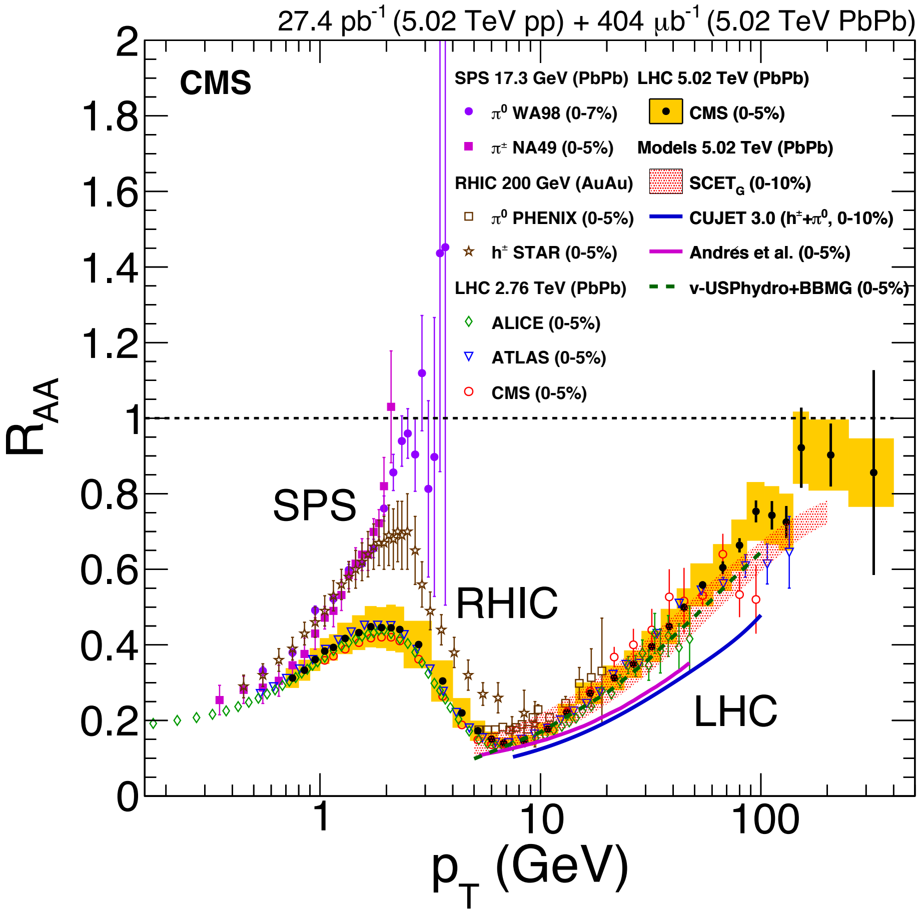

Figure 1.10: Nuclear modification factor as a function of transverse momemtum for neutral pions and identified particles in central collisions at SPS, RHIC and LHC [19].

cause of high gluon density, $s\bar{s}$ pair formed through $gg \rightarrow s\bar{s}$ channel. This channel dominates the $q\bar{q} \rightarrow s\bar{s}$ channel. However, in pp collisions, since no QGP formation is expected, the main channel for producing strange quarks is the annihilation of light quarks to strange quarks. This is quantified through enhancement factor, and it is defined as,

$$Enhancement factor = \frac{2}{\langle N_{part} \rangle} \left. \frac{\text{Yield}_{\text{AA}}}{\text{Yield}_{\text{pp}}} \right|_{y=0}, \tag{1.4}$$

where, $\langle N_{part} \rangle$ is the average number of participants (centrality). The yield of hyperons enhancement factor as a function $\langle N_{part} \rangle$ is shown in Fig. 1.11 [21]. This enhanced production of the strange particle in Pb+Pb collisions relative to pp collisions indicates the formation of QGP in LHC energies. Further, the enhancement factor is observed to be higher for hadron with more number of strange quarks.

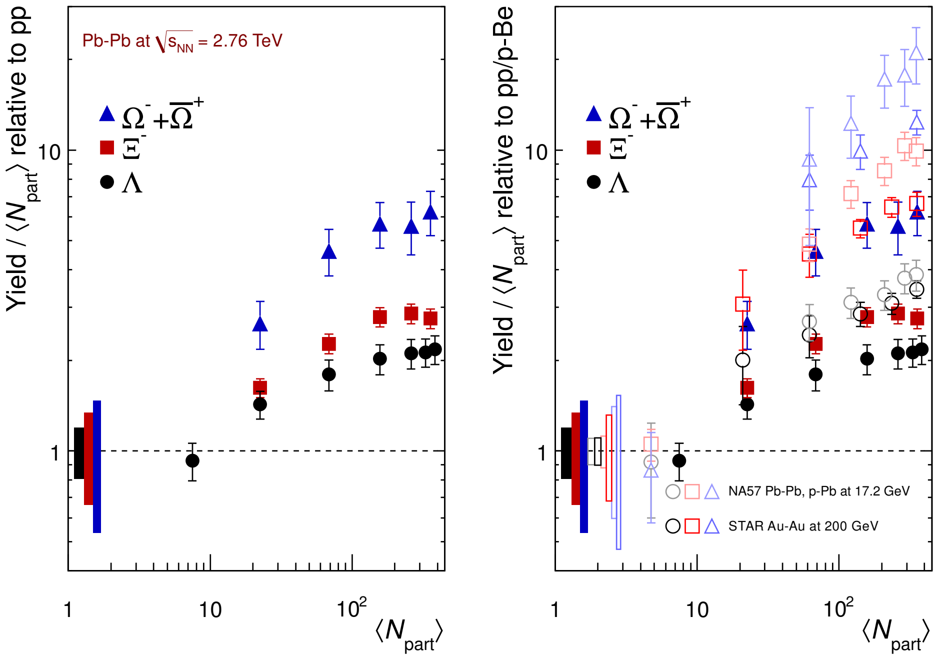

ALI-DER-80680

Figure 1.11: The yield of multi-strange hadrons in Pb+Pb relative to pp collisions measured in ALICE (left panel) and NA57, STAR (right panel) as function of centrality, $\langle N_{part} \rangle$ [21].

It is noted that the signatures of QGP in heavy-ion collisions discussed above were proposed with the assumption that the pp system has no QGP medium. However, in recent observations, it has been found that pp collision shows features identical to heavy-ion collisions. For example, in 2017, ALICE reported the enhanced production of (multi)strange particles relative to pions in high-multiplicity pp collisions [22], which is one of the signatures of the formation of QGP-droplet in high energy collisions. It is further supported by the long-range correlations, ridge-like structure as seen by the CMS experiment [23]. This motivates the scientific community to re-investigate the use of pp collisions as a baseline to study system formation in heavy-ion collisions. And also to understand, if at all formed, the QGP-droplet in a small system like pp collisions. This forms the thrust of this thesis. Perhaps to study the possibility of formation of QGP medium in pp collisions, available signatures may not be sufficient and require "second generation" signatures. In the next section 1.3, we focus on some of these signatures and their experimental observation.

1.4 Proton on Proton collisions - possible QGP-like signatures

One of the characteristics of the formation of QGP matter is the production of a large number of particles. And several thousand final state charged particles are produced in the collision of heavy ions like lead on lead. This makes the formation of highly dense matter in heavy-ion collisions more probable, and it is also observed indirectly, as discussed in the previous section 1.3.4. In a central rapidity region, pp collisions are measured to have an average of (5-10) particles produced at the LHC energies. But for certain events, this number reaches up to 100 or more. Such events are called high-multiplicity events. It has been argued recently that the QGP-droplets, if at all formed, could be possible in such events [24, 26, 27, 39]. Here, we briefly discuss some observations of the possibility of QGP-droplet formation in high-multiplicity pp collisions.

- **Strangeness enhancement:** Fig. 1.12 shows the p_{T}-integrated yield ratio of strange and multi-strange particles with pions (having no strange quarks) as a function of charged particle multiplicities. It is clearly observed that there is an enhancement in strange particle production in high-multiplicity pp collisions, similar to heavy-ion collisions.

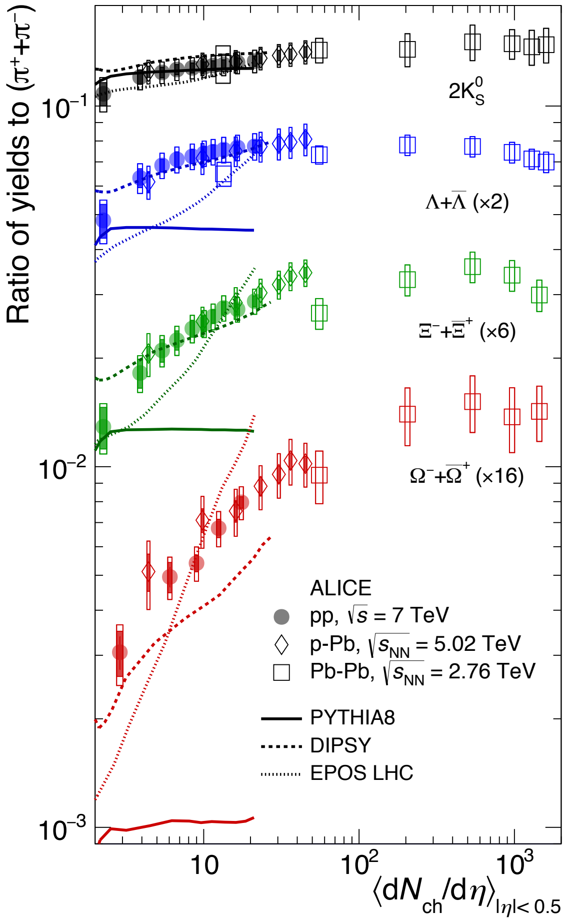

Figure 1.12: Ratio of multi(strange) particles to pions as a function of charged particle pseudorapidity density for proton on proton, proton on lead and lead on lead collisions at LHC energies [22].

- **Multiparticle Ridge-like Correlations:** Fig. 1.13 shows ridge-like structure formation in high-multiplcity pp collisions at $\sqrt{s}$ = 13 TeV [23]. In heavy-ion collisions, formation of such structure (long-range with large $\Delta\eta$ and near-side with small $\Delta\phi$) in two-particle azimuthal correlations is due to the collective expansion of strongly interacting matter.

- **Large radial flow velocity:** Fig. 1.14 shows the measurement of kinetic freeze-out temperature (T_{kin}) and radial flow velocity ($\langle\beta_T\rangle$) obtained from

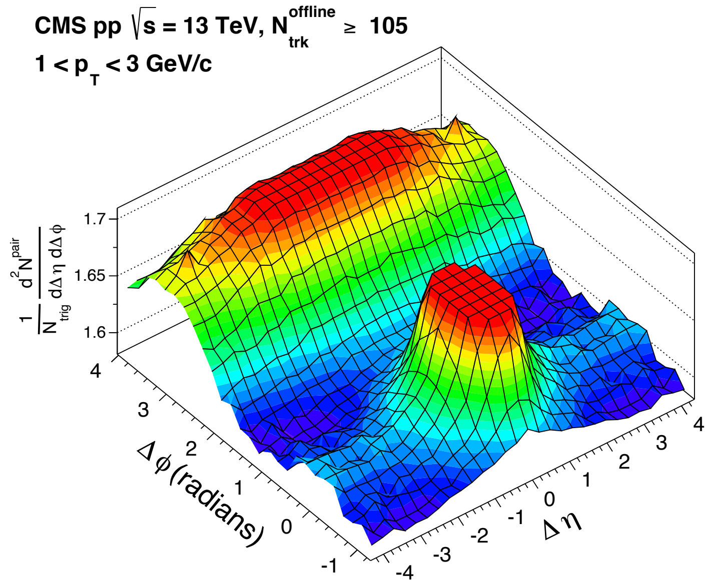

Figure 1.13: Two-particle correlation function in high-multilpcity pp collisions at $\sqrt{s} = 13$ TeV for pairs of charged particles showing ridge-like structure, with each particle within 1< $p_{\mathrm{T}<3}$ GeV/c [23].

the Blast-wave fit of low part of the p_{T} spectra of identified particles [28]. This analysis gives a radial flow velocity of 0.49 ± 0.02 for pp collisions at $\sqrt{s} = 7$ TeV. This infers a high degree of collectivity in high-multiplicity pp collisions, as observed in heavy-ions collisions.

These are indeed fascinating observations of the LHC energies in the context of the possibility of medium formation in high-multiplicity pp collisions. Additionally, experimental evidence of the presence of hadronic phase in pp collisions has been observed, as discussed in refs [29, 30], which indeed needs further investigations. This opens a new door toward re-aligning our understanding of small systems, which were considered devoid of any thermalized medium for a long time. This observation motivates this thesis to explore pp collisions extensively, both experimentally and phenomenologically, which is briefly discussed in the next section 1.5.

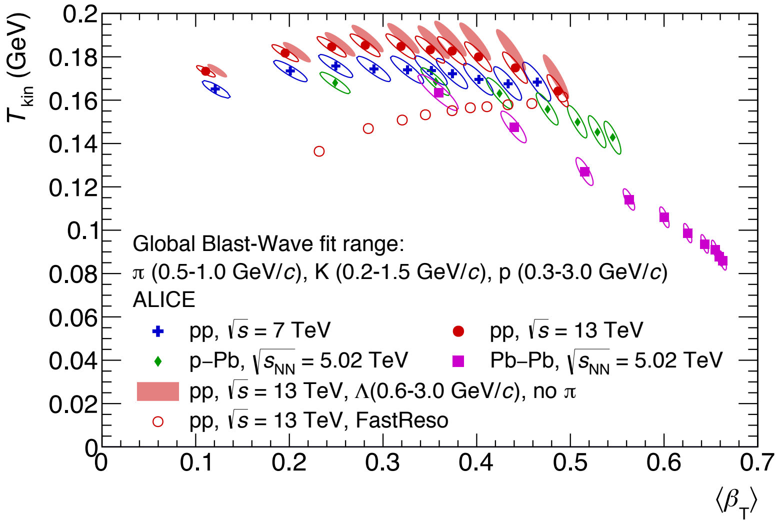

Figure 1.14: Measurement of kinetic freeze-out temperature and radial flow velocity for proton on proton, proton on lead and lead on lead collisions at the LHC energies [28].

1.5 Thesis motivation

The major objectives of this thesis are to understand the interplay of various processes in the hadronic phase with event shape and high-multiplicity dependence study of $K^{*\pm}$ meson production using ALICE detectors at the LHC (CERN). Also, we phenomenologically attempt to explore the possibility of a thermalized medium formation in pp collisions through geometric, statistical, and Monte-Carlo approach. The main objectives of the thesis are briefly discussed below.

1.5.1 Event shape and multiplicity dependence of $K^{*}(892)^{\pm}$ meson production in pp collisions

This thesis reports the first measurement of $K^{*}(892)^{\pm}$ meson in pp collisions at $\sqrt{s}$ = 13 TeV as a function of transverse spherocity and charged-particle multiplicity. The results include the spherocity distribution obtained at different multiplicity intervals, invariant mass plots (before and after uncorrelated background subtraction), peak fits to extract the signal, efficiency ×acceptance, the corrected p_{T} spectra with systematic uncertainties, and particle ratios of $\mathrm{K}^{*}(892)^{\pm}$ with long-lived identified particles.

In order to have a contrast with light-flavored hadrons, we have extensively studied transverse spherocity and final-state multiplicity dependence of heavy-flavored hadrons production in pp collisions at $\sqrt{s}$ = 13 TeV using the pQCD inspired PYTHIA8 model. As the recent observations in high-multiplicity pp collisions show heavy-ion-like nature, the possible formation of QGP-droplets in such small systems cannot be neglected. Heavy-flavor hadrons, containing open or hidden charm and beauty flavors are believed to be important probes for the understanding of Quantum Chromodynamics (QCD) in high-energy hadronic collisions: starting from the study of production mechanisms in proton-proton (pp) collisions to the investigation of Cold Nuclear Matter (CNM) effects in proton-nucleus (p–A) collisions and their suppression in the search of Quark Gluon Plasma (QGP) in nucleus-nucleus (A–A) collisions [31–33]. In addition, the study of heavy-flavor production as a function of the charged-particle multiplicity and event topology may provide insights into multiple hard partonic scatterings [34–36]. Recently, the observation of heavy-ion-like features in small systems (pp and p$-$A) continues to generate considerable interest in the scientific community. For example, the discovery of collective-like phenomena [14], strangeness enhancement [12] etc., and corresponding phenomenological studies [39, 65] in high-multiplicity pp and p$-$A collisions are few among them. In this context, the observed QGP-like phenomena warrants a deeper understanding involving many complex dynamical processes like resonance decays, jets, underlying events (UE) etc. Therefore, small systems need to be re-investigated properly including the light and heavy-flavor sectors, as the production dynamics of these sectors are different in nature. To observe similar effects and in particular, the interplay of hard processes and UE, heavy-flavors are very useful tools.

1.5.2 Glauber model for a small system using anisotropic and inhomogeneous density profile of a proton

Glauber model for heavy-ion collisions helps to estimate quantities such as the number of binary nucleon-nucleon collisions, $N_{\text{coll}}(\text{b})$, number of participants ($N_{\text{part}}(\text{b})$), b being impact parameter, etc., which relies on knowing the nuclear overlap function ($T_{AA}(\text{b})$). And this overlap function depends on a realistic model of the collision geometry. One of the assumptions of such a model is that the proton is a point particle, and thus $N_{\text{coll}}(\text{b})$ for a proton is simply one. But assumption might not be true at high energies, where the structure of a proton becomes significant geometrically. Motivated by the fact that at ultra-relativistic energies, this assumption might not be true, in this present work, we have presented a Glauber-like model for pp collisions employing spherically symmetric distribution densities for three effective quarks from their respective centers and cylindrically symmetric densities for the gluonic flux tubes about the lines joining two adjacent quarks. And obtained interesting results like nuclear modification-like factor (R_{HL}), elliptic flow (v_2) etc., which we believe, would be very useful in studying the dynamics of proton collisions at the TeV energies.

1.5.3 Study of QCD dynamics in a small system using ALICE data

We have used Tsallis parameters obtained from the fitting of experimental ALICE data in pp collisions at center-of-mass energy ($\sqrt{s}$) = 7 TeV to calculate the markers of thermalization like heat capacity (C_V), conformal symmetry breaking measure (CSBM) and speed of sound (c_s) using identified charged particles, with the quantities like multiplicity, system size, and collision energy.

1.5.4 Deciphering QCD dynamics in small collision systems using event shape and final state multiplicity at the Large Hadron Collider

Particle production dynamics in high-energy physics have two domains: the hard perturbative-QCD (processes with high momentum transfer) sector and the soft physics domain (processes with low momentum transfer), which do not necessarily have a sharp boundary. The soft (hard) sector event topology is isotropic (pencil-like). With high-multiplicity events at the LHC in *pp* collisions and the observation of heavy-ion-like features, it has become necessary to look into event shape and multiplicity dependence of various observables and system events thermodynamics. In order to accomplish that, transverse spherocity (S_0) could be used, as recent studies on transverse spherocity at the LHC suggest that using event shape, one can separate the jetty and isotropic events from the average shaped events [40–42]. In this work, in view of the production dynamics dependence of event topology, we have used a thermodynamically consistent form of Tsallis non-extensive statistical distribution function [43], which nicely describes the $p_{\rm T}$-spectra in LHC *pp* collisions to calculate the specific heat, CSBM, and speed of sound for small collision systems like *pp* as a function of event shape and multiplicity using PYTHIA8 event generator [44].

After a brief introduction to the standard model of particle physics, quantum chromodynamics, signatures of QGP in heavy-ion collisions, the possibility of thermalized medium formation in pp collisions, and thesis motivation in this chapter, we now proceed to chapter 2, where we discuss the ALICE detector system in detail giving more emphasis to the detectors specifically used for our analysis.

Bibliography

[1] R. Stock, Prog. Part. Nucl. Phys. **42**, 295 (1999).

[2] S. L. Glashow, Nucl. Phys. **22**, 579 (1961).

[3] A. Salam and J. C. Ward, Phys. Lett. **13**, 168 (1964).

[4] S. Weinberg, Phys. Rev. Lett. **19**, 1264 (1967).

[5] Y. Maezawa, T. Umeda, S. Aoki, S. Ejiri, T. Hatsuda, K. Kanaya and H. Ohno, Prog. Theor. Phys. **128**, 955 (2012).

[6] H. Perkins, Introduction to High Energy Physics.

[7] C. Patrignani *et al.* [Particle Data Group], Chin. Phys. C **40**, 100001 (2016).

[8] Gordon L. Kane. MODERN ELEMENTARY PARTICLE PHYSICS. Cambridge University Press, 2017.

[9] A. Bazavov, T. Bhattacharya, M. Cheng, N. H. Christ, C. DeTar, S. Ejiri, S. Gottlieb, R. Gupta, U. M. Heller and K. Huebner, *et al.* Phys. Rev. D **80**, 014504 (2009).

[10] T. Niida and Y. Miake, AAPPS Bull. **31**, 12 (2021).

[11] R. Snellings, J. Phys. G **41**, 124007 (2014).

[12] I. Arsene *et al.* (BRAHMS Collaboration), Nucl. Phys. A **757**, 1 (2005).

[13] A. Andronic, P. Braun-Munzinger and J. Stachel, Acta Phys. Polon. B **40**, 1005 (2009).

[14] R. Sahoo, arXiv:1604.02651.

[15] M. Kliemant, R. Sahoo, T. Schuster and R. Stock, Lect. Notes Phys. **785**, 23 (2010).

[16] R. Arnaldi *et al.* (NA60 Collaboration), Nucl. Phys. A **783**, 261 (2007).

[17] A. Adare *et al.* (PHENIX Collaboration), Phys. Rev. Lett. **98**, 232301 (2007).

[18] B. B. Abelev *et al.* (ALICE Collaboration), Phys. Lett. B **734**, 314 (2014).

[19] R. Pasechnik and M. Šumbera, Universe **3**, 7 (2017).

[20] P. Koch, B. Muller and J. Rafelski, Phys. Rept. **142**, 167 (1986).

[21] B. B. Abelev *et al.* (ALICE Collaboration), Phys. Lett. B **728**, 216 (2014).Erratum: Phys. Lett. B **734**, 409 (2014).

[22] J. Adam *et al.* (ALICE Collaboration), Nature Phys. **13**, 535 (2017).

[23] V. Khachatryan *et al.* (CMS Collaboration), Phys. Rev. Lett. **116**, 172302 (2016).

[24] M. T. AlFiky, O. T. ElSherif and A. M. Hamed, arXiv:1902.05114.

[25] A. N. Mishra, G. Paić, C. Pajares, R. P. Scharenberg and B. K. Srivastava, Eur. Phys. J. A **57**, 245 (2021).

[26] R. Sahoo, AAPPS Bull. **29**,16 (2019).

[27] R. Sahoo and T. K. Nayak, Curr. Sci. **121**, 1403 (2021).

[28] S. Acharya *et al.* (ALICE Collaboration), Eur. Phys. J. C **80**,693 (2020).

[29] S. Acharya *et al.* (ALICE Collaboration), Phys. Lett. B **807**, 135501 (2020).

[30] A. Khuntia (ALICE Collaboration), Nucl. Phys. A **1005**, 121939 (2021).

[31] Y. Xu, M. Nahrgang, J. E. Bernhard, S. Cao and S. A. Bass, Nucl. Phys. A **967**, 668 (2017).

[32] A. Adare *et al.* [PHENIX Collaboration], Phys. Rev. Lett. **109**, 242301 (2012).

[33] Z. B. Tang, W. M. Zha and Y. F. Zhang, Nucl. Sci. Tech. **31**, 81 (2020).

[34] B. Abelev *et al.* [ALICE Collaboration], Phys. Lett. B **712**, 165 (2012).

[35] J. Adam *et al.* [ALICE Collaboration], JHEP **09**, 148 (2015).

[36] S. Acharya *et al.* [ALICE Collaboration], Phys. Lett. B **810**, 135758 (2020).

[37] V. Khachatryan *et al.* [CMS Collaboration], JHEP **09**, 091 (2010).

[38] S. Deb, S. Tripathy, G. Sarwar, R. Sahoo and J. e. Alam, Eur. Phys. J. A **56**, 252 (2020).

[39] A. N. Mishra, G. Paić, C. Pajares, R. P. Scharenberg and B. K. Srivastava, Eur. Phys. J. A **57**, 245 (2021).

[40] S. Acharya *et al.* (ALICE Collaboration), Eur. Phys. J. C **79**, 857 (2019).

[41] S. Acharya (ALICE Collaboration), PoS HardProbes **2018**, 153 (2019).

[42] A. Ortiz (ALICE, ATLAS, CMS and LHCb Collaborations), PoS LHCP **2019**, 091 (2019).

[43] J. Cleymans and D. Worku, J. Phys. G **39**, 025006 (2012).

[44] Pythia8 online manual: (URL: https://pythia.org/manuals/pythia8245/Welcome.html).

Chapter 2

A Large Ion Collider Experiment at the LHC in nutshell

"For the things we have to learn before we can do them, we learn by doing them."

- Aristotle

Since the dawn of the existence of homo sapiens on the Earth, for their survival, they continuously gathered knowledge and subsequently evolved. They mainly learned by doing experiments like smashing pieces of stones together, which led to the discovery of fire. And this nature of continuous learning has drastically transformed our way of living via various technological advances. This continuous persuades of knowledge by the modern civilization have led to the building of "Large Hadron Collider (LHC)", a scientific and engineering marvel at CERN, Geneva. It is the world's largest and the most powerful particle accelerator, inaugurated on 10 September 2008. A Large Ion Collider Experiment (ALICE) is one of the major experiments at the LHC. It has been taking data of nuclear and hadronic collisions since the LHC became operational in November 2009, with pp collisions at $\sqrt{s}$ = 900 GeV [1]. ALICE is built to address the physics of the quark-gluon plasma at extreme energy density and temperature in the high-multiplicity hadronic collisions and nucleus-nucleus collisions.

This chapter presents a detailed discussion on the ALICE detector at the LHC.

It is divided into three sections. The first section 2.1 gives a detailed discussion of the LHC overview and its different experiments. The second section 2.2 describes the ALICE detector system with the primary focus on the detectors used for the data analysis in this thesis. The final section 2.3 of the chapter is devoted to the online-offline computing and reconstruction system based on the AliROOT framework.

2.1 The Large Hadron Collider (LHC): An Overview

The LHC is a circular particle collider [2] and consists of a double-rings superconducting hadron accelerator. It is installed in an underground tunnel with a circumference of 27 kilometers (km) at a depth of 47-170 m across the Switzerland and France border. It has several accelerating structures to boost the energy of the particles along the way. The design of the LHC allows the maximum energies for a beam of protons (lead ions) to be 7 TeV (2.76 TeV). Thus providing collision energies for pp collisions up to $\sqrt{s} = 14$ TeV and for Pb+Pb collisions up to $\sqrt{s_{NN}} = 5.5$ TeV. In Run 2 of LHC operation, the accelerator was able to reach $\sqrt{s_{NN}} = 5.02$ TeV for Pb+Pb collisions and $\sqrt{s} = 13$ TeV for pp collisions. Fig. 2.1 depicts a schematic view of the LHC accelerator complex at CERN.

To achieve ultra-relativistic energies, the particles pre-accelerate through several processes before entering the LHC. An electric field is used to strip off the hydrogen atoms of their electrons. This is followed by the injection of bunches carrying protons into the LHC. Various accelerators like the LINAC2 achieve this injection (accelerates to an energy of 50 MeV), PS booster (accelerates to an energy of 1.4 GeV), PS (accelerates to an energy of 25 GeV), and SPS (accelerates to an energy of 450 GeV). While in the case of heavy-ions, the accelerating structures consist of LINAC3, LEIR, PS, and SPS accelerators. Figure 2.1 shows different stages of the LHC accelerator. The beams are now injected into the LHC clockwise and anti-clockwise. Under normal operating conditions, the beams cir-

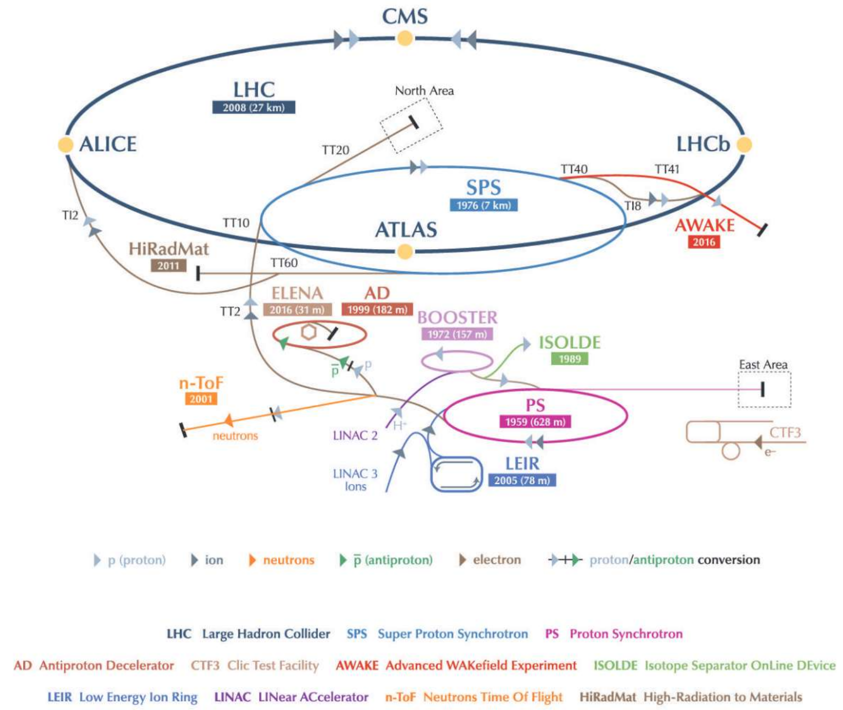

Figure 2.1: The CERN accelerator complex [3].

culate for many hours inside beam pipes.

Once in the accelerator, two beams of particles having achieved high energy by the chain of accelerators travel close to the speed of light before they are made to collide. The beams travel in opposite directions in two separate tubes kept at ultrahigh vacuum, called the beam pipes. A strong magnetic field generated and controlled by superconducting electromagnets guides the beams around the accelerator ring. Now the combination of electric and magnetic fields keeps the bunches focused and accelerated them to their final collision energy. In addition to collision energy, instantaneous luminosity (Ł) plays a vital role in ensuring a high collision rate at the collision points. The LHC is designed to have a luminosity of 10^{34} (10^{27}) $\mathrm{cm}^{-2}\mathrm{s}^{-1}$ for pp (heavy-ion) collisions. The LHC produces collisions in four so-called Interaction Points (IPs), accordingly consists of four main detectors with different goals and dimensions. These are

- **ATLAS (A Toroidal LHC Apparatus)**: This is a general-purpose detector and is used for the study of dark matter, Super Symmetric particle (SUSY), evidence of extra dimensions, etc.

- **CMS (Compact Muon Solenoid)**: The purpose of this detector is the same as the ATLAS.
- **LHCb (LHC beauty)**: It is dedicated detector for the study of CP violation in the b-quark sector and related b-physics.
- **ALICE (A Large Ion Collider Experiment)**: It is a dedicated detector for the study of quark-gluon plasma (QGP) at a very high energy density. A detailed description of the ALICE experiment and its different sub-detectors are given in the next section.

2.2 A Large Ion Collider Experiment (ALICE)

ALICE (A Large Ion Collider Experiment) [4] is a general-purpose, heavy-ion detector at the LHC, focusing on Quantum Chromodynamics, the strong interaction sector of the Standard Model. It is 26 m long, 16 m wide, and 16 m high and weighs around 10,000 tons. This experiment has been designed to study the physics of the produced QGP at high energy density and temperature in heavy-ion collisions. This hot and dense state of matter is believed to have existed up to a few millionths of a second after the Big Bang. ALICE is designed with the aim of recreating and studying this state of matter. The main features of the ALICE detector are its excellent capability of particle identification with the help of specific energy loss, time of flight, electromagnetic calorimetry, muon spectrometry, etc. These features, in turn, allow one to make a comprehensive study of hadrons, electrons, muons, and photons produced in the collision, down to very low transverse momentum (0.1 GeV/c).

Fig. 2.2 shows the various detector subsystems (19 in number) in ALICE used

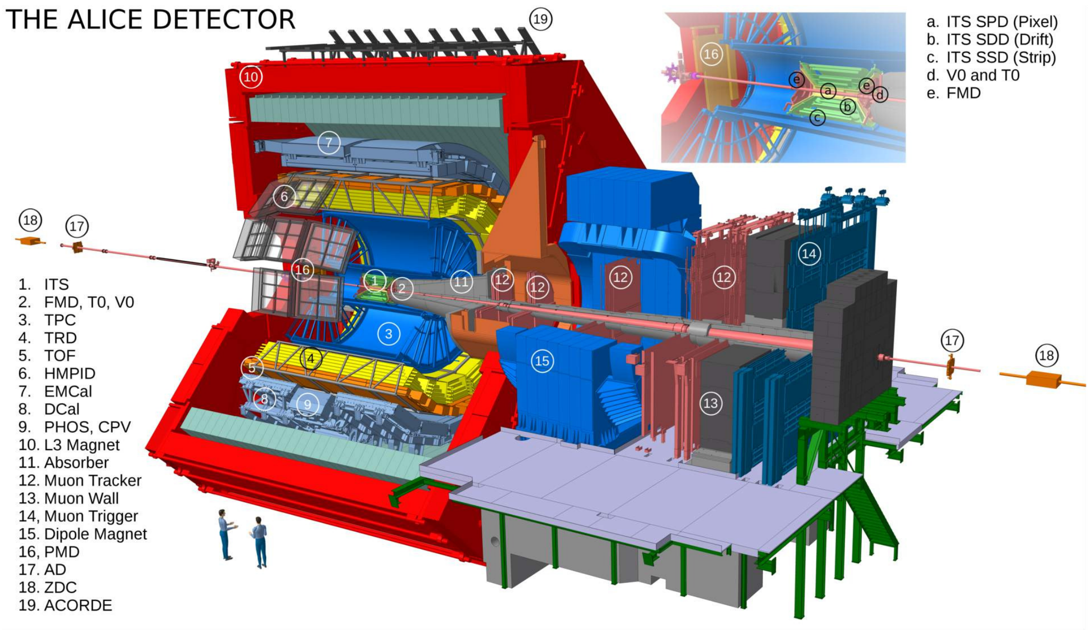

Figure 2.2: Schematic Layout of ALICE detector at LHC [5].

for mainly triggering and event characterization. This detector subsystem can be divided into three groups, viz.,

- **Central barrel detectors**, covers a mid rapidity region ($|\eta| < 0.9$) and azimuthal range of 2π, used for tracking, vertex and particle identification etc. It consists of Inner Tracking System (ITS) [6], Time Projection Chamber (TPC) [7], Transition Radiation Detector (TRD) [8], Time of Flight (TOF) [9] detector, Cherenkov counter (HMPID) [10], Photon Spectrometer (PHOS) [11], Electro-magnetic calorimeter (EMCAL) [12] and the ALICE Cosmic Ray Detector (ACORDE) [13]

- **Muon spectrometer**, covers a forward rapidity region ($-4.0 < |\eta| < -2.5$). It has a dipole magnet providing a field of 0.67 T. Mostly used in the reconstruction of heavy-resonance particle from their dimuon decay channel.

- **Forward detectors**, placed in the high pseudorapidity region and are used for triggering or for measuring global event characteristics. It consists of Time Zero (T0) detector, VZERO (V0), Forward Multiplicity Detector (FMD), Photon Multiplicity Detector (PMD), Zero Degree Calorimeter (ZDC)

Figure 2.3 shows the wide range of pseudorapidity (η) coverage in ALICE at the LHC. This wide η range, along with the azimuthal acceptance (ϕ), position, and purpose of each detector subsystem in ALICE, is listed in Table 2.1.

In the following sub-section, we discuss in detail the detectors used for the ALICE data analyses in this thesis: TPC, ITS, and V0.

Besides these detectors, several other detectors are stationed inside the L3 magnet (0.5 T magnetic field). Detailed information about these detectors can be found in Ref. [4].

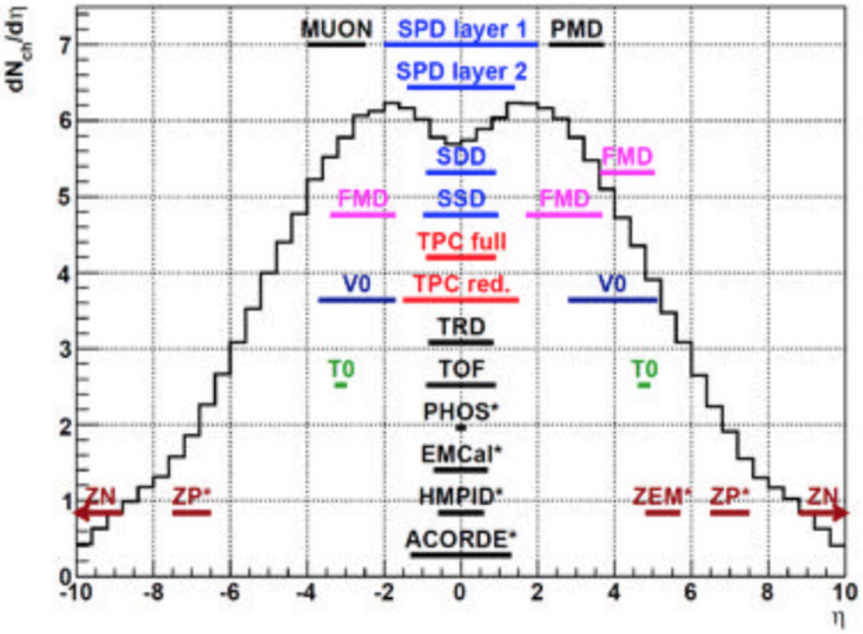

Figure 2.3: Pseudo-rapidity (η) coverage of various sub-detectors of ALICE at LHC [14].

Table 2.1: Detail description of sub-detectors in ALICE at the LHC. The detectors marked with an asterisk (*) are used for triggering [15].

Detector	**Acceptance (η)**	**Acceptance (ϕ)**	**Position**	**Main Purpose**
SPD*	±2.0	full	r = 3.9 cm	tracking, vertex
	±1.4	full	r = 7.6 cm	tracking, vertex
SDD	±0.9	full	r = 15.0 cm	tracking, PID
	±0.9	full	r = 23.9 cm	tracking, PID
SSD	±1.0	full	r = 38.0 cm	tracking, PID
	±1.0	full	r = 43.0 cm	tracking, PID
TPC	±0.9	full	85 < r/cm < 247	tracking, PID
TRD*	±0.8	full	290 < r/cm < 368	tracking, $e^{\pm}$ id
TOF*	±0.9	full	370 < r/cm < 399	tracking, PID
PHOS*	±0.12	220^0 — 320^0	460 < r/cm < 478	photons
EMCal*	±0.7	80^0 — 187^0	430 < r/cm < 455	photons and jets
HMPID	±0.6	1^0 — 59^0	r = 490.0 cm	PID
ACORDE*	±1.3	30^0 — 150^0	r = 850.0 cm	cosmics
PMD	2.3 — 3.9	full	z = 367.0 cm	photons
FMD	3.6 — 5.0	full	z = 320.0 cm	charged particles
	1.7 — 3.7	full	z = 80.0 cm	charged particles
	(-3.4) — (-1.7)	full	z = -70.0 cm	charged particles
V0*	2.8 — 5.1	full	z = 329.0 cm	charged particles
	(-3.7) — (-1.7)	full	z = -88.0 cm	charged particles
T0*	4.6 — 4.9	full	z = 370.0 cm	time, vertex
	(-3.3) — (-3.0)	full	z = -70.0 cm	time, vertex
ZDC*	> 8.8	full	z = ± 113.0 m	forward neutrons
	6.5 — 7.5	$< 10^0$	z = ± 113.0 m	forward neutrons
	4.8 — 5.7	$2\phi < 10^0$	z = 7.3 3 m	photons
MCH	(-4.0) — (-2.5)	full	-14.2 < z/m < -5.4	muon tracking
MTR*	(-4.0) — (-2.5)	full	-17.1 < z/m < -16.1	muon trigger

2.2.1 Inner Tracking System

ITS is the main detector responsible for measuring the primary vertex of the collisions as it is closest to the beam pipe [6]. ITS consists of six layers of concentric cylindrical silicon detectors based on the three different technologies of silicon detectors (pixels, drifts, and strips). These cylindrical layers surround the LHC beryllium beam pipe (having a radius of 2.9 cm and thickness of 800 μm) and cover full azimuth. It is positioned within the radii (4 - 43) cm. The corresponding geometrical layout of the ITS is shown in Fig 2.4. The main purpose of ITS is the precise estimation of primary and secondary vertices, which is vital for the reconstruction of light or heavy flavored resonance particles. In addition, ITS also helps in the identification and tracking of low-momentum particles. It further helps to improve the measurement of the TPC by providing additional tracking points nearer to the interaction point.

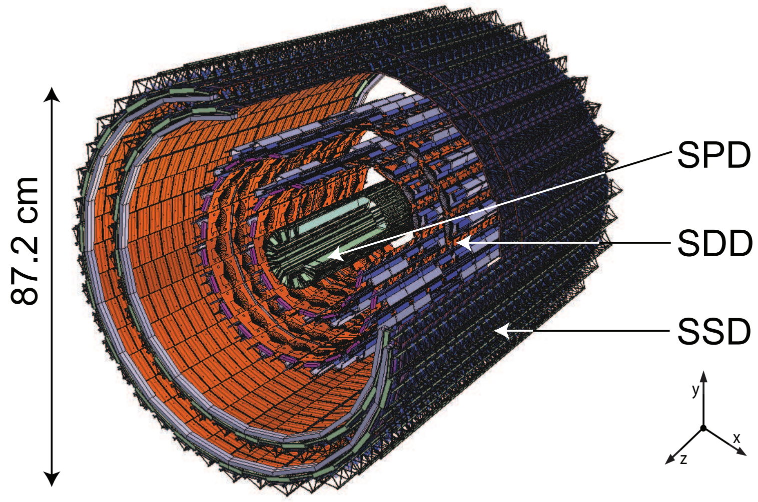

Figure 2.4: Geometrical layout of ALICE Inner Tracking System at the LHC [16].

The Silicon Pixel Detector (SPD) is based on hybrid silicon pixels, consisting of a two-dimensional matrix (sensor ladder) of reverse-biased silicon detector diodes bump-bonded to readout chips. Each diode is connected through a conductive solder bump to contact on the readout chip corresponding to the input of an electronics readout cell. The basic detector module is the half-stave. Each half-stave consists of two ladders, one Multi-Chip Module (MCM), and one high-density aluminum/polyamide multi-layer interconnect. The ladder consists of a silicon sensor matrix bump bonded to 5 front-end chips. The sensor matrix includes 256 x 160 cells measuring 50 μm (rϕ) by 425 μm (z). Longer sensor cells are used in the boundary region to ensure coverage between readout chips. The sensor matrix has an active area of 12.8 mm (rϕ) x 70.7 mm (z). The front-end chip reads out a sub-matrix of 256 (rϕ) x 32 (z) detector cells. In total, the SPD (60 staves) includes 240 ladders with 1200 chips for a total of 9.8 x 106 cells. The inner (outer) SPD layer is located at an average distance of 3.9 cm (7.6 cm) from the beam axis. The detector design implements several specific solutions to minimize the material budget. The SPD has the best spatial resolution of the ITS detectors, thus providing a resolution on the impact parameter measurement adequate for charm flavor detection.

The Silicon Drift Detector (SDD) is based on modules with a sensitive area of 70.17 (rϕ) x 75.26 (z) mm^2, which is divided into two drift regions where electrons move in opposite directions under a drift field of approximately 500 V/cm. The SDD modules are mounted on a linear structure called a ladder. The SDD inner layer is made of 14 ladders with six modules each, and the outer layer has 22 ladders with eight modules. The position of the particle along z is reconstructed from the centroid of the collected charge along the anodes, while the position along the drift coordinate (r) is obtained from the measured drift time with respect to the trigger time. This reconstruction requires precise knowledge of the drift speed that is measured during frequent calibration runs, given its strong dependence on the humidity and temperature gradients in the SDD volume.

The Silicon Strip Detector (SSD) building block is a module composed of one double-sided strip detector connected to two hybrids hosting the front-end electronics. The sensors are 300 μm thick and with an active area of 73 (r) x 40 (z) mm^2. There are 768 strips, with a pitch of 95 μm on each side, almost parallel to the z beam axis direction. The innermost SSD layer consists of 34 ladders, each of them housing 22 modules along the beam direction, while the other SSD layer has 38 layers, each of them with 25 modules. The outer four layers are used for particle identification via energy loss (dE/dx) measurement in the non-relativistic ($1/\beta^2$) region for low momentum particles as low as $p_{\rm T}$ =100 MeV via analogue readout. Fig. 2.5 shows the average energy loss (dE/dx) distribution of charged particles vs their momentum, both measured by the ITS alone (ITS pure standalone track) in pp collisions at $\sqrt{s}$ = 13 TeV LHC15f pass2 period (ITS pure standalone reconstruction). The lines in Fig. 2.5 are a parametrization of the detector response based on a hybrid parametrization with a polynomial function at low p/m (p and m being particle momentum and mass, respectively) and a "PHOBOS" Bethe-Bloch formula. This result shows the particle identification capability of ITS using the concept of dE/dx. A clear separation of pions, kaons, and the proton is observed.

With these marvelous capabilities, ITS helps to track and identify low momentum particles. We now move on to another crucial tracking detector in the central barrel detector systems called the Time Projection Chamber or TPC in the next section 2.2.2.

2.2.2 The Time Projection Chamber (TPC)

The Time Projection Chamber (TPC) [17] is the main tracking detector of ALICE, covering the pseudorapidity range $|\eta| < 0.9$ and the full azimuth angle. The optimization of the detector design has been done to provide excellent tracking

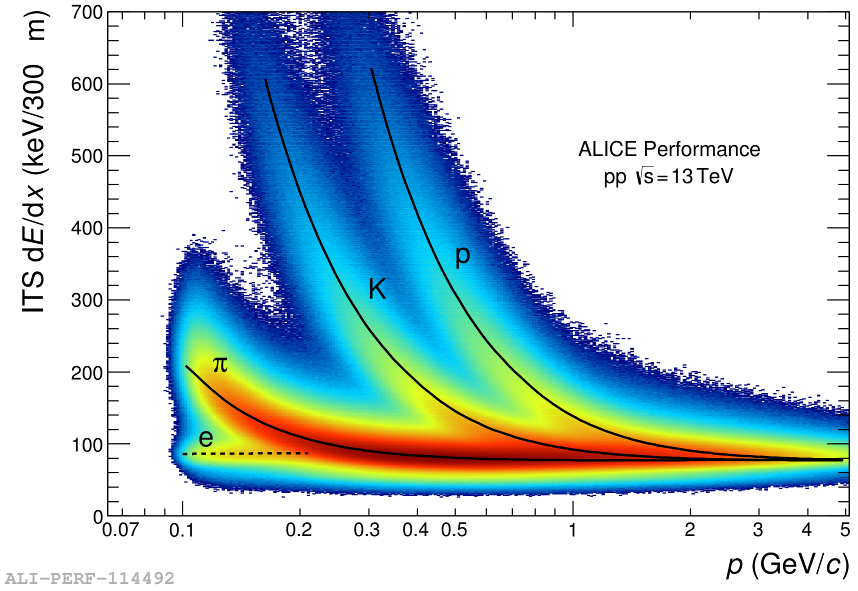

Figure 2.5: Average energy loss (dE/dx) distribution of charged particles vs their momentum for ITS pure standalone tracks measured in pp collisions at $\sqrt{s} = 13$ TeV [18]. The lines are the parametrization of the detector response based on the Bethe-Bloch formula.

performance in a high multiplicity environment, to keep the material budget as low as possible in order to have low multiple scattering and secondary particle production, to limit the detector occupancy at the inner radius but still guarantee a good momentum resolution for high -p_{T} particles. TPC is cylindrical in shape 500 cm long along the beam pipe, with 80 cm and 250 cm inner and outer radii, respectively, determined by maximum acceptable track density and minimum track length for which the resolution on dE/dx is lower than 10%. The TPC volume was filled with 90 m^3 of a mixture of Ne/CO$_2$/N$_2$ during Run 1, optimized for drift velocity, low electron diffusion, and low radiation length. Argon replaced neon for Run 2. The electron drift velocity of 2.7 cm/s over 250 cm (each of the two TPC drift regions separated by the central cathode) gives a maximum drift time of 88 μs, therefore limiting the maximum event rate TPC can sustain. At a high interaction rate, pile-up effects and the long TPC dead time are the two main factors that force ALICE to run at a lower instantaneous luminosity to the other LHC experiments.

The TPC can reconstruct a primary track in a wide momentum range, from about $p_{\mathrm{T}} \sim 0.1$ -100 GeV/c with a very good momentum resolution. And for $p_{\mathrm{T}} > 100$ MeV/c, it is observed that efficiency > 90%, where the limiting factor are the interactions in the ITS material. By measuring the deflection in the magnetic field, the ITS, in combination with the TPC are able to determine the momentum of the charged particles with a resolution better than 1% at low p_{T} and 20% for $p_{\mathrm{T}} \sim 100$ GeV/c as shown in the Fig. 2.6.

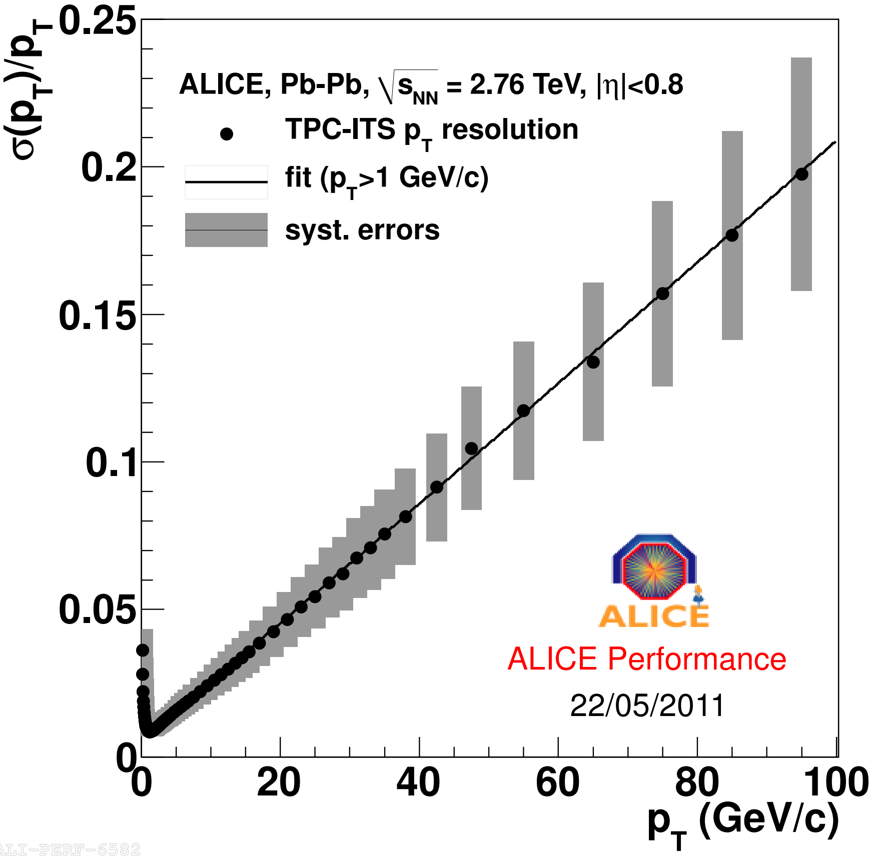

Figure 2.6: Transverse momentum resolution of combine TPC + ITS tracking [19].

The charge collected in the TPC readout pads is used to measure particle energy loss. The particle energy loss and the momentum are simultaneously measured. And this information allows one to separate the various charged particle species in the low momentum region and thereby helps in particle identification. The energy loss (dE/dx) of a charged particle in the detector medium is estimated using the Bethe-Bloch formula given as,

$$-\langle\frac{dE}{dx}\rangle = \frac{4\pi N e^4}{mc^2\beta^2}\left(\ln\frac{2mc^2\beta^2\gamma^2}{I} - \beta^2 - \frac{\delta(\beta)}{2}\right) \tag{2.1}$$

Where, N, e and m are the number density, electric charge and mass of the electron respectively, β is the velocity of the traveling particle ($\gamma^2 = 1/(1-\beta^2)$, the Lorentz factor) and z is its corresponding charge. I is the mean excitation energy of the atom. $\delta(\beta)$ is the correction term for the density effect [20]. From Eq. 2.1, it can be inferred that the energy loss decreases in the low-velocity region due to the $1/\beta^2$ term. The ionization value becomes minimum for the relativistic limit, and particles in this region are called ionization particles.

This method of particle identification via energy loss is done by a simple parametrization of the dE/dx factor along with $\beta\gamma$. ALICE experiment uses the similar parameterization of the Beth-Bloch curve, originally used in the ALEPH collaboration [20, 21] and is given by,

$$f(\beta\gamma) = \frac{P_1}{\beta^{P_4}}\left[P_2 - \beta^{P^4} - \ln\left(P_3 + \frac{1}{(\beta\gamma)^{P_5}}\right)\right], \tag{2.2}$$

Where the parameter P_{1-5} is the fit parameter, γ is the Lorentz factor, and β is the particle velocity. The dE/dx distribution for various charged particles is shown in Fig. 2.7, where the solid line is the expectations from the Bethe-Bloch formula. Low momentum particles are identified on a track-by-track basis. And higher momentum particles are determined from the difference of measured and parameterized value (as given in Eq. 2.2) of dE/dx via multi-Gaussian fits.

There is yet another method to identify particles is by using $n\sigma$ cut (σ is the resolution). It is defined as,

$$n\sigma = \frac{(dE/dx)_{measured} - (dE/dx)_{expected}}{\sigma_{TPC}^{PID}}, \tag{2.3}$$

where, $(\mathrm{dE/dx})_{measured}$ is the energy loss of the TPC measured tracks and $(\mathrm{dE/dx})_{expected}$ is the expectation of the modified Bethe-Bloch function. σ_{TPC}^{PID} is the PID resolution of the TPC.

The $n\sigma$ method of particle identification is extensively used in the analysis of $\mathrm{K}^{*}(892)^{\pm}$ in this thesis.

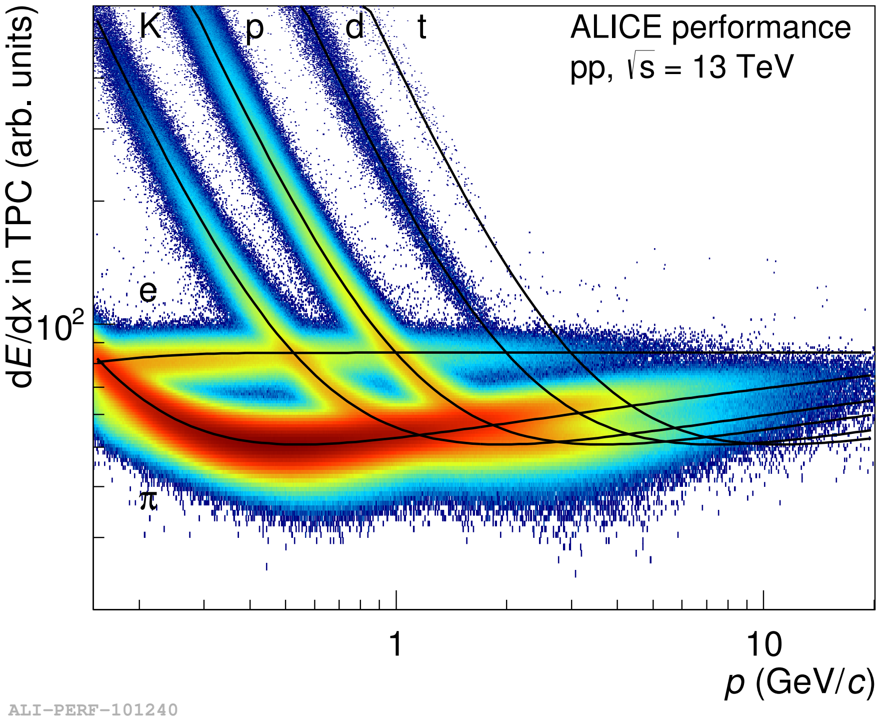

Figure 2.7: ALICE TPC energy loss (dE/dx) performance in Run2 for pp collisions at $\sqrt{s}$ =13 TeV with magnetic field of 0.2 T) [22].

2.2.3 VZERO (V0)

The V0 [23] is a trigger detector that provides a minimum-bias trigger for all colliding systems and three centrality triggers in Pb-Pb collisions (multiplicity, central and semi-central). It has a vital role in rejecting background from beam-gas collisions by exploiting the relative time-of-flight measurement between the two arrays: when the beam-gas collision takes place outside the region between the two arrays, particles arrive six nanoseconds before or after the time of a beam-beam collision. It consists of two segmented arrays of plastic scintillator counters, called V0A and V0C, placed around the beam pipe on either side of the IP: one at z = 340 cm ($2.8 < \eta < 5.1$), and the other at z = -90 cm (in front of the absorber), covering the pseudo-rapidity range, $-3.7 < \eta < -1.7$.

2.3 ALICE online and offline system

2.3.1 ALICE online system

The central online systems control the data-taking activities in ALICE. It comprises of Detector Control System (DCS), Data Acquisition (DAQ), Trigger system (TRG), High-Level Trigger (HLT), and experiment Control System (ECS) [24, 25]. DCS controls hardware operation while DAQ defines the configuration of the detectors during data-taking periods. It is integrated with the TRG and HLT systems. ECS is responsible for the coordination of all the central systems. Although the detectors can function independently (known as a standalone mode), they are grouped in partitions with a given set of trigger inputs to operate concurrently. This is done during the physics data-taking period. The main purpose of standalone mode is to perform calibration, commissioning, and debugging activities.

2.3.1.1 Trigger System

The main purpose of the Trigger system (TRG) is to decide within microseconds, for every bunch-crossing of the LHC, whether the resulting event is worth being recorded. It consists of Central Trigger Processor (CTP) and a High-Level Trigger (HLT). Depending upon the arrival times of the trigger inputs and the time synchronization of the detector, CLP has three levels of triggers, namely, level-0 (L0) or first level trigger, level-1 (L1) or second level, and level-2 (L2) or final level. After crossing each bunch, L0 delivered the combined signal information from different detectors in 1.2 μs while L1 delivered after 6.5 μs. The final level tigger decides 100 μs. At the end of the last and final level trigger, the system chooses whether the selected event is to be asserted, negated, or not relevant. Then the recording of the data is done through the DAQ system.

2.3.1.2 High Level Trigger

The ALICE High-Level Trigger (HLT) is responsible for collecting inputs from all significant detectors at the end of trigger selection and processes to choose events of interest. This is done through a filtering mechanism using firmware and software. The raw data is collected via Detector Data Links (DDL) into HLT. Then the event is reconstructed for each detector individually, and the selection of events is performed with the reconstructed physics observables. This is followed by the reconstruction of events for each detector separately. Thus, HLT helps to reduce the volume of physics events by selecting and compressing the events.

2.3.1.3 Data Acquisition

The DAQ system is responsible for the handling of data flow from detector-related electronics to permanent storage. This is done using the Local Data Concentrators (LDCs), which read the events from the optical Detector Data Links. This collected events information is further moved to Global Data Collectors (GDCs), which record the events to the Transient Data Storage. Finally, it is moved into permanent storage. In addition, it also includes software packages to perform monitoring of data quality and system performance. Fig. 2.8 shows an overview of the ALICE DAQ architecture.

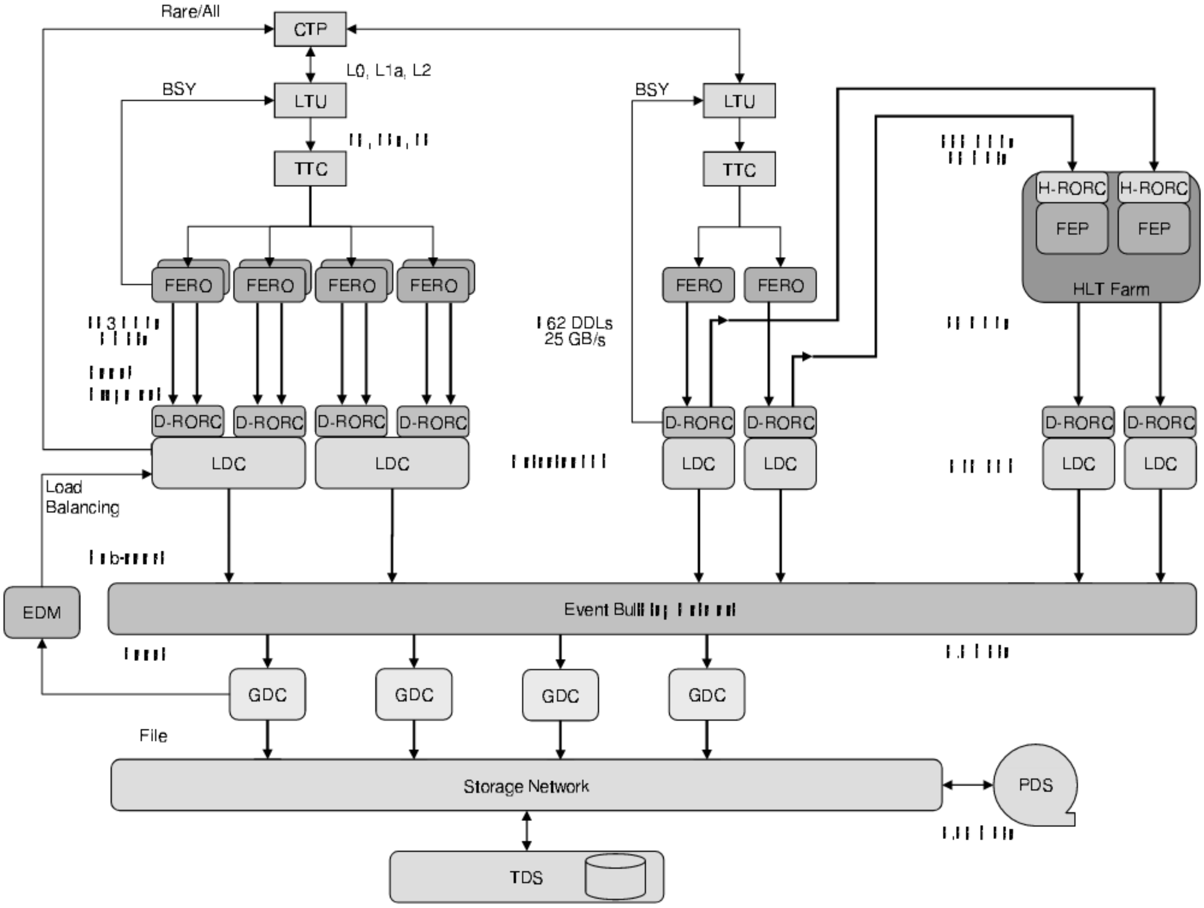

Figure 2.8: The overall architecture of the ALICE DAQ system and the interface to the HLT system [26].

2.3.1.4 Detector and Experimental Control System

The core purpose of the Detector Control System (DCS) is to allow a safe and easy operation of the ALICE at the LHC. It controls and handles all the services related to detectors like high and low-voltage power supplies, gas, magnet, cooling, etc.

It is always operational, even during shutdown periods. The ALICE Experiment Control System (ECS) is responsible for coordinating the operations of all the online systems to fulfill their common goal.

2.3.2 ALICE Offline system

To ensure the proper data processing, ALICE offline project is devoted to the development of the framework. This includes ALICE Grid and Aliroot framework.

2.3.2.1 ALICE grid system

To handle and process a vast amount of data distributed among computing resources, the concept of ALICE Grid was introduced. In ALICE Grid, the data processing is distributed worldwide to several computing centers. The distributed computing infrastructure used in the LHC experimental program is managed under Worldwide LHC Computing Grid. (WLCG) project. The ALICE grid uses the Models of networked analysis at regional centers (MONARC) model, which is classified into different stages and tiers. All actual or real data originate from CERN, which is called Tier-0. In Tier-1, large regional computing centers share the role of safe data storage with CERN. Tier-2 are the smaller centers that are logically clustered around Tier-1. The main function of Tier-2 is to perform Monte-Carlo simulations and user analysis tasks. ALICE Offline project also develops ALICE Environment (ALIEN), which allows ALICE users to have transparent access to grid computing and storage resources.

2.3.2.2 AliRoot Framework

ALICE uses the ROOT framework [27], a scientific software framework. ROOT is primarily C++ based, while other languages such as R and Python are also integrated into ROOT. It is well equipped to handle big data processing, statistical analysis, and storage of physics analysis. Besides the package for physics analysis, the software for the simulation of events and detector is required. AliRoot [28] framework was developed, which is based on ROOT, to fulfill all such requirements. AliRoot also includes widely used Monte-Carlo software like GEANT3 [29], GEANT4 [30], and FLUKA [31] to simulate the interaction of particles with the materials of the detector. Different event generators (like PYTHIA, EPOS, AMPT, etc.) simulate events for pp and heavy-ion collisions.

Bibliography

[1] J. Schukraft (ALICE Collaboration), J. Phys. G **38**, 124003 (2011).

[2] LHC Design Report, http://cds.cern.ch/record/782076, (2004).

[3] The CERN accelerator complex: https://cds.cern.ch/record/2197559.

[4] K. Aamodt *et al.* (ALICE Collaboration), JINST **3**, S08002 (2008).

[5] https://alice-figure.web.cern.ch/node/11218.

[6] ALICE Inner Tracking System (ITS): Technical Design Report, CERN-LHCC-99-012, http://edms.cern.ch/file/398932/1.

[7] ALICE Time Projection Chamber: Technical Design Report, CERNLHCC-2000-001, http://cdsweb.cern.ch/record/451098.

[8] A. Andronic (ALICE TRD), Nucl. Instrum. Meth. A **522**, 40 (2004).

[9] ALICE Time-Of-Flight system (TOF): Technical Design Re- port, CERN-LHCC-2000-012; http://cdsweb.cern.ch/record/430132; ALICE Time-Of Flight system (TOF): addendum to the technical design report, CERN-LHCC-2002-016, http://cdsweb.cern.ch/record/545834.

[10] ALICE high-momentum particle identication: Technical Design Report, CERN-LHCC-98-019, http://cdsweb.cern.ch/record/381431.

[11] ALICE Technical Design Report of the Photon Spectrometer (PHOS), CERN/LHCC 99-4 (1999), https://edms.cern.ch/document/398934/1.

[12] ALICE electromagnetic calorimeter: addendum to the ALICE technical proposal, CERN-LHCC-2006-014, http://cdsweb.cern.ch/record/932676.

[13] ACORDE a cosmic ray detector for ALICE, Nucl. Instrum.Meth. A **572**, 102 (2007).

[14] M. Venaruzzo: https://cds.cern.ch/record/1377846.

[15] B. B. Abelev et al. (ALICE Collaboration), Int. J. Mod. Phys. A **29**, 1430044 (2014).

[16] K. Aamodt *et al.* (ALICE Collaboration), JINST **5**, P03003 (2010).

[17] J. Alme, Y. Andres, H. Appelshauser, S. Bablok, N. Bialas, R. Bolgen, U. Bonnes, R. Bramm, P. Braun-Munzinger and R. Campagnolo, *et al.*, Nucl. Instrum. Meth. A **622**, 316 (2010).

[18] ITS performance: https://alice-figure.web.cern.ch/node/9865

[19] Transverse Momentum Resolution for TPC-ITS: https://alice-figure.web.cern.ch/node/1240

[20] W. Blum, W. Riegler, and L. Rolandi, "Particle detection with drift chambers"; Springer, Berlin (2008). https://cds.cern.ch/record/1105920

[21] S. Singha, PhD thesis, http://cds.cern.ch/record/2654944

[22] TPC performance: https://alice-figure.web.cern.ch/node/8670

[23] E. Abbas *et al.* (ALICE Collaboration), JINST **8**, P10016 (2013).

[24] J. F. Grosse-Oetringhaus *et al.* (ALICE Collaboration), J. Phys. Conf. Ser. **219**, 022010 (2010).

[25] F. Carena *et al.* (ALICE Collaboration), Nucl. Instrum. Meth. A **741**, 130 (2014).

[26] https://cds.cern.ch/record/684651.

[27] https://root.cern.ch/

[28] ALICE Collaboration, ALICE Offline framework, AliRoot. URL: http://aliceinfo. cern.ch/Offine.

[29] Rene Brun, Federico Carminati, and Simone Giani, "GEANT Detector: Description and Simulation Tool."(1994)

[30] S. Agostinelli et al. (GEANT4 Collaboration), Nucl. Instrum. Meth. A **506**, 250 (2003).

[31] A. Fasso et al., eConf C **0303241**, MOMT004 (2003).

Chapter 3

Event topology and multiplicity dependence of $\mathrm{K}^{*}(892)^{\pm}$ production in proton+proton collisions

"It doesn't matter how beautiful your theory is, it doesn't matter how smart you are. If it doesn't agree with experiment, it's wrong." - Richard P. Feynman.

Resonances are commonly known as the hadrons which are more massive than their ground state particles and have different excited quantum states but identical quark contents. These particles usually have a short lifetime (τ) as they decay strongly, and it is in the order of a few fm/c, a typical proton diameter. Because of their short lifetime, reconstructed hadronic resonances through their decay products in a detector can be used to study the hadronic medium between the chemical and the kinetic freeze-out. Experimentally measured typical lifetime of hadronic resonances range for 1.3 to 46.3 fm/c [1]. As hadronic resonances of varying masses (770 - 1019 MeV/c^2), hadron class (meson and baryon), strangeness (0 - 2), and lifetimes are available, they can be used to study the properties of the hadronic phase and its different stages of evolution. A comprehensive study of hadronic resonances plays a vital role in understanding ultra-relativistic heavy-ion collisions. In such collisions, expansion of the produced fireball can be probed by the hadronic resonances, as their lifetime is comparable to the lifetime of the fireball ($\tau \approx 10$ fm/c at LHC energies [2]) created in the heavy-ion collisions. This helps to understand in-medium phenomena like rescattering (interaction of decay daughters with other in-medium particles, results in suppression of resonances when reconstructed, as the invariant mass of the daughter particles mismatches with the parent particle) and regeneration (enhancement of resonances because of pseudo-elastic collisions in the hadronic phase). Resonance particle like $\phi(1020)$ having $\tau \approx 46.3$ fm/c might not go through the above mentioned processes. The sensitivity of hadronic resonances to rescattering and regeneration processes in the hadronic phases is depicted in Figure 3.1.

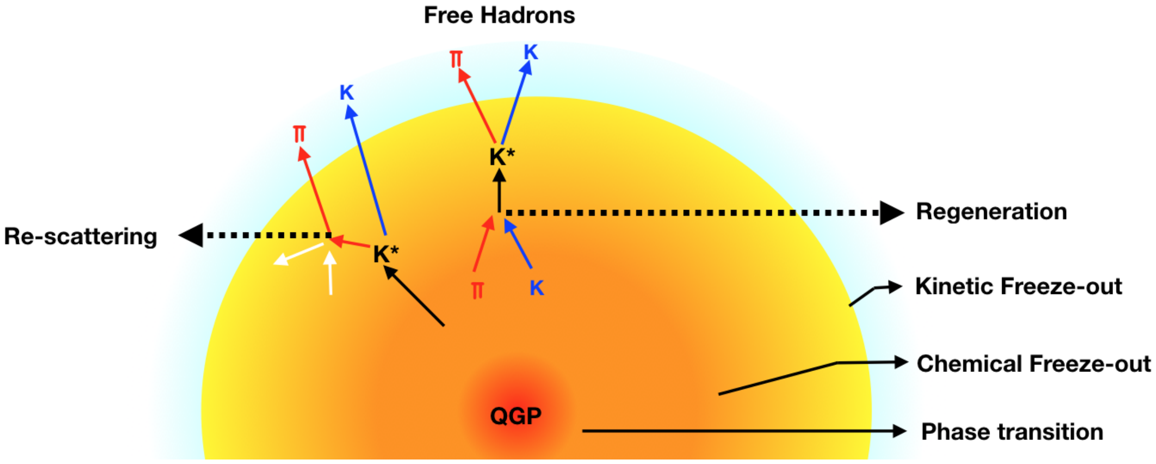

Figure 3.1: (Color Online) Depiction of re-scattering and regeneration processes in hadronic phase in heavy-ion collisions.

Recent results (in 2017) reported by ALICE have observed enhanced production of strange and multi-strange particles in high-multiplicity proton+proton (pp collisions [3] and observation of evidence of collectivity in pp collisions by CMS [4], which was traditionally considered as one of the signatures of QGP. These observations compel one to ask whether high-multiplicity pp collisions create QGP-droplets. Extensive investigation using strange quarks containing resonance particles could provide hints towards the possible formation of QGP-like medium in pp collisions (specifically high-multiplicity events). Soft-QCD and hard-QCD processes could govern particle production in small system collisions like pp. While the study of bulk properties of the system would give an understanding of the underlying mechanism of the soft-QCD process, the study of jets could reveal the physics of hard-QCD processes. One of the event-shape techniques called transverse spherocity (S_0) can disentangle events dominated by soft/hard-QCD processes based on its geometrical structure. The study of resonance particles in the light of transverse spherocity and multiplicity could provide deeper insight into the dynamics of particle production in high multiplicity pp collisions.

This chapter describes the differential study of transverse spherocity and multiplicity dependence measurement of $K^*(892)^{\pm}$ meson production at the LHC. It is divided into two sections. The first section 3.1 describes the production of $K^*(892)^{\pm}$ mesons in pp collisions at $\sqrt{s} = 13$ TeV as a function of the transverse spherocity and charged-particle multiplicity (V0M) using the ALICE detector. This study is essential as it will help to understand the resonance particle production in high multiplicity events. In order to have better insight, a comparison of $K^*(892)^{\pm}$ with long-lived identified particles is also studied in this section. The second section 3.2 describes the production dynamics of heavy-flavored hadrons like J/ψ, D^0 and Λ_c^+ through the transverse momentum spectra, double differential yield, and mean transverse momentum in pp collisions as a function of transverse spherocity and charged-particle multiplicity using PYTHIA8 [5] event generator. Further to investigate the hadronization mechanism of the heavy and light quarks, transverse spherocity dependence ratios like Λ_c^+/D^0 and Λ^0/K^- are also studied in this section. The third and final section 3.3 covers a brief summary of the chapter.

3.1 $\mathrm{K}^{*}(892)^{\pm}$ production as a function of event topology and multiplicity in pp collisions at $\sqrt{s} = 13$ TeV with ALICE

In 15th March 1961, a paper published in Physical review letters called "RESONANCE IN THE K- π SYSTEM" by Prof. Luis Walter Alvarez et al., where for the first time, the discovery of $\mathrm{K}^{*}(892)^{\pm}$ meson along with other 'resonance states' utilizing the Lawrence Radiation Laboratory 15-inch hydrogen bubble chamber in the collision of 1.15-BeV/c K^{-} mesons and hydrogen [6] was reported (in some older documents BeV is used, which is equivalent to the GeV). He has been conferred with the Nobel Prize in Physics for this groundbreaking work in 1968 [7]. The discovery of mass distribution of K^{*-} from the collision of K^{-} mesons and hydrogen in this work is shown in Fig. 3.2 [6]. Being a resonance particle, $\mathrm{K}^{*\pm}$ is produced through strong interaction and is identified via their two-step hadronic decay channel, $\mathrm{K}^{*\pm} \rightarrow \mathrm{K}^0_{\mathrm{S}} + \pi^{\pm}$ with a branching ratio of 33.4% and $\mathrm{K}^0_{\mathrm{S}}$ decays weakly to two charged pions via decay topology, $\mathrm{K}^0_{\mathrm{S}} \rightarrow \pi^{+} + \pi^{-}$ with a branching ratio of $69.2 \pm 0.05\%$. Fig. 3.3 shows the schematic diagram of decay topology of $\mathrm{K}^{*\pm}$. For the sake of completeness, the typical properties of $\mathrm{K}^{*\pm}$ particle are listed in Table 3.1. In this thesis, we have explored how transverse spherocity affects the production of $\mathrm{K}^{*\pm}$ meson in the high-multiplicity pp collisions in ALICE. It has been reported that event shape observables like transverse spherocity allow the possibility to separate the high and the low number of multipartonic interaction (MPI) events [8–10]. This result can help us to understand more about the dynamics of jet production, particle ratios of strange or multi-strange particles with long-lived hadrons [3], observation of double ridge structure [4] and behavior of mean transverse-momenta of charged particles in hadronic systems compared to heavy-ion systems [11]. Below is a detailed discussion on the event topology dependence of K$^{*\pm}$ meson production in pp collisions using the ALICE detector.

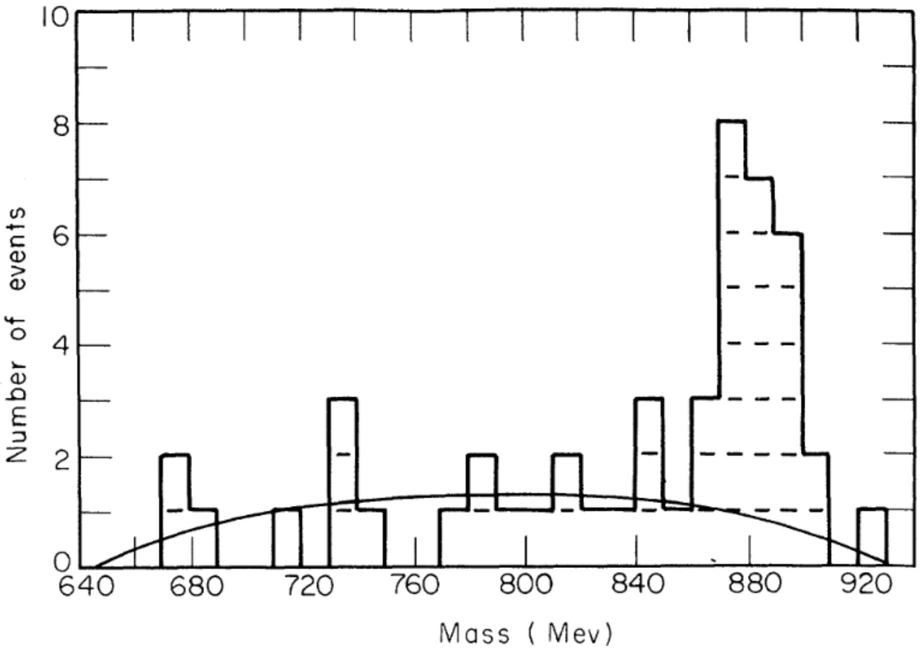

Figure 3.2: Mass distribution of K^{*-} from K^0_S and π^- in the interaction of K$^-$ and hydrogen. The solid line represents the phase-space curve normalized to background events [6].

Table 3.1: Typical properties of charged K$^{*\pm}$.

Mass (MeV/c^2)	**Width (MeV/c^2)**	**Quark Contents**	**Decay mode**	**Lifetime**	**Branching ratio**
891.66 ± 0.26	50.8 ± 0.9	$\bar{u}s, u\bar{s}$	$K^0_S\pi^{\pm}$	$\approx 3.6 fm/c$	≈ 0.33

3.1.1 Dataset and Event Selection

The production of K$^{*\pm}$ is measured at midrapidity ($|y| < 0.5$) in pp collisions at $\sqrt{s}$ = 13 TeV using ALICE detector [12]. For pp minimum-bias collisions at $\sqrt{s}$ = 13 TeV, the data were collected during Run 2 operation at the LHC. The data were collected with a minimum bias trigger (an electronic-based system that makes a decision whether the collision data are worth saving or not).

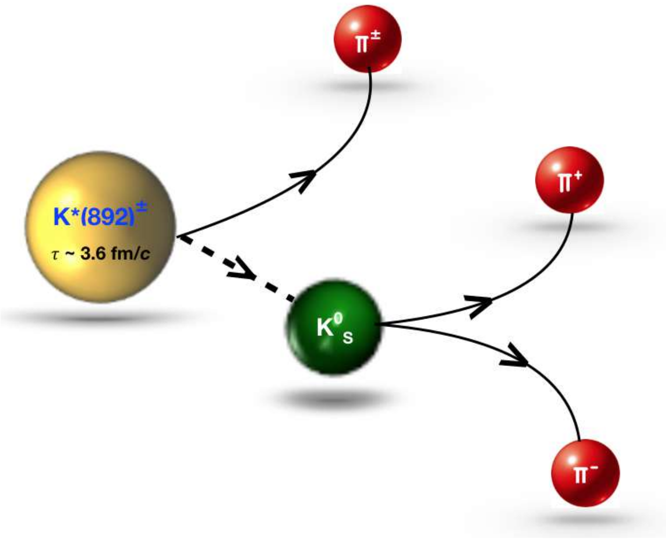

Figure 3.3: (Color Online) Hadronic decay topology of the $K^*(892)^\pm$ into a K^0_S and a charged pion followed by weak decay of K^0_S into charged pion pairs.

This trigger requires a hit in both V0 detectors (here, kINT7), coinciding with the arrival of proton bunches from both directions. A detailed discussion on the working of V0 detectors for event selection is given in chapter 2. The physics selection framework is widely used within ALICE to select events satisfying certain trigger criteria and reject beam-gas. The physics selection framework is also used to reject pileup events. The physics selection is performed in two steps: (1) selection of events with relevant trigger classes fired, (2) rejection of background, pileup events, and poor quality events. Whenever a collision occurs, the triggering detector sends the signal, which acts as an input to the trigger system. Consequently, the trigger system output is fed to the readout detectors. The primary task of the readout detector is to detect and save the collisions. This analysis is carried out using the reconstructed data in the Analysis Object Data (AOD) format, and it is in the form of root trees. The details on the format of data stored in ALICE are given in chapter 2. Large data periods with minimum bias triggers are added to increase the statistics. This enables us to look into more differential studies as a function of charged particle multiplicity and event shape classes. A complete list of datasets and run-list analyzed are given in the appendix section 3.4.2. The consistency of different data samples were checked before merging them for this analysis and it is shown in appendix section 3.4.3. After the event selection, around 1392 million minimum bias events are accepted for $\sqrt{s}$ = 13 TeV are used in this analysis.

3.4.3

The following event-selection cuts were used:

1. kINT7 trigger: This tigger should correspond to a logical AND between trigger input from V0A and V0C detectors.
2. Standard Physics Selection.
3. IsIncompleteDAQ check
4. Pileup rejection using AliAnalysisUtils::IsPileUpEvents()
5. SPD clusters vs. tracklets check using AliAnalysisUtils::IsSPDClusterVsTrackletBG() with defalult parameters.
6. Track vertex are chosen by default. If it is missing, the vertex from the SPD is selected or at least events needs to have a track. Only events with vertex $|\mathrm{v_z}| < 10$ cm have been taken into consideration.
7. SPD vertex z resolution < 0.25 cm
8. SPD vertex dispersion < 0.04 cm
9. z-position difference between track and SPD vertex $(|\mathrm{v_z}(\mathit{diff})|) <$ 0.5 cm

The upper panel of figure 3.4 shows the event statistics after implementing all the above event-selection cuts. The fourth bin shows the total number of accepted events for this analysis, which is around 1392 million events. The lower panel shows the accepted events as a function of multiplicity.

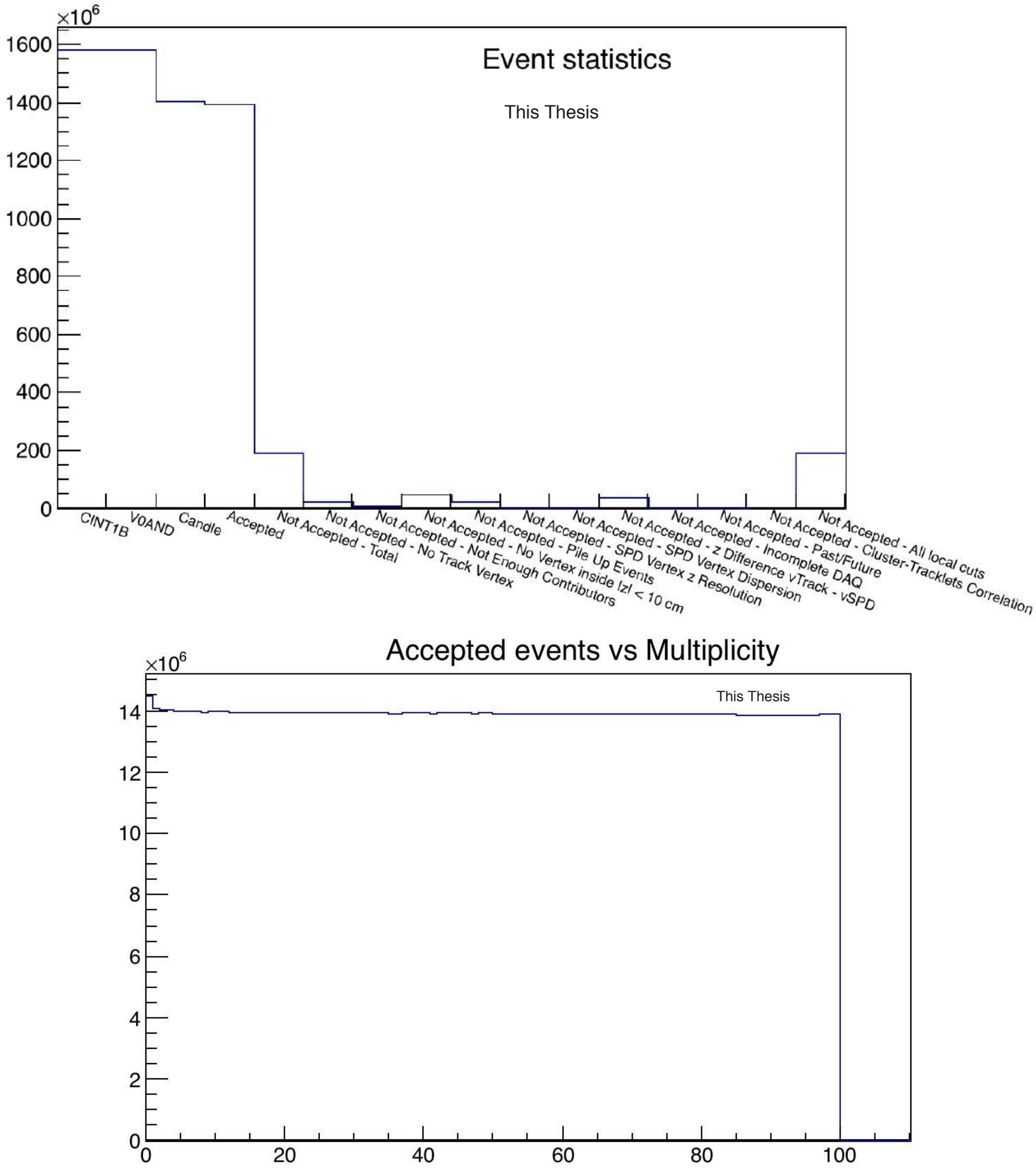

Figure 3.4: **Upper Panel**: Event statistics after implementing event-selection cuts. The fourth bin shows the total number of accepted events for this analysis. **Lower Panel**: Accepted events as a function of multiplicity [12].

3.1.2 Spherocity Selection

We begin by defining transverse spherocity for an event. In general, it is defined for a unit vector $\hat{n}$ in the transverse direction (n_T,0) which minimizes the following ratio [8, 9, 13].

$$S_0 = \frac{\pi^2}{4}\left(\frac{\Sigma_i\, |\vec{p}_{\mathrm{T_i}} \times \hat{n}|}{\Sigma_i\, p_{\mathrm{T_i}}}\right)^2. \tag{3.1}$$

By restricting it to the transverse plane, spherocity becomes infrared and collinear safe [14]. By construction, the extreme limits of spherocity are related to specific configurations of events in the transverse plane. The limit of spherocity is between 0 to 1. Spherocity becoming 0 would mean that the events are jet-like (back-to-back structure), while 1 would mean the events are isotropic. The jet-like events are hard, while the isotropic events result from soft processes. Figure 3.5 depicts the jetty and isotropic events in the transverse plane.

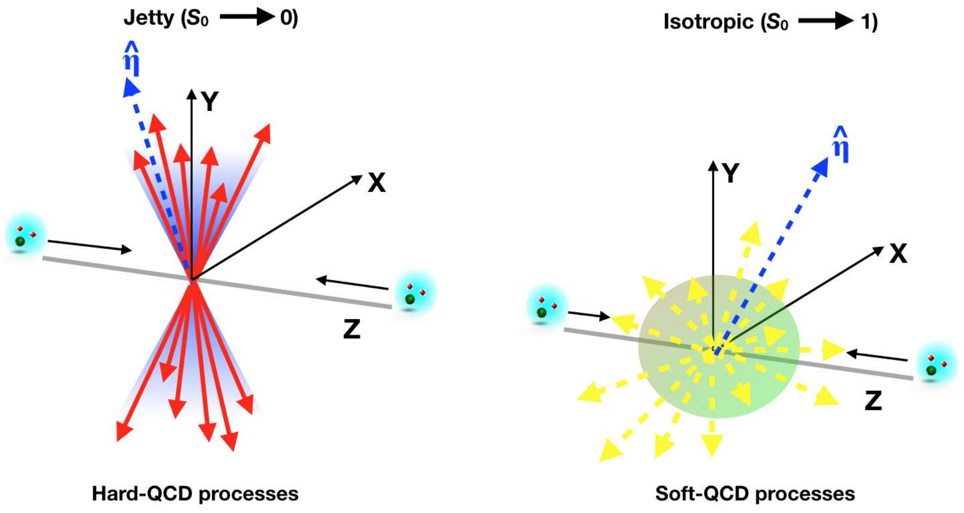

Figure 3.5: (Color Online) Depiction of jetty and isotropic events in the transverse plane.

In the current analyses, only events with more than 10 tracks are considered for the transverse spherocity distribution, which is in line with previous analysis [15].

It is worth mentioning here that calculating spherocity using the definition given by Eq. 3.1 introduces a neutral jet bias and the detector smearing effect as investigated in Ref. [15]. This problem was fixed by introducing a new estimator denoted by $S_0^{p_{\rm T}=1}$. In this new estimator, the magnitude of the $p_{\rm T}$ for each track is 1.0. This implies S_0 will now only consider the angular component when calculating the transverse spherocity. It has been shown in ref. [15] that the new estimator $S_0^{p_{\rm T}=1}$ consistently has a smaller smearing effect than for the normal S_0 estimator. Furthermore, the region between 0.7-5.0 GeV/c should be safe to use the new estimator without considering the unfolding procedure, which has been considered in the present analysis. Following track cuts were used for spherocity calculation, which is the same as the analysis of charged particle production as a function of spherocity in pp collisions at $\sqrt{s} = 13$ TeV [16] and analysis of identified particle production as a function of spherocity in pp collisions at $\sqrt{s} = 13$ TeV [17].

1. minimum number of clusters in TPC: 50
2. maximum χ^2 per cluster in TPC: $\chi^2 < 4$
3. reject kink daughters
4. require ITS refits
5. require TPC refits
6. $|DCA_z| < 3.2$ cm
7. $|DCA_{xy}| < 2.4$ cm
8. AliESDtrackCuts::SetDCAToVertex2D(kFALSE)
9. $p_{T,track} > 0.15$ GeV/c
10. $|\eta_{track}| < 0.8$ GeV/c

After implementation of the above cuts, spherocity ($S_0^{p_\mathrm{T}=1}$) distribution for different multiplicity classes in pp collisions at $\sqrt{s} = 13$ TeV is shown in Fig. 3.6. As expected, the lowest multiplicity class is dominated by the jetty events, and the highest multiplicity class is dominated by the isotropic events, with isotropic events increasing with event multiplicity. Now we consider high multiplicity events given by (0-10%) V0M multiplicity class and extracted $S_0^{p_\mathrm{T}=1}$ quantiles. An illustration figure to explain the scenario lucidly is shown in Fig. 3.7. The numerical cuts for the corresponding $S_0^{p_\mathrm{T}=1}$ quantiles are listed in Table 3.2, which is in line with previous analyses like Ref. [15]. These cuts are in accordance with one obtained in Ref. [15, 18]. It is to point out here that the $S_0^{p_\mathrm{T}=1}$ distribution obtained using the AOD dataset was not in line with one obtained using ESD data. This problem is fixed by considering ITS, TPC refit for the AOD dataset followed by modification of filterbit in the current resonance package used for AOD tracks. Brief details of this modification are given in the appendix 3.4.1.

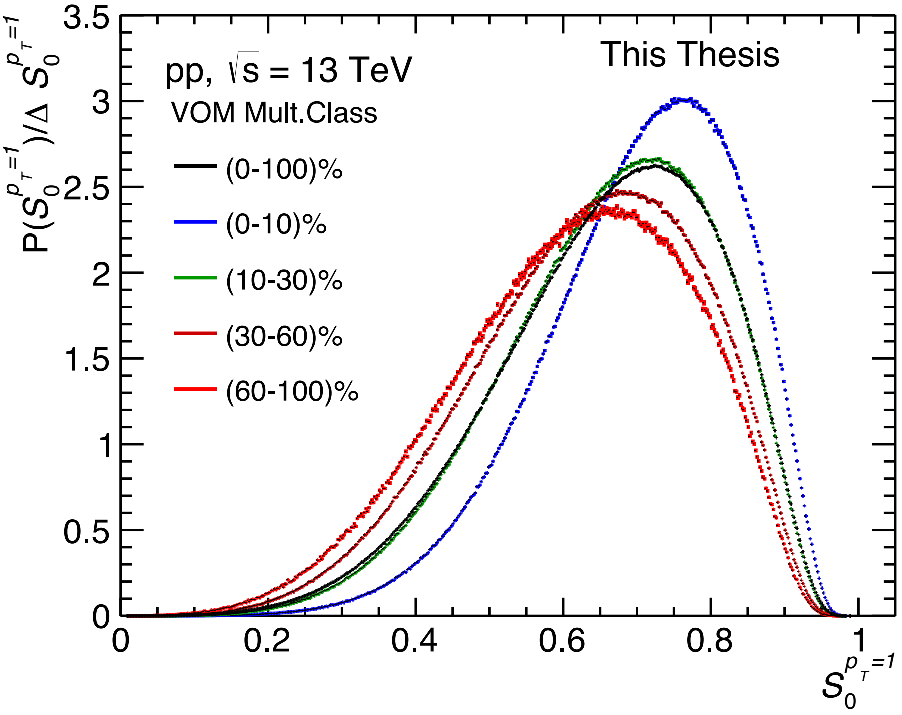

Figure 3.6: (Color Online) Spherocity distribution for different multiplicity classes in pp collisions at $\sqrt{s}$ = 13 TeV using AOD dataset [12].

3.1.3 Track Selection and Particle Identification

The $K^*(892)^\pm$ mesons were identified by reconstructing their decays products, a charged pion ($\pi^\pm$) and a K^0_S pair. Here, K^0_S is a V^0 particle. Different criteria are used to select strongly decayed primary pions and K^0_S. Selection criteria are also used for daughter tracks (pions) from weak decay of K^0_S. Detailed selection criteria for primary pions and K^0_S are given below.

3.1.4 Primary pion selection

Primary charged tracks were selected by applying the following cuts:

1. $p_{\mathrm{T}} > 0.15$ GeV/c
2. $-0.8 < \eta < 0.8$

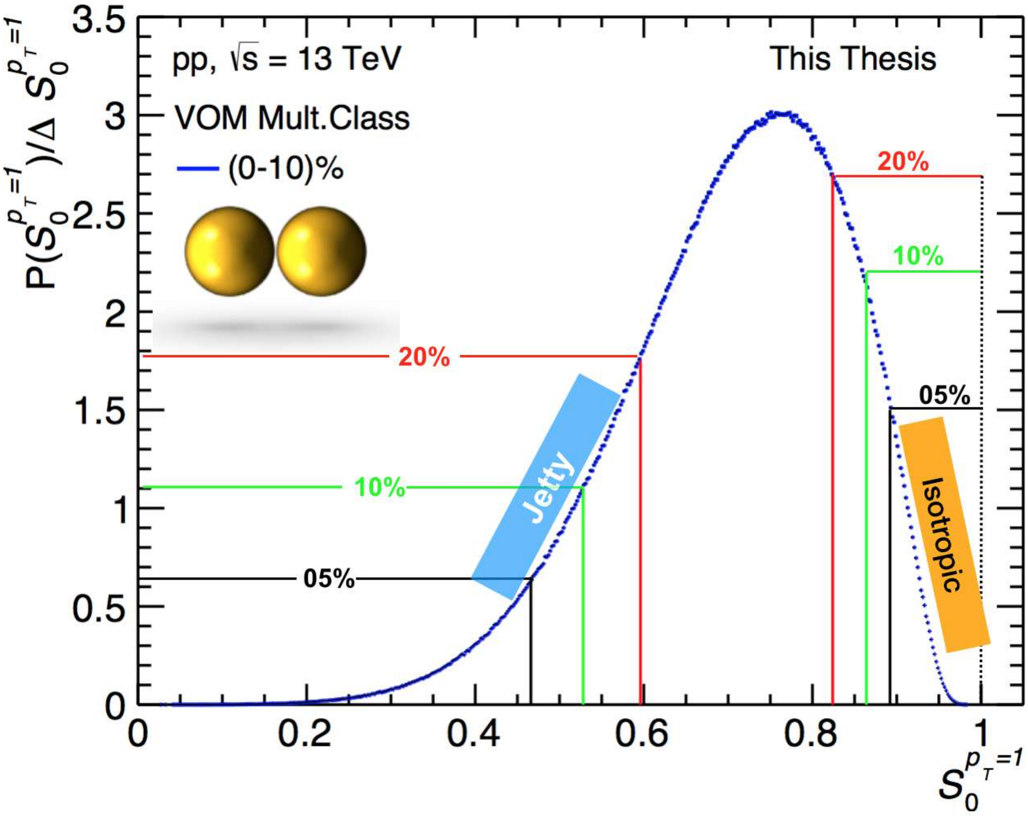

Figure 3.7: (Color Online) Spherocity quantiles (20%, 10% and 5%) considering low and high -$S_0^{p_T=1}$ distribution for (0-10%) V0M multiplicity class in pp collision at $\sqrt{s}$ = 13 TeV using AOD dataset.

3. Reject kink daughters
4. Minimum number of rows crossed in TPC is 70
5. Ratio of number of crossed rows to number of findable clusters in TPC > 0.8
6. Require ITS refits
7. Require TPC refits
8. TPC χ^2 per clusters < 4.0

Table 3.2: Table containing the ranges for jetty and isotropic like events for V0M multiplicity class (0-10)% with different spherocity quantiles [12].

$S_0^{p_{\mathrm{T}}=1}$ **quantiles**	**Jetty events**	**Isotropic events**
20%	0 – 0.596	0.824 – 1
10%	0– 0.528	0.864– 1
5%	0– 0.466	0.892– 1

9. ITS χ^2 per clusters $<$ 36.0
10. χ^2 per clusters in TPC-Constrained global fit $<$ 36.0
11. Minimum number of clusters in SPD: 1 (AliESDtrackCuts::SetClusterRequirementITS(kSPD, kAny))
12. AliESDtrackCuts::SetDCAToVertex2D(kFALSE)
13. AliESDtrackCuts::SetDCAToVertex2D(kFALSE)
14. $|DCA_z| < 2$ cm
15. $|DCA_r| < 0.0105{+}0.0350\ p_T^{-1.1}$ (a 7σ p_{T} dependent cut)

These cuts, but the first two, are included in the function **AliESDtrackCuts: GetStandardITSTPCTrackCuts2011(kTRUE, 1)** which implements the standard ITS/TPC track cuts from 2011.

The primary pions were identified through their energy loss dE/dx in the Time Projection Chamber (TPC). For this analysis, wider TPC cuts were used at low momentum due to a problem with TPC PID. The following p-dependent PID selection cuts were applied:

- $|N\sigma_{TPC}| <$ 6 for $p <$ 0.3 GeV/c
- $|N\sigma_{TPC}| <$ 4 for $0.3 \leqslant p \leqslant$ 0.4 GeV/c

- $|N\sigma_{TPC}| <$ 3 for $p >$ 0.4 GeV/c

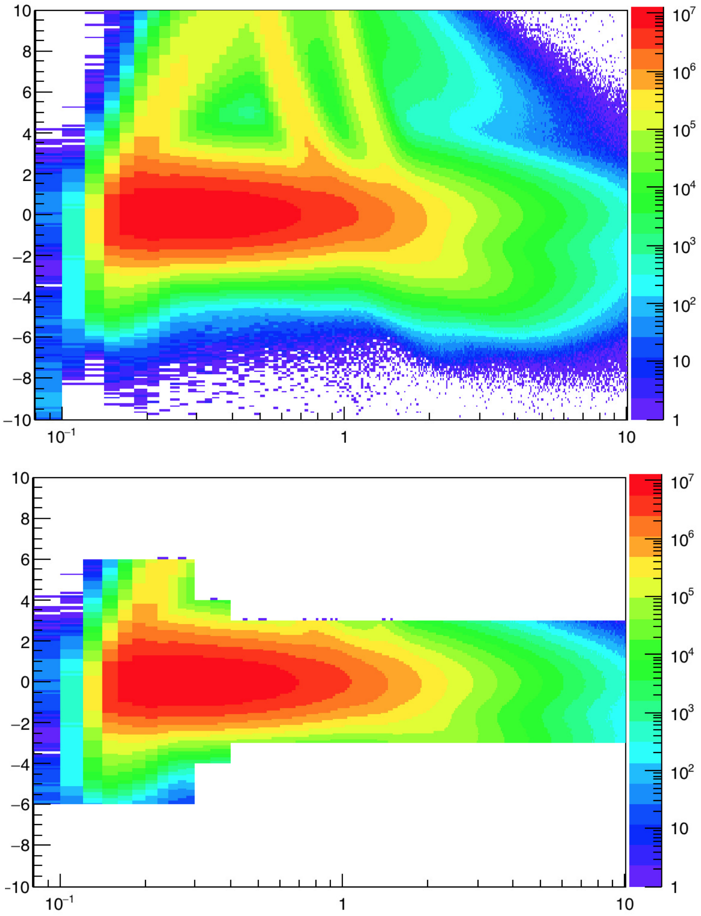

Figure 3.8: (Color online) $N\sigma_{TPC}$ versus momentum p for pions without any PID cut (upper panel) and after p-dependent PID cut is applied (lower panel) [12].

In Fig. 3.8 $N\sigma_{TPC}$ versus momentum (p) for pions without any PID cut (left panel) and after that p-dependent PID cut is applied (right panel) are shown.

3.1.5 V^0 selection

We reconstruct K^0_S by applying topological cuts on the daughter tracks. The V^0 is identified by its decay $K^0_S \rightarrow \pi^+ + \pi^-$. The decay topology of V^0 particle is shown in Fig. 3.9. The following selection criteria were applied for daughter tracks (pions) from the weak decay of K^0_S.

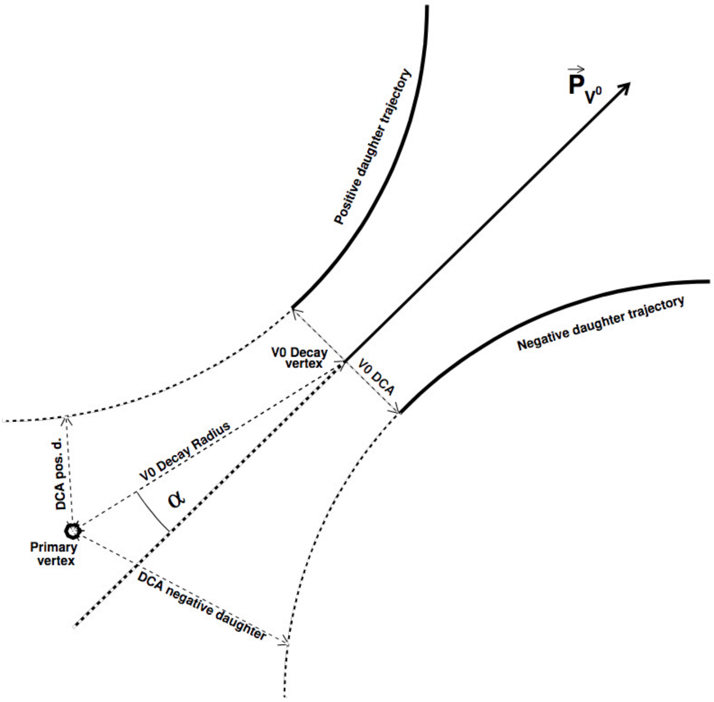

Figure 3.9: Decay topology of V^0 particle [19].

1. $-0.8 < \eta < 0.8$
2. Reject kink daughters
3. Require TPC refits
4. Minimum number of rows crossed in TPC $>$ 70
5. Ratio of number of crossed rows to number of findable clusters in TPC >0.8
6. DCA of tracks to PV $>$ 0.06 cm

Furthermore secondary pions were identified through their energy loss dE/dx in the Time Projection Chamber (TPC), by a wide PID cut —N$\sigma_{TPC}| <$ 6.

The pairs of $\pi^+\pi^-$ which fulfill the following V^0 selection were taken as K^0_S candidates

1. Only Offline V^0

2. Rapidity $|y| <$ 0.8
3. Fiducial Volume (V^0 2D decay radius) $>$ 0.5 cm
4. V^0 cosine of pointing angle $>$ 0.97
5. DCA V^0 daughters $<$ 1.0 s
6. V^0 Mass Tolerance $<$ 4 s
7. Proper Lifetime (mL/p) $<$ 20 cm

This selection criteria is inline with Ref. [20].

The multiplicity class and events with high and low spherocity are selected using the above selection cuts. We proceed to reconstruct the invariant mass of the K$^{*\pm}$ from their decay daughters, $\pi^\pm$ K^0_S. This will help to understand the K$^{*\pm}$ meson production in an environment rich with high MPI events and back-to-back jets.

3.1.6 Signal Extraction

In this analysis, the raw yield of K*(892)$^\pm$ was estimated in the following eight p_{T} -bins (0.8 - 1.2, 1.2 - 1.6, 1.6 - 2.0, 2.0 - 2.5, 2.5 - 3.0, 3.0 - 3.5, 3.5 - 4.0, 4.0 - 5.0). To extract the yields of K*(892)$^\pm$ mesons in each p_{T} -bin, the following procedure is used. First, the invariant-mass distribution of K$^0_S\pi^\pm$ was computed in the same event by the invariant mass of K^0_S and pion pairs. This gave a peak over a large combinatorial background estimated by the event-mixing technique. In this method, the shape of the uncorrelated background is estimated from the invariant mass distribution of pions and K^0_S pairs from different events. To avoid mismatch due to different acceptance and to assure a similar event structure, particles from events with similar vertex position z ($\Delta z <$1cm) and track multiplicity n ($\Delta n <$ 5) were used. To reduce statistical uncertainties, each event was mixed with the other 10 events. The mixed-event distribution was then normalized to the same event distribution in the invariant mass region 1.1 < M < 1.2 GeV/c^2. The signal is obtained by subtracting the mixed-event combinatorial background from the same event invariant mass distribution. The $K_S^0\pi^{\pm}$ invariant mass distribution for the bin 1.6 < p_T < 2.0 GeV/c^2 with the background estimated by pairs of different events is shown in the top panel of Fig. 3.10. For the same p_T -bin, the signal obtained after background subtraction is shown in the bottom panel of the same figure.

3.1.7 K*(892)$^{\pm}$ peak fits

The invariant mass distribution is obtained after subtracting the combinatorial background estimated by the event mixing technique described above. However, after such an ideal background subtraction, a residual background will remain along with the K$^{*\pm}$ signal, as seen in the bottom of Fig. 3.10. The dominant sources of such background are correlated real $\pi^{\pm}$ K_S^0 pairs and correlated but unrecognized pairs. This residual background is fitted by the following function

$$F_{BG}(M_{k\pi}) = [M_{k\pi} - (m_{\pi} + m_K)]^n exp(A + BM_{k\pi} + CM_{k\pi}^2) \tag{3.2}$$

where, m_{π} = 139.57018 GeV/c^2 [21] and m_K = 497.611 GeV/c^2 [21] are respectively the pion and K_S^0 masses. And n, A, B, C are the fit parameters. It is worth noting that the parameter A for each p_T bin gives the raw yield counts of K*(892)$^{\pm}$. To have a good fit the width was fixed to its PDG value (50.8 MeV/c^2).

In line with other resonance analysis [20, 22–24], the total fit function is the sum of a non-relativistic Breit-Wigner function and Eq. 3.2 and is given as

$$\frac{A}{2\pi}\frac{\Gamma_0}{(M_{k\pi} - M_0)^2 + \frac{\Gamma_0^2}{4}} + F_{BG}. \tag{3.3}$$

where, M_0 and Γ_0 are the mass and the width of the K*(892)$^{\pm}$. The parameter A is the integral of the peak function from 0 to ∞. The residual background shape

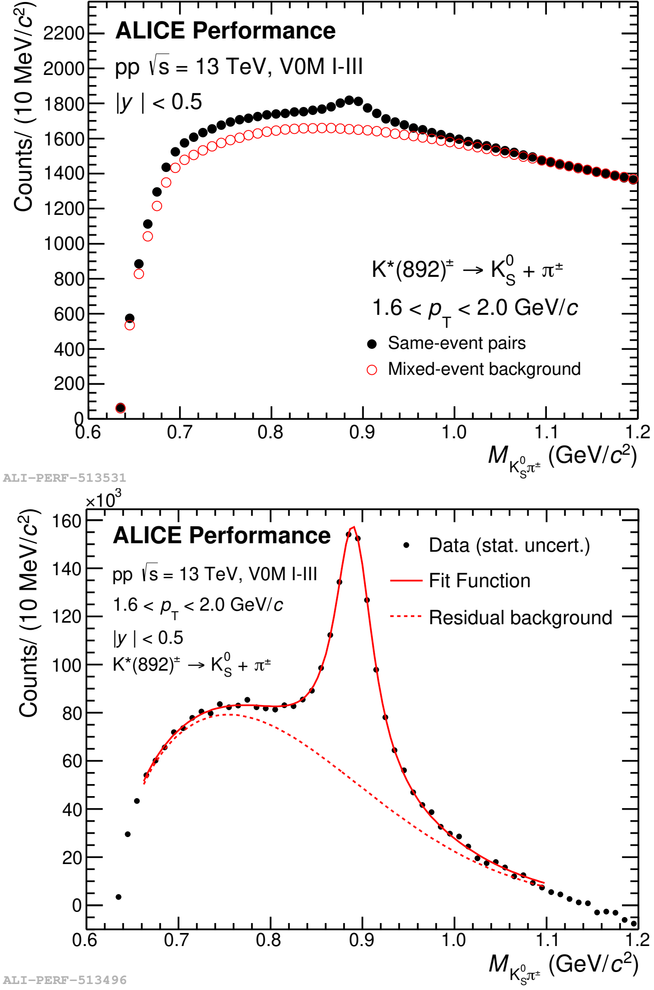

ALI-PERF-513531

ALI-PERF-513496

Figure 3.10: (Color Online) The $K_S^0\pi^{\pm}$ invariant mass distribution in $|y| < 0.5$ for the bin $1.6 < p_T < 2.0$ GeV/c^2 in pp collisions at $\sqrt{s}$ = 13 TeV. The background shape estimated using pairs from different events (event-mixing technique) is shown as open red circles. (Right panel) The $K_S^0\pi^{\pm}$ invariant mass distribution for the bin $1.6 < p_{\mathrm{T}} < 2.0$ GeV/c^2 after background subtraction. The solid red curve is the results of the fit by Eq. 3.3, the dashed red curve describes the residual background given by Eq. 3.2 [12].

for the different p_{T} bins was extracted from Monte Carlo simulated data.

Figure 3.11, 3.12 and 3.13 show the event-mixing background-subtracted signals with residual background and peak fits for (0 –10)% V0M multiplicity class in pp collisions at $\sqrt{s}$ = 13 TeV for spherocity-integrated and $S_0^{p_{\mathrm{T}}=1}$ in 20% quantiles for isotropic and jetty events, respectively. Corresponding spherocity selection cuts for jetty and isotropic events are mentioned in Table 3.3. For other $S_0^{p_{\mathrm{T}}=1}$ quantiles, please see Appendix. B.

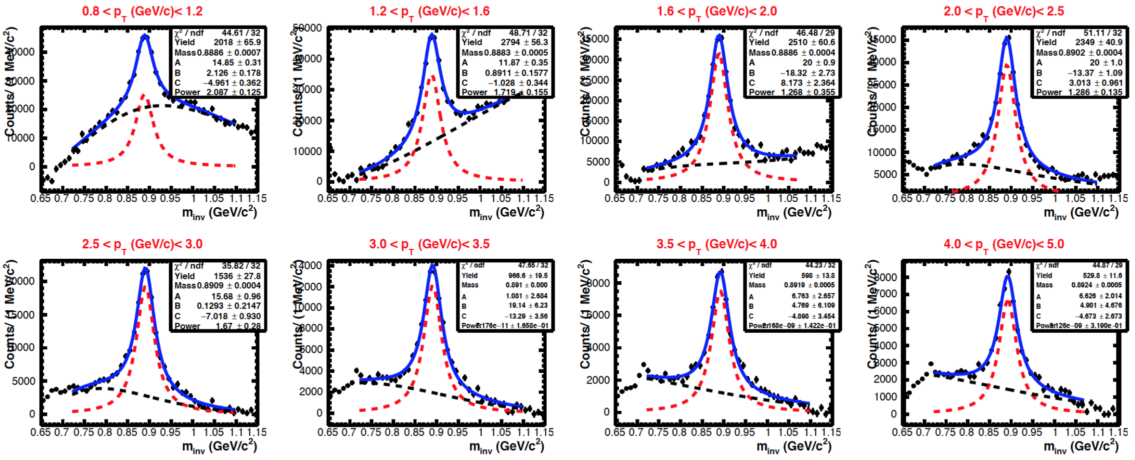

Figure 3.11: (Color Online) Invariant-mass distributions and fits for p_{T} bins ranging from $0.8 < p_{\mathrm{T}} < 5$ after event-mixing background subtraction for **spherocity integrated** events for (0 –10)% V0M multiplicity class in pp collisions at $\sqrt{s}$ = 13 TeV. The residual background is fitted using eq. 3.2 shown by black dotted line. Blue line shows the fitting of signal + residual background. Dotted red line shows the signal and residual background separately [12].

3.1.8 Extraction of K$^*(892)^{\pm}$ raw Yield

The raw yield of K$^*(892)^{\pm}$ is obtained using two different methods: the fit function (Y$_{FI}$) or bincounting (Y$_{BC}$), where the first was used as default and the second was used for systematic study.

Function Integral(Y$_{FI}$): The parameter A of the fit is the integral of the peak function from 0 to ∞, but the mass region 0< $M_{k\pi} < (m_\pi + m_K)$, where, m_π = 139.57018 GeV/c^2 [21] and m_K = 497.611 GeV/c^2 [21] are the masses of

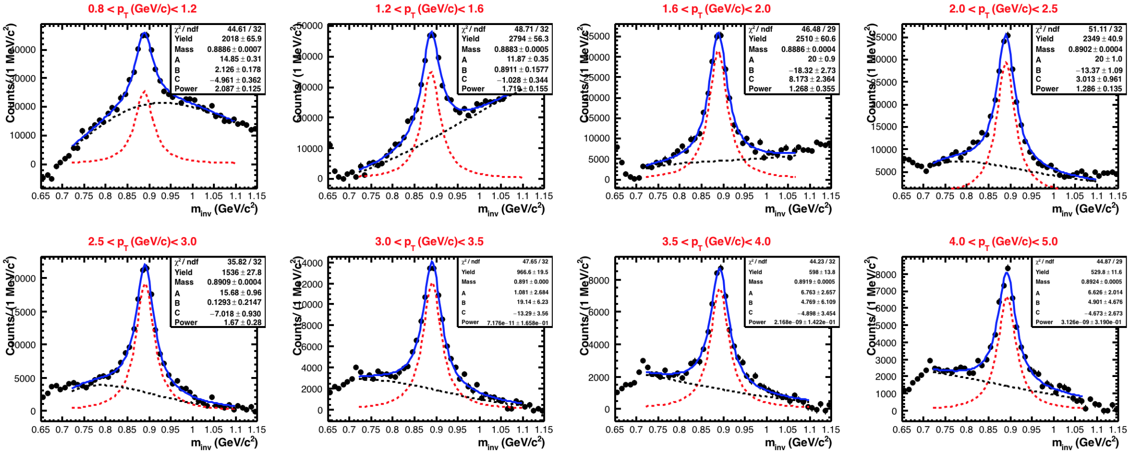

Figure 3.12: (Color Online) Invariant-mass distributions and fits for p_{T} bins ranging from $0.8 < p_{\mathrm{T}} < 5$ after event-mixing background subtraction for **isotropic** events ($S_0^{p_{\mathrm{T}}=1}$ in 20% quantiles) for (0-10)% multiplicity classes in pp collisions at $\sqrt{s} = 13$ TeV. The residual background is fitted using eq. 3.2 shown by black dotted line. Blue line shows the fitting of signal + residual background. Dotted red line shows the signal and residual background separately [12].

charged pion and K_S^0 respectively, is kinematically forbidden. Therefore

$$Y_{FI} = A - \int_0^{m_\pi + m_K} fit(m_{inv}) dm_{inv} \tag{3.4}$$

The integral in the kinematically forbidden region is about 2.5 % of the total integral, with the exact ratio depending on the peak parameters.

Bin counting (Y$_{BC}$):

The raw yield (N$_{BC}$) in the region I$_{min}$ $< M_{K\pi} <$I$_{max}$ (where I$_{min}$ $= M_0 - 2\Gamma_0$ (0.79 GeV/c^2) and I$_{max}$ $= M_0 + 2\Gamma_0$ (0.99 GeV/c^2)), respectively was extracted by integrating the invariant mass histogram (N$_{counts}$) over the region I$_{min}$ $< M_{K\pi} < I_{max}$ and subtracting the integral of the residual background portion estimated over that same interval (N$_{RB}$).

The raw yield (N$_{BC}$) in the region I$_{min}$ $< M_{K\pi} < I_{max}$ (where I$_{min}$ $= M_0 - 2\Gamma_0$ (0.79 GeV/c^2) and I$_{max}$ $= M_0 + 2\Gamma_0$ (0.99 GeV/c^2)), respectively was extracted by

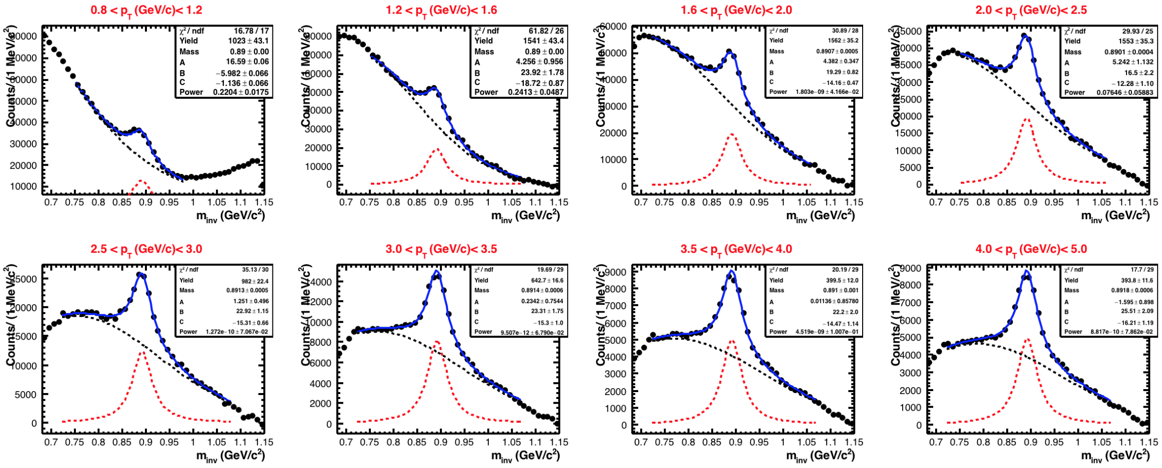

Figure 3.13: (Color Online) Invariant-mass distributions and fits for p_{T} bins ranging from 00.8 < p_{T} < 5 after event-mixing background subtraction for **jetty** events ($S_0^{p_{\mathrm{T}}=1}$ in 20% quantiles) for (0-10)% multiplicity classes in pp collisions at $\sqrt{s} = 13$ TeV. The residual background is fitted using eq. 3.2 shown by black dotted line. Blue line shows the fitting of signal + residual background. Dotted red line shows the signal and residual background separately [12].

integrating the invariant mass histogram (N$_{counts}$) over the region I$_{min}$ $< M_{K\pi} <$ I_{max} and subtracting the integral of the residual background portion estimated over that same interval (N$_{RB}$).

$$N_{BC} = N_{counts} - N_{RB} \tag{3.5}$$

The error on N$_{RB}$ was calculated by using the root function fBgOnly → IntegralError(I$_{min}$, I$_{max}$, Par[4],a), where a is the covariance matrix, fBgOnly is the residual background function and Par[4] is a vector with the value of the parameters of the residual background function. To obtain the total raw yield we have to correct the N$_{raw}$ value for the the yields in the regions m$_\pi$$+m_K < M_{K\pi} <$ $I_{min}(N_{low})$ and M$_{K\pi}$ $> I_{max}(N_{high})$. N$_{low}$ and N$_{high}$ were estimated integrating in the regions $m_\pi + m_K <$ M$_{K\pi}$ $<$ I$_{min}$ and I$_{max}$ $< M_{K\pi} <\infty$ the non-relativistic

Breit-Wigner function extracted from the fit.

$$N_{low} = \int_{m_\pi + m_K}^{M_0 - 2\Gamma_0} fit(m_{inv}) dm_{inv} \tag{3.6}$$

$$N_{high} = \int_{M_0 + 2\Gamma_0}^{\infty} fit(m_{inv}) dm_{inv} \tag{3.7}$$

This accounts for about 13% of the total yield. The total raw yield was obtained adding low and high invariant mass tail contributions to the bin counting yield.

$$N_{raw} = N_{BC} + N_{low} + N_{high} \tag{3.8}$$

It is assumed that the statistical uncertainties of the yields in the tail regions are fully correlated with each other and with the statistical uncertainty of the yield calculated from the histogram. This means that the uncertainty on N_{BC}, N_{low}, N_{high} was summed. For the N_{BC}, the signal and the background are considered uncorrelated, and then their uncertainties are quadratically summed.

Fig. 3.14 presents the raw yield as a function of p_{T} for different $S_0^{p_{\mathrm{T}}=1}$ quantiles at high-multiplicity class (0-10)%. The errors reported in the following plots are statistical only.

3.1.9 Simulations

After obtaining the raw p_{T} -spectra, one must correct it with detector efficiency and acceptance. Simulated datasets are analyzed to extract the K*(892)$^\pm$ reconstruction efficiency × acceptance (calculation is given in section 3.1.10.1). The simulated dataset (AOD) for $\sqrt{s}$ = 13 TeV consists of 369 million events in the LHC16_17_18_GP_AOD235 production. Particle production and decays are simulated using the event generators like PYTHIA 8, while particle interactions with the ALICE detector are simulated using GEANT3. The same event selection,

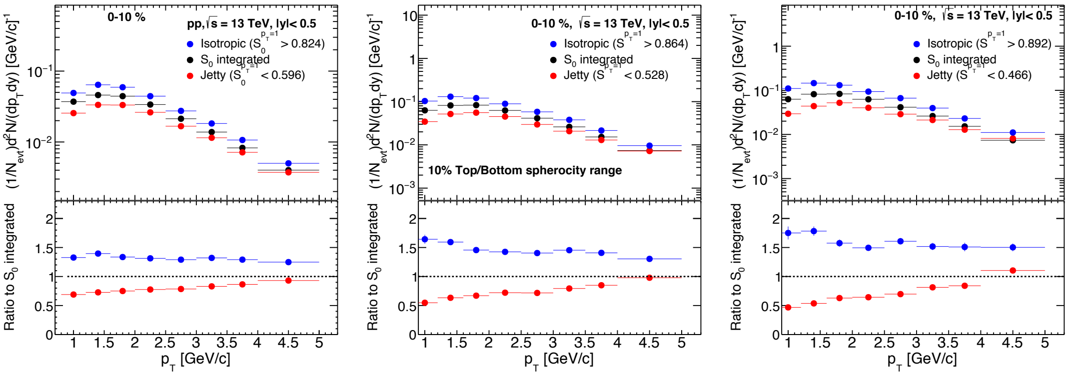

Figure 3.14: (Color Online) Raw Yield as a function of p_{T} for different $S_0^{p_{\mathrm{T}}=1}$ quantiles (**left** is for 20%, **middle** is for 10%, **right** is for 5%) for (0-10)% in pp collisions at at $\sqrt{s} = 13$ TeV [12].

track quality cuts, and topological cuts were used for the real and simulated data. The particles produced by the event generator (without any detector effects) are referred to as the ”generated” particles. These particles are the input for the GEANT3 detector simulation and the track, V^0 and signal reconstruction algorithms. The tracks and the V_0 are identified by the reconstruction algorithms, and which pass track and the topological selection and PID cuts are referred to as ”reconstructed” tracks and V^0. A reconstructed $\mathrm{K}^*(892)^{\pm}$ meson is a particle for which both the daughters (track, and V^0) have been reconstructed via GEANT3.

3.1.10 Correction and Normalization of Spectra

3.1.10.1 Reconstruction efficiency × acceptance

The reconstruction efficiency × acceptance, denoted as ϵ_{rec}, is calculated using the same simulated data described in Section 3.1.9. In each transverse-momentum bin, ϵ_{rec} is the ratio of two quantities described as follows:

Numerator: Reconstructed $\mathrm{K}^*(892)^{\pm}$: the number of reconstructed $\mathrm{K}^*(892)^{\pm}$ mesons with $|y| < 0.5$.

Denominator: Generated $\mathrm{K}^*(892)^{\pm}$: the number of generated $\mathrm{K}^*(892)^{\pm}$

mesons with $|y| < 0.5$ that decay in a K^0_S and a charged pion ($\pi^{\pm}$).

The uncertainty in ϵ_{rec} is calculated using the Bayesian approach [25]. The standard deviation in an efficiency $\epsilon = k/n$, where the numerator k is a subset of the denominator n, is:

$$\sigma = \sqrt{\frac{k+1}{n+2}\left(\frac{k+2}{n+3} - \frac{k+1}{n+2}\right)} \tag{3.9}$$

The fractional statistical uncertainty in ϵ_{rec} was added in quadrature with the statistical uncertainty of the uncorrected K$^*(892)^{\pm}$ yield to give the total statistical uncertainty of the corrected K$^*(892)^{\pm}$ yield.

Figure 3.15 shows the K$^*(892)^{\pm}$ meson reconstruction efficiency (ϵ_{rec}) as a function of p_{T} for minimum bias in pp collisions at $\sqrt{s}$ = 13 TeV. Inline with Ref. [15, 18], to avoid bias for spherocity calculation, we use the minimum bias reconstruction efficiency for all the spherocity classes.

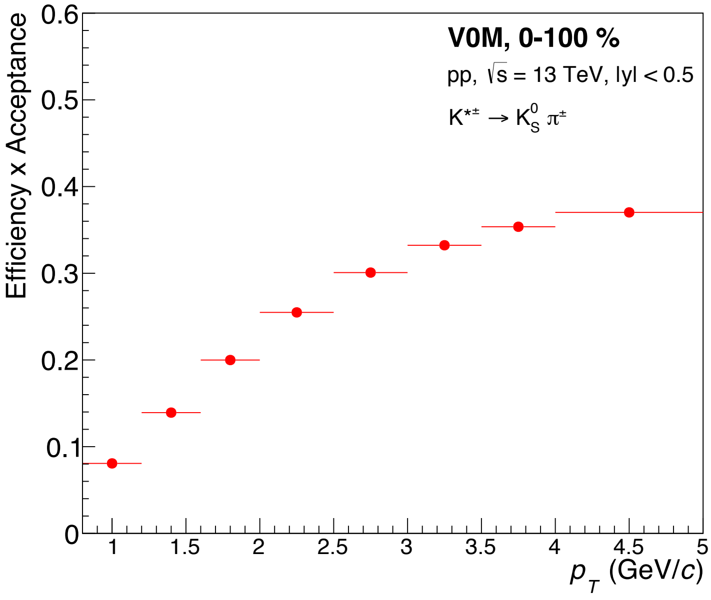

Figure 3.15: (Color Online) K$^*(892)^{\pm}$ meson reconstruction efficiency (ϵ_{rec}) as a function of p_{T} for multiplicity class for (0-100)% in pp collisions at at $\sqrt{s}$ = 13 TeV [12].

3.1.10.2 Efficiency corrected p_{T} spectra

The normalized and efficiency corrected differential transverse momentum spectra of $K^{*\pm}$ meson for different $S_0^{p_{\mathrm{T}}=1}$ quantiles in high-multiplcity classes (0-10)% V0M multiplicity class in pp collisions at $\sqrt{s} = 13$ TeV is calculated as follows:

$$\frac{d^2N}{dp_T dy} = \frac{\text{raw counts}}{N_{evt}.BR.dp_T dy} \times \frac{1}{\epsilon_{rec}} \tag{3.10}$$

where N_{evt} is the number of events analyzed for a given multiplicity class, BR (= 0.66 × 0.5 = 0.33) is the branching ratio for $K^*(892)^\pm \rightarrow K_S^0 + \pi^\pm$ decay channel, dy =1 and ϵ_{rec} is the efficiency × acceptance described in the above subsection. The signal loss and event loss correction factors are negligible for high multiplicity pp collisions. Figure 3.16 shows the efficiency corrected p_{T} spectra with spherocity classes for different $S_0^{p_{\mathrm{T}}=1}$ quantiles namely, 20%, 10% and 5% at (0-10)% V0M multiplicity class.

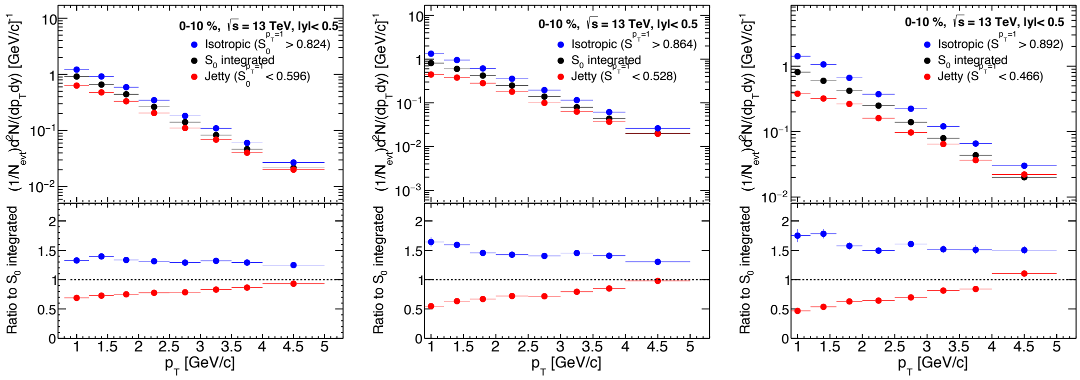

Figure 3.16: (Color Online) Corrected spectra as a function of p_{T} for different $S_0^{p_{\mathrm{T}}=1}$ quantiles (**left** is for 20%, **middle** is for 10%, **right** is for 5%) for (0-10)% in pp collisions at at $\sqrt{s} = 13$ TeV [12].

3.1.11 Cross-check

Before proceeding to systematics calculations, we want to cross-check the validity of our results with previous measurements of $\mathrm{K}^{*}(892)^{\pm}$ at the same center of mass-energy. In this regard, we compared our spherocity integrated corrected yield obtained at minimum bias multiplicity class with Ref. [20], where the $\mathrm{K}^{*}(892)^{\pm}$ Min. Bias spectrum in pp at $\sqrt{s}$ =13 TeV is obtained. The main difference between Ref. [20] and current work is that Ref. [20] uses an ESD dataset, which will include a set of slightly different corrections than this analysis. This comparison is shown in Fig. 3.17. The lower panel of Fig. 3.17 shows the fitting of the ratio (current analysis to Ref. [20]) by a constant function of a parameter. Moreover, this parameter comes out to be 0.9707 ± 0.0118. This shows that the comparison seems to match reasonably well within uncertainties.

3.1.12 Estimation of systematic uncertainties

For each transverse-momentum bin, several measurements of the yield and its statistical uncertainties exist. Generally, the yield is calculated for every possible permutation of the analysis parameters (PID cuts, combinatorial background, etc.), which constitutes the systematic uncertainties. The systematic uncertainties associated with the experimental data are one of the significant parts of the data analysis. A commonly used method to find systematic uncertainties (e.g., in the p_{T} -spectra of a particle) is to repeat the analysis several times to get many measurements. Each of these measurements has to be performed with one or more variations on the analysis parameters (e.g., PID/track selection cuts, varying raw yield extraction techniques, etc.). Same datasets (or datasets with large overlap) are used to make these measurements, ensuring they are statistically dependent. The systematic uncertainties associated with the measurement are calculated by finding the differences between the "alternate" and the "default" measurement. Here, the default measurement is one measurement or perhaps an average (the

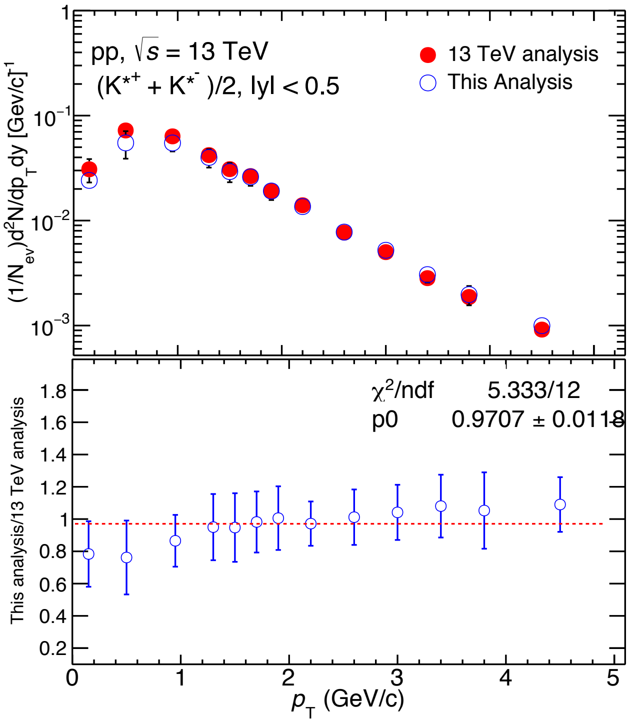

Figure 3.17: (Color Online) Minimum Bias cross-check with the equivalent $\sqrt{s}$ =13 TeV analysis (the data in the ratio are both 13 TeV). **Upper panel**: Mini. bias. p_{T} -spectra of current analysis is compared with Ref. [20]. **Lower panel**: Dotted red lines is a constant function of one parameter. Here, 13 TeV analysis mentioned in the Legend of the upper panel is Ref. [20] [12].

central value). As the default and alternate measurements are statistically consistent. i.e., they are not statistically independent; one needs to know whether they are consistent within their statistical uncertainties. A celebrated method has been used by ALICE called "Barlow checks," as prescribed by Prof. R. Barlow in the Ref. [26], to identify systematic uncertainties from statistical uncertainties.

Let us denote the default (alternate) measurement as Y_d (Y_a) and its statistical uncertainties by σ_d (σ_a). The difference between the two measurements is given by,

$$\Delta = Y_d - Y_a \tag{3.11}$$

and the quadrature difference of their statistical uncertainties is given by,

$$\sigma_{cc} = \sqrt{\sigma_d^2 - \sigma_a^2} \tag{3.12}$$

As described in the Ref. [26], the difference between the default and alternate measurements is compared to the difference in quadrature of the statistical uncertainties of those measurements. Now, to check systematic uncertainties from statistical uncertainties, ratio of Eq. 3.11 to Eq. 3.12 (Δ/σ_{cc}) is calculated for each p_{T} -bin. It is expected that if the two measurements are purely statistical, the distribution of Δ/σ_{cc} should be approximately a Gaussian with a mean near 0, a standard deviation near 1, and 68% of the entries would lie within Δ/σ_{cc} <1. A large deviation from the ideal behavior implies that the difference between the default and alternate measurements is not purely statistical and should be included in the systematic uncertainties. In this analysis, we plotted the Δ/σ_{cc} distribution for each variation. And we considered a source as a systematic source if three out of the following four criteria have failed.

1. $\Delta/\sigma_{cc} < 0.1$
2. $\sigma_{cc} < 1.1$
3. fraction of entries with $\pm\ 1\sigma > 55$
4. fraction of entries with $\pm\ 2\sigma > 90$

For the p_{T} spectrum, the following sources of systematic uncertainty were considered: PID cuts, primary pion track selection, signal extraction, secondary track selection for K_S^0, primary vertex selection, material budget, hadronic interaction, and global tracking uncertainty, etc. These variations are divided into subgroups, and the general strategy of calculating the total systematic uncertainties is summarised below:

- Choose one set of analysis parameters as the default set

- Observe the deviations in the yield from the default measurement when one of those parameters is changed
- The RMS value is taken to be the systematic uncertainty for a given source
- The systematic uncertainties for different sources are added in quadrature to obtain the total systematic uncertainty from all sources

The default set of parameters chosen for $\mathrm{K}^*(892)^\pm$ measurements are given below:

- **Combinatorial background:** Mixed event
- **Normalization Region:** $1.1 < m_{inv} <$1.2 GeV/c^2
- **Fit Region:** Depending up on the background shape the fit region is chosen for each p_T bin for default case.
- **Residual Background Fit:** Given by Eq. 3.2
- **Peak Fit:** Breit-Wigner, where the width parameter is a free parameter, given by first term of Eq. 3.3
- **Yield Extraction Method:** Bin counting

A brief description of the sources of systematic uncertainties are listed below.

3.1.12.1 Global tracking uncertainty

The global tracking uncertainty in ITS-TPC matching for tracks in the runs used for this analysis has been estimated equal to 1% in each p_T bin [27].

3.1.12.2 Material budget

The systematic uncertainty due to uncertainties in the ALICE material budget is p_T dependent and considered from the analysis of Ref. [20].

3.1.12.3 Hadronic interaction cross-section

The systematic uncertainty due to uncertainties in the ALICE hadronic interaction cross-section of particles those are traversing the ALICE material is taken from the analysis Ref. [20].

3.1.12.4 Track cut variations for primary pion track selection

Systematic error is calculated by varying one track cut at a time.

DCA$_z$ Cut: DCA$_z$ <2 cm is taken as default; DCA$_z$ $<$ 56 cm and DCA$_z$ $<$ 6 cm are taken for systematic study.

TPC χ^2 Cut: TPC χ^2 $<$ 2.3 is taken as default; TPC χ^2 $<$ 2.3 is taken for systematic study.

N$_{cr,TPC}$ Cut: N$_{cr,TPC}$ $\geq$ 70 is taken as default; N$_{cr,TPC}$ $\geq$ 100 and N$_{cr,TPC}$ $\geq$ 80 is taken for systematic study.

Findable cluster (FC) Cut: FC $\geq$ 0.8 is taken as default; FC $\geq$ 0.9 is taken for systematic study.

Vertex Cut : $|v_z| <$ 10 cm is taken as default; $|v_z| <$ 8 cm and $|v_z| <$ 12 cm are taken for systematic study.

3.1.12.5 Track cut variations for K^0_S selection

For N$_{cr,TPC}$ and findable cluster (FC), variation are exactly similar to above used for primary pion selection.

DCA tracks to PV (cm): 0.06 is taken as default; 0.07 (shorthand: Var-1) and 0.05 (shorthand: Var-2) are taken for systematic study.

PID secondary π (σ): 5 is taken as default; 4.5 (shorthand: Var-1) and 4 (shorthand: Var-2) are taken for systematic study.

V^0 decay radius (cm): 0.5 is taken as default; 0.7 (shorthand: Var-1) and 0.3 (shorthand: Var-2) are taken for systematic study.

Cosine PA : 0.97 is taken as default; 0.95 (shorthand: Var-1) and 0.99 (shorthand: Var-2) are taken for systematic study.

DCA V^0 daughters (σ) : 1 is taken as default; 1.25 (shorthand: Var-1) and 0.75 (shorthand: Var-2) are taken for systematic study.

Lifetime (cm) : 20 is taken as default; 12 (shorthand: Var-1) is taken for systematic study.

K_S^0 mass tolerance (σ) : 4 is taken as default; 5 (shorthand: Var-1) and 3 (shorthand: Var-2) are taken for systematic study.

K$_S^0$ rapidity : 0.8 is taken as default; 0.9 (shorthand: Var-1) and 0.7 (shorthand: Var-2) are taken for systematic study.

3.1.12.6 Signal Extraction

Normalization range (GeV/c^2): 1.1 $<$ m_{inv} $<$1.2 is taken as default; 1.1 $<$ m_{inv} $<$1.3 (shorthand: Var-1) and 1.1 $<$ m_{inv} $<$1.4 (shorthand: Var-2)are taken for systematic study.

Fit Range (GeV/c^2): 0.72 $<$ m_{inv} $<$1.05 is taken as default; 0.75 $<$ m_{inv} $<$1.0 (shorthand: fr1) and 0.7 $<$ m_{inv} $<$1.15 (shorthand: fr2) are taken for systematic study.

Residual Background Fit function : Eq. 3.2 is taken as default; polynomial of order 3 (shorthand: Poly3) is taken for systematic study.

Width (GeV/c^2) : 0.0508 (PDG value) is taken as default; 0.0517 (shorthand: Var1) and free parameter (Var2) are taken for systematic study.

For each variation considered above, we have obtained a comparative figure by considering ratio of the corrected p_{T} -spectra (obtained from variation) with the default one. Some of this figures are displayed in the appendix section 3.4.4.

3.1.12.7 Total Systematic uncertainty

The total systematic uncertainty is the sum in quadrature of the uncertainties from the sources described above.

3.1.13 Systematic uncertainty uncorrelated with $S_0^{p_{\rm T}=1}$

The fraction of systematic uncertainty uncorrelated with $S_0^{p_{\rm T}=1}$ is also computed in the present analysis. This is done to consider the contribution of uncorrelated systematics when we take the ratio between $S_0^{p_{\rm T}=1}$ biased and $S_0^{p_{\rm T}=1}$ integrated spectra. In general, the same variations in the selection criteria will cause similar spectrum deviations for different $S_0^{p_{\rm T}=1}$ classes because the error is correlated across the spherocity classes. Here, the intention is to measure the fraction of the total uncertainty that depends on the spherocity class considered. This assignment could be done by computing a double ratio as described in ref. [15, 28]. The double ratio is given as

$$R(p_T) = (\frac{Y_{var}^{S_0^{p_{\rm T}=1}}}{Y_{def}^{S_0^{p_{\rm T}=1}}})^X \Big/ (\frac{Y_{var}^{S_0^{p_{\rm T}=1}}}{Y_{def}^{S_0^{p_{\rm T}=1}}})^{int.} \tag{3.13}$$

where, X is isotropic/jetty events, int is the spherocity-integrated events, $Y_{var}^{S_0^{p_{\rm T}=1}}$ denotes the corrected variated $p_{\rm T}$ spectra and $Y_{def}^{S_0^{p_{\rm T}=1}}$ denotes the corrected default $p_{\rm T}$ spectra. Here, R factor is computed as a function of $p_{\rm T}$ and its value equal to unity for a given variation would mean a fully correlated systematic uncertainty. The fraction of uncorrelated systematic uncertainty is given by $|1 - R|$ for a specific variation and the total uncertainty is equal to the sum in quadrature of the different components. Figure 3.18 shows the the magnitude of the total uncorrelated uncertainty across $S_0^{p_{\rm T}=1}$ for jetty and isotropic events in $S_0^{p_{\rm T}=1}$ 20% quantiles, respectively.

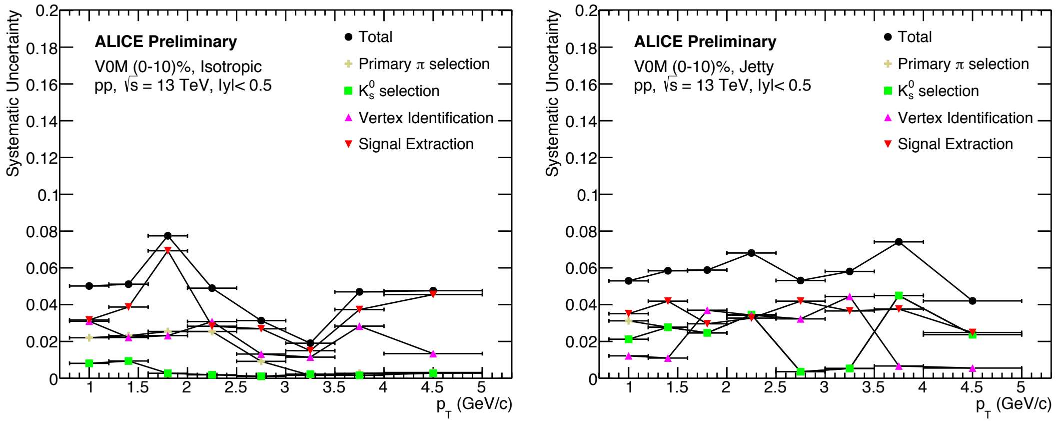

Figure 3.18: (Color Online) **Left panel**: Total uncorrelated systematic uncertainty across $S_0^{p_{\rm T}=1}$ in the $p_{\rm T}$-spectra of isotropic events. **Right panel**: Total uncorrelated systematic uncertainty across $S_0^{p_{\rm T}=1}$ in the $p_{\rm T}$-spectra of jetty events [12].

3.1.14 Fractional Uncertainty

Figure 3.19 shows the fractional uncertainties from all the sources as a function of $p_{\rm T}$ for different spherocity classes in (0 -10%) V0M multiplicity class in pp collisions at at $\sqrt{s}$ = 13 TeV. A smoothing procedure was applied to smoothen the systematic uncertainties [29].

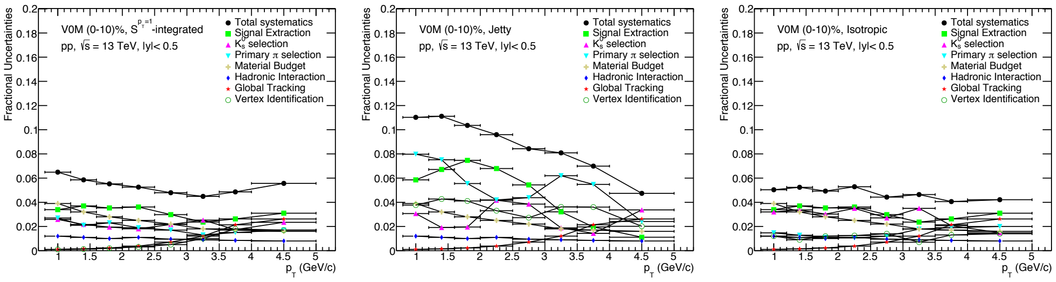

Figure 3.19: (Color Online) Fractional uncertainties from all the sources as a function of $p_{\rm T}$ for different spherocity classes [12].

3.1.15 Results and discussion

3.1.15.1 Corrected p_{T}-spectra with systematic uncertainty

The upper panel of Fig. 3.20 shows the final transverse momentum spectra for isotropic, jetty, and spherocity integrated event classes with systematic and statistical uncertainties for (0-10)% V0M multiplicity class and at different $S_0^{p_{\mathrm{T}}=1}$ quantiles namely, 20%, 10%, and 5%. And the lower panel shows the ratio of yield obtained considering isotropic and jetty events to the $S_0^{p_{\mathrm{T}}=1}$-integrated events. The bars show systematic uncertainties calculated in Sec 3.1.12.

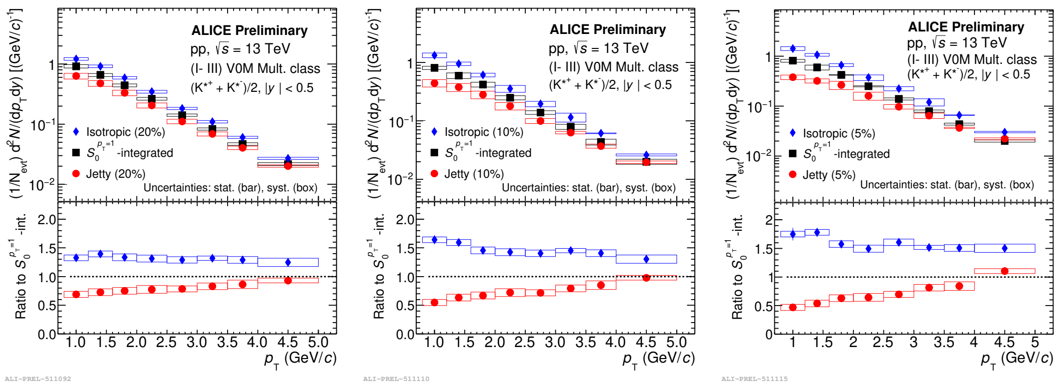

Figure 3.20: (Color Online) Corrected K*(892)$^{\pm}$ spectra as a function of p_{T} for different $S_0^{p_{\mathrm{T}}=1}$ quantiles (**left** is for 20%, **middle** is for 10%, **right** is for 5%) for (0-10)% V0M multiplicity class in pp collisions at $\sqrt{s} = 13$ TeV [12].

3.1.15.2 Particle ratio

Besides p_{T}-spectra, in this analysis, we have also looked into the p_{T} -differential particle ratio of K*(892)$^{\pm}$ meson to the long-lived stable hadrons such as pion ($\pi^+ + \pi^-$), kaon (K$^+$ + K$^-$)) and proton (p + $\bar{p}$). The upper panel of Fig. 3.21 shows the p_{T} differential particle ratio of K*(892)$^{\pm}$ to $\pi^+ + \pi^-$ (left), K$^+$ + K$^-$ (middle) and p + $\bar{p}$ (right) for (0-10)% V0M multiplicity class with 20% $S_0^{p_{\mathrm{T}}=1}$-quantiles in pp collisions at $\sqrt{s}$ =13 TeV for all the three spherocity classes. And the lower panel shows the ratio of particle ratio obtained considering isotropic and jetty events to the $S_0^{p_{\mathrm{T}}=1}$-integrated events.

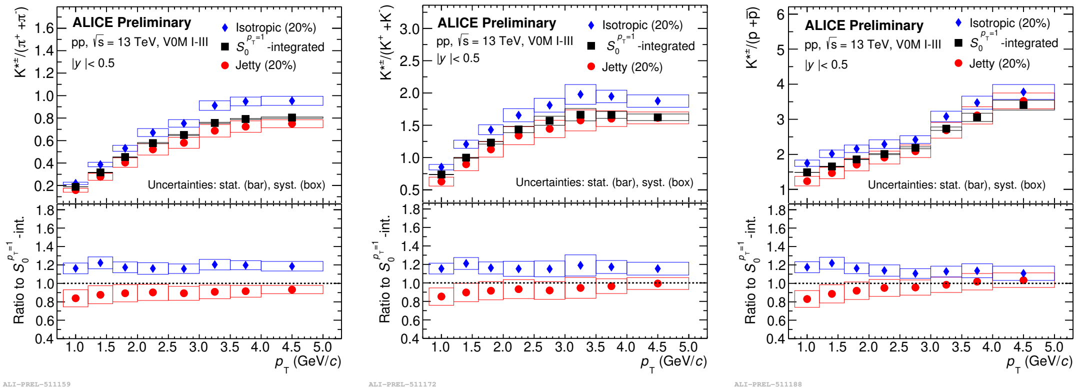

Figure 3.21: (Color Online) p_{T} differential particle ratio of K$^*(892)^{\pm}$ meson with $\pi^+ + \pi^-$) (**left**), K$^+ + K^-$ (**middle**) and p $+ \bar{p}$ (**right**) for (0-10)% V0M multiplicity class with $S_0^{p_{\mathrm{T}}=1}$ in 20% quantiles in pp collisions at $\sqrt{s} = 13$ TeV [12].

3.2 Event topology and multiplicity dependence of heavy-flavoured hadrons production in pp collisions at $\sqrt{s}$ = 13 TeV with PYTHIA8

Having seen the significant dependence of transverse spherocity on the production of a resonance particle-like K$^{*\pm}$ in pp collisions at $\sqrt{s} = 13$ TeV with ALICE in the above section, in this section[1], we have explored how heavy-flavored hadrons like D^0, J/ψ and Λ_c^+ behave in hard and soft QCD processes using transverse spherocity in the same system and at the same center-of-mass energy. It is worth noting that although K$^{*\pm}$ is a light-flavor particle, alone it may behave differently from other light-flavored hadrons in the hadronic phase (if present) because of its short lifetime and the processes it undergoes, e.g., rescattering and regenera-

---

[1] S. Deb, R. Sahoo, D. Thakur, S. Tripathy and A. Khuntia, J. Phys. G **48**, 095104 (2021).

tion. Thus, a direct comparison of heavy-flavored particles with $\mathrm{K}^{*\pm}$ may not be sufficient as $\mathrm{K}^{*\pm}$ alone cannot be a representative of light-flavored hadrons. The following work explores the heavy-flavored sector to understand the interplay of hard processes and underlying events in the light of event topology.

3.2.1 Event generation and Analysis methodology

PYTHIA8, a standalone Monte-Carlo event generator, is widely used to simulate ultra-relativistic collisions among the particles like electron-electron, electron-positron, proton-proton and proton-antiproton. It has been quite successful in explaining many features of the experimental data from the LHC qualitatively with different incorporated physics processes. PYTHIA8 includes MultiParton Interaction (MPI) scenario, which allows heavy-flavor quarks to be produced through $2 \rightarrow 2$ hard sub-processes. Detailed explanation on PYTHIA8 physics processes and their implementation can be found in Ref. [5]. The results reported in this work are obtained from simulated inelastic, non-diffractive events using PYTHIA version 8.215 [30] with the 4C tune (Tune:pp = 5) [31]. Further, non-diffractive component of the total cross section for all hard QCD processes (HardQCD:all=on) are considered, which includes the production of heavy quarks along with MPI-based scheme of color reconnection (ColourReconnection:reconnect = on). A cut of $p_{\mathrm{T}} \geq 0.5$ GeV/c (using PhaseSpace:pTHatMinDiverge) is used to avoid the divergences of QCD processes in the limit $p_{\mathrm{T}} \rightarrow 0$. For the production of quarkonia through NRQCD framework [32–34], we use Charmonium:all flag in the simulation. Study of D^0, J/ψ and Λ_c^+ production are done at the midrapidity. J/ψ, D^0 and Λ_c^+ are reconstructed via the $e^+ + e^-$ ($|y| < 0.9$) [35], $K^- + \pi^+$ ($|y| < 0.5$) [36] and $p + K^- + \pi^+$ ($|y| < 0.5$) [37] decay channels and their yields are obtained through invariant mass reconstruction keeping the detector acceptance of ALICE in mind. This analysis is performed by generating 100 million events for J/ψ and approximately 50 million events each for D^0

and Λ_c^+ in pp collisions at $\sqrt{s}$ = 13 TeV. The charged-particle multiplicity, N_{ch} is measured at the midrapidity ($|\eta| < 1.0$), considering all the charged particles including the decay product of J/ψ, D^0 and Λ_c^+. As the aim of this work is to perform a multi-differential study using transverse spherocity and the charged-particle multiplicities (N_{ch}), we have chosen the minimum bias (0-100%) collisions and events with top 20% of N_{ch} for our study.

Transverse spherocity is already discussed briefly in subsection 3.1.2. However, in order to have a quantitative understanding, in this work, we assumed there is no detector bias/smearing effect. With this assumption, in this analysis only the events with at least 5 charged-particles in $|\eta| < 0.8$ with $p_{\text{T}} > 0.15$ GeV/c are considered, so that the concept of event topology becomes statistically meaningful. S_0 cuts on the generated events are applied in order to sort out jetty and isotropic events from the total events. For minimum bias collisions, the cuts for jetty events is $0 \leq S_0 < 0.37$ with lowest 20% of S_0 distribution and $0.72 < S_0 \leq 1$ is for isotropic events with highest 20% of S_0 distribution. Further, minimum bias events are divided into six multiplicity classes and the corresponding spherocity cuts for isotropic and jetty events are tabulated in Table 3.3. For consistency, N_{ch} intervals chosen here are the same as in Ref. [38]. In order to maximize the statistics, the bin-width is taken smaller at lower multiplicities and then subsequently higher at high multiplicity bins. Figure 3.22 represents the transverse spherocity distribution in different multiplicity classes for pp collisions at $\sqrt{s} = 13$ TeV. Here, it is observed that high-multiplicity events are more towards isotropic in nature which is in accordance with earlier works on transverse spherocity [38–40]. The peak of the transverse spherocity distribution shifts towards isotropic events with increasing charged-particle multiplicity. This shows that higher contribution of softer events come from multiple hard partonic scatterings in high-multiplicity pp collisions, which generate an almost isotropic distribution of particles [40]. Therefore, the differential study of particle production as a function of multiplicity and event shape classes has great importance to understand the particle production mechanism. As transverse spherocity distribution depends on charged-particle multiplicity, the cuts for jetty and isotropic events vary for different transverse spherocity classes, which is shown in Table 3.3. For the sake of simplicity, here onwards we refer transverse spherocity as spherocity.

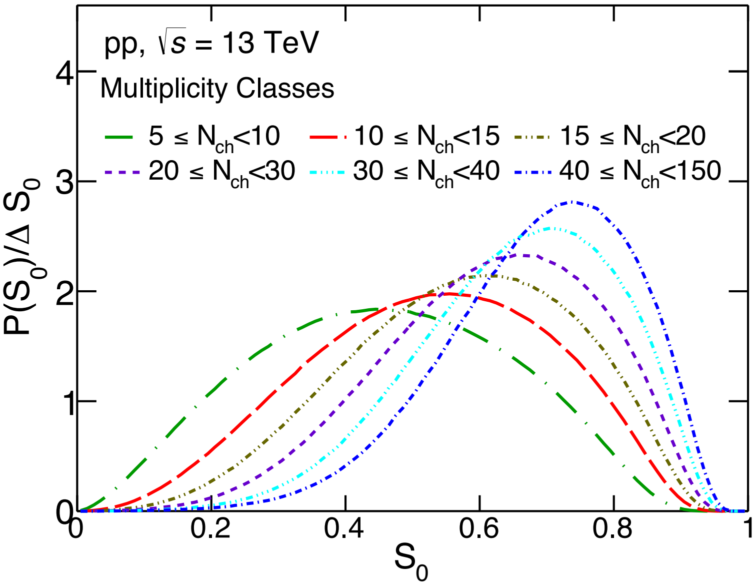

Figure 3.22: (Color Online) Transverse spherocity distributions for different charged-particle multiplicity in pp collisions at $\sqrt{s}$ = 13 TeV using PYTHIA8. Different line styles and colors are for different multiplicity classes [41].

With this detailed analysis methodology, we now proceed for the estimation of transverse momentum spectra, relative integrated yield and relative mean transverse momentum of D^0, J/ψ and Λ_c^+ in pp collisions at $\sqrt{s}$ = 13 TeV.

3.2.2 Results and Discussion

Before proceeding with the analysis, we have checked the consistency of PYTHIA8 simulated data with the experimental results. This consistency is discussed briefly in the appendix section 3.4.5.

Table 3.3: Charged-particle multiplicity (Mult.) classes ($N_{\rm ch}$) ($|\eta| < 1.0$) and corresponding spherocity ranges for jetty and isotropic events. Here the lowest and highest 20% events of the spherocity distribution for a given multiplicity class are considered as jetty and isotropic events, respectively [41].

Mult. Classes ($N_{\rm ch}$)	S_0 **range**	
	Jetty events	**Isotropic events**
$5 - 10$	$0 - 0.29$	$0.64 - 1$
$10 - 15$	$0 - 0.38$	$0.70 - 1$
$15 - 20$	$0 - 0.44$	$0.74 - 1$
$20 - 30$	$0 - 0.49$	$0.77 - 1$
$30 - 40$	$0 - 0.54$	$0.80 - 1$
$40 - 150$	$0 - 0.58$	$0.82 - 1$

3.2.2.1 Transverse momentum spectra

Left panels of Fig. 3.23 show the transverse momentum ($p_{\rm T}$) spectra for $\rm D^0$ (top), J/ψ (middle) and Λ_c^+ (bottom) for isotropic, jetty and spherocity-integrated events in minimum bias pp collisions at $\sqrt{s}$ = 13 TeV. The right panels show the ratio of the $p_{\rm T}$ spectra for isotropic and jetty events to the spherocity-integrated ones. The ratios clearly indicate that the particle production from isotropic events dominate at low-$p_{\rm T}$ and after a certain $p_{\rm T}$, the particle production from jetty events starts to dominate. The crossing point of the jetty and isotropic events for Λ_c^+ and J/ψ are found to be similar. However, for $\rm D^0$ the crossing point is at a higher $p_{\rm T}$. This may suggest that the soft production of $\rm D^0$ is dominant till higher-$p_{\rm T}$ compared to Λ_c^+ and J/ψ. We also estimate the $p_{\rm T}$ spectra in high-multiplicity pp collisions in different spherocity classes, which is shown in Fig. 3.24. Here, the crossing point of the jetty and isotropic events for all the studied

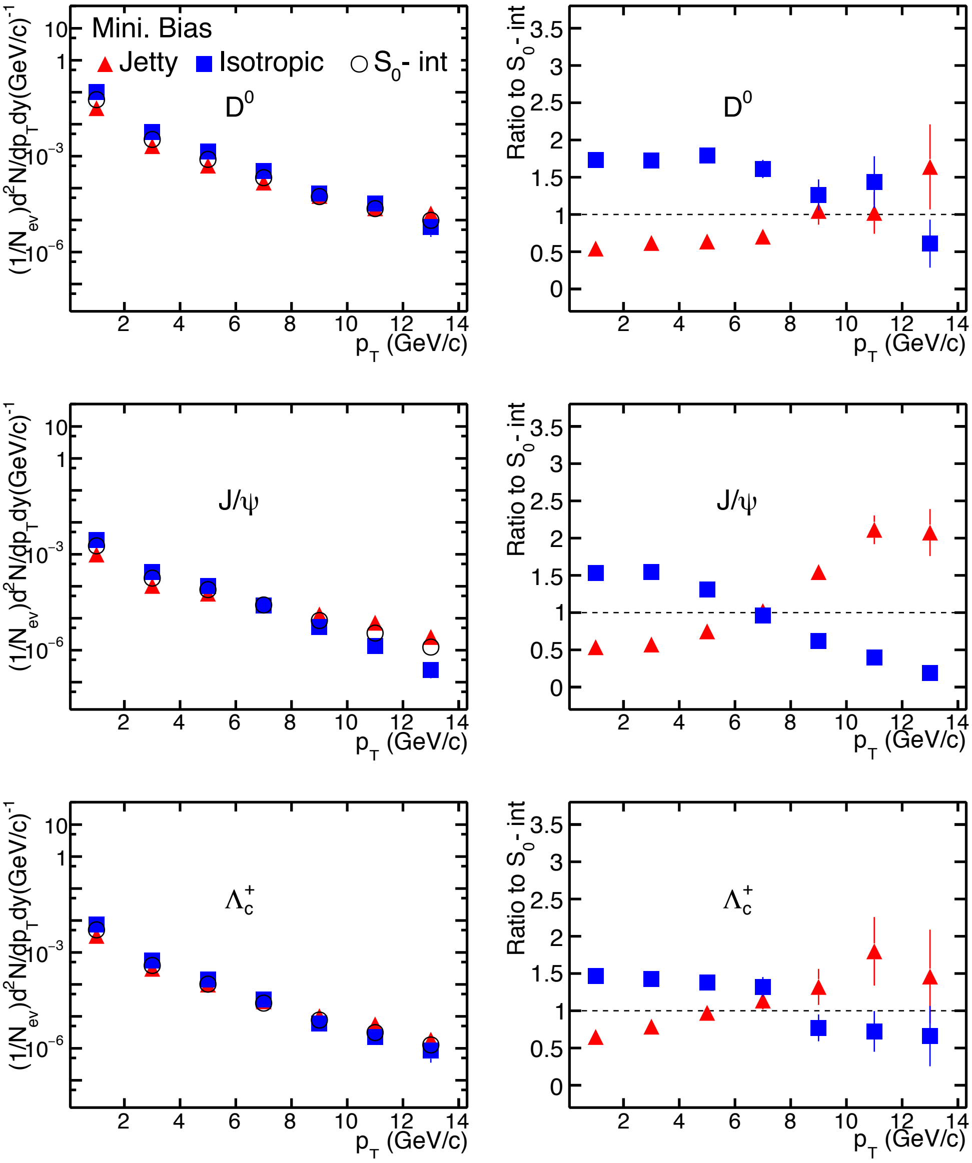

Figure 3.23: (Color online) $p_{\rm T}$-spectra (left panel) of isotropic, jetty and spherocity-integrated events, and their ratios (right panel) to the spherocity-integrated ones for D^0 (top), J/ψ (middle) and Λ_c^+ (bottom) for minimum bias pp collisions at $\sqrt{s}$ = 13 TeV using PYTHIA8 [41].

particles are found to be similar. The comparison between Fig. 3.23 and Fig. 3.24 indicates that the heavy-flavor particle production from jetty events dominates

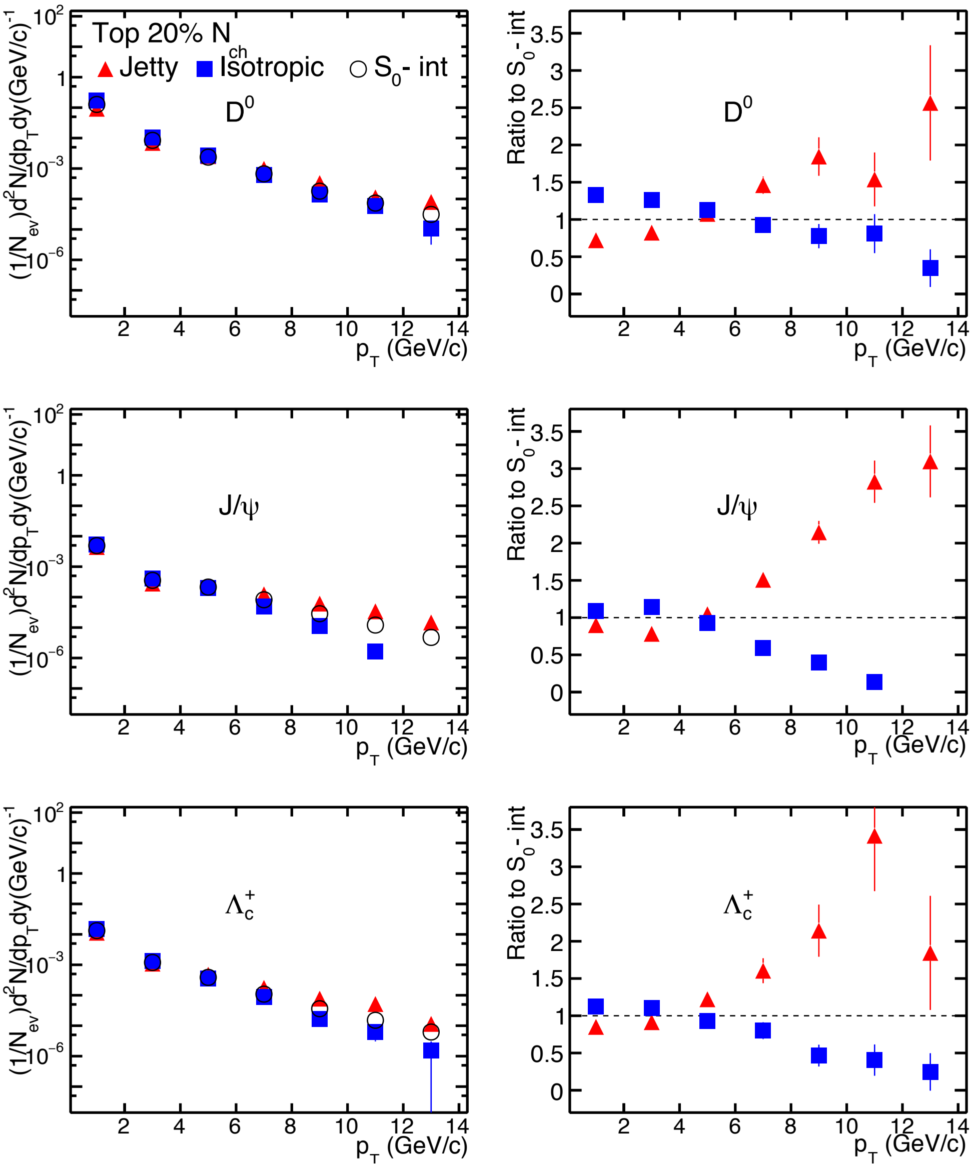

Figure 3.24: (Color online) p_{T}-spectra (left panel) of isotropic, jetty and spherocity-integrated events, and their ratios (right panel) to the spherocity-integrated ones for D^0 (top), J/ψ (middle) and Λ_c^+ (bottom) for high-multiplicity pp collisions at $\sqrt{s}$ = 13 TeV using PYTHIA8 [41].

at a lower p_{T} in high-multiplicity pp collisions compared to the minimum bias ones. At high multiplicity for low-p_{T} region, the separation between the isotropic and jetty events are small compared to minimum bias events.

3.2.2.2 Relative integrated yield and relative mean transverse momentum

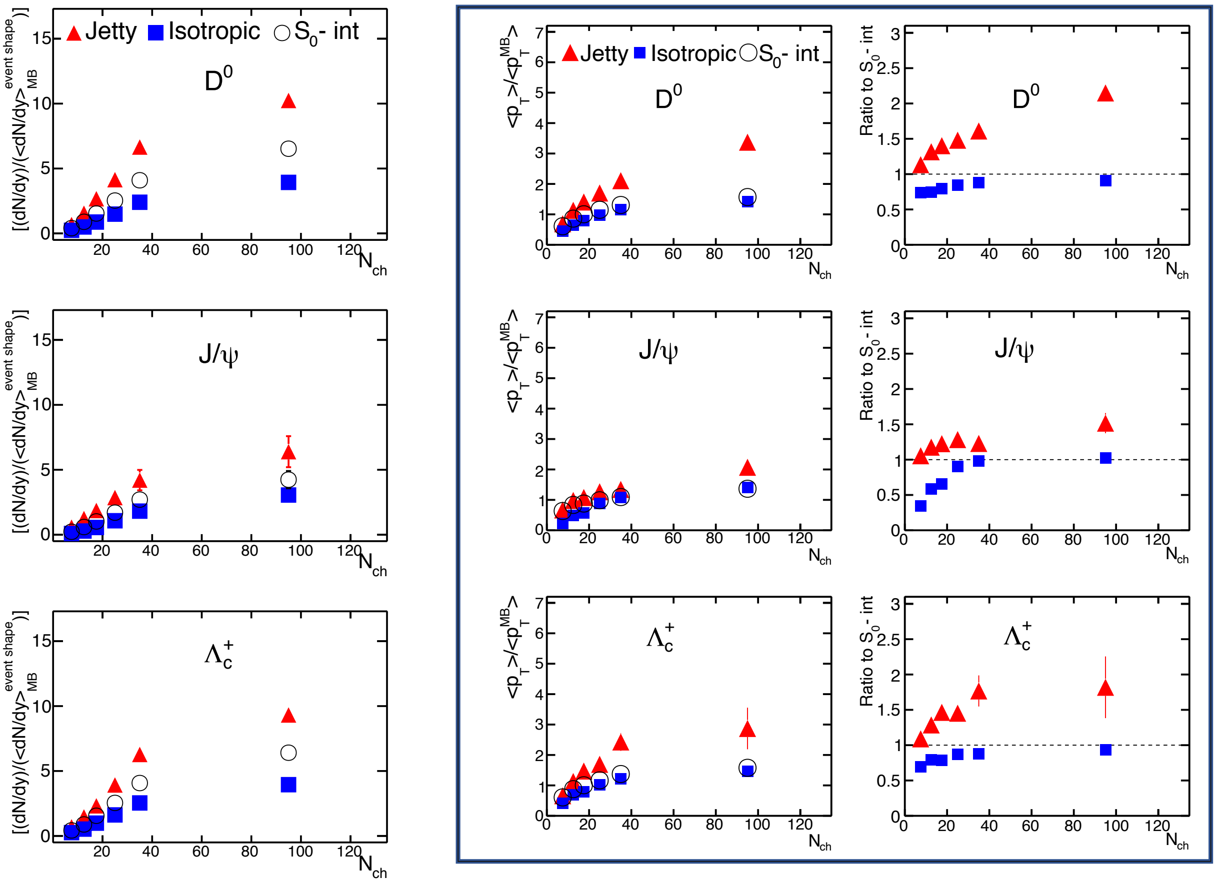

Figure 3.25: (Color online) Left panel: Self-normalised yields with respect to the corresponding event types, Middle panel: mean transverse momenta ($\langle p_{\rm T}\rangle$) scaled to its MB values, and Right panel: ratio of $\langle p_{\rm T}\rangle$ in different event types to the spherocity-integrated ones as a function of multiplicity for $\rm D^0$ (top), J/ψ (middle) and Λ_c^+ (bottom). The error bars in the data points are the statistical uncertainties [41].

The relative yields of $\rm D^0$, J/ψ and Λ_c^+ are measured at the midrapidity ($|y| <$

0.9) using the following relation:

$$\frac{Y_{particle}}{< Y_{particle} >} = \frac{N^{i}_{particle}}{N^{total}_{particle}} \frac{N^{total}_{evt}}{N^{i}_{evt}}, \tag{3.14}$$

where, N^{i}_{particle} and N^{i}_{evt} are the number of D^0, J/ψ and Λ_c^+, and number of events in i^{th} multiplicity bin, respectively. $N^{\text{total}}_{\text{particle}}$ and $N^{\text{total}}_{\text{evt}}$ are the total number of D^0, J/ψ and Λ_c^+ produced, and total number of minimum-bias events, respectively. The uncertainties in the measurement of the number of D^0, J/ψ and Λ_c^+ particles are $\sqrt{N_{\text{D}^0}}$, $\sqrt{N_{J/\psi}}$ and $\sqrt{N_{\Lambda_c^+}}$, respectively . These uncertainties are propagated using standard error propagation formula to estimate the uncertainties in relative D^0, J/ψ and Λ_c^+ yields. The mean transverse momenta ($\langle p_{\text{T}} \rangle$) of D^0, J/ψ and Λ_c^+ are calculated for each multiplicity bin and corresponding uncertainty is given by the ratio of standard deviation (σ) and square root of the number of entries in that bin ($\sigma/\sqrt{N^{p_{\text{T}}}_{\text{bin}}}$).

Left(middle) panel of Fig. 3.25 shows the integrated yields ($\langle p_{\text{T}} \rangle$) of D^0, J/ψ and Λ_c^+ scaled to the corresponding integrated yields ($\langle p_{\text{T}} \rangle$) of spherocity-integrated events in minimum bias collisions as a function of charged-particle multiplicity. For all the particles, the relative yield and the relative mean transverse momentum increase with charged-particle multiplicity. Enabling the CR in PYTHIA8, produces effects on the final particle distributions, which could resemble those due to flow [42]. An increase in the $\langle p_{\text{T}} \rangle$ with N_{ch} is attributed to the presence of CR between the interacting strings. The relative yields and relative $\langle p_{\text{T}} \rangle$ are found to be higher for jetty events compared to isotropic ones. The right panel of Fig. 3.25 shows the ratio of relative mean transverse momentum from isotropic and jetty events to the S_0-integrated events. Interestingly, the relative $\langle p_{\text{T}} \rangle$ of the studied particles for isotropic events stay systematically below the spherocity-integrated ones for low-multiplicity events and approaches towards spherocity integrated ones with increase of multiplicity. For jet-like events the $\langle p_{\text{T}} \rangle$ is higher than that of spherocity-integrated events and the relative increase in $\langle p_{\rm T} \rangle$ saturates at high multiplicity. This behavior is similar to the observed behavior of $\langle p_{\rm T} \rangle$ of light-flavor charged-particles in different spherocity classes by ALICE at the LHC [43].

Figure 3.25 further reveals a clear distinction in the production mechanisms between $\rm D^0$ and Λ_c^+ versus $\rm J/\psi$. For example, relative yields of $\rm J/\psi$ for jetty, isotropic and S_0-integrated events are close to each other and are less than that of $\rm D^0$ and Λ_c^+. This means more number of open flavors are produced in high-multiplicity events as compared to charmonia and is also reflected in the complementary study of $\langle p_{\rm T} \rangle$. The $\langle p_{\rm T} \rangle$ of $\rm J/\psi$ has the dominant effect of jetty events, whereas, $\langle p_{\rm T} \rangle$ of $\rm D^0$ and Λ_c^+ are dominated by isotropic ones. This can be explained by the multi-quark dynamics by the fact that $\rm D^0$-mesons and Λ_c^+ baryons are produced via string fragmentation. Here, the latter carry the flow-like characteristics originating from CR mechanism [42]. But, $\rm J/\psi$ which is a bound state of heavy charm and anti-charm quarks, has a very little contribution from CR [44, 45]. Further, greater number of light-quarks are produced from MPI compared to heavy-quarks, which makes more light quarks to come to the close proximity of a c-quark, as compared to its own counter part ($\bar{c}$) and hence higher probability of production of open heavy-flavors than charmonia in a high-multiplicity environment. However, enhancement of heavy-baryon over meson still need to be understood which we have tried to explore in the next section.

3.2.2.3 Baryon-to-meson ratio

A significant enhancement of baryon-to-meson ratios for light hadrons has been observed in central heavy-ion collisions compared to pp collisions in the intermediate $p_{\rm T}$ region [46]. The enhancement can be explained by coalescence model through hadronize-combination of constituent quarks [47–49]. Recently, ALICE and LHCb have observed enhancement of charmed baryon-to-meson ratio which indicates charm quarks may hadronize through coalescence as well. Although, minimum bias pp collisions do not show significant enhancement of baryon-to-meson ratio in the intermediate p_{T} region [50, 51], in this paper we have tried to unfold the possibility of such effects in high-multiplicity events in different event shapes. Indication of such enhancement would be sensitive to thermalization effect in pp collisions [52]. The relative abundance of baryons and mesons can shed light on the process of fragmentation - a non-perturbative process. Formation of jets of partons into high transverse momentum hadrons is described by fragmentation function which incorporate how partons from jet combine with quarks and antiquarks from the vacuum to form hadrons. Because of MPIs, jet-partons in pp collisions can combine with quarks and antiquarks produced from MPIs to form hadrons via string fragmentation. Since the momenta of quarks and antiquarks from secondary MPIs are smaller than those of partons from jets, these hadrons have momenta lower than independent fragmentation of jet partons and that is what we observe from Fig. 3.26. The p_{T}-differential Λ_c^+/D^0 ratio for jetty events is higher compared to isotropic events in minimum bias sample. One interesting observation from Fig. 3.26 is that the behaviour of Λ_c^+/D^0 p_{T}-differential ratio for all event topologies follow heavy-ion-like trend i.e. enhancement of baryon-to-meson ratio in the intermediate p_{T} region followed by a decreasing behaviour. Although, the minimum bias samples show a clear event topology dependence, the top 20% high-multiplicity pp events are driven by the final state multiplicity without a distinction of event types.

Contrary to heavy-flavors, when we study similar ratio in the light flavor sector (Λ^0/K^-), we observe a completely opposite trend with spherocity classes for $p_{\mathrm{T}} > 4$ GeV/c (Fig. 3.27): ratio is higher for isotropic samples as compared to jetty ones. This is because of the fact that the former are driven predominantly by hard collisions and can have maximum contributions from jettiness of the events in comparison with the contributions from hadronization. However, for light flavors, most of the contributions could be MPI dominant. Here, the Λ enhancement is linked to the increased density of quarks and gluons, particularly

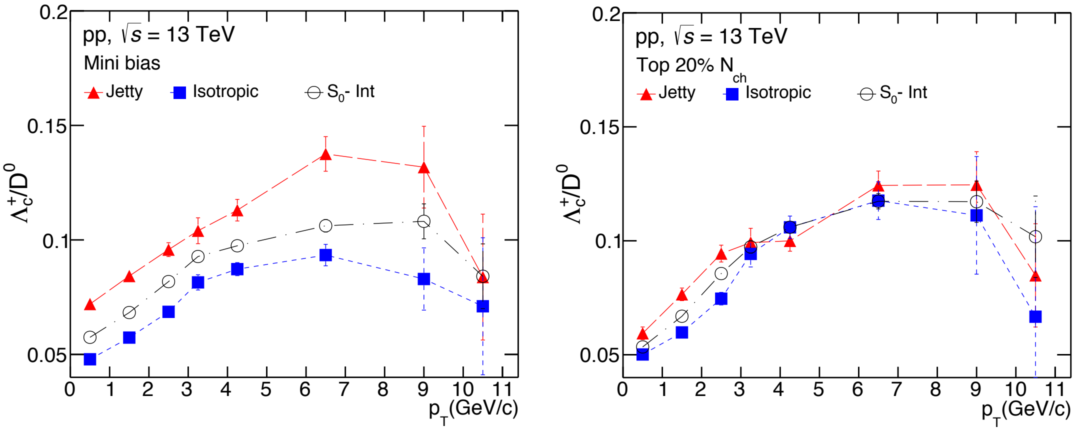

Figure 3.26: (Color online) p_{T}-differential particle ratio of Λ_c^+ to D^0, for minimum bias (**left**) and high-multiplicity (top 20%) (**right**) pp collisions in isotropic (blue squares), jetty (red triangles) and spherocity integrated (open circles) events using PYTHIA8 [41].

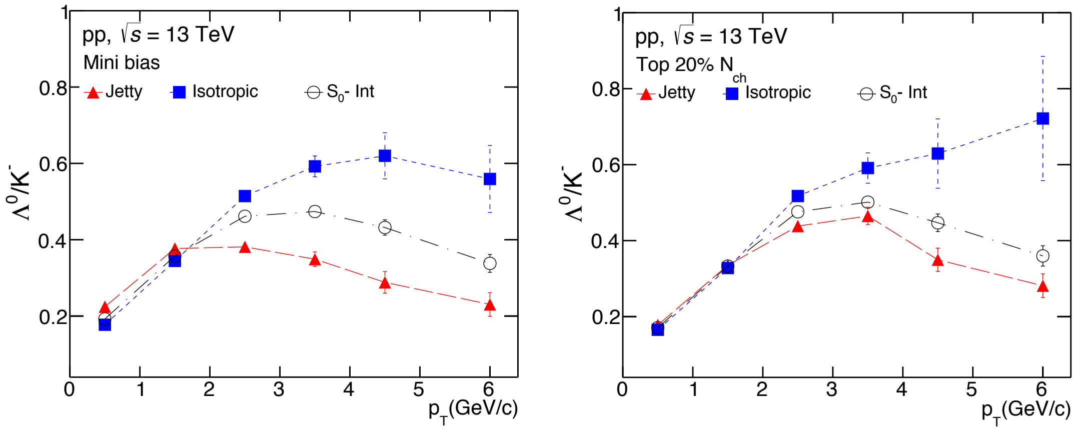

Figure 3.27: (Color online) p_{T}-differential particle ratio of Λ^0 to K^-, for minimum biased (**left**) and high-multiplicity (top 20%) (**right**) pp collisions in isotropic (blue squares), jetty (red triangles) and spherocity integrated (open circles) events using PYTHIA8 [41].

the strange quarks (s) from MPI and CR in the final state.

For the heavy flavor versus light flavor behaviour of the baryon over meson ratio, heavier particles will have a larger boost which will be reflected in the baryon-to-meson ratios. Therefore, one can see the shift of peak of the ratio to higher p_{T} for heavy-flavors. For the top 20% high-multiplicity pp events, as seen from Figs. 3.26 and 3.27, event topology has no effect on heavy-flavor sector, whereas in case of the light-flavors, we do observe a clear dependence of the discussed ratio on different event types.

With the above findings, we finally summarize all the important results in the next section.

3.3 Summary

Section 3.1: The first measurements of $\mathrm{K}^{*}(892)^{\pm}$ resonance production at midrapidity in pp collisions at $\sqrt{s}$ =13 TeV at different $S_{0}^{p_{\mathrm{T}}=1}$ quantiles and (0 –10)% V0M multiplicity class have been reported in this thesis using ALICE at the LHC. Furthermore, spherocity distribution obtained using AOD dataset by correcting/modifying the resonance package is also reported here. The results include the spherocity distribution obtained at different multiplicities, invariant mass plots (before and after uncorrelated background subtraction), peak fits to extract the signal, efficiency ×acceptance, the corrected p_{T} spectra with systematic uncertainties, and particle ratios of $\mathrm{K}^{*}(892)^{\pm}$ with long-lived identified particles. From the transverse momentum spectra results shown in Fig. 3.20, we observe $\mathrm{K}^{*\pm}$ are mainly produced in isotropic events in the measured p_{T} interval, but for $p_{\mathrm{T}} > 3.5$ GeV/c in-jet production increases. Also with the increase in $S_{0}^{p_{\mathrm{T}}=1}$ quantiles, spherocity dependence of $\mathrm{K}^{*\pm}$ production seems to be more prominent. To understand the dynamics of particles with different quark content, mass, etc., the particle ratio of $\mathrm{K}^{*\pm}$ with long-lived stable hadrons is shown in Fig. 3.21, an important observation from these results is that the isotropic/integrated ratio is higher and stays flat, while the jetty/integrated rises with p_{T}, implying an increasing relative contribution of hard processes with increasing p_{T}. These results can shed light on exploring the QGP-like conditions in high-multiplicity pp collisions. However, a clear theoretical explanation of this fact needs to be investigated.

Section 3.2: In the second section of this chapter, we focused on the production of heavy-flavor hadrons like J/ψ, D^0 and Λ_c^+ in pp collisions at $\sqrt{s} = 13$ TeV using 4C tuned PYTHIA8 event generator at midrapidity. In addition, for the first time, we explored spherocity in the heavy-flavor sector as a differentiator of integrated events into jetty and isotropic to better understand the production dynamics of the heavy-flavor hadrons. Important findings from this study are summarized below:

- We see a clear dependence of the spherocity distribution with charged-particle multiplicity even with Monte -Carlo generator like PYTHIA8. The spherocity distribution is increasingly skewed with the increase in charged-particle multiplicity.

- A clear spherocity dependence of heavy-flavor $p_{\rm T}$-spectra, integrated yield, $\langle p_{\rm T}\rangle$ and particle ratios is observed in both minimum bias and high-multiplicity pp collisions.

- The crossing point of the ratios of $p_{\rm T}$-spectra from jetty and isotropic events to the spherocity-integrated ones shifts to lower $p_{\rm T}$ with the increase in charged-particle multiplicity. This indicates that spherocity differentiates events (jetty versus isotropic) more accurately in high-multiplicity pp collisions keeping a small gap in the multiplicity of heavy-flavor hadrons.

- Relative yield and relative $\langle p_{\rm T}\rangle$ are found to be increasing with the increase in charged-particle multiplicity and they are higher for jetty events as compared to isotropic ones. These results suggest that spherocity acts as a nice tool to differentiate events dominated by soft versus hard particle production processes.

- The spherocity dependence of relative yields and relative $\langle p_{\rm T} \rangle$ for $\rm D^0$ and Λ_c^+ show a similar trend while for J/ψ the difference from jetty to isotropic events is found to be lesser. This novel observation hints to different production dynamics of open charm compared to charmonia and the MPIs with color reconnection mechanism plays a major role for such a behavior in PYTHIA8.

- The $\Lambda_c^+/\rm D^0$ ratio in jetty events is found to be higher compared to the isotropic events while an opposite trend for Λ^0/K^- ratio is observed for the minimum bias sample. This is an interesting observation as spherocity dependence of particle ratios show a completely different behaviour for heavy flavor compared to light flavor sector. This clearly indicates to a MPI dominant contribution for Λ^0/K^- while the $\Lambda_c^+/\rm D^0$ ratio is driven predominantly by hard collisions and can have maximum contributions from jets.

A multi-differential study taking event topology and multiplicity is necessary in small systems at LHC energies when looking into the observation of heavy-ion like features in high-multiplicity pp collisions. The LHC experiments have planned for a dedicated high-multiplicity triggered events and the associated detector upgrades that will provide a proper platform in this direction. Study of heavy-flavor production will play an important role for the test of the pQCD, as they are produced early in time and witness the complete spacetime evolution of the system. However, the present limitations in terms of proper identification of secondary vertices, efficiency at low-$p_{\rm T}$ and dealing with signal to background ratio will be overcome to a greater extent with the detector upgrades. It is worth mentioning here that ALICE ITS3 planned for installation in LHC Long Shutdown3 (LS3), will have a novel vertex detector consisting of curved wafer-scale ultra-thin silicon sensors arranged in perfectly cylindrical layers. This will feature an unprecedented low material budget of 0.05% X0 per layer, with the innermost layer positioned at only 18 mm radial distance from the interaction point [53, 54].

This will help with higher efficiency of detection of heavy-flavor particles, opening up a new domain of pQCD studies. The present study will be more exciting to carry out in experimental data in the upcoming LHC Run-3 and Run-4.

3.4 Appendix

3.4.1 Estimation of spherocity distribution using AOD dataset

While using the AOD dataset for estimation of spherocity distribution, we observe discrepancies in the spherocity distribution obtained using AOD and ESD dataset, which is shown below in the fig. 3.28 (**left**). This discrepancy was due to not taking care of refit TPC and ITS for the AOD dataset. Once this discrepancy was worked out, we obtained a symmetric spherocity distribution with respect to both the AOD and ESD dataset, which is depicted in the right side (lower panel) plot of Fig. 3.28.

3.4.2 Data set and run-list

In particular, the Analysis Object Data (AOD) of LHC16 kl, LHC17 lmorijk, and LHC18 bdefhimnopl metadataset were analysed for data. The following runs were analysed:

- **LHC16k** : 258537, 258499, 258477, 258456, 258454, 258452, 258426, 258393, 258391, 258387, 258359, 258336, 258332, 258307, 258306, 258303, 258302, 258301, 258299, 258278, 258274, 258273, 258271, 258270, 258258, 258257, 258256, 258204, 258203, 258202, 258198, 258197, 258178, 258117, 258114, 258113, 258109, 258108, 258107, 258063, 258062, 258060, 258059, 258053, 258049, 258045, 258042, 258041, 258039, 258019, 258017, 258014, 258012, 258008, 258003, 257992, 257989, 257986, 257979, 257963, 257960, 257957,

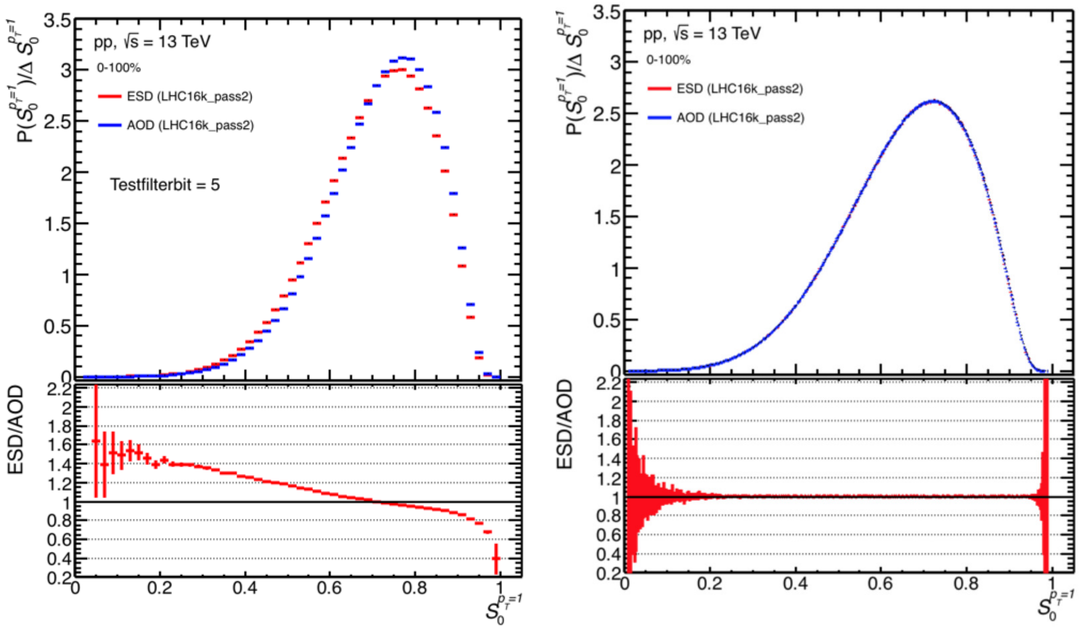

Figure 3.28: (Color Online) (**Left**) Comparison of spherocity distribution for (0-100)% multiplicity classes in pp collisions at at $\sqrt{s}$ = 13 TeV using AOD and ESD dataset without refit correction. (**Right**) Comparison of spherocity distribution for (0-100)% multiplicity classes in pp collisions at at $\sqrt{s}$ = 13 TeV using AOD and ESD dataset with refit TPC and ITS correction [12].

257939, 257937, 257936, 257892, 257855, 257853, 257851, 257850, 257804, 257803, 257800, 257799, 257798, 257797, 257773, 257765, 257757, 257754, 257737, 257735, 257734, 257733, 257727, 257725, 257724, 257697, 257694, 257692, 257691, 257689, 257688, 257687, 257685, 257684, 257682, 257644, 257642, 257636, 257635, 257632, 257630, 257606, 257605, 257604, 257601, 257595, 257594, 257592, 257590, 257588, 257587, 257566, 257562, 257561, 257560, 257541, 257540, 257539, 257537, 257531, 257530, 257492, 257491, 257490, 257488, 257487, 257474, 257468, 257457, 257433, 257364, 257358, 257330, 257322, 257320, 257318, 257260, 257224, 257209, 257206, 257204, 257144, 257141, 257139, 257138, 257137, 257136, 257100, 257095, 257092, 257086, 257084, 257082, 257080, 257077, 257028, 257026, 257021, 257012, 257011, 256944, 256942, 256941

- **LHC16l** : 259888, 259868, 259867, 259866, 259860, 259842, 259841, 259822, 259789, 259788, 259781, 259756, 259752, 259751, 259750, 259748, 259747, 259477, 259473, 259396, 259395, 259394, 259389, 259388, 259382, 259378, 259342, 259341, 259340, 259339, 259336, 259334, 259307, 259305, 259303, 259302, 259274, 259273, 259272, 259271, 259270, 259269, 259264, 259263, 259261, 259257, 259204, 259164, 259162, 259118, 259117, 259099, 259096, 259091, 259090, 259088, 258964, 258962

- **LHC17l** : 278216, 278215, 278191, 278189, 278167, 278166, 278165, 278164, 278158, 278127, 278126, 278123, 278122, 278121, 277996, 277991, 277989, 277987, 277952, 277930, 277907, 277904, 277903, 277900, 277899, 277898, 277897, 277876, 277870, 277848, 277847, 277845, 277842, 277841, 277836, 277834, 277805, 277802, 277801, 277800, 277799, 277795, 277794, 277749, 277747, 277746, 277745, 277725, 277723, 277722, 277721, 277577, 277576, 277575, 277574, 277537, 277536, 277534, 277531, 277530, 277479, 277478, 277477, 277476, 277473, 277472, 277418, 277417, 277416, 277389, 277386, 277385, 277384, 277383, 277360, 277314, 277312, 277310, 277293, 277262, 277257, 277256, 277197, 277196, 277194, 277193, 277189, 277188, 277184, 277183, 277182, 277181, 277180, 277155, 277121, 277117, 277091, 277087, 277082, 277079, 277076, 277073, 277037, 277017, 277016, 277015, 276972, 276971, 276970, 276969, 276967, 276920, 276917, 276916, 276762, 276675, 276674, 276672, 276671, 276670, 276644, 276608, 276557, 276556, 276553, 276552, 276551

- **LHC17m**:280140, 280135, 280134, 280131, 280126, 280118, 280114, 280111, 280108, 280107, 280066, 280052, 280051, 279879, 279855, 279854, 279853, 279830, 279827, 279826, 279773, 279749, 279747, 279719, 279718, 279715, 279689, 279688, 279687, 279684, 279683, 279682, 279679, 279677, 279676, 279642, 279641, 279632, 279630, 279559, 279550, 279491, 279488, 279487, 279483, 279441, 279439, 279435, 279410, 279391, 279355, 279354, 279349, 279348, 279344, 279342, 279312, 279310, 279309, 279274, 279273, 279270, 279268, 279267, 279265, 279264, 279242, 279238, 279235, 279234, 279232, 279208, 279207, 279201, 279199, 279157, 279155, 279130, 279123, 279122, 279118, 279117, 279107, 279106, 279075, 279074, 279073, 279069, 279068, 279044, 279043, 279041, 279036, 279035, 279008, 279007, 279005, 279000, 278999, 278964, 278963, 278960, 278959, 278941, 278939, 278936, 278915, 278914

- **LHC17o**: 281961, 281956, 281953, 281940, 281939, 281932, 281931, 281928, 281920, 281918, 281916, 281915, 281895, 281894, 281893, 281892, 281633, 281592, 281583, 281574, 281569, 281568, 281563, 281562, 281557, 281511, 281509, 281477, 281475, 281450, 281449, 281446, 281444, 281443, 281441, 281415, 281321, 281301, 281277, 281275, 281273, 281271, 281244, 281243, 281242, 281241, 281240, 281213, 281212, 281191, 281190, 281189, 281181, 281180, 281179, 281081, 281080, 281062, 281061, 281060, 281036, 281035, 281033, 281032, 280999, 280998, 280997, 280996, 280994, 280990, 280947, 280943, 280940, 280936, 280897, 280880, 280856, 280854, 280849, 280848, 280847, 280844, 280842, 280793, 280792, 280787, 280786, 280768, 280767, 280766, 280765, 280764, 280763, 280762, 280761, 280757, 280756, 280755, 280754, 280753, 280729, 280706, 280705, 280681, 280679, 280671, 280647, 280645, 280639, 280637, 280636, 280634, 280613, 280583, 280581, 280574, 280551, 280550, 280547, 280546, 280519, 280518, 280499, 280490, 280448, 280447, 280446, 280445, 280443, 280419, 280415, 280412, 280406, 280405, 280403, 280375, 280374, 280351, 280350, 280349, 280348, 280312, 280310, 280290, 280286, 280285, 280284, 280282

- **LHC17r**: 282704, 282703, 282702, 282700, 282677, 282676, 282673, 282671, 282670, 282667, 282666, 282651, 282629, 282622, 282620, 282618, 282609, 282608, 282607, 282606, 282580, 282579, 282575, 282573, 282546, 282545, 282544, 282528

- **LHC17i**: 274442, 274390, 274389, 274388, 274387, 274386, 274385, 274364, 274363, 274360, 274352, 274329, 274283, 274281, 274280, 274278, 274276, 274271, 274270, 274269, 274268, 274266, 274264, 274263, 274259, 274258, 274232, 274212, 274174, 274148, 274147, 274125, 274094, 274092, 274058, 273986, 273985, 273946, 273943, 273942, 273918, 273889, 273887, 273886, 273885, 273825, 273824, 273654, 273653, 273593, 273592, 273591

- **LHC17j**: 274671, 274669, 274667, 274657, 274653, 274601, 274596, 274595, 274594, 274593

- **LHC17k**: 276508, 276507, 276506, 276462, 276439, 276438, 276437, 276435, 276351, 276348, 276302, 276297, 276294, 276292, 276290, 276259, 276257, 276230, 276205, 276178, 276177, 276170, 276169, 276166, 276145, 276140, 276135, 276104, 276102, 276099, 276098, 276097, 275847, 275664, 275661, 275650, 275648, 275647, 275624, 275623, 275622, 275621, 275617, 275612, 275559, 275558, 275515, 275472, 275471, 275467, 275459, 275457, 275456, 275453, 275452, 275448, 275443, 275406, 275404, 275401, 275372, 275369, 275361, 275360, 275333, 275332, 275328, 275326, 275324, 275322, 275314, 275283, 275247, 275246, 275245, 275239, 275188, 275184, 275180, 275177, 275174, 275173, 275151, 275150, 275149, 275076, 275075, 275073, 275068, 275067, 274979, 274978, 274886, 274882, 274878, 274877, 274822, 274821, 274815, 274806, 274803, 274802, 274801, 274708, 274690

- **LHC18b**: 285396, 285365, 285364, 285347, 285328, 285327, 285224, 285222, 285203, 285202, 285200, 285165, 285127, 285125, 285108, 285106, 285066, 285065, 285064, 285015, 285014, 285013, 285012, 285011, 285009

- **LHC18d**: 286350, 286349, 286348, 286345, 286341, 286340, 286337, 286336, 286314, 286313, 286312, 286311, 286310, 286309, 286308, 286289, 286288, 286287, 286284, 286282, 286263, 286261, 286258, 286257, 286254, 286231, 286230, 286229, 286203, 286202, 286201, 286199, 286198, 286159, 286130, 286129, 286127, 286124, 286064, 286025, 286014, 285980, 285979, 285978

- **LHC18e**: 286937, 286936, 286933, 286932, 286931, 286930, 286911, 286910, 286907, 286877, 286876, 286874, 286852, 286850, 286846, 286809, 286805, 286801, 286799, 286731, 286695, 286661, 286653, 286633, 286592, 286591, 286569, 286568, 286567, 286566, 286511, 286509, 286508, 286502, 286482, 286455, 286454, 286428, 286427, 286426, 286380

- **LHC18f**: 287658, 287657, 287656, 287654, 287578, 287575, 287524, 287521, 287518, 287517, 287516, 287513, 287486, 287484, 287481, 287480, 287451, 287413, 287389, 287388, 287387, 287385, 287381, 287380, 287360, 287356, 287355, 287353, 287349, 287347, 287346, 287344, 287343, 287325, 287324, 287323, 287283, 287254, 287251, 287250, 287249, 287248, 287209, 287208, 287204, 287203, 287202, 287201, 287185, 287155, 287137, 287077, 287072, 287071, 287066, 287064, 287063, 287021, 287000

- **LHC18h**: 288804, 288806

- **LHC18i**: 288861, 288862, 288863, 288864, 288868, 288902, 288903, 288908, 288909

- **LHC18m**: 292839, 292836, 292834, 292832, 292831, 292811, 292810, 292809, 292804, 292803, 292752, 292750, 292748, 292747, 292744, 292739, 292737, 292704, 292701, 292698, 292696, 292695, 292693, 292586, 292584, 292563, 292560, 292559, 292557, 292554, 292553, 292526, 292524, 292523, 292521, 292500, 292497, 292496, 292495, 292461, 292460, 292457, 292456, 292434, 292432, 292430, 292429, 292428, 292406, 292405, 292398, 292397, 292298, 292273, 292265, 292242, 292241, 292240, 292218, 292192, 292168, 292167, 292166, 292164, 292163, 292162, 292161, 292160, 292140, 292115, 292114, 292109, 292108, 292107, 292106, 292081, 292080, 292077, 292075, 292067, 292062, 292061, 292060, 292040, 292012, 291982, 291977, 291976, 291953, 291948, 291946, 291945, 291944, 291943, 291942, 291803, 291796, 291795, 291769, 291768, 291766, 291762, 291760, 291756, 291755, 291729, 291706, 291698, 291697, 291690, 291665, 291661, 291657, 291626, 291624, 291622, 291618, 291615, 291614, 291590, 291485, 291484, 291482, 291481, 291457, 291456, 291453, 291451, 291447, 291424, 291420, 291417, 291416, 291402, 291400, 291399, 291397, 291377, 291375, 291363, 291362, 291361, 291360, 291286, 291285, 291284, 291282, 291266, 291265, 291263, 291262, 291257, 291240, 291209, 291188, 291143, 291116, 291111, 291110, 291101, 291100, 291093, 291069, 291066, 291065, 291041, 291037, 291035, 291006, 291005, 291004, 291003, 291002, 290980, 290979, 290976, 290975, 290974, 290948, 290944, 290943, 290941, 290935, 290932, 290895, 290894, 290888, 290887, 290886, 290862, 290860, 290853, 290848, 290846, 290843, 290841, 290790, 290787, 290766, 290689, 290687, 290665, 290660, 290645, 290632, 290627, 290615, 290614, 290613, 290612, 290590, 290588, 290553, 290550, 290549, 290544, 290540, 290539, 290538, 290501, 290500, 290499, 290469, 290467, 290459, 290458, 290456, 290427, 290426, 290425, 290423, 290412, 290411, 290404, 290401, 290399, 290376, 290375, 290374, 290350, 290327, 290323

- **LHC18n**: 293357, 293359

- **LHC18o**: 293898, 293896, 293893, 293891, 293886, 293856, 293831, 293830, 293829, 293809, 293807, 293806, 293805, 293802, 293776, 293774, 293773, 293770, 293741, 293740, 293698, 293696, 293695, 293692, 293691, 293588, 293587, 293583, 293582, 293579, 293578, 293573, 293571, 293570, 293475

- **LHC18p**: 294925, 294916, 294884, 294883, 294880, 294875, 294852, 294818, 294817, 294816, 294815, 294813, 294809, 294805, 294775, 294774, 294772, 294769, 294749, 294747, 294746, 294745, 294744, 294742, 294741, 294722, 294718, 294715, 294710, 294703, 294653, 294636, 294633, 294632, 294593, 294591, 294590, 294587, 294586, 294563, 294562, 294558, 294556, 294553, 294531, 294530, 294529, 294527, 294526, 294525, 294524, 294310, 294308, 294307, 294242, 294241, 294212, 294210, 294208, 294205, 294201, 294200, 294199, 294156, 294155, 294154, 294152, 294131, 294013, 294012, 294011, 294010, 294009

- **LHC18l**: 289971, 289966, 289965, 289943, 289941, 289940, 289935, 289931, 289928, 289884, 289880, 289879, 289857, 289856, 289855, 289854, 289852, 289849, 289830, 289818, 289817, 289816, 289815, 289814, 289811, 289808, 289775, 289757, 289732, 289731, 289729, 289724, 289723, 289721, 289547, 289521, 289494, 289493, 289468, 289466, 289465, 289463, 289462, 289444, 289426, 289374, 289373, 289370, 289369, 289368, 289367, 289366, 289365, 289356, 289355, 289354, 289353, 289309, 289308, 289306, 289303, 289300, 289281, 289280, 289278, 289277, 289276, 289275, 289254, 289253, 289249, 289247, 289243, 289242, 289241, 289240

For Monte Carlo, the AOD of the entire run-list of LHC GeneralPurpose, LHC17f (5, 6, 9, 5_extra, 6_extra, 9_extra), LHC17d (17, 3, 16, 18, 17_extra, 3_extra, 16_extra, 18_extra), LHC17e (5, 5_extra), LHC17h (1, 11), LHC17l5, LHC17k4 , LHC18k (1, 2, 3,), LHC18j (1, 4), LHC18h (4, 2), LHC18f1 , LHC18g (4, 5, 6), LHC18c (12, 13), LHC18d(3, 3_extra,8), LHC18a (1,8,9) has been used.

3.4.3 Consistency of different data samples used in the analysis

To check the consistency of different datasets (LHC16, LHC17 and LHC18) used in the present analysis, we have compared the raw/corrected spectra obtained from these datasets as shown in Fig. 3.29 and 3.30 and are found to be consistent within uncertainties.

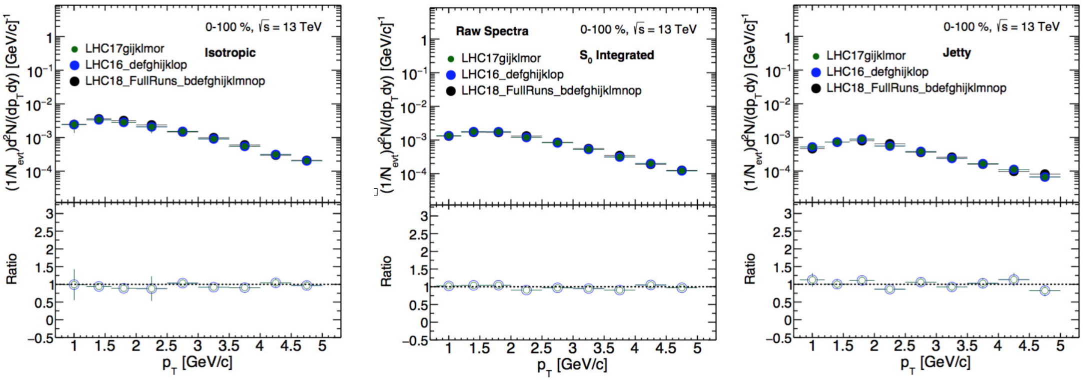

Figure 3.29: (Color Online) Comparison of raw p_{T}-spectra obtained from different datasets used in the present analysis for isotropic (**left panel**), S_0-integrated (**middle panel**) and jetty (**right panel**) events.

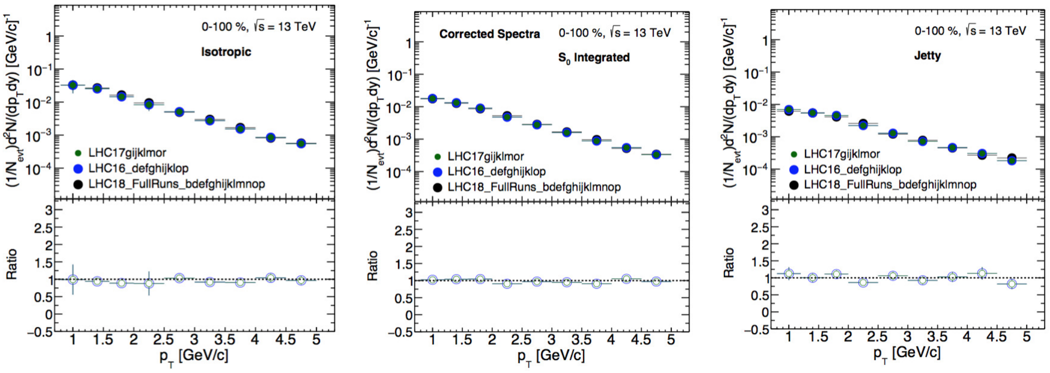

Figure 3.30: (Color Online) Comparison of corrected p_{T}-spectra obtained from different datasets used in the present analysis for isotropic (**left panel**), S_0-integrated (**middle panel**) and jetty (**right panel**) events.

3.4.4 Comparison of corrected p_{T} spectra obtained from different variations to default

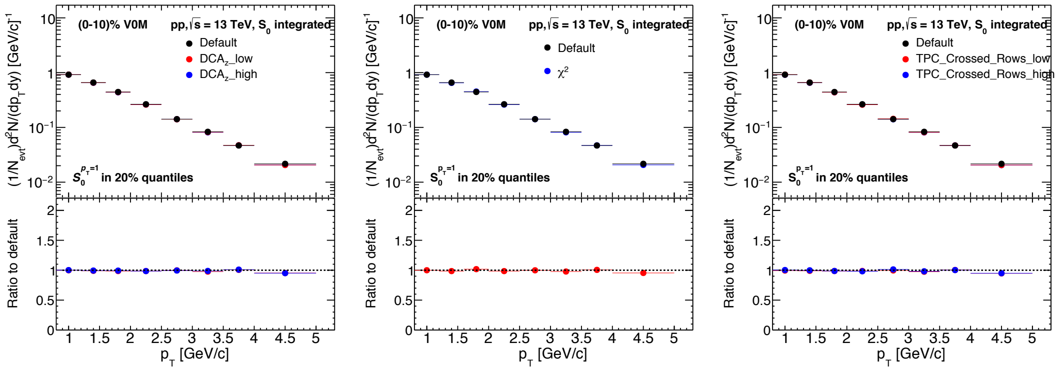

Figure 3.31: (Color Online) **Left panel**: Corrected $K^*(892)^{\pm}$ and ratios to default due to DCA_z cut variations, **Middle panel**: Corrected $K^*(892)^{\pm}$ and ratios to default due to TPC χ^2 cut variations, and **Right panel**: Corrected $K^*(892)^{\pm}$ and ratios to default due to $N_{cr,TPC}$ cut variations.

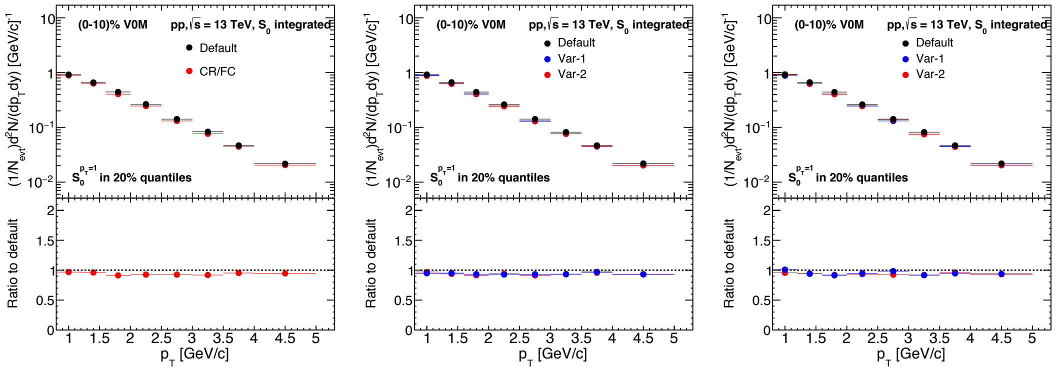

Figure 3.32: (Color Online) **Left panel**: Corrected $K^*(892)^{\pm}$ and ratios to default due to Findable cluster cut variations, **Middle panel**: Corrected $K^*(892)^{\pm}$ and ratios to default due to DCA tracks to PV variations, and **Right panel**: Corrected $K^*(892)^{\pm}$ and ratios to default due to PID secondary π variations [12].

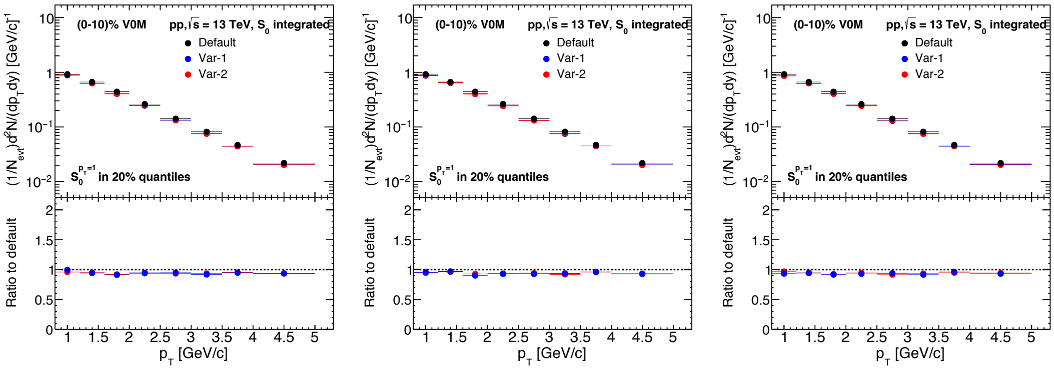

Figure 3.33: (Color Online) **Left panel**: Corrected K*(892)$^\pm$ and ratios to default due to V^0 decay radius variations, **Middle panel**: Corrected K*(892)$^\pm$ and ratios to default due to Cosine PA variations, and **Right panel**: Corrected K*(892)$^\pm$ and ratios to default due to DCA V^0 daughters variations [12].

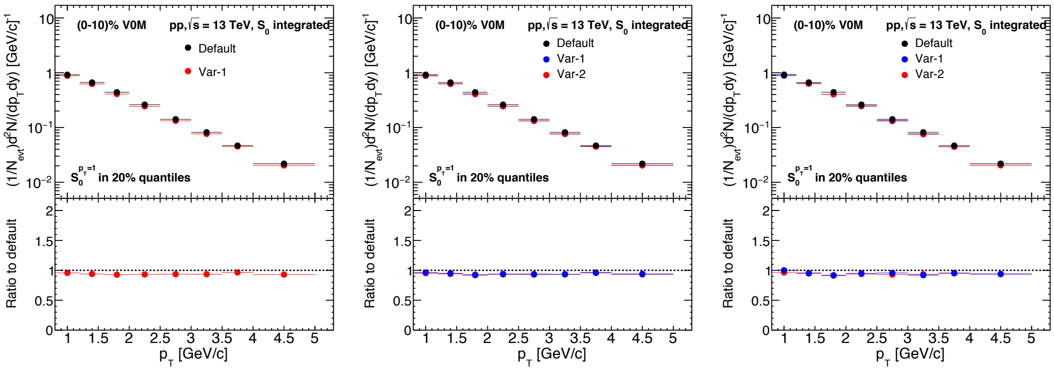

Figure 3.34: (Color Online) **Left panel**: Corrected K*(892)$^\pm$ and ratios to default due to lifetime variations, **Middle panel**: Corrected K*(892)$^\pm$ and ratios to default due to K_S^0 mass tolerance variations, and **Right panel**: Corrected K*(892)$^\pm$ and ratios to default due to K_S^0 rapidity variations [12].

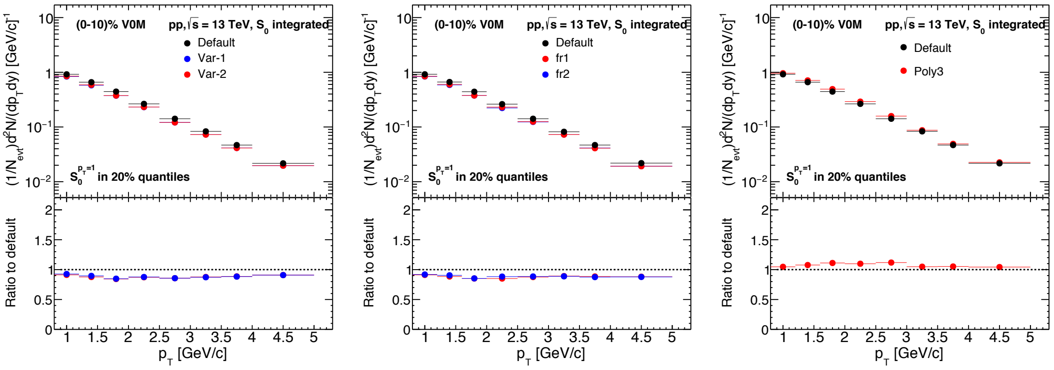

Figure 3.35: (Color Online) **Left panel**: Corrected K$^*(892)^\pm$ and ratios to default due to Normalization range variations, **Middle panel**: Corrected K$^*(892)^\pm$ and ratios to default due to Fit range variations, and **Right panel**: Corrected K$^*(892)^\pm$ and ratios to default due to residual background fitting function variations [12].

3.4.5 Consistency of PYTHIA8 with the experimental data

To check the compatibility of PYTHIA8 with the experimental data, we have compared the production cross-sections of J/ψ and D^0 between experimental data from ALICE and PYTHIA8 in the same kinematic range. Left (Right) panel of Fig. 3.36 shows the comparison of J/ψ (D^0) production cross-section in pp collisions as a function of p_{T}, respectively for minimum bias events. The open symbols represent the data obtained from ALICE experiment [35]([36]) and the solid circles show the results from PYTHIA8 event generator in pp collisions at $\sqrt{s}$ = 13 TeV. In order to see how well the spectral shapes obtained from the PYTHIA8 simulation match the experimental data, we have used some arbitrary multipliers. Within uncertainties, PYTHIA8 seems to reproduce similar spectral shapes as from experimental data for both J/ψ and D^0.

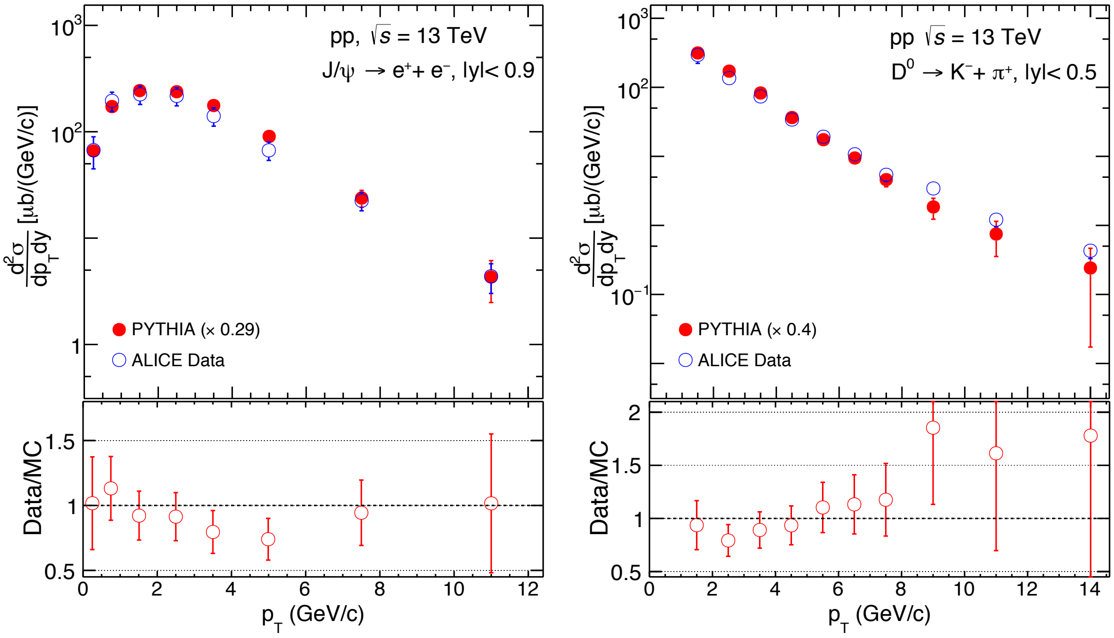

Figure 3.36: (Color online) Top panel shows the comparison of ALICE data [35, 36] and PYTHIA8 of J/ψ (left) and D^0 (right) production cross-section as a function of transverse momentum ($p_{\rm T}$) for pp collisions at $\sqrt{s}$ = 13 TeV. The open blue circles are ALICE data and solid red circles represent PYTHIA8 results. The quadratic sum of statistical and systematic uncertainties of ALICE data are presented in a single error bar. Bottom panels show the ratio between ALICE data and PYTHIA8, and the error bars are estimated using standard error propagation formula [41].

Bibliography

[1] C. Patrignani *et al.* [Particle Data Group], Chin. Phys. C **40**, 100001 (2016).

[2] K. Aamodt *et al.* (ALICE Collaboration), Phys. Lett. B **696**, 328 (2011).

[3] J. Adam *et al.* (ALICE Collaboration), Nature Phys. **13**, 535 (2017).

[4] V. Khachatryan *et al.* (CMS Collaboration)], Phys. Lett. B **765**, 193 (2017).

[5] Pythia8 online manual:(https://pythia.org/manuals/pythia8215/Welcome.html). Accessed 20 Oct 2020

[6] M. Alston, L. W. Alvarez, P. Eberhard, M. L. Good, W. Graziano, H. K. Ticho and S. G. Wojcicki, Phys. Rev. Lett. **6**, 300 (1961).

[7] URL: https://www.nobelprize.org/prizes/physics/1968/summary/

[8] A. Ortiz, Adv. Ser. Direct. High Energy Phys. **29**, 343 (2018).

[9] A. Ortiz, G. Paić and E. Cuautle, Nucl. Phys. A **941**, 78 (2015).

[10] B. Abelev *et al.*, Eur. Phys. J. C **72**, 2124 (2012).

[11] B. B. Abelev *et al.* (ALICE Collaboration), Phys. Lett. B **727**, 371-380 (2013).

[12] ALICE Analysis Note: “Event shape and multiplicity dependence of $K^{*}(892)^{\pm}$ production in pp collisions at $\sqrt{s}$ = 5.02 TeV and 13 TeV with ALICE at the LHC”, https://alice-notes.web.cern.ch/node/946.

[13] E. Cuautle, R. Jimenez, I. Maldonado, A. Ortiz, G. Paic and E. Perez, arXiv:1404.2372.

[14] G. P. Salam, Eur. Phys. J. C **67**, 637 (2010).

[15] ALICE Analysis Note: "Identified light flavor particle production in "jetty" and "isotropic" pp collisions at $(\sqrt{s}) = 13$ TeV with ALICE at the LHC", https://alice-notes.web.cern.ch/system/files/notes/analysis/961/2019-09-05-ALICE_analysis_note.pdf

[16] S. Acharya *et al.* (ALICE Collaboration), Eur. Phys. J. C **79**, 857 (2019). ALICE Analysis Note: "Spherocity analysis for the average transverse momentum versus multiplicity in pp colisions at 13 TeV", https://alice-notes.web.cern.ch/node/634.

[17] ALICE Analysis Note: "Identified hadron production as a function of multiplicity and spherocity in pp collisions at $\sqrt{s} = 13$ TeV", https://alice-notes.web.cern.ch/node/673.

[18] ALICE Analysis Note: "Identified light flavor particle production in "jetty" and "isotropic" pp collisions at $(\sqrt{s}) = 13$ TeV with ALICE at the LHC", https://alice-notes.web.cern.ch/system/files/notes/analysis/961/2021-10-06-Spherocity_ALICE_Analysis_Note_v7.pdf

[19] S. Acharya *et al.* (ALICE Collaboration), Eur. Phys. J. C **81**, 256 (2021). ALICE Analysis Note: "K0S, Λ and antiΛ production in proton?proton collisions at $\sqrt{s} = 13$ TeV", https://alice-notes.web.cern.ch/node/425.

[20] ALICE Analysis Note: "K$^*(892)^{\pm}$ resonance production in pp collisions at $\sqrt{s} = 13$ TeV", https://alice-notes.web.cern.ch/system/files/notes/analysis/631.

[21] C. Patrignani et al., Chin. Phys. C **40**, 100001 (2016).

[22] S. Acharya *et al.* (ALICE Collaboration), Phys. Rev. C **99**, 064901 (2019). ALICE Analysis Note: "Rho->pipi production in pp collisions at sqrt(s) = 2.76 TeV with TPC-PID", https://aliceinfo.cern.ch/Notes/node/374

[23] P. Abreu *et al.* (DELPHI Collaboration), Z. Phys. C **65**, 587 (1995).

[24] S. Acharya *et al.* (ALICE Collaboration) , Phys. Rev. C **99**, 064901 (2019).

[25] T. Ullrich, Z. Xu, arXiv:physics/0701199.

[26] R. Barlow, arXiv:hep-ex/0207026.

[27] https://twiki.cern.ch/twiki/bin/viewauth/ALICE/AliDPGtoolsTrackSystematicUncertaintyBookkeping

[28] J. Adam *et al.* (ALICE Collaboration), Phys. Lett. B **758**, 389 (2016). ALICE Analysis Note: "Multi-Strange Baryon Production in p-Pb Collisions at at $\sqrt{s_{NN}} = 5.02$ TeV", https://alice-notes.web.cern.ch/node/279

[29] S. Acharya *et al.* (ALICE Collaboration), Phys. Lett. B **807**, 135501 (2020). ALICE Analysis Note: "Measurement of phi Mesons at Mid-Rapidity in pp Collisions at 13 TeV as a Function of Charged-Particle Multiplicity", https://aliceinfo.cern.ch/Notes/node/627.

[30] T. Sjöstrand, S. Ask, J. R. Christiansen, R. Corke, N. Desai, P. Ilten, S. Mrenna, S. Prestel, C. O. Rasmussen and P. Z. Skands, Comput. Phys. Commun. **191**, 159 (2015).

[31] R. Corke and T. Sjostrand, JHEP **03**, 032 (2011).

[32] H. S. Shao, Comput. Phys. Commun. **184**, 2562 (2013).

[33] W. E. Caswell and G. P. Lepage, Phys. Lett. B **167**, 437 (1986).

[34] G. T. Bodwin, E. Braaten and G. P. Lepage, Phys. Rev. D **51**, 1125 (1995).

[35] I. M. Lofnes (ALICE Collaboration) Proceedings of European Physical Society Conference on High Energy Physics — PoS(EPS-HEP2019) **364**, 287 (2020).

[36] J. Hamon (ALICE Collaboration), Nucl. Part. Phys. Proc. **32**, 294 (2018).

[37] S. Acharya *et al.* (ALICE Collaboration), JHEP **04**, 108 (2018).

[38] A. Khatun , D. Thakur, S. Deb and R. Sahoo, J. Phys. G **47**, 055110 (2020).

[39] S. Tripathy, A. Bisht, R. Sahoo, A. Khuntia and Malavika P. S., Adv. High Energy Phys. **2021**, 8822524 (2021).

[40] A. Khuntia, S. Tripathy, A. Bisht and R. Sahoo, J. Phys. G **48**, 035102 (2021).

[41] S. Deb, R. Sahoo, D. Thakur, S. Tripathy and A. Khuntia, J. Phys. G **48**, 095104 (2021).

[42] A. Ortiz Velasquez, P. Christiansen, E. Cuautle Flores, I. Maldonado Cervantes and G. Paić, Phys. Rev. Lett. **111**, 042001 (2013).

[43] S. A charya *et al.* (ALICE Collaboration), Eur. Phys. J. C **79**, 857 (2019).

[44] D. Thakur, S. De, R. Sahoo and S. Dansana, Phys. Rev. D **97**, 094002 (2018).

[45] S. Deb, D. Thakur, S. De and R. Sahoo, Eur. Phys. J. A **56**, 134 (2020).

[46] B. B. Abelev *et al.* (ALICE Collaboration), Phys. Rev. Lett. **111**, 222301 (2013).

[47] Y. Oh, C. M. Ko, S. H. Lee and S. Yasui, Phys. Rev. C **79**, 044905 (2009).

[48] V. Greco, C. M. Ko and P. Levai, Phys. Rev. C **68**, 034904 (2003).

[49] V. Minissale, F. Scardina and V. Greco, Phys. Rev. C **92**, 054904 (2015).

[50] R. Aaij *et al.* (LHCb Collaboration), JHEP **02**, 102 (2019).

[51] S. Acharya *et al.* (ALICE Collaboration), arXiv:2011.06079.

[52] D. Sarkar, S. Das and S. Chattopadhyay, Nucl. Phys. A **989**, 13 (2019).

[53] Expression of Interest for an ALICE ITS Upgrade in LS3, ALICE-PUBLIC-2018-013.

[54] Z. Citron, *et al.* CERN Yellow Rep. Monogr. **7**, 1159 (2019).

Chapter 4

Exploring the possibility of thermalized medium formation in a small system

"The study of physics is also an adventure. You will find it challenging, sometimes frustrating, occasionally painful, and often richly rewarding."

- Hugh D. Young

One of the main goals of relativistic heavy-ion collision experiments (RHICE) is to create and characterize Quark Gluon Plasma (QGP) in the laboratory [1]. QGP is a deconfined state of quarks and gluons, which can be realized at the extreme conditions of high density and temperature. In QGP phase, the relevant degrees of freedom are quarks and gluons rather than mesons and baryons, which are confined color neutral states [2]. It is expected that such extreme conditions of high density and temperature can be created by colliding nuclei at relativistic energies. To this, experiments like Relativistic heavy-ion Collider (RHIC) at Brookhaven National Laboratory (BNL), USA and Large Hadron Collider (LHC) at CERN, Geneva, Switzerland have got prime importance. The enhancement of the number of strange particles and suppression in the number of J/ψ in collisions of heavy-ions with respect to that of pp (approximately scales by binary collisions), along with many others are taken as signatures of QGP formation in relativistic heavy-ion collisions [3–11]. Apart from taking values of such a ratio as confirmation for the creation of QGP in heavy-ion collisions, they are also used in characterizing QGP as well as in verifying and constraining different theoretical models. For such interpretations, it is assumed that, in *pp* collisions, no partonic medium is formed. However, in a baffling development, the experiments at the LHC show that such assumptions may not be correct for high multiplicity *pp* collisions [12–14]. These experiments at the LHC discovered QGP-like properties such as strangeness enhancement [12], double-ridge structure [15] etc., in smaller collision systems like *pp* and p-Pb collisions. These developments have important consequences on the results obtained from heavy-ion collisions as *pp* collisions so far have been used as a benchmark or base line for interpreting various results of heavy-ion collisions (AA) at relativistic energies to understand a possible medium formation.

In high energy heavy-ion collisions, the interpretation of results relies on the use of a model based on initial matter distribution resulting from the overlap of the two colliding nuclei at a given impact parameter (b). Indeed, for estimating quantities such as the following: (i) the centrality dependence of any observable expressed by the number of participating nucleons in the collision, $N_{\text{part}}(\text{b})$; (ii) the number of binary nucleon-nucleon collisions, $N_{\text{coll}}(\text{b})$ used to derive the nuclear modification factor (R_{AA}) from the ratio of AA over *pp* spectra; (iii) the elliptic and triangular flow parameters (v_2) and (v_3) normalized by the eccentricity ($\epsilon_2(\text{b})$) and triangulation ($\epsilon_3(\text{b})$) of the overlap region; (iv) the average surface area, A(b); and (v) path length, L(b) of the interaction region, knowing the nuclear overlap function ($T_{AA}(\text{b})$) is important. And, this overlap function depends on a realistic model of the collision geometry [16]. Similar to heavy-ion collisions, it is imperative to understand the initial conditions of the medium formed in *pp* collisions for high multiplicity events. Apart from this, knowing the proper initial conditions can also give a possible way to define centrality classes and the base needed for properly defining suppression factors or ratios for comparing results of event of different multiplicity classes produced in *pp* collisions [17]. Appropriate initial conditions can be chosen by considering that it should reproduce certain aspects of results such as multiplicity distribution or centrality distribution of various observables related to the collision events. For constructing the proper initial conditions for *pp* collisions, at the first attempt, one follows a way similar to that of heavy-ion collisions. Initial conditions for heavy-ion collisions are modeled in two kinds of distinct approaches: (i) one considers nucleonic or partonic collisions for energy deposition in the collision zone, and those are based on Glauber model [18–21], and (ii) QCD based calculations are employed to estimate initial energy deposition by gluonic fields originated from partonic currents of colliding nuclei [22]. So, these will also be obvious approaches for modeling initial conditions in *pp* collisions. As models based on Glauber modeling are very successful in reproducing various results of relativistic heavy-ion collisions, one can consider models for initial conditions of *pp* collisions which are based on similar kind of assumptions as used for Glauber approach used in heavy-ion collisions. The Initial transverse shape of the nuclei as described by the Glauber model for heavy-ion collisions depends on Wood-Saxon distribution, which is a two-parameter (half-density radius (R) and diffusivity (a)) Fermi-like distributions (2 pF) extracted from fits to elastic lepton-nucleus data [23, 24], which describes the multinucleon interactions occurring in the overlap region between the colliding nuclei via a Glauber eikonal approach [25]. Whereas, in the Monte Carlo Glauber (MCG) models [26–31], event-by-event sampling of individual nucleons is done from a Wood-Saxon distribution and the average over multiple events is used to calculate properties related to collisions. Presently, an available partonic Glauber model for *pp* collisions does not consider the full anisotropic density profile of protons, though radial homogeneity is assumed. In the first section 4.1 of this chapter, we present the results of Glauber-like model calculations for $N_{\text{coll}}(\text{b})$, $N_{\text{part}}(\text{b})$ due to the quark and gluon based proton density profile, which is a realistic picture obtained by results of deep inelastic scattering that reveals the structure of proton [18], and we used it to obtain charged-particle multiplicity distribution in pp collisions at $\sqrt{s} = 7$ TeV. Calculated multiplicity distribution is contrasted with ALICE data, a relation of an impact parameter with multiplicity is calculated, and the multiplicity distribution of eccentricity and flow harmonics is estimated for pp collisions. In order to understand the possibility of medium formation in high-multiplicity pp collisions, we have estimated nuclear modification-like factor, R_{HL}, considering low multiplicity yields as the base.

The characterization of QGP (i.e, determination of its equation of state, transport properties, etc.) can be done by analyzing experimental data with the help of theoretical models. But the applicability of these theoretical models relies on certain assumptions. For example, relativistic dissipative hydrodynamics [32] can be used to analyze experimental data on anisotropic flow for the estimation of the viscous coefficients of QGP. Currently, it is not possible to prove from the first principle that the system produced in RHICE has achieved thermal equilibrium. Therefore, study on the validity of the assumption of local thermalization (and hence applicability of hydrodynamics) with the help of experimental data is crucial. The assumption for the formation of partonic medium in RHICE is substantiated by experimental observations such as non-zero collective flow [33], suppression of high transverse momentum (p_T) hadrons [34], etc. These observations have been attributed to the formation of locally thermalized partonic medium which hydrodynamically evolves in space and time. Several parameters which are used to characterize the QGP formed in RHICE have been extracted by analyzing experimental data, where data from pp collision has been used as a benchmark. However, as mentioned above, recent results of LHC in regards to pp collisions shows that the role of pp collisions as a benchmark could be obscured (although it is shown that non-medium effects can explain the features observed in experiments [35, 36]). In this regard, it is important to understand the role of the number of constituents for the formation of the QCD medium, and pp collisions can serve as a platform to address such issues. The multiplicity serves as a proxy to the number of constituents in a system formed in pp collisions. It may be recalled that the issue of thermalization in small systems was studied in 1953 by Landau [37–40] and in 1982, van Hove investigated thermalization and quark-hadron phase transition in proton-antiproton collisions using variation of average transverse momentum ($\langle p_T \rangle$) with multiplicity [41]. Recently, QCD thermodynamics in pp collisions has been studied in [42]. In the second section 4.2 of this chapter, we discuss, how some of the markers of thermalization *e.g.* the thermodynamic quantities like, heat capacity (C_V), conformal symmetry breaking measure (CSBM) and speed of sound (c_s) for small system vary with the quantities like multiplicity, size and collision energy. Because the chances for the system to achieve thermalization will increase with the increase of these quantities. Therefore, any change in the variation of C_V, CSBM and c_s with multiplicity (say) which is different from the change obtained from Monte-Carlo generators, which is devoid of thermalization (like PYTHIA8) will signal on the possibility of thermalization.

Particle production dynamics in high-energy physics has got two domains, namely the hard perturbative-QCD (pQCD) sector and the soft physics domain, which are not necessarily having a sharp boundary. The hard pQCD sector corresponds to high momentum transfer processes, whereas the soft domain is governed by low momentum. The soft sector event topology is isotropic in nature, while the hard or the jet and mini-jet dominated sector is pencil-like. With high-multiplicity events at the LHC in pp collisions and the observation of heavy-ion-like features, it has become a necessity to look into event shape and multiplicity dependence of various observables and system thermodynamics. In order to do that, transverse spherocity (S_0) is one of the event-shape observables which has given a new direction for underlying events in pp collisions to have further differential study along with charged-particle multiplicity as an event classifier. Recent studies on transverse spherocity at the LHC suggest that, using event shape one can separate the jetty and isotropic events from the average shaped events [43–45]. Recently, the chemical and kinetic freeze-out scenario and system thermodynamics are studied using event shape and multiplicity in pp collisions at $\sqrt{s}$ = 13 TeV using PYTHIA8 event generator [46–48]. Further, to describe the particle production mechanism and the QCD thermodynamics, the statistical models are more useful due to high multiplicities produced in high-energy collisions. Lately, it has been seen that the experimental particle spectra in high-energy hadronic collisions are successfully explained by Tsallis non-extensive statistics [49, 51–57, 101]. Earlier, Tsallis non-extensive statistics has been used as initial distribution in Boltzmann Transport Equation to calculate the elliptic flow and nuclear modification factor in heavy-ion collisions [58–60]. In the third section 4.3 of this chapter, in view of the production dynamics dependence of event topology, we choose to use a thermodynamically consistent form of Tsallis non-extensive statistical distribution function [61], which nicely describes the p_{T}-spectra in LHC pp collisions to calculate the specific heat, CSBM and speed of sound for small collision systems like pp as a function of event shape and multiplicity using PYTHIA8 event generator [62].

We try to be as informative as possible. However, for the detailed analysis, the reader is suggested to follow the Refs. [63–65]. A concise summary is given in the fourth section 4.4 of this chapter.

4.1 Glauber model for small system using anisotropic and inhomogeneous density profile of a proton

In literatures, the density profiles like hard sphere and Fermi-like distribution (2 pF) functions are used traditionally to formulate Glauber model for heavy-ions and even for protons [31]. All these profiles can also be extended to the proton model by considering the radially symmetric parton density. In fact, in the case of a proton, several density profiles have been considered to estimate the initial conditions, most of them assume an azimuthally symmetric density profile, and those are mainly different in the phenomenological parameterization of radial variations [66]. But the standard model postulates that a proton consists of three effective quarks (constituent) and gluons within it. Thus distribution of such a configuration is less likely to be radially symmetric, because we expect individual peaks in a wave function in the quarks position inside a proton indicating its presence. The necessary condition is, however, that the wave function of each effective quarks and gluons should decay rapidly around the boundary of a proton (within the root mean square (RMS) area). In this regard, we find only one previous work [18] to consider the azimuthally asymmetric and inhomogeneous density distribution of a proton [67, 68], which is motivated by the shape of the structure function obtained in deep inelastic scattering, pointing out that multiplicity distribution produced by different models can be used to discriminate them, which can better reproduce experimental results. The difference between our work[1] described in this section and that reported in Ref. [18] are as follows: (i) We have considered different possible configurations of a Gaussian-fluctuating model thereby ensuring each collision as unique by assuming the initial position

---

[1] S . Deb, G. Sarwar, D. Thakur, P. Subramani, R. Sahoo and J. e. Alam, Phys. Rev. D **101**, 014004 (2020).

vectors of the three quarks to be vertices of an equilateral triangle in an xy plane, and then in order to account for all possible configurations, position vectors of the quarks are parametrized by varying azimuthal and polar angles. This parametrization is done by considering tilts of the quarks' initial configuration by some angle along the x-axis followed by the rotation of some other angles. A similar approach is applied along y-axis as well. In this process of parametrization, angles are chosen in such a way that there is no repetition of the particular configuration. (ii) For the estimation of charged-particle multiplicity (N_{ch}), in Ref. [18], it is assumed that N_{ch} for each event is in a linear scaling with a number of binary collisions (N_{coll}). But, in the present work, we have considered the contribution of a number of participants (N_{part}) along with N_{coll} for the estimation of charged-particle multiplicity as N_{part} dominates the low-p_T region and the N_{coll} contribution is higher in the high-p_T domain. A combination of both, which is our approach, appears to be more reasonable. We have calculated elliptic flow using linear response to eccentricity.

4.1.1 Formalism

In this study, we have used a model with fluctuating proton orientation, and it has three effective quarks and gluonic flux tubes connecting them as shown in Fig. 4.1. The densities of quarks (ρ_q) and gluons (ρ_g) are taken as the Gaussian type assuming a spherically symmetric distribution of quark densities from their respective centers and cylindrically symmetric gluon densities about the line joining two adjacent quarks as

$$\rho_q(\mathbf{r}; r_q) = \frac{1}{(2\pi)^{3/2} r_q^3} e^{-\frac{r^2}{2r_q^2}} \tag{4.1}$$

$$\rho_g(\mathbf{r}; r_s, r_l) = \frac{1}{(2\pi)^{3/2} r_s^2 r_l} e^{-\frac{x^2+y^2}{2r_s^2} - \frac{z^2}{2r_l^2}} \tag{4.2}$$

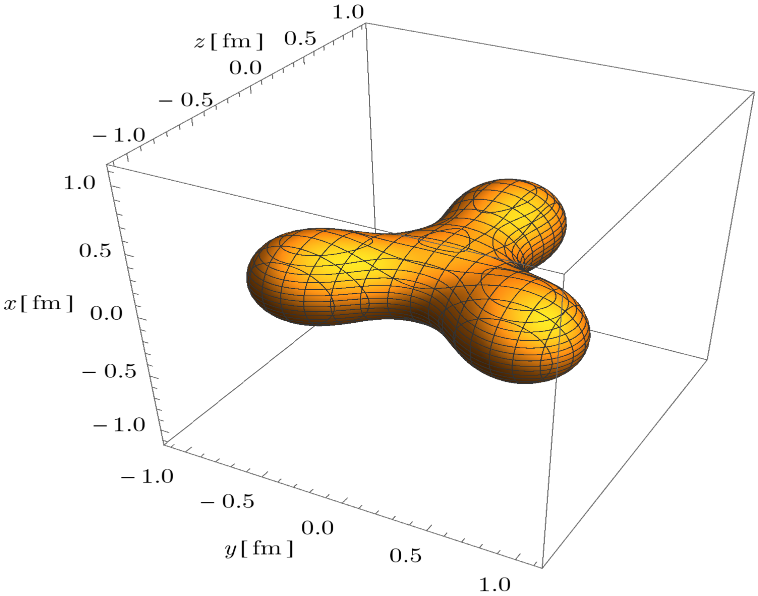

Figure 4.1: (Color online) Depiction of effective quarks and gluonic flux tubes connecting them within a proton [18].

where r_q is the radius of quark, r_s and r_l are, respectively, the radius and the length of the gluon tube.

The density function under study here was taken to be [18]

$$\begin{aligned}\rho_{G-f}(\mathbf{r};\mathbf{r}_1,\mathbf{r}_2,\mathbf{r}_3) = N_g\frac{1-\kappa}{3}\sum_{k=1}^{3}\rho_q(\mathbf{r}-\mathbf{r}_k;r_q) + N_g\frac{\kappa}{3}\sum_{k=1}^{3}\rho_g[\mathcal{R}^{-1}[\theta_k,\phi_k]\\ (\mathbf{r}-\frac{\mathbf{r}_k}{2};r_q,\frac{r_k}{2}]\end{aligned} \tag{4.3}$$

where, $\mathcal{R}[\theta,\phi]$ transforms vector (0,0,1) into $(\cos\phi\sin\theta, \sin\phi\cos\theta, \cos\theta)$ and $\mathbf{r}_k = r_k(\cos\phi_k\sin\theta_k, \sin\phi_k\cos\theta_k, \cos\theta_k)$ (where, k = 1,2 and 3) is the position vector of k^{th} effective quark. N_g is a collision energy dependent normalization factor for the density function of proton and accounts for the number of partons inside a proton. One can obtain this number by confronting the estimations to experimental observables. The free parameter κ allows one to control the percentage of gluon body content, and here it is taken to be 0.5 as a first approximation

[18]. This is the fraction of gluons (total number of gluons being κN_g) out of all partons inside a proton at a given collision energy.

4.1.1.1 Calculation of Thickness function and Overlap function

The collision plane is taken to be in x – y; hence the dependence along z axis is integrated out as follows:

$$T(x, y) = \int \rho(x, y, z) dz \tag{4.4}$$

The calculated thickness function for the ρ_{G-f} is

$$T(x, y) = \sum_{k=1}^{3} \frac{N_g}{3} \frac{1-\kappa}{2\pi r_q^2} e^{-l_k} + \frac{N_g \kappa}{3} (\frac{1}{(2\pi)^{3/2} r_s^2 r_l} \sqrt{\frac{\pi}{2}} (\frac{sin^2\theta_k}{2r_s^2} + \frac{cos^2\theta_k}{2r_l^2})^{-1/2}) e^{-a_k(x-\frac{x_k}{2})^2} e^{-b_k(y-\frac{y_k}{2})^2} e^{-c_k(x-\frac{x_k}{2})(y-\frac{y_k}{2})} \tag{4.5}$$

where, $r_s = r_q$ and $r_l = \frac{r_k}{2}$; for the present studies, we have taken $r_q = r_s = 0.25$ fm following Ref. [18],

$$l_k = \frac{(x - x_k)^2 + (y - y_k)^2}{2r_q^2} \tag{4.6}$$

and

$$a_k = -cos^2\phi_k P_k + [\frac{1}{2r_s^2}(sin^2\phi_k + cos^2\phi_k cos^2\theta_k) + \frac{1}{2r_l^2}(cos^2\phi_k sin^2\theta_k)], \tag{4.7}$$

$$b_k = -sin^2\phi_k P_k + [\frac{1}{2r_s^2}(cos^2\phi_k + sin^2\phi_k cos^2\theta_k) + \frac{1}{2r_l^2}(sin^2\phi_k + sin^2\theta_k)], \tag{4.8}$$

$$c_k = -sin^2\phi_k P_k[1 - 2[\frac{tan^2\theta_k}{r_s^2} + \frac{1}{r_l^2}]] \tag{4.9}$$

and

$$P_k = \frac{r_l^2 - r_s^2}{4(\frac{r_l^2}{cos^2\theta_k} + \frac{r_s^2}{sin^2\theta_k})} \tag{4.10}$$

The overlap function $T_{pp}(b)$ for projectile proton (**A**) and target proton (**B**) is defined as

$$T_{pp}(b) = \int\int T_A(x - \frac{b}{2}, y) T_B(x + \frac{b}{2}, y) dx dy \tag{4.11}$$

Here T_{pp} is sum of 4-components, namely quark-quark, quark-gluon, gluon-quark, gluon-gluon. Primed (unprimed) indices indicate variables corresponding to **B** (**A**). In the following, we provide an overlap function for all the possible combinations of partons.

1. **The quark-quark term**

   The overlap function for the interaction of two quarks:

$$(T_{pp})_{qq}(b) = \frac{N_g^2(1-\kappa)^2}{36\pi r_q^2} \sum_{k,k'=1}^{3} exp[-\frac{(b - x_k - x'_{k'})^2 - (y_k - y'_{k'})^2}{4r_q^2})] \tag{4.12}$$

2. **The gluon-gluon term**

   The overlap function for the interaction of two gluon tubes:

$$(T_{pp})_{gg}(b) = \sum_{k,k'=1}^{3} C_{k,k'} \sqrt{\frac{\pi}{\lambda_{k,k'}}} e^{-\frac{\gamma_{k,k'}^2}{4\lambda_{k,k'}}} \tag{4.13}$$

   where,

$$\gamma_{k,k'} = \frac{c_k + c'_{k'}}{4(b_k + b'_{k'})}[c_k(b + x_k) - c'_{k'}(b - x_{k'}) + 2(b_k y_k - b'_{k'} y'_{k'})] \tag{4.14}$$

$$\lambda_{k,k'} = (a_k + a'_{k'}) - \frac{c_k + c'_{k'}}{4(b_k + b'_{k'})} \tag{4.15}$$

$$C_{k,k'} = A_k A'_{k'} \sqrt{\frac{\pi}{b_k + b'_{k'}}} exp[\frac{[\frac{1}{2}[c_k(b + x_k) - c'_{k'}(b - x'_{k'})] + (b_k y_k + b'_{k'} y'_{k'})]^2}{4(b_k + b'_{k'})}]$$
$$exp[-\frac{a_k}{4}(b + x_k)^2 - \frac{a'_{k'}}{4}(b - x'_{k'})^2 - \frac{c_k y_k}{4}(b + x_k) + \frac{c'_{k'} y'_{k'}}{4}(b - x'_{k'})] \tag{4.16}$$

$$A_k = \frac{N_g\kappa}{3}\frac{1}{(2\pi)^{3/2}r_s^2 r_l}(\frac{\pi}{2})^{1/2}[\frac{sin^2\theta_k}{2r_s^2} + \frac{cos^2\theta_k}{2r_l^2}]^{-1/2} \tag{4.17}$$

3. The quark-gluon term

The overlap function for the interaction of a quark and a gluon tube:

$$(T_{pp})_{qg}(b) = \sum_{k,k'=1}^{3} D_{k,k'}\sqrt{\frac{\pi}{\alpha_{k,k'}}}e^{\frac{\beta_{k,k'}^2}{4\alpha_{k,k'}}} \tag{4.18}$$

where,

$$\alpha_{k,k'} = \frac{1}{2r_q^2} + a'_{k'} - \frac{(c'_{k'})^2}{4(\frac{1}{2r_q^2} + b'_{k'})} \tag{4.19}$$

$$\beta_{k,k'} = 2c'_{k'}[\frac{y_k}{r_q^2} + b'_{k'}y'_{k'} - \frac{c'_{k'}}{2}(b - x'_{k'}) - \frac{y'_{k'}}{4}] - \frac{\frac{b}{2} + x_k}{r_q^2} + a'_{k'}(b - x'_{k'}) \tag{4.20}$$

$$\begin{aligned} D_{k,k'} = E_{k,k'}\sqrt{\frac{\pi}{\frac{1}{2r_q^2} + b'_{k'}}}\exp[-\frac{y_k^2}{2r_q^2} - \frac{b'_{k'}(y'_{k'})^2}{4}]\exp[-\frac{(\frac{b}{2} + x_k)^2}{2r_q^2} - \frac{a'_{k'}}{4}(b - x'_{k'})^2] \\ \exp[\frac{1}{4(\frac{1}{2r_q^2} + b'_{k'})}[\frac{y_k}{r_q^2} + b'_{k'}y'_{k'} - \frac{c'_{k'}}{2}(b - x'_{k'})]^2]\exp[\frac{c'_{k'}y'_{k'}}{4}(b - x'_{k'})] \end{aligned} \tag{4.21}$$

$$E_{k,k'} = \frac{N_g^2\kappa(1-\kappa)}{36\pi^2 r_q^4 r_{k'}}[\frac{sin^2\theta'_{k'}}{2r_q^2} + \frac{2cos^2\theta'_{k'}}{r_{k'}^2}]^{-1/2} \tag{4.22}$$

4. The gluon-quark term

The overlap function for the interaction of a gluon tube and a quark:

$$(T_{pp})_{gq}(b) = \sum_{k,k'=1}^{3} F_{k,k'}\sqrt{\frac{\pi}{\delta_{k,k'}}}\exp[\frac{\eta_{k,k'}^2}{4\delta_{k,k'}}] \tag{4.23}$$

where,

$$\delta_{k,k'} = a_k + \frac{1}{2r_q^2} - \frac{c_k^2}{4(\frac{1}{2r_q^2} + b_k)} \tag{4.24}$$

$$\eta_{k,k'} = a_k(b+x_k) - \frac{1}{r_q^2}(\frac{b}{2} - x'_{k'}) - \frac{2c_k}{4(\frac{1}{2r_q^2}+b_k)}[b_k y_k + \frac{y'_{k'}}{r_q^2} + \frac{c_k}{2}(b+x_k)] \tag{4.25}$$

$$F_{k,k'} = G_{k,k'}\sqrt{\frac{\pi}{\frac{1}{2r_q^2}+b_k}}\exp[\frac{1}{4(\frac{1}{2r_q^2}+b_k)}[b_k y_k + \frac{y'_{k'}}{r_q^2} + \frac{c_k}{2}(b+x_k)]^2]\exp[-\frac{c_k y_k}{4}(b+x_k) - \frac{{y'_{k'}}^2}{2r_q^2} - \frac{b_k y_k^2}{4}]\exp[-\frac{a_k}{4}(b+x_k)^2 - \frac{1}{2r_q^2}(\frac{b}{2} - x'_{k'})^2] \tag{4.26}$$

$$G_{k,k'} = \frac{N_g^2\kappa(1-\kappa)}{36\pi^2 r_q^4 r_k}[\frac{sin^2\theta_k}{2r_q^2} + \frac{2cos^2\theta_k}{r_k^2}]^{-1/2} \tag{4.27}$$

Together total overlap function is the sum of four terms given by Eq. 4.12, 4.13, 4.18, 4.23,

$$T_{pp}(b) = (T_{pp})_{qq}(b) + (T_{pp})_{gg}(b) + (T_{pp})_{qg}(b) + (T_{pp})_{gq}(b) \tag{4.28}$$

4.1.1.2 Calculation of N_{coll} and N_{part}

We define the number of binary collisions (N_{coll}) of partons in a *pp* collision at a given impact parameter (b) as follows:

$$N_{\text{coll}}(b) = \sigma_{eff}T_{pp}(b), \tag{4.29}$$

where σ_{eff} is the effective partonic cross sections. It should be mentioned here that quark-quark, quark-gluon and gluon-gluon interaction cross sections will be different due to different color factors of quarks and gluons [69]. However, we use a common partonic cross section here, which is extracted from the fits to the data as in Ref. [70], which avoids limitations of theoretical calculations at the cost of losing the information regarding the difference in individual type of interactions. In the absence of experimental information and non-perturbative QCD based calculations of the individual cross-section (*e.g.* gg, qg and qq processes), we have taken a common cross section for all partons as σ_{eff}. In line with the previous studies [18, 71], we fix $\sigma_{eff} = 4.3 \pm 0.6$ mb [70] with N_g= 10 partons, so as to reproduce the experimental value of inelastic cross section, $\sigma_{pp} = 60$ mb [72] for the pp collision at $\sqrt{s} = 7$ TeV. This accounts for the only non-trivial dependence of the Glauber calculation on the beam energy $\sqrt{s}$. Previous studies [18, 70] have assumed linear scaling of charged hadron ($N_{\rm ch}$) multiplicity with $N_{\rm coll}$ only. In contrast to this assumption, we have considered the dependence of $N_{\rm ch}$ on a number of participant partons ($N_{\rm part}$) and $N_{\rm coll}$. Further, relationship between $N_{\rm part}$ and $N_{\rm coll}$ is considered nonlinear as that of the heavy-ion collisions assuming a three-dimensional shape. Thus, the number of participating partons at impact parameter b is given as

$$N_{\rm part}(b) \propto N_{\rm coll}^{1/x}(b), \tag{4.30}$$

where x is a parameter.

By considering f as a fraction of charged hadron multiplicity produced from binary collisions, we have a two component model for the estimation of a number of charged particles given as

$$\frac{dN_{\rm ch}}{d\eta} = n_{pp}[(1-f)\frac{N_{\rm part}}{2} + fN_{\rm coll}], \tag{4.31}$$

where n_{pp} is a constant of proportionality, which represents the charged-particle multiplicity density in pseudorapidity for pp collisions, and f is a free parameter.

4.1.2 Results

Assuming initial position vectors of three quarks to be vertices of the equilateral triangle in the xy plane as $\mathbf{r}_1 = (\frac{d}{4}, \frac{\sqrt{3}}{4}d, 0)$, $\mathbf{r}_2 = (\frac{d}{4}, -\frac{\sqrt{3}}{4}d, 0)$, $\mathbf{r}_3 = (-\frac{d}{2}, 0, 0)$, where d is the free parameter of the model which ensures that the length of the gluon tubes connecting quarks are fixed, i.e., $(|\mathbf{r}_1|^2 = |\mathbf{r}_2|^2 = |\mathbf{r}_3|^2) = \frac{d^2}{4})$. For the present study, we have taken $d = 1.5$ fm [18]. Now, in order to account for all possible configurations, position vectors of quarks are parameterised by varying azimuthal and polar angles. The generalised configurations considering the tilt by ψ along x axis and the rotation by the angle α are $\mathbf{r}_1 = (\frac{d}{2}\cos(\frac{\pi}{3}+\psi), \frac{d}{2}\sin(\frac{\pi}{3}+\psi)\cos\alpha, -\frac{d}{2}\sin(\frac{\pi}{3}+\psi)\sin\alpha)$, $\mathbf{r}_2 = (\frac{d}{2}\cos(\frac{5\pi}{3}+\psi), \frac{d}{2}\sin(\frac{5\pi}{3}+\psi)\cos\alpha, -\frac{d}{2}(\sin\frac{\pi}{3}+\psi)\sin\alpha)$, and $\mathbf{r}_3 = (\frac{d}{2}\cos(\psi), \frac{d}{2}\sin\psi\cos\alpha, -\frac{d}{2}\sin\psi\sin\alpha)$, and considering tilt by γ along y axis and the rotation by the angle β are $\mathbf{r}_1 = (\frac{d}{2}\cos(\frac{\pi}{3}+\gamma)\cos\beta, \frac{d}{2}\sin(\frac{\pi}{3}+\gamma), \frac{d}{2}\cos(\frac{\pi}{3}+\gamma)\sin\beta)$, $\mathbf{r}_2 = (\frac{d}{2}\cos(\frac{5\pi}{3}+\gamma)\cos\beta, \frac{d}{2}\sin(\frac{5\pi}{3}+\gamma), -\frac{d}{2}\cos(\frac{\pi}{3}+\gamma)\sin\beta)$, $\mathbf{r}_3 = (\frac{d}{2}\cos(\gamma)\cos\beta, \frac{d}{2}\sin\gamma, \frac{d}{2}\cos\gamma\sin\beta)$.

In the above configurations, ψ and $\gamma \in (0,\frac{2\pi}{3})$, $\alpha \in (0,\pi)$ and $\beta \in (0,2\pi)$. In the present study, we have taken x in Eq. 4.30 to be 0.75 as N_{coll} scales as $A^{4/3}$ for similar target and projectile nuclei with mass numbers A for heavy-ion collisions and are spherical in shape. In our work, this consideration of x = 0.75 holds well because when the plane formed by connecting centres of each quark is randomly rotated as part of the Monte Carlo simulation for accounting all possible configurations of collision geometry, the overall angular space is exhausted, thus making collision geometry to be a closely spherical overlap with preserving contributions from each of the different configurations; hence the factor of 0.75 is taken so that it accounts for general spherical overlap in heavy-ion collisions. We have also chosen the RMS radius of proton and quark as 1 fm and 0.25 fm, respectively.

4.1.2.1 Number of binary collisions and participants as a function of impact parameter

We have used Eqs. 4.29 and 4.30, to estimate N_{coll} and N_{part}. Fig.4.2 shows the mean value of N_{coll} (upper curve) and N_{part} (lower curve) as a function of impact parameter (b). Towards higher values of b, the difference between the two curves effectively vanishes. Similar trends were observed for Au+Au and Cu+Cu collisions at $\sqrt{s_{NN}} = 200$ TeV [16].

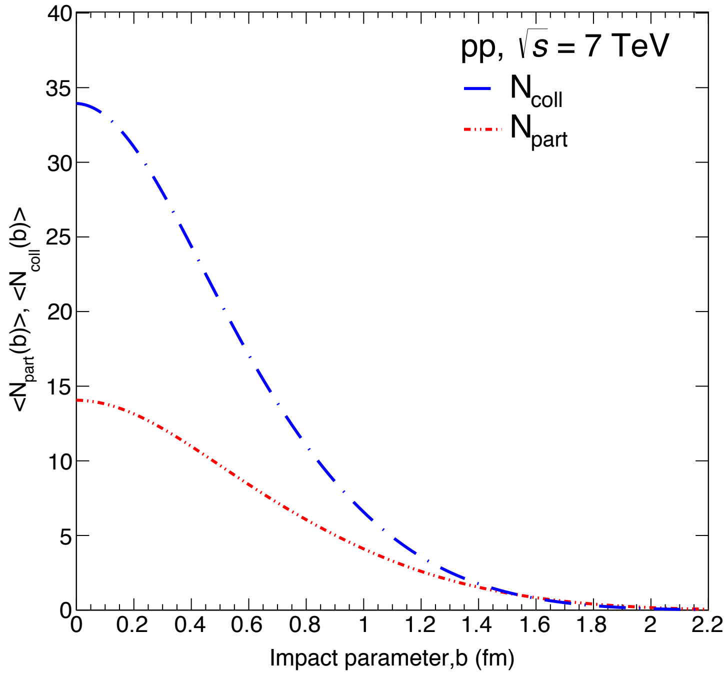

Figure 4.2: (Color online) N_{coll} and N_{part} as a function of impact parameter (b) for different number of terms contraction [63].

4.1.2.2 Charged particle multiplicity estimation

Two-component models have been used in heavy-ion phenomenology for a long time to estimate the charged-particle multiplicity [73, 74]. The inelastic cross section, σ_{NN}^{inel}, which depends on collision energy, is used as input for the MC Glauber model. In the present work, we have used similar approach for *pp* collisions as well, where nucleons are replaced by partons (quarks and gluons) and σ_{NN}^{inel} by σ_{eff}. The model provides N_{part} and N_{coll}, for an event with a given impact parameter and collision energy which is discussed in the previous section. As in heavy-ion collisions, the concept of “ancestors” (independently emitting sources of particles) has been introduced for a given value of N_{part} and N_{coll}. The number of ancestors can be parametrized by a two-component model given by [73, 74],

$$N_{ancestors} = fN_{\text{part}} + (1-f)N_{\text{coll}} \tag{4.32}$$

The two-component model divides the parton-parton collisions into *soft* and *hard* interactions: the multiplicity of particles produced by soft interaction is proportional to N_{part} and hard interaction is proportional to N_{coll}. As negative binomial distribution (NBD) is able to well reproduce the charged-particle distribution in *pp* collisions [75], we use the two-parameter NBD to calculate the probability of producing n particles per ancestor:

$$P(n;\bar{n},k) = \frac{\Gamma(n+k)}{\Gamma(k)\Gamma(n+1)} \left[\frac{\bar{n}}{k+\bar{n}}\right]^{n} \left[\frac{k}{k+\bar{n}}\right]^{k}, \tag{4.33}$$

where $\bar{n}$ is the average multiplicity and k characterizes the width of the distribution. By the use of different combination of f (Eq. 4.32), $\bar{n}$ and k (Eq. 4.33) we have repeated the process of obtaining the multiplicity distribution for a large sample of events, until our model simulates the experimental multiplicity distribution. We have also calculated the ratio of N_{ch} obtained from our model to that of experimental value [76] and is represented in Fig. 4.3 for *pp* collisions at $\sqrt{s} = 7$ TeV. The best agreement for N_{ch} distribution obtained by our model with experimental data is found for $f = 0.85$, $\bar{n} = 8$ and $k = 0.13$. From Fig. 4.3, it can be seen that our model well describes the data in the mid multiplicity region ($15 < N_{\text{ch}} < 90$), with 5%-10% discrepancy. However, towards the low and high multiplicity it is unable to reproduce the experimental measurement. The inability of the model to explain the extreme low and high multiplicity region might be due to the lower probability of collision impact parameter, when derived in the Monte Carlo model from a Gaussian distribution.

4.1.2.3 Centrality estimation

The centrality is usually expressed as a percentage of the total interaction cross section, σ [77]. Impact parameter distribution is taken as input to our current model. So, the centrality percentile of a *pp* collision with b is defined by integrating

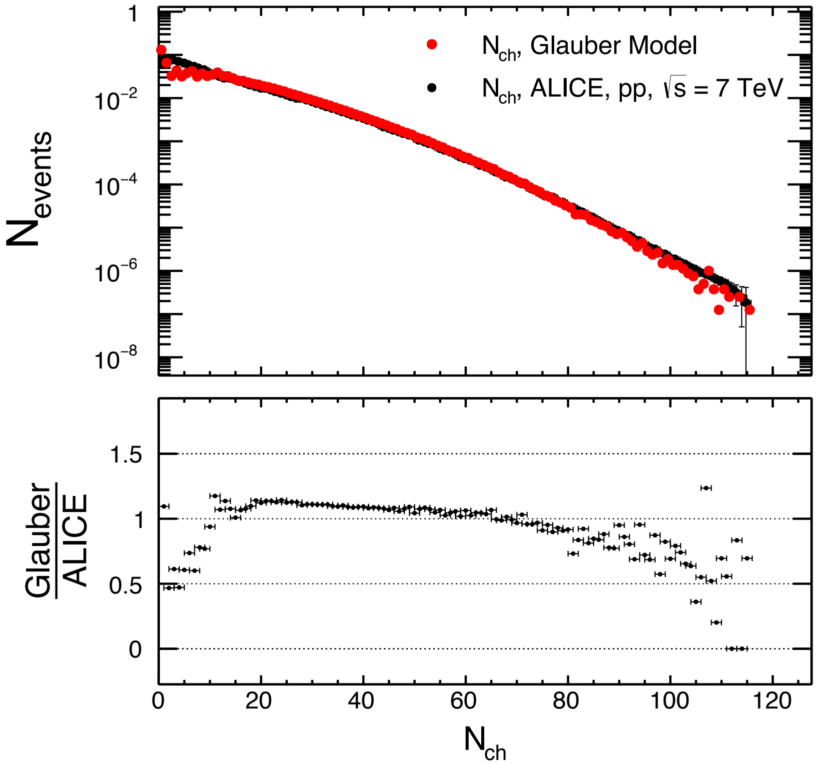

Figure 4.3: (Color online) Upper panel: Comparison of charged multiplicity distribution obtained from present work and ALICE experiment for *pp* collisions at $\sqrt{s}$ = 7 TeV [76]. Black dots represents ALICE data and red dots represent present work. Lower panel: Ratio of this work to the ALICE experimental data [63].

the impact parameter distribution as,

$$c_1 = \frac{\int_0^{b1} (dN/db)\ db}{\int_0^{\infty} (dN/db)\ db}, \qquad c_2 = \frac{\int_{b1}^{b2} (dN/db)\ db}{\int_0^{\infty} (dN/db)\ db}, ... \tag{4.34}$$

where c_1, c_2,...., are the percentile bins and b_1, b_2,..., are the impact parameters. More clearly, the c_1 percentage of total number of events of impact parameter distribution fall in the interval (b_1, b_2) and so on. For the current analysis, a Gaussian distribution with mean 1 and standard deviation of 0.32 has been used as an input impact parameter distribution, which is shown in Fig. 4.4, so that the distribution function vanishes beyond the proton radius (≈ 1 fm).

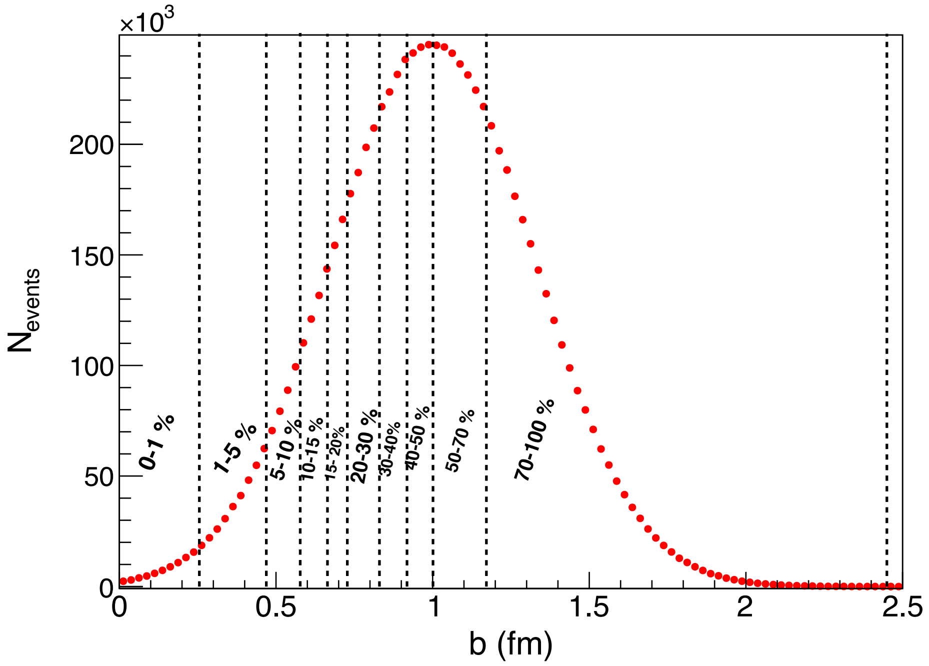

Figure 4.4: (Color online) Input impact parameter (b) profile for *pp* collisions [63].

We have also tested different forms of impact parameter distributions, but the Gaussian distribution is found to be a suitable choice to describe the charged-particle multiplicity distribution. Once, we get the ranges of the impact parameter corresponding to each centrality, we have projected it to N_{ch}, N_{part} and N_{coll} to calculate $\langle N_{\text{ch}}\rangle$, $\langle N_{\text{part}}\rangle$ and $\langle N_{\text{coll}}\rangle$ corresponding to each b-ranges. Fig. 4.5 represents the multiplicity distribution for each percentile bin. Table 4.1 shows the value of $\langle N_{\text{ch}}\rangle$, $\langle N_{\text{part}}\rangle$, and $\langle N_{\text{coll}}\rangle$, obtained by using our model along with $\langle N_{\text{ch}}\rangle$ value of ALICE for *pp* collisions at $\sqrt{s} = 7$ TeV.

It can be clearly seen that the calculated $\langle dN_{\text{ch}}/d\eta\rangle$ is well consistent with experimental value, except for the high and low multiplicity regions. This is because of the artifact of incapability of our model to describe the charged-particle

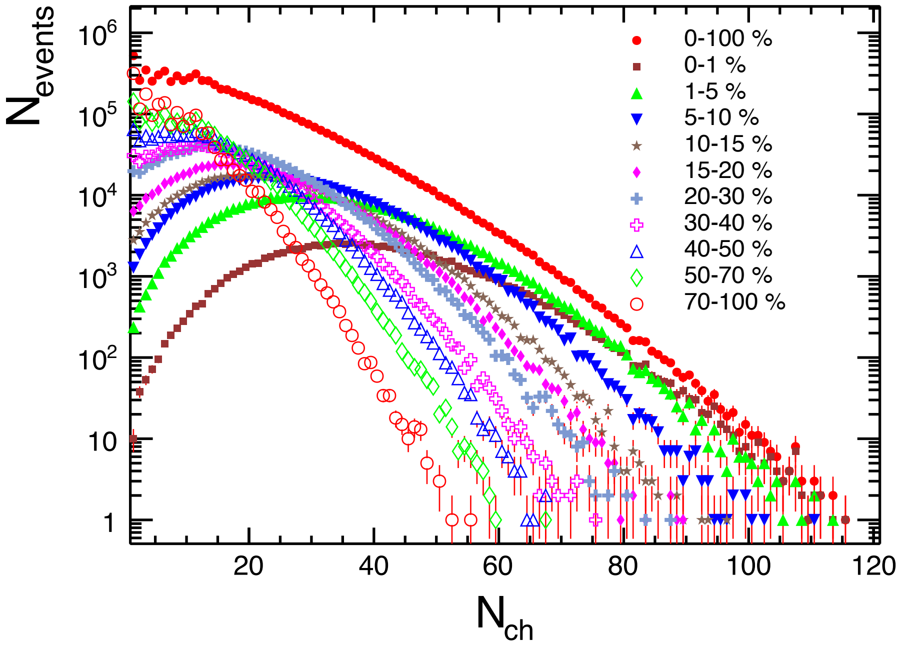

Figure 4.5: (Color online) Charged-particle multiplicity distribution in different percentile bins for pp collisions at $\sqrt{s}$ = 7 TeV [63].

distribution in that region (Fig. 4.3). However, it is to be noted that the input $\sigma_{gg}^{inel} = 0.43 \pm 0.06\ fm^2$ contain 14% uncertainty and the same amount of uncertainty (14%) is associated with each $\langle dN_{\rm ch}/d\eta \rangle$. From our model, we found $\langle dN_{\rm ch}/d\eta \rangle = 7.47$ for minimum bias (0-100%) collisions, which is a little higher from the experimental value, $\langle dN_{\rm ch}/d\eta \rangle = 6.01 \pm 0.01^{+0.20}_{-0.12}$ [76]. This discrepancy needs to be understood.

4.1.2.4 The ratio, R_{HL} for high to low multiplicity events

In order to understand the possibility of a formation of a medium in high-multiplicity events in pp collisions, we define a variable as:

$$R_{HL}(p_T) = \frac{d^2N/dp_T d\eta|^{HM}}{d^2N/dp_T d\eta|^{LM}} \times \frac{\langle N_{\rm coll}^{LM} \rangle}{\langle N_{\rm coll}^{HM} \rangle}, \tag{4.35}$$

Table 4.1: Geometric properties ($b, N_{\rm ch}, N_{\rm part}, N_{\rm coll}$) of pp collisions for different multiplicity classes using the Glauber Monte Carlo calculation along with a negative binomial distribution fit to a charged-particle multiplicity distribution at $\sqrt{s}$ = 7 TeV for the ALICE experiment at the LHC [63].

Multiplicity (%)	$b - range(fm)$	$\langle dN_{\rm ch}/d\eta\rangle^{glauber}$	$\langle dN_{\rm ch}/d\eta\rangle^{expt}$	$\langle N_{\rm part}\rangle$	$\langle N_{\rm coll}\rangle$
0-1	0 - 0.25534	19.69	$28.82^{+0.86}_{-0.84}$	13.142	31.156
1-5	0.25535 - 0.46909	16.24	$20.34^{+0.58}_{-0.57}$	11.164	24.815
5-10	0.46909 - 0.58484	13.37	$15.80^{+0.34}_{-0.32}$	9.244	19.478
10-15	0.58484 - 0.66430	11.61	$13.07^{+0.24}_{-0.22}$	8.037	16.153
15-20	0.66431 - 0.72766	10.28	$11.25^{+0.19}_{-0.18}$	7.131	13.818
20- 30	0.72767 - 0.83026	8.94	$9.21^{+0.15}_{-0.14}$	6.116	11.326
30-40	0.83027 - 0.91819	7.48	$7.13^{+0.12}_{-0.11}$	5.268	9.215
40-50	0.91820 - 1.00117	6.49	$5.65^{+0.11}_{-0.09}$	4.418	7.340
50-70	1.00118 - 1.17163	5.12	$3.81^{+0.07}_{-0.06}$	3.395	5.208
70-100	1.17164 - 2.54998	3.66	$1.66^{+0.05}_{-0.04}$	1.968	2.591

which is similar to the nuclear modification factor R_{AA} in heavy-ion collisions. Here, $d^2N/d\eta dp_T|^{HM}$, $d^2N/d\eta dp_T|^{LM}$, and $\langle N_{\rm coll}^{LM}\rangle$ ($\langle N_{\rm coll}^{HM}\rangle$) are charged particle yields in high-multiplicity, low-multiplicity pp collisions at $\sqrt{s}$ = 7 TeV [78], the mean number of binary collisions in low (high) multiplicity pp events, respectively. The upper panel of Fig. 4.6 shows the transverse momentum spectra of charged particles in high-multiplicity (VOM I), second high multiplicity (VOM II), and low multiplicity (VOM X) events obtained from Ref. [78]. And the lower panel shows the R_{HL} defined in Eq. 4.35. For such a definition of R_{HL}, it is observed for all charged particles for p_T < 1 GeV/c, value of R_{HL} < 1 and for p_T > 1 GeV/c , it is greater than 1. However, it tends to reduce at very high p_T. And for p_T >1 GeV, the value of the factor is higher for higher multiplicities.

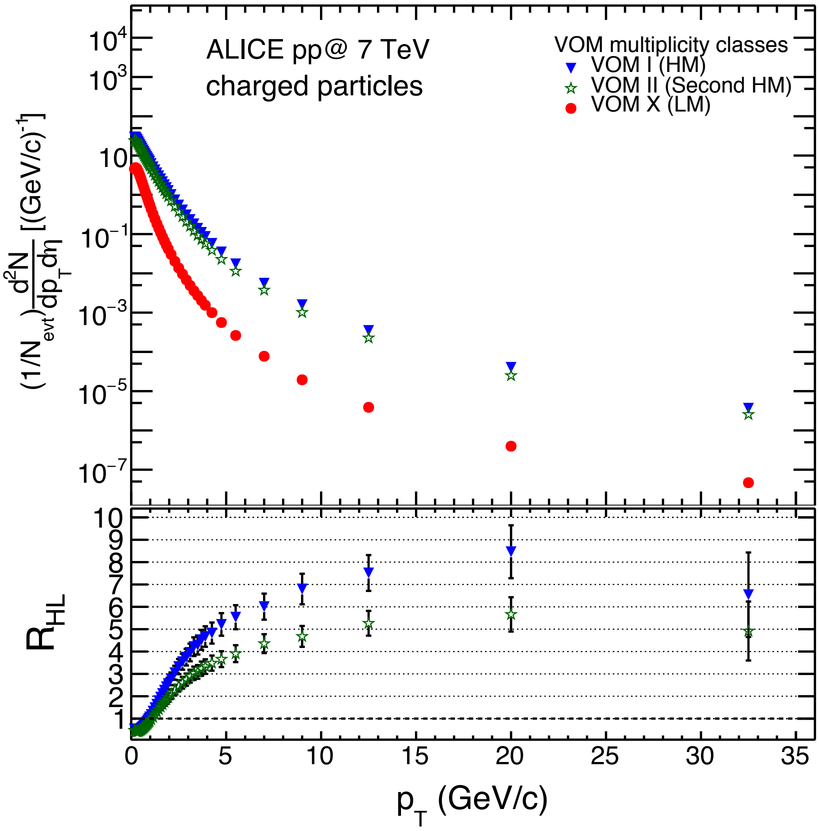

Figure 4.6: (Color online) Upper panel: Transverse momentum spectra of charged particle in pp collisional at $\sqrt{s}$ = 7 TeV [78] for VOM multiplicity classes, viz., highest (HM), second highest (second HM) and lowest multiplicity (LM) class. Lower Panel: R_{HL} obtained from the ratio of differential yield at high-multiplicity and second high multiplicity classes with low multiplicity class scaled by $\langle N_{\rm coll}\rangle$ [63].

Fig. 4.7 shows results of R_{HL} for identified particles, pion $(\pi^+ + \pi^-)$, kaon $(K^+ + K^-)$, proton $(p + \bar{p})$ for pp collisions at $\sqrt{s}$ = 7 TeV. It is found that $R_{HL} < 1$ for a proton for $p_T < 1$ GeV, which is the same as observed in the case of charged particles. However, for pion and kaon $R_{HL} < 1$ for $p_T < 0.8$ GeV. It is also observed that for $p_T < 1.9$ GeV, these identified particles have almost the same value of R_{HL} and for $p_T > 1.9$ GeV, the value is almost the same for the pion and kaon but the value for the proton is larger and increases with p_T sharply up to $p_T = 5$ GeV, and then saturates within uncertainties. But for the pion and kaon, the factor increases monotonically with a decreasing slope from $p_T > 1.9$ GeV, where the trend splits for the proton and the other two hadrons.

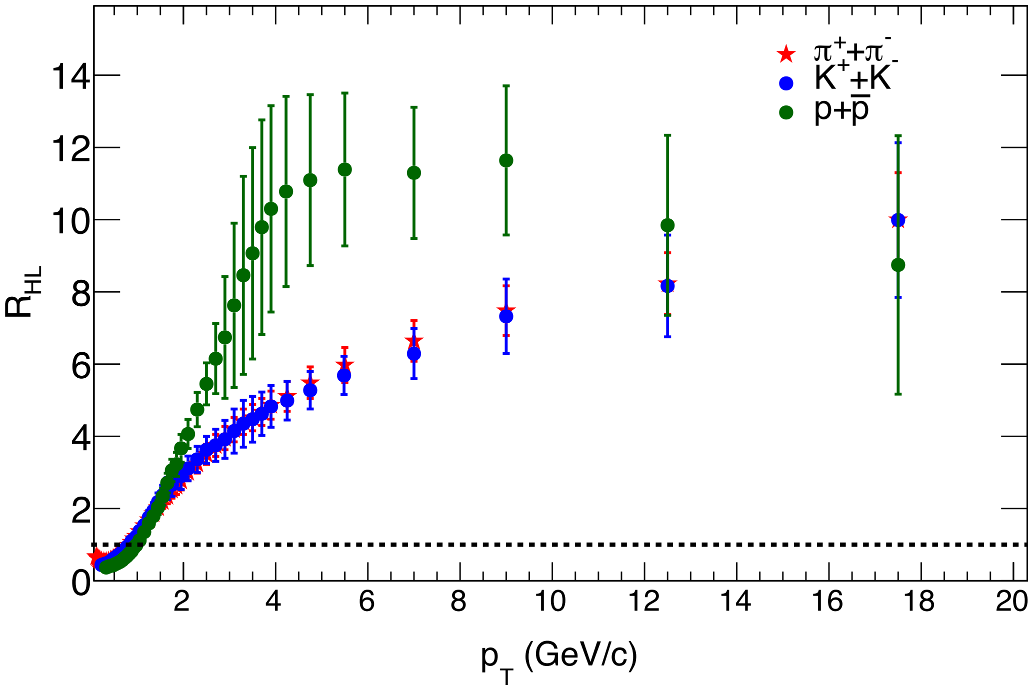

Figure 4.7: (Color online) Nuclear modification-like factor obtained from Eq. 4.35 for pion, Kaon and proton in pp collisional at $\sqrt{s} = 7$ TeV [78] [63].

It is reported in ref. [79] that the proton shows a distinct behavior in this regard other than the hadrons produced in p-Pb collisions. Also for p-Pb collisions, it is reported that the factor, $R_{pPb} > 1$, for all charged particles for $p_T > 2.5$ GeV [79, 80]. For p-Pb, R_{pPb} saturates to unity for $p_T > 2$ GeV, and it is also found that for pp, R_{HL} shows an almost similar trend but with a larger value of the factor with saturationlike behavior starting after $p_T = 2$ GeV. We note that the R_{HL} values above unity for $p_T > 1$ GeV may be qualitatively similar to other observed enhancements due to the Cronin effect and radial flow in pA and dA systems [81, 82], as conjectured for a similar behavior of R_{pPb} [80], where the moderate excess at high p_T is suggestive of anti-shadowing effects in the nuclear parton distribution function [83].

4.1.2.5 Estimation of Elliptic-flow

For a long time, pp collisions were considered as the baseline measurements for the determination of the deconfined state of matter, i.e., QGP formed in a nuclear collision. A recent observation of pp collisions at LHC energies hints toward a collective effect; thus, it becomes imperative to review the earlier view. In this regard, we have also calculated eccentricity (ϵ) using the present approach. The asymmetry ratio between semiaxis dimensions of the overlap region weighted by $N_{\rm coll}$ at a particular b can be used to obtain ϵ as [71]:

$$\epsilon(b) = \frac{\int (y^2 - x^2) N_{\rm coll}(x, y, b) dx dy}{\int (y^2 + x^2) N_{\rm coll}(x, y, b) dx dy}, \tag{4.36}$$

where $N_{\rm coll}(x, y, b) = \sigma_{gg} T_a(x - \frac{b}{2}, y) T_b(x + \frac{b}{2}, y)$ represents the impact plane binary collision density. We have calculated $\epsilon(b)$ by using Eq. 4.36 by considering a sum of four components, namely quark-quark, quark-gluon, gluon-quark and gluon-gluon. Fig. 4.8 shows the eccentricity for the pp collision at $\sqrt{s} = 7$ TeV obtained using Eq. 4.36 and it is observed to increase with b and seems to saturate towards larger b.

Using ϵ, we have obtained the elliptic flow (v_2) as a function of b by considering the scaling: $v_2 = \Omega\epsilon$, where $\Omega = 0.3 \pm 0.02$ [70]. Although we have considered a linear scaling to understand the variation of v_2 with multiplicity, as a matter of fact v_2 should be calculated by using relativistic hydrodynamics with relevant initial conditions and equation of state as inputs.

By geometry, $v_2(b)$ will follow the general trend of ϵ(b). It is found that the overlap of two hard spheres with infinitely sharp edges yields artificially large

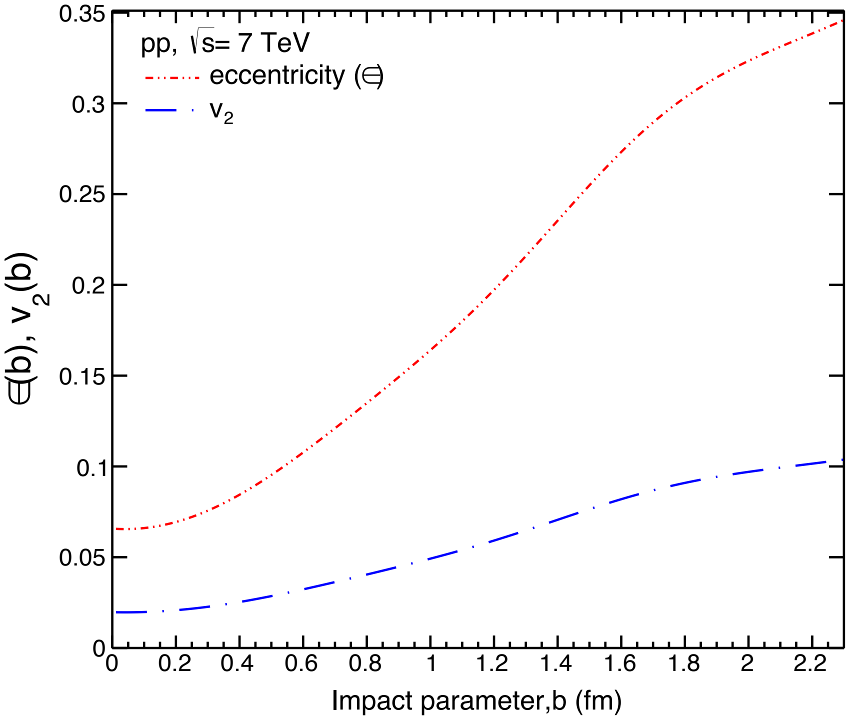

Figure 4.8: (Color online) Eccentricity (ϵ) and elliptic-flow (v_2) as a function of impact parameter in *pp* collisions at $\sqrt{s} = 7$ TeV [63].

eccentricities [84].

In Fig. 4.9, we have compared our estimation of the variation of v_2 with the charged-particle multiplicity for *pp* collision at $\sqrt{s} = 7$ TeV with the experimental result at $\sqrt{s} = 13$ TeV [85]. This is due to the fact that the data for collisions at $\sqrt{s} = 13$ TeV were not available at the time of the reporting of this work to constrain our model. That does not prevent us from the comparison, since in Ref. [86], it is reported that the value of v_2 for collisions at $\sqrt{s} = 2.76$ TeV and $\sqrt{s} = 13$ TeV are almost the same when measured for different transverse momenta, indicating that the collision energy dependence of v_2 is weak. It is observed that for $N_{\rm ch} \gtrsim 8$, our estimation of v_2 with linear response to initial geometry reproduces the value obtained from the experiment within the error bars. However, for lower multiplicities, our estimation with a linear response to the initial eccentricity falls short of that obtained from experimental data. This may be due to effects other than the collective linear response or final state effects. Though the charged-particle multiplicity variation of v_2 for *pp* collisions at $\sqrt{s}$ = 7 TeV is not available, the elliptic flow coefficient extracted from the CMS Collaboration data at $\sqrt{s}$ =7 TeV is 0.04 – 0.08 [87] and our estimation of v_2 falls within this range. We also note that this model gives v_2 similar to that of the IP-Glasma model as presented in Ref [88] for low multiplicity region (< 8).

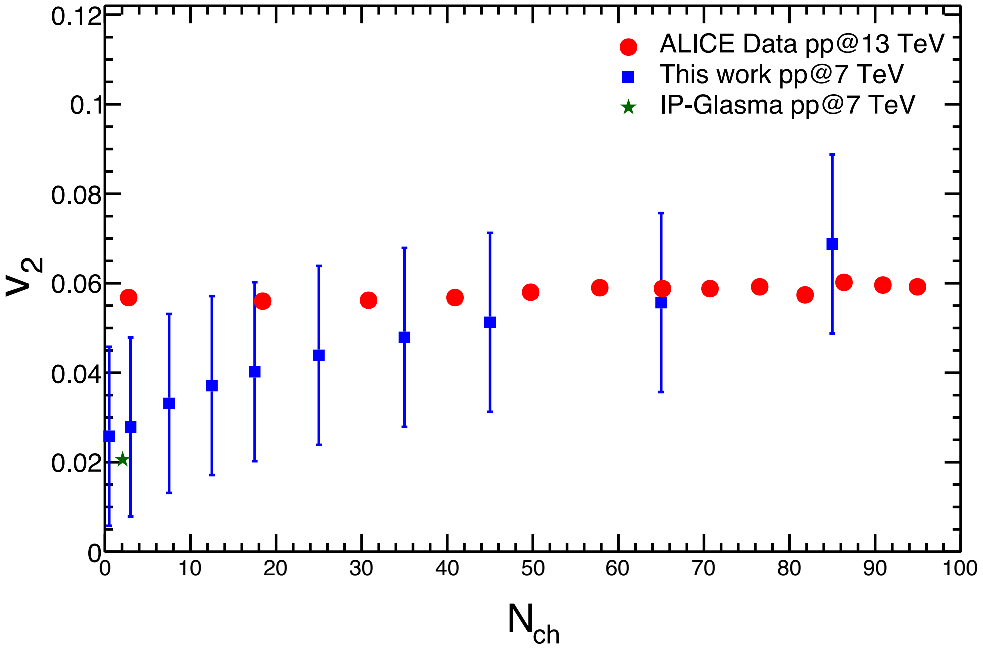

Figure 4.9: (Color online) Elliptic-flow, v_2 as a function of multiplicity in *pp* collisions at LHC energies [63].

4.2 Study of QCD dynamics in small system using ALICE data

Having seen the geometric approach in exploring the collisions of a small system like pp in the previous section, the aim of this section[2] is to study the charged-particle multiplicity, system size and collision energy dependence of the thermodynamic quantities like, heat capacity (C_V), conformal symmetry breaking measure (CSBM) and speed of sound (c_s) for a small system. These quantities have been chosen because C_V is one of the most basic and commonly used quantities which records the response of the system subjected to temperature stimulus. It is estimated via temperature fluctuations, which characterizes the equation of the state of the system. Similarly, c_s provides the information on the equation of state of a thermal medium and it is used to quantify the softest point of the phase transition along with the location of the critical point [89]. The CSBM plays an important role for QCD dynamics and phase transition, which can be expressed in terms of energy density (ϵ), pressure (P) and temperature (T) as CSBM $= (\epsilon - 3P)/T^4$ (see [90, 91] for details). In this context the variation of $\langle p_T \rangle$ of the hadrons with multiplicity connected to the temperature and entropy of a thermal system respectively will also be discuss. As there is no way to directly probe, the spectra of produced hadrons are used to gain insight about the possible partonic phase. The ALICE data for pp collisions at $\sqrt{s} = 7$ TeV have been used to obtain C_V, CSBM and c_s and the results have been contrasted with PYTHIA8. The analysis using PYTHIA8 shows some degree of success in explaining some of the observations made in pp and p-Pb collisions, such as saturation of $\langle p_T \rangle$ of J/ψ [92, 93] and that of charged particles [94], as a function of charged-particle multiplicity [95]. Though variation of heat capacity with collision energy has been investigated [96, 97] through temperature fluctuations for

---

[2] S. Deb, G. Sarwar, R. Sahoo and J. e. Alam, Eur. Phys. J. A **57**, 195 (2021).

systems formed in RHICE, we are not aware of any studies in literature similar to the present one for small systems formed in *pp* collisions for understanding thermalization.

4.2.1 Formalism

We will recall some of the well-known thermodynamic relations in this section. The system formed at the LHC energies at the central rapidity region will be dominated by gluons, which neither carry electric nor baryonic charges. Such a system can be described by one single thermodynamic variable, the temperature (T).

Now we would like to quote the standard thermodynamic expressions [98] for C_V, c_s^2 and entropy density (s) below for a system with vanishing chemical potential as:

$$C_V = \left(\frac{\partial \epsilon}{\partial T}\right)_V, \tag{4.37}$$

$$s = \left(\frac{\partial P}{\partial T}\right)_V, \tag{4.38}$$

$$c_s^2 = \left(\frac{\partial P}{\partial \epsilon}\right)_s = s/C_V, \tag{4.39}$$

where V is the volume of the system. Now it is clear that to estimate the thermodynamic quantities of our interest we need to know energy density (ϵ), pressure (P), s, etc and these quantities can be calculated by using the phase space distribution functions ($f(E)$) [99]. At kinetic freeze-out, the momentum distribution of the final state particles is frozen. Thus, these thermodynamical quantities could be estimated from the moments of the momentum distribution at the freeze-out. Interestingly, $f(E)$ for different hadrons can be measured experimentally by detecting their momentum distribution functions which allows us to connect data with C_V, c_s, CSBM etc.

In the present work the Tsallis non-extensive statistics [100] is used to reproduce the p_T-spectra of hadrons at kinetic freeze-out [101–103]. The Tsallis-Boltzmann (TB) distribution function [104–106] has been widely used to describe the results from RHICE. The TB distribution which is given by [107]

$$f(E) \equiv \frac{1}{\exp_q(\frac{E}{T})} \tag{4.40}$$

where,

$$\exp_q(x) \equiv \begin{cases} [1+(q-1)x]^{\frac{1}{q-1}} & \text{if } x > 0 \\ [1+(1-q)x]^{\frac{1}{1-q}} & \text{if } x \leq 0 \end{cases} \tag{4.41}$$

where $x = E/T$, E is the energy ($E = \sqrt{p^2 + m^2}$), p and m are momentum and mass of the particle, respectively. It is important to note that in the limit, $q \to 1$, Eq. (4.41) reduces to the standard exponential function,

$$\lim_{q \to 1} \exp_q(x) \to \exp(x).$$

T and q appearing in TB distribution are extracted by fitting experimental data on hadronic p_T-spectra with this distribution. The parameter q is called the non-extensive parameter which is a measure of degree of deviation from Boltzmann-Gibbs (BG) statistics and T appearing in this formalism obeys the fundamental thermodynamic relation:

$$T = \left.\frac{\partial U}{\partial S}\right|_{N,V}, \tag{4.42}$$

where U is the internal thermal energy, S is the total entropy ($= sV$), N is the number of particles and hence, the parameter T can be called temperature, even though the system obeys the Tsallis and not the BG statistics.

The calculation of the number density (n), ϵ, P from the thermal phase space density, $f(E)$ is straight forward [99]. These are given by, $n = g/(2\pi)^3 \int d^3p f(E)$, $\epsilon = g/(2\pi)^3 \int d^3p E f(E)$ and $P = g/(2\pi)^3 \int d^3p \frac{p^2}{3E} f(E)$. Analogously ϵ, P, etc can be estimated for TB distribution by inserting $f(E)$ from Eq. 4.40. The expression for energy density (ϵ) then reads as [107, 108]:

$$\epsilon = \frac{g}{2\pi^2}\int dp\ p^2\sqrt{(p^2+m^2)} \times [1+\frac{(q-1)\sqrt{(p^2+m^2)}}{T}]^{\frac{-q}{q-1}}, \tag{4.43}$$

where, g is the degeneracy factor.

Similarly the expression for pressure (P) is given by [107, 108]:

$$P = \frac{g}{2\pi^2}\int dp\ p^4\frac{1}{3\sqrt{(p^2+m^2)}} \times [1+\frac{(q-1)\sqrt{(p^2+m^2)}}{T}]^{\frac{-q}{q-1}}, \tag{4.44}$$

The expression for C_V as given in Eq. 4.37 can be obtained from Eq. 4.43 as:

$$C_V = \frac{qg}{2\pi^2T^2}\int dp\ p^2(p^2+m^2) \times [1+\frac{(q-1)\sqrt{(p^2+m^2)}}{T}]^{\frac{1-2q}{q-1}}, \tag{4.45}$$

The dimensionless quantity I/T^4, where $I = \epsilon - 3P$ called the trace anomaly [90, 91] or CSBM can be expressed as:

$$\frac{I}{T^4} = \frac{g}{2\pi^2T^4}\int dp\ p^2\sqrt{(p^2+m^2)} \quad [1-\frac{p^2}{(p^2+m^2)}] \times [1+\frac{(q-1)\sqrt{(p^2+m^2)}}{T}]^{\frac{-q}{q-1}}, \tag{4.46}$$

The squared velocity of sound (c_s^2) in QGP is given by:

$$c_s^2 = \frac{\frac{gq}{6\pi^2T^2}\int dp\ p^4 \times [1+\frac{(q-1)\sqrt{(p^2+m^2)}}{T}]^{\frac{1-2q}{q-1}}}{C_V} \tag{4.47}$$

and finally, the $\langle p_T \rangle$ for the TB distribution can be estimated from the following expression:

$$\langle p_T \rangle = \frac{\int dp_T\ p_T^2 f(E)^q}{\int dp_T\ p_T f(E)^q}. \tag{4.48}$$

i.e.

$$\langle p_T \rangle = \frac{\int dp_T\ p_T^2[1+(q-1)\frac{\sqrt{(p_T^2+m^2)}}{T}]^{\frac{-q}{q-1}}}{\int dp_T\ p_T[1+(q-1)\frac{\sqrt{(p_T^2+m^2)}}{T}]^{\frac{-q}{q-1}}}. \tag{4.49}$$

4.2.2 Event generation and Analysis Methodology

In order to make a comparative study, results obtained in this work using ALICE data are compared with pQCD-inspired Monte-Carlo generator PYTHIA8, which is a amalgam of various physics mechanisms like hard and soft interactions, initial and final-state parton showers, fragmentation, multipartonic interactions, color reconnection, rope hadronization etc [109]. This model is used in this study to simulate *pp* collisions at ultra-relativistic energies. Detailed explanation on PYTHIA8 physics processes and their implementation can be found in Ref.[62].

We have used 8.215 version of PYTHIA, which includes multi-partonic interaction (MPI). MPI is crucial to explain the underlying events multiplicity distributions. Also, this version includes color reconnection (CR) which mimics the flow-like effects in *pp* collisions [110]. It is crucial to mention here that PYTHIA8 does not have in-built thermalization. However, as reported in Ref. [110], the CR mechanism along with the MPI in PYTHIA8 produces the properties which mimics thermalization of a system such as radial flow and mass dependent rise of mean transverse momentum. Apparently the PYTHIA8 with MPI and CR has the ability to produce the features similar to thermalization.

QCD processes in PYTHIA8 are categorised as soft and hard QCD processes, where production of heavy quarks are included in the latter. We have simulated the inelastic, non-diffractive component of the total cross-section for all the soft QCD process (SoftQCD:all = on) and Hard QCD process (HardQCD:all = 0) separately. MPI based scheme of color reconnection (ColorReconnection:reconnect =0) are also included. We have generated 100 million events with 4C tune (Tune:pp=5) [111], which give sufficient statistics to obtain p_T-spectra even in high-multiplicity events. To check the compatibility of tunes used in this work, we have compared simulated results obtained from hard and soft QCD tune of PYTHIA8 with the experimental data [112] as shown in Fig. 4.10. Here, we have compared PYTHIA8 simulated data with ATLAS data [112] as at the time of this work, there is no mini-biased ALICE data available for transverse momentum distribution of charged particles in *pp* collisions at $\sqrt{s} = 7$ TeV. The motivation to contrast the PYTHIA8 generated results with the experimental data is to show that the soft processes fit the data reasonably well as shown in Fig 4.10. This comparison makes it clear that softQCD tune of the PYTHIA8 is suitable for the present work.

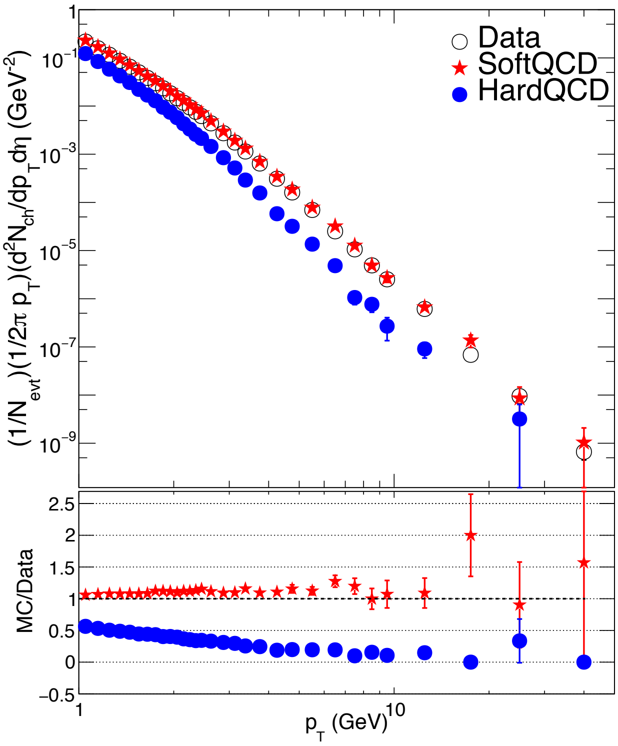

Figure 4.10: (Color online) The upper panel shows the comparison of experimental data [112], HardQCD and SoftQCD tunes of PYTHIA8 for *pp* collisions at $\sqrt{s}$ = 7 TeV. The black open circles are experimental data, red stars and blue solid circles are PYTHIA8 simulated data with SoftQCD and HardQCD tunes, respectively. The lower panel shows the ratio of PYTHIA8 to experimental data for both softQCD and hardQCD cases. The vertical lines indicate the error bars [64].

The generated events are categorised into seven multiplicity bins as (0-2), (2-4), (4-8), (8-11), (11-14), (14-18), (18-24) from which charged-particle pseudorapidity densities ($\langle dN_{\rm ch}/d\eta\rangle$) at mid-rapidity are obtained. The p_T distribution generated by PYTHIA8 for different multiplicity bins are now fitted with the following expression having T and q as fitting parameter [113]:

$$\frac{1}{p_T}\frac{d^2N}{dp_Tdy}\bigg|_{y=0} = \frac{gVm_T}{(2\pi)^2}\left[1+(q-1)\frac{m_T}{T}\right]^{-\frac{q}{q-1}}, \tag{4.50}$$

where $m_{\rm T} = \sqrt{p_T^2+m^2}$. The fitting parameters, T and q depends on the mass of the hadrons.

The p_T-spectra of $\pi^{\pm}$, $K^{\pm}$, $K^{*0}+\overline{K^{*0}}$ and $p+\overline{p}$ from simulated data at the mid-rapidity ($|\eta|<0.5$) for different multiplicity bins in pp collisions at $\sqrt{s}=7$ TeV have been considered. The fitting of the PYTHIA8 generated spectra by Eq. 4.50 is displayed in Fig. 4.11. Figure 4.12 shows the quality of the fitting in terms of χ^2/NDF as function of multiplicity which shows that the quality of fitting is reasonably good for all the particles under consideration at all multiplicity classes except for $p+\overline{p}$ at low multiplicity class.

Figures 4.13 and 4.14 show the comparison of the parameters T and q extracted from the experimental data and the PYTHIA8 generated results for different charged-particle multiplicities [52, 114].

With the detailed analysis methodology and (T, q) values obtained from PYTHIA8, we now move to discuss the results obtained by comparing ALICE experimental data and simulated data in the next subsection.

4.2.3 Results and Discussions

The thermodynamic quantities, C_V, CSBM, c_s and $\langle p_T\rangle$ can be estimated by using Eqs. 4.45, 4.46, 4.47, and 4.49 with the values of T and q extracted by parameterizing the p_T spectra of identified hadrons using TB distribution. We note that a similar kind of approach has been used to study the variation of C_V

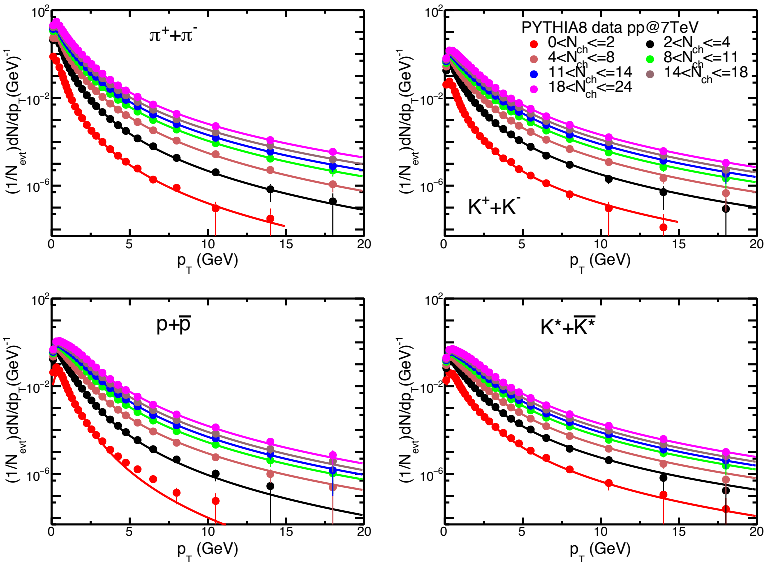

Figure 4.11: (Color online) Fitting of PYTHIA8 generated p_{T}-spectra of $\pi^{\pm}$, $K^{\pm}$, $K^{*0}+\overline{K^{*0}}$ and $p+\overline{p}$ using Tsallis distribution (Eq. 4.50) for various multiplicity classes at mid-rapidity for pp collisions at $\sqrt{s}=7$ TeV. In the legend of the figure, we have used a short notation N_{ch}. The vertical lines indicate the error bars [64].

with $\sqrt{s_{NN}}$ at the freeze-out surfaces in the context of heavy-ion collisions [96]. The ALICE data on the p_T-spectra originating from pp collisions at $\sqrt{s}=7$ TeV collision energy [78] have been used to extract the values of T and q for each multiplicity in Ref. [114]. It is found that the values of T and q depend on hadronic species hinting at different decoupling or freeze out temperature for different hadrons [52]. In general, the hadrons with higher inverse slope (of p_T-spectra) is expected to come either from early stage and/or suffer more transverse flow. In the present study, we consider hadronic spectra of pion ($\pi^{\pm}$), kaon ($K^{\pm}$), neutral kstar ($K^{*0}+\overline{K^{*0}}$) and proton ($p+\overline{p}$).

The variation of C_V, $C_V/\langle n_i\rangle$, (where i=$\pi^{\pm}$, $K^{\pm}$, $K^{*0}+\overline{K^{*0}}$ and $p+\overline{p}$), C_V/T^3, $C_V/(\epsilon+P)$, CSBM, c_s^2 and $\langle p_T\rangle$ with $\langle dN_{\mathrm{ch}}/d\eta\rangle$ at mid-rapidity have been considered. Here $<n_i>$ (in GeV^3) is the number density (number per unit volume) of the hadron i, obtained by integrating Eq. 4.40 over three momentum and $(\epsilon+P)$

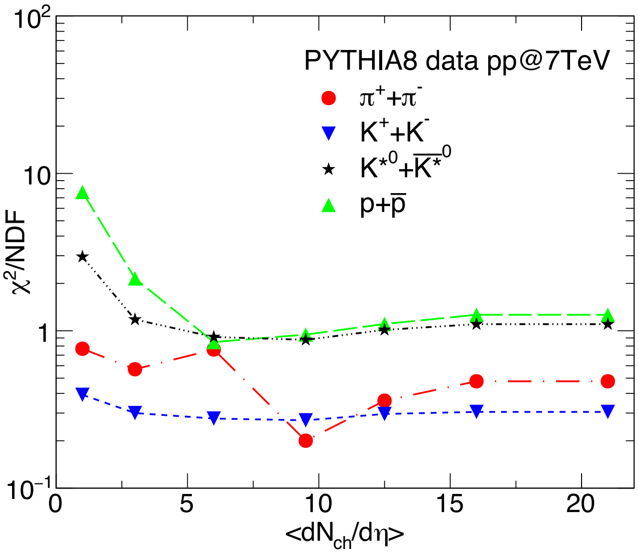

Figure 4.12: (Color online) χ^2/NDF for $\pi^{\pm}$, $K^{\pm}$, $K^{*0} + \overline{K^{*0}}$ and $p + \overline{p}$ as a function of charged-particle multiplicity obtained by fitting Tsallis distribution (Eq. 4.40) [64].

is the enthalpy density. The values of $\langle dN_{\text{ch}}/d\eta \rangle$ obtained in the experiment for different multiplicity classes tabulated in Table 4.2 (see Ref. [78] for details). We also investigated whether finite system size alone can account for non-extensivity observed in the spectra. To make a distinction between systems with and without thermalization we contrast the results with the PYTHIA8 simulated outputs under the same collision condition.

Table 4.2: Average charged-particle pseudorapidity densities corresponding to different event multiplicity classes [78] [64].

Class name	Mul1	Mul2	Mul3	Mul4	Mul5	Mul6	Mul7	Mul8	Mul9	Mul10
$\langle \frac{dN_{ch}}{d\eta} \rangle$	21.3±0.6	16.5±0.5	13.5±0.4	11.5±0.3	10.1±0.3	8.45±0.25	6.72±0.21	5.40±0.17	3.90±0.14	2.26±0.12

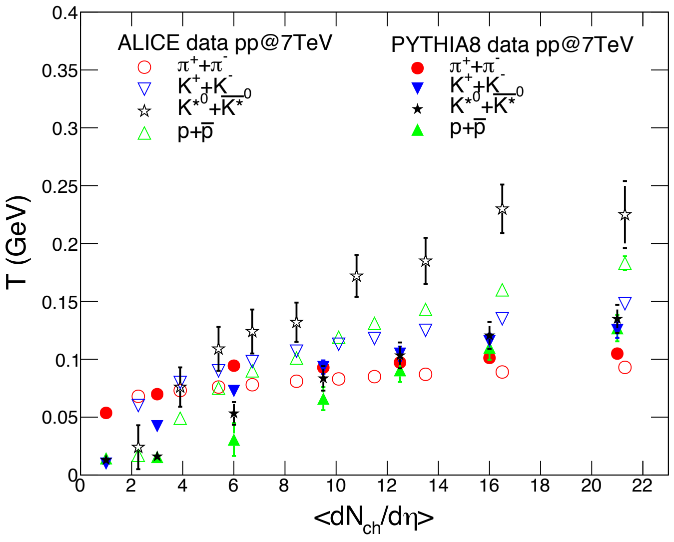

Figure 4.13: (Color online) Multiplicity dependence of T for *pp* collisions at $\sqrt{s} =$ 7 TeV obtained by using Eq. 4.50 as a fitting function for the PYTHIA8 simulated numbers (solid markers) and experimental data (open markers) [114] [64].

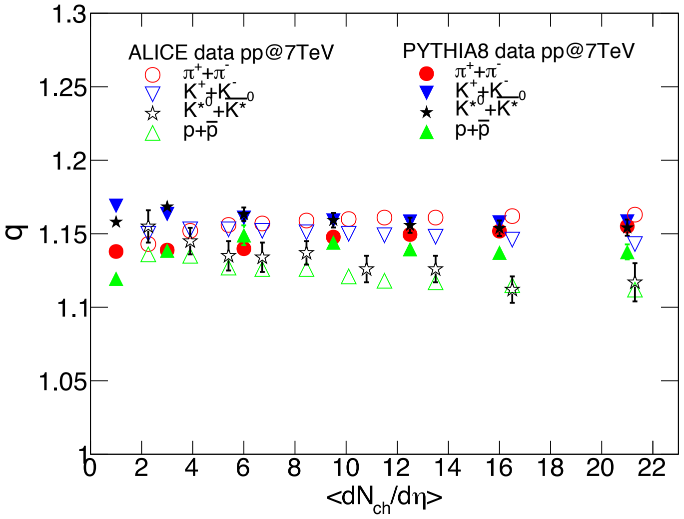

Figure 4.14: (Color online) Same as Fig.4.13 for variation of the parameter *q* with charged-particle multiplicity [64].

4.2.3.1 Multiplicity dependence of heat capacity

As mentioned before, C_V is one of the most fundamental quantities that gives the response of a thermal system under the influence of temperature stimulus. It gives the measure of how variation of temperature changes the entropy of a system ($\Delta S = \int \frac{C_V}{T} dT$). The change in entropy is a good observable for studying the phase transition. In the context of heavy-ion collisions, entropy (S) per unit rapidity (y), dS/dy can be connected to the the corresponding multiplicity (dN/dy). Therefore, the heat capacity acts as bridging observable for experimental measurement and theoretical models. For a strongly interacting system sufficient heat energy should be supplied to overcome the 'binding force' caused by the interaction to increase the temperature *i.e.* to supply adequate randomized kinetic energy by the constituents of the system. In other words, the mechanism of randomization to increase the temperature will require supply of more heat energy for strongly interacting system compared to that needed for the weakly interacting system. That is heat energy supplied to the strongly interacting system will not be entirely utilized to increase the temperature, some amount will be used to weaken the binding. Hence the increase in temperature in a strongly interacting system will be less than a weakly interacting system for a given amount of energy supplied to the system. Thus, the heat capacity bears the effects of strength of interaction among constituents of the system and represents the ease of randomization for the particular phase of the matter. Therefore, for weakly interacting gas increase of temperature has negligible effects on change in interaction strength. As a result its scaled value, $C_V/\langle n_i \rangle$ will display a plateau. This makes heat capacity a good observable to study how correlation and randomization competes in the system. The variation of heat with multiplicity in *pp* collision gives opportunities to better understand the randomization and the change in the strength of correlation with number of constituents in the QCD system.

The variation of C_V with $\langle dN_{\mathrm{ch}}/d\eta\rangle$ for $\pi^{\pm}$, $K^{\pm}$, $K^{*0}+\overline{K^{*0}}$ and $p+\bar{p}$ extracted from ALICE data has been displayed in Fig. 4.15. The result has been contrasted with the output obtained from PYTHIA8 simulation at the same *pp* colliding energy. It is observed that results from PYTHIA8 which do not contain medium effects differ from data. Also, it is noted that the heat capacity increases with increase in multiplicity. If a thermalized medium is formed, then, in the ideal gas limit, heat capacity varies linearly with number of particles ($C_V \propto \langle n_i\rangle$).

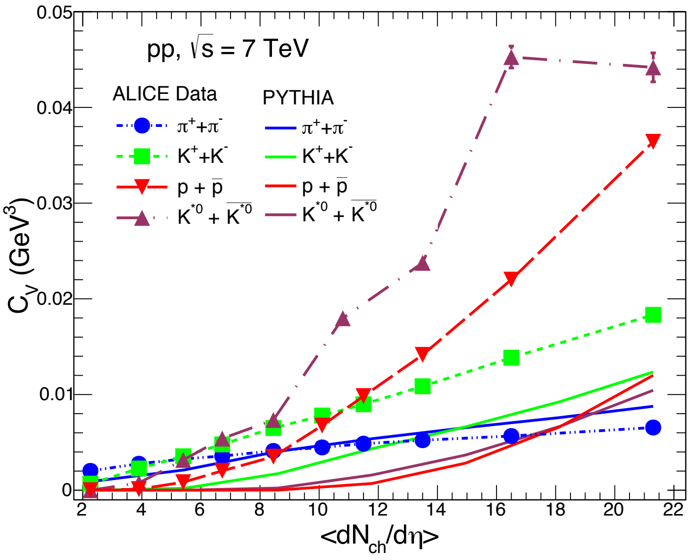

Figure 4.15: (Color online) Heat capacity obtained using TB distribution as a function of multiplicity. Dashed (solid) lines represent results obtained using ALICE (PYTHIA8 simulated) data, respectively for *pp* collisions at $\sqrt{s} = 7$ TeV [64].

Therefore, in Fig. 4.16 we depict the variation of C_V scaled by $\langle n_i\rangle$ extracted from ALICE data as well as PYTHIA8 as a function of $\langle dN_{\mathrm{ch}}/d\eta\rangle$ for $\pi^{\pm}$, $K^{\pm}$, $K^{*0}+\overline{K^{*0}}$ and $p+\bar{p}$ of ALICE data and results from PYTHIA8. It is observed that $C_V/\langle n_i\rangle$, (where i $= \pi^{\pm}$, $K^{\pm}$) tend to almost saturate for high-multiplicity, however, a slow variation is observed for $i = \overline{K^{*0}}$ and $p+\bar{p}$. It is important to note that the pionic and kaonic matter (for $\langle dN_{\mathrm{ch}}/d\eta\rangle > 8$) have approximately similar value of $C_V/\langle n_i\rangle$ for both experimental and MC data.

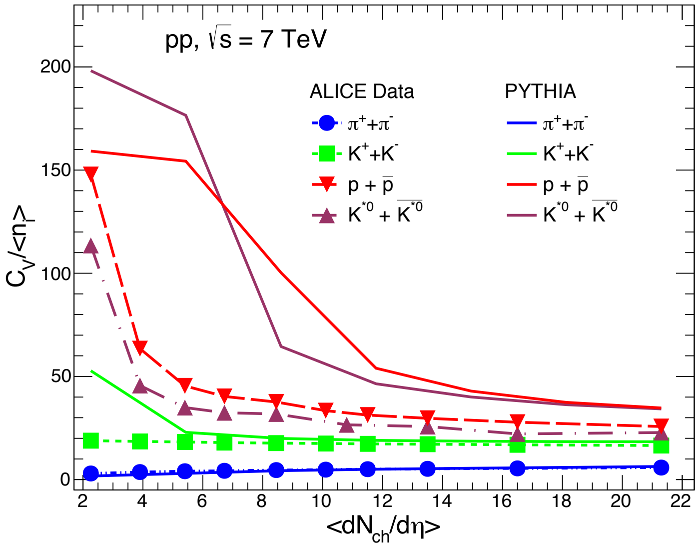

Figure 4.16: (Color online) Same as Fig. 4.15 showing the variation of $C_V/<n_i>$ with charged multiplicity [64].

The observed saturation in specific heat in its variation with multiplicity can be attributed to the possibility of thermalization in the system. We also notice that results from PYTHIA8 are not in good agreement with ALICE data for heavier particles like $K^{*0}+\overline{K^{*0}}$ and $p+\overline{p}$. Here $\langle n_i\rangle$ has a fractional value in unit GeV^3, this makes the value of $C_V/\langle n_i\rangle$ greater than C_V, as evident from the results displayed in Figs. 4.15 and Fig 4.16.

Fig. 4.17 shows the variation of C_V (scaled by T^3) with $\langle dN_{\rm ch}/d\eta\rangle$ for $\pi^{\pm}$, $K^{\pm}$, $K^{*0}+\overline{K^{*0}}$ and $p+\overline{p}$ extracted from ALICE data and PYTHIA8. It is observed that C_V/T^3 for $\pi^{\pm}$, $K^{\pm}$, $K^{*0}+\overline{K^{*0}}$ increases with multiplicity and display a saturation (within the error bars) when $\langle dN_{\rm ch}/d\eta\rangle > 8$, whereas $p+\overline{p}$ displays an increasing trend with $\langle dN_{\rm ch}/d\eta\rangle$ without any sign of saturation. This may be a hint to the fact that lower mass particles like $\pi^{\pm}$, $K^{\pm}$ behave as weakly interacting thermalized particles beyond certain multiplicity, whereas heavier mass particles may not witness a thermalized medium. Here, also PYTHIA8 results are not in good agreement with ALICE data.

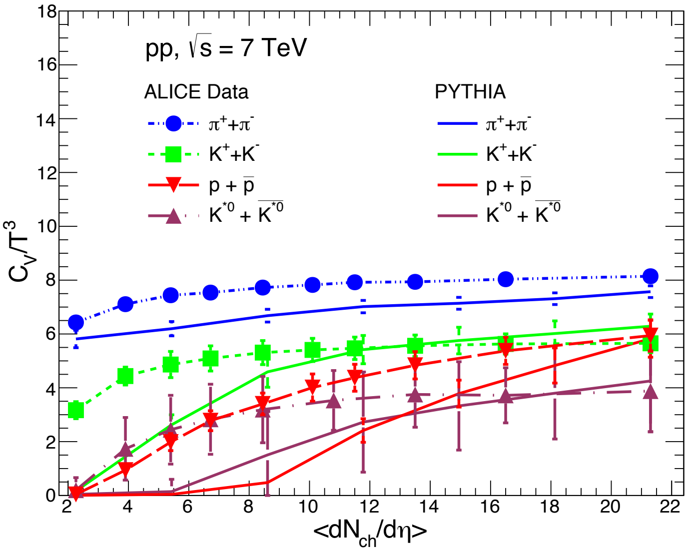

Figure 4.17: (Color online) Same as Fig. 4.15 showing the variation of C_V/T^3 with charged multiplicity [64].

Fluid dynamical equation in non-relativistic limit (Euler equation in the limit of small flow velocity (v) for ideal fluid) can be written as: $(\epsilon+P)\partial\vec{v}/\partial t = -\vec{\nabla}P$, where $(\epsilon + P)$ is the enthalpy density. Comparison of this equation with the non-relativistic classical mechanical equation of a particle moving with velocity v in a potential, ϕ: $md\vec{v}/dt = -\vec{\nabla}\phi$, indicates that enthalpy density plays the role of mass (inertia) in fluid dynamics.

Since enthalpy density, $(\epsilon + P)$, acts as inertia for change in velocity for a fluid cell in thermal equilibrium, we display the change in C_V scaled by enthalpy density as a function of multiplicity in Fig 4.18. The saturations of $C_V/(\epsilon + P)$ and $C_V/\langle n_i\rangle$ in their variations with multiplicity show an interesting trend in which, at the saturation region, corresponding values for all the particle species tend to converge. This means that with the increase in the number of particles the system achieved randomization. This is expected when particles in the system evolves collectively with common interaction environment.

The effects of non-extensive parameter, q on heat capacity has been shown in

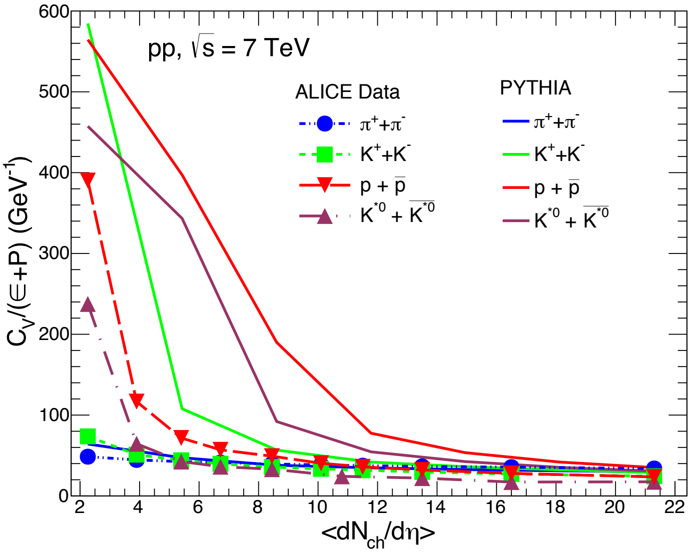

Figure 4.18: (Color online) Same as Fig. 4.15 showing the variation of $C_V/(\epsilon + P)$ with charged multiplicity [64].

Fig 4.19 through the ratio, $c_v/c_{vq\to1}$, where, $c_v = C_V/ < m_i n_i >$, here, $< m_i n_i >$ is the mass density of the hadron i. It may be mentioned that the C_V is obtained here by fitting the TB distribution to the ALICE data, therefore, C_V depends on q. From Fig 4.19, the ratio seems to approach toward saturation for $\langle dN_{\rm ch}/d\eta\rangle > 5$, implying that new environment of interaction is set-off after $\langle dN_{\rm ch}/d\eta\rangle \approx (4-6)$, however, the ratio does not approach unity except for $K^{\pm}$. This indicates that the system has not achieved the state to be described by BG statistics.

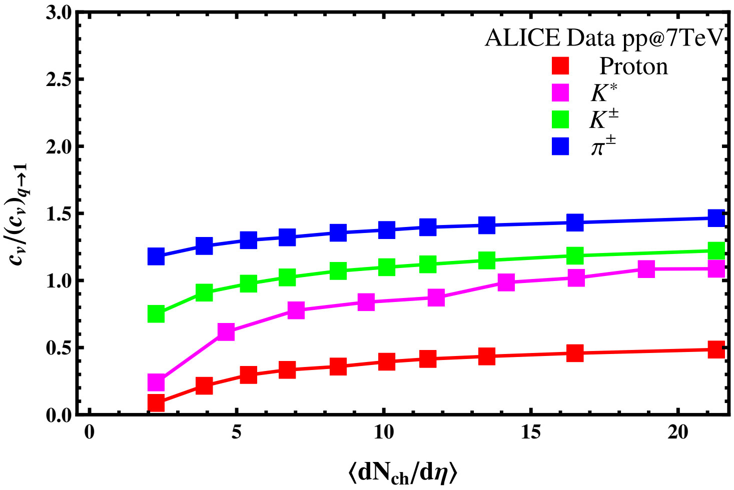

Figure 4.19: (Color online) Heat capacity scaled by the mass density is plotted as a function of charged-particle multiplicity (see text). The errors are within the marker size [64].

4.2.3.2 Multiplicity dependence of CSBM, speed of sound and mean transverse momentum

The speed of sound is a useful quantity which helps in characterizing the nature of interaction in a system e.g., whether it is strongly interacting or not, or how much it differs from ideal gas of massless particles. Interaction can cause change in the effective mass of constituents, thereby, changing the speed of sound in the medium. CSBM gives the measure of deviation from masslessness of the constituents (particle mass and temperature dependence of CSBM for weakly interacting system is discussed in [115]). For massless particles, $c_s^2 = 1/3$, however for massive particles, $c_s^2 < 1/3$. This is due to the fact that the massive particles do not contribute to the change in pressure as much as they contribute to the change in energy of the system. Variation of these quantities with multiplicity is expected to capture the change in effective interaction among constituents with increase in number of constituents. Also the variation of $\langle p_T \rangle$ of a system with the number of constituents can capture the onset of thermalization in the system.

Variation of CSBM, c_s^2 and $\langle p_T \rangle$ with multiplicity for pp collisions have been estimated with the help of Eqs. 4.46, 4.47, 4.49 respectively.

It may be noted here that $(\epsilon - 3P)$ is zero for massless ideal gas, therefore, its non-zero value is a measure of interaction in the system. Fig. 4.20 shows variation of CSBM $[\sim (\epsilon - 3P)/T^4]$ of $\pi^{\pm}$, $K^{\pm}$, $K^{*0} + \overline{K^{*0}}$ and $p + \overline{p}$ with $\langle dN_{\rm ch}/d\eta \rangle$. It is observed that the CSBM for pions slowly reduces and as multiplicity increases while for kaons and K^* it shows almost remains constant for $\langle dN_{\rm ch}/d\eta \rangle > 5$ (within error bars). CSBM displays an increasing behavior with $\langle dN_{\rm ch}/d\eta \rangle > 5$. In comparison with PYTHIA8 generated results, we observed that $\pi^{\pm}$ and $K^{\pm}$ trend underestimates the ALICE data while to some extent PYTHIA8 explains $K^{*0} + \overline{K^{*0}}$ and $p + \overline{p}$. It is expected that for a thermalized medium, the contribution of a hadron of particular species to CSBM peaks when the temperature of the system is half of its mass [115]. The value of T obtained from the present analysis is less than 190 MeV [114]. Therefore, for pions the peak in CSBM can be achieved for $T \geq m_{\pi}/2$. However, all other hadrons can not achieve the peak in CSBM as they are heavy and $T < m_H/2$, where m_H is mass of the hadrons heavier than pion. The larger values of CSBM indicates significant amount of interactions among hadrons or pressure is low in the non-relativistic limit.

Fig. 4.21 shows the variation of c_s^2 (Eq. 4.47) of $\pi^{\pm}$, $K^{\pm}$, $K^{*0} + \overline{K^{*0}}$ and $p + \overline{p}$ as a function of $\langle dN_{\rm ch}/d\eta \rangle$. It is observed that as we move from low to high-multiplicity of ALICE data, the c_s^2 for $\pi^{\pm}$ almost remains constant, while c_s^2 for $K^{\pm}$ increases upto $\langle dN_{\rm ch}/d\eta \rangle \approx 4$ and then saturates. c_s^2 for $K^{*0} + \overline{K^{*0}}$ and $p + \overline{p}$ increase with multiplicity. It is also observed that PYTHIA8 overestimates the ALICE data. As expected, low mass particles will have higher c_s^2 than heavier mass particles. The saturated value of c_s^2 beyond $\langle dN_{\rm ch}/d\eta \rangle \approx 6$ follows the mass ordering. The results obtained from PYTHIA8 data, however, is less than the values obtained from experimental data.

Fig. 4.22 shows $\langle p_T \rangle$ of $\pi^{\pm}$, $K^{\pm}$, $K^{*0} + \overline{K^{*0}}$ and $p + \overline{p}$ as a function of $\langle dN_{\rm ch}/d\eta \rangle$ for ALICE data and PYTHIA8 generated results estimated using Eq. 4.49 with

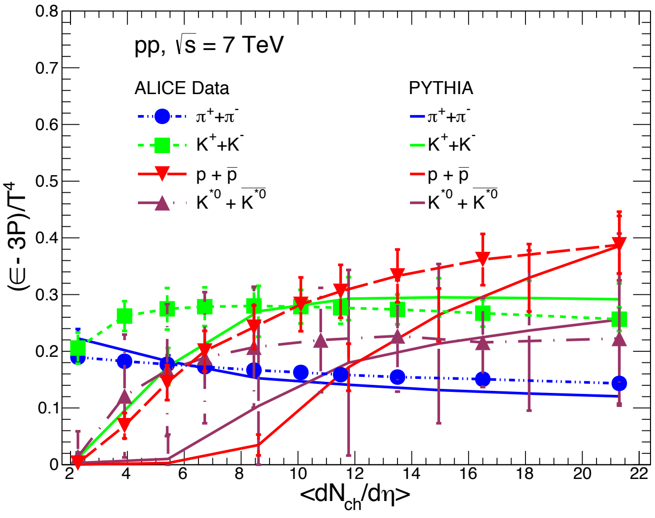

Figure 4.20: (Color online) Variation of CSBM with $\langle dN_{\mathrm{ch}}/d\eta\rangle$ is shown. Dashed (solid) lines represent results obtained by using ALICE data (PYTHIA8 simulation) for pp collisions at $\sqrt{s} = 7$ TeV [64].

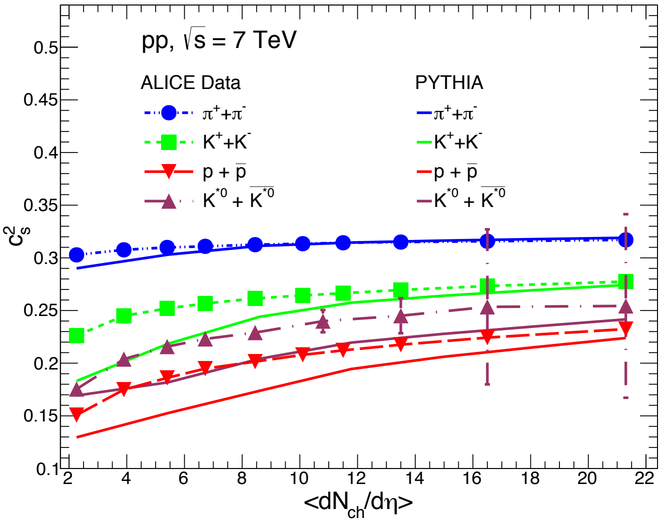

Figure 4.21: (Color online) Same as Fig. 4.20 for speed of sound [64].

lower limit of integration varying from 0.17 to 0.22 GeV/c to reproduce the $\langle p_T\rangle$ reported in Ref. [78] (this limit on integration is now used for all other calculations for $\langle p_T\rangle$, which have no apparent effect on other observables considered here). It is observed that $\langle p_T \rangle$ of all hadrons increase very slowly as multiplicity increases. The higher are the mass of hadrons, the higher are the values of $\langle p_T \rangle$. This may be indicative of the presence of collectivity in the system through transverse flow as higher mass hadrons get affected by the flow more ($p_T \sim m v_T$ where m is the mass of the hadrons and v_T is the transverse flow velocity).

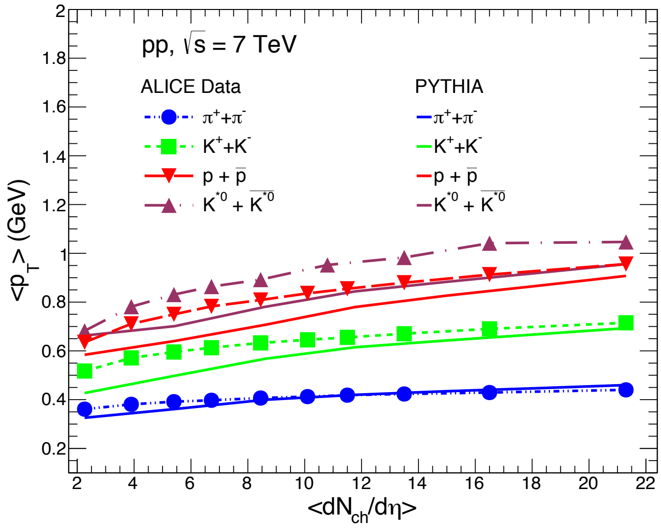

Figure 4.22: (Color online) Mean transverse momentum in GeV is presented as a function of charged-particle multiplicity. Dashed (solid) lines are obtained by using ALICE data (PYTHIA8 simulation) [64].

It is interesting to find that all of the above quantities for lighter hadrons show saturation for $\langle dN_{\text{ch}}/d\eta \rangle \geq$ (4-6) in their variation with $\langle dN_{\text{ch}}/d\eta \rangle$. This general feature may be the hint of onset of their possible randomized collective nature. This is more prominent in the variation of speed of sound and CSBM with multiplicity, where heavier hadrons show different trends from that of lighter hadrons. Moreover, the saturation found here is vastly different from the saturation of $\langle p_T \rangle$ of all charged particles which occurs at $\langle dN_{\text{ch}}/d\eta \rangle \approx 20$ as in Ref. [94]. This may be due to the inclusion of heavier particles in calculation of $\langle p_T \rangle$. In fact, in this work, it is found that heavier particles like proton shows different nature; for them instead of saturation, quantities considered here increases monotonically. It is also interesting to note that heavier hadrons are described well by PYTHIA8. It further emboldens the possibility of formation of strongly correlated but randomized medium, as this can not be explained by color reconnection (CR) effect of final state which is included in PYTHIA8. This mismatch points out something more than CR effect is responsible for such saturation, hinting scope of presence of collectivity in the system from which these particles originate.

4.2.3.3 Finite system size dependence of heat capacity

In case of RHICE, the thermal nature of produced particles is extensive type (BG), but for pp collisions, Tsallis (TB) distribution fits the particle spectra very well [116, 117]. The appearance of non-extensive statistics in a system may be for several reasons e.g., finite size effect, long-range interaction or correlation. For this reason, in this work, it is investigated whether finite size effect alone can explain the deviation of the value of q from unity. We incorporate the finite-size effect by considering a lower momentum cutoff, $p_{min} = \pi/R$, in the momentum integration, where, R is the radius of the system [118]. As the collision energy is the same, large multiplicity events are expected to be originating from larger overlap region in pp collisions. We have considered different radius (R) with each multiplicity following the relation $\mathrm{R} \sim \langle dN_{\mathrm{ch}}/d\eta\rangle^{1/3}$ [119–121]. The R dependence of C_V, CSBM, c_s and $\langle p_T\rangle$ have been extracted by fitting data from pp collision at $\sqrt{s}$ = 7 TeV to TB distribution with T and q as fitting parameters. The data sets have also been studied by using BG statistics (in the limit $q \to 1$) with the same value of T obtained from TB statistics, to check whether extensive TB distribution with finite size effect can account for the q-value extracted by fitting experimental data.

In order to account for the effects of system size, we have studied variation of heat capacity, heat capacity scaled by average number of particles and T^3 with finite system size using Eq. 4.45. We find the lower limit of R as 1.3 fm and the upper limit to be 2.7 fm. This is used to represent the available multiplicity classes such that the values with $q \neq 1$ same as that of earlier plots showing variation with multiplicity. Finite system size is also reflected through the value of $q > 1$ in contrast to $q \to 1$.

Fig. 4.23 shows C_V of $\pi^{\pm}$, $K^{\pm}$, $K^{*0} + \overline{K^{*0}}$ and $p+\overline{p}$ obtained by using ALICE data as a function of system size. It is observed that the C_V of $\pi^{\pm}$, $K^{\pm}$ and $p+\overline{p}$ increases with system size for $q \neq 1$. The slope of C_V for $\pi^{\pm}$ is less compared to $K^{\pm}$ and $p+\overline{p}$. Results with $q \to 1$ (corresponding to BG statistics) represented by solid curves indicate that C_V of $K^{\pm}$, $p+\overline{p}$ are underestimated by PYTHIA8 unlike $\pi^{\pm}$.

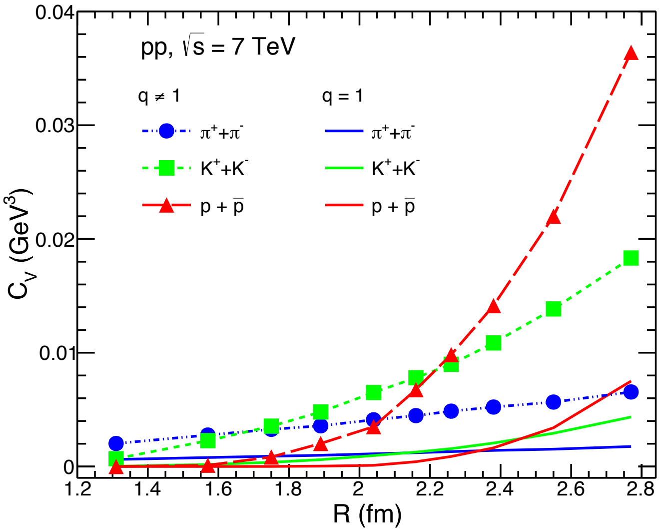

Figure 4.23: (Color online) Heat capacity obtained by using BG and TB distribution as a function of system size. Dashed (solid) lines represent results for $q \neq 1$ ($q = 1$)for pp collisions at $\sqrt{s} = 7$ TeV [64].

Fig. 4.24 shows C_V scaled by T^3 for $\pi^{\pm}$, $K^{\pm}$, $K^{*0} + \overline{K^{*0}}$ and $p+\overline{p}$ extracted from ALICE data as a function of system size. It is observed that C_V/T^3 for $\pi^{\pm}$, $K^{\pm}$, $K^{*0} + \overline{K^{*0}}$ and $p+\overline{p}$ vary slowly with increasing system size for both with

TB and BG statistics (except for $p+\overline{p}$).

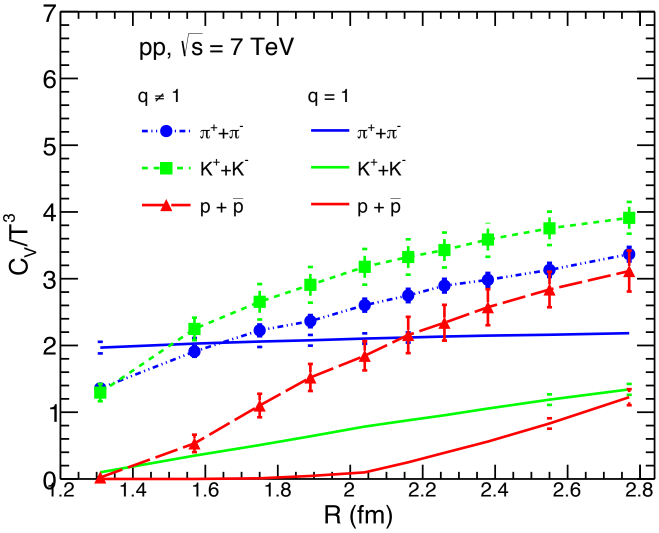

Figure 4.24: (Color online) Heat capacity obtained by using BG and TB distribution as a function of system size. Dashed (solid) lines represent results for $q \neq 1$ $(q=1)$for pp collisions at $\sqrt{s} = 7$ TeV [64].

4.2.3.4 Finite system size dependence of CSBM and speed of sound

Fig. 4.25 shows CSBM of $\pi^{\pm}$, $K^{\pm}$ and $p+\overline{p}$ obtained from ALICE data as a function of system size. Results with $q \neq 1$ represented by dashed lines, it is observed that CSBM of $\pi^{\pm}$ decreases slowly while CSBM of $K^{\pm}$ increases slightly at small R. But $p+\overline{p}$ displays an increasing trend. Results for BG statistics represented by solid curves show similar trend. It may be noted that the heavier hadrons contribute more to the energy density than pressure through their rest mass energy, therefore for proton $(\epsilon - 3P)$ will be more than pions.

Fig. 4.26 shows c_s^2 for $\pi^{\pm}$, $K^{\pm}$, $K^{*0}+\overline{K^{*0}}$ and $p+\overline{p}$ extracted from ALICE data as a function of system size. The c_s^2 shows a plateau as a function of R both for BG and TB statistics for all the hadronic species.

It is generally observed that the incorporation of finite size effect in BG sta-

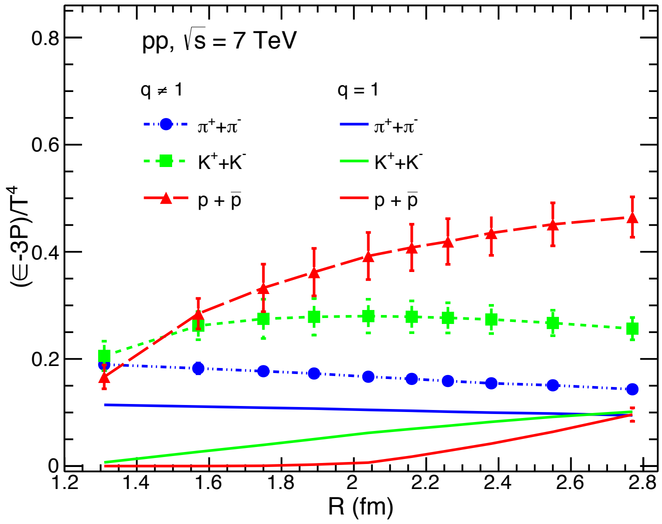

Figure 4.25: (Color online) Same as Fig. 4.23 showing variations of CSBM with system size (R) [64].

tistical approach can not reproduce the value of the observables calculated with non-extensivity parameter (q) extracted from the pp collisions. This may suggest that the appearance of non-extensivity in pp collisions may not be completely explained by finite size effect alone, thereby hinting the presence of other physical effects like long-range correlation that also contributes to the origin of non-extensivity.

4.2.3.5 Energy dependence of C_V, $CSBM$, c_s^2

The collision energy dependence of heat capacity scaled by average number of particles and T^3 obtained from RHICE and ALICE pp data at different $\sqrt{s}$ has been studied by using the values of T and q extracted from the TB distribution fit of the p_T-spectra [122], where $\sqrt{s}$ ranges from 0.0624 TeV to 13 TeV.

Fig. 4.27 shows C_V scaled by the average density of charged pions ($\langle n_\pi \rangle = \langle n_{\pi^+} \rangle + \langle n_{\pi^-} \rangle$) as a function of $\sqrt{s}$. Here, scaling by $\langle n_\pi \rangle$ is considered as production of (π^+ and π^-) is abundant in relativistic collisions. It is observed that

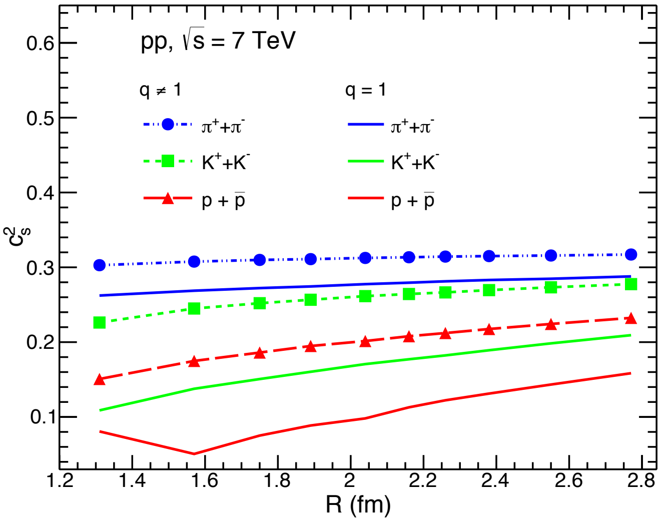

Figure 4.26: (Color online) Same as Fig. 4.23 for c_s^2 [64].

$C_V/\langle n_\pi \rangle$ increases sharply upto $\sqrt{s} = 1.5$ TeV beyond which it increases very slowly. In the same figure we also display the variations of C_V/T^3 and CSBM of charged particles obtained from RHICE and ALICE data as a function of $\sqrt{s}$. Both the quantities tend to saturate (within error bars) for $\sqrt{s} > 2$ TeV. We find that speed of sound seems to be almost constant (Fig. 4.27) for $\sqrt{s} > 2$ GeV. Possibly for pp collisions with $\sqrt{s} \leq 2$ TeV a thermal medium is formed with the value of $c_s^2 \approx 0.24$. Such a value of c_s^2 is obtained in hadronic resonance gas model calculation [115].

The general observation in this regard is that the thermodynamic quantities considered here show a saturation starting for $\sqrt{s} \geq 2$ TeV. The nature of variation of $C_V/\langle n_\pi \rangle$ beyond $\sqrt{s} \approx 2$ TeV is similar to that found in heavy-ion collisions at the chemical-freeze out surface as in Ref. [96]. Therefore, this may be taken as a hint for the formation of medium similar in kind to that of heavy-ion collisions. Indicating that for $\sqrt{s} \geq 2$ TeV sufficient number of particles are produced to form QCD medium. It is interesting to further note that the average multiplicity for $\sqrt{s} \approx 1.5$ lies between 3 to 7 as in Ref. [123]. This again puts weight to the possibility that the saturation effect as observed in variation of above thermodynamic quantities with multiplicity is potentially due to formation of a medium in *pp* collisions for multiplicity, $\langle dN_{\rm ch}/d\eta \rangle \geq 4-6$. We note that for observing saturation effects in PYTHIA8 simulated results (in which CR is thought to be responsible for the saturation), this kind of saturation starts at $\langle dN_{\rm ch}/d\eta \rangle \approx 20$.

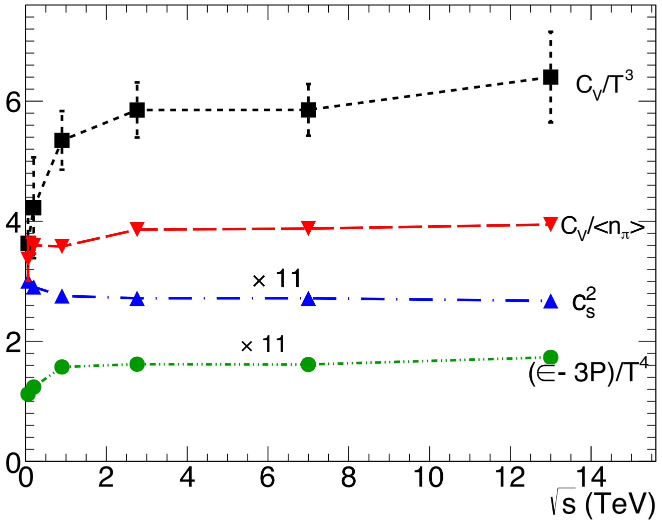

Figure 4.27: (Color online) Variation of heat capacity scaled by T^3 and average charged pion density ($\langle n_\pi \rangle$), speed of sound and CSBM with $\sqrt{s}$ for *pp* collisions [64].

The summary of the important results from this section is given in Section 4.4. Let us now continue with the exploration of thermalised medium formation in a small system using thermodynamical approach but in the light of the event topology and the final state multiplicity in the next section.

4.3 Deciphering QCD dynamics in small collision systems using event shape and final state multiplicity at the Large Hadron Collider

The aim of this work[3] is to study the event shape and multiplicity dependence of specific heat capacity, conformal symmetry breaking measure and speed of sound in *pp* collisions. The non-availability of event topology dependent experimental data for *pp* collisions at $\sqrt{s} = 13$ TeV on the spectra of non-strange and strange hadrons constrains us to use the PYTHIA8 simulated numbers to extract temperature-like parameters.

4.3.1 Formalism

In this work, we have followed the similar formalism as mentioned in section 4.2. In brief, we have used thermodynamically consistent Tsallis distribution function [107], to extract T and q by fitting Tsallis distribution function to $p_{\rm T}$ spectra of identified particles produced in *pp* collisions at $\sqrt{s} = 13$ TeV. Using Tsallis distribution function, we have obtained the mathematical form for the energy density (ϵ), pressure (P), heat capacity (C_V), conformal symmetry breaking ($\frac{\epsilon - 3P}{T^4}$), squared speed of sound (c_s^2) as shown in Eqs. 4.43, 4.44, 4.45, 4.46 and 4.43.

4.3.2 Event generation and Analysis methodology

For this analysis, PYTHIA8 event generator is used to simulate ultra-relativistic *pp* collisions. It is a blend of many-body physics/theoretical models relevant for hard and soft interactions, initial and final-state parton showers, fragmentation,

---

[3] S. Deb, S. Tripathy, G. Sarwar, R. Sahoo and J. e. Alam, Eur. Phys. J. A **56**, 252 (2020).

multipartonic interactions, color reconnection and decay [109]. We use 8.235 version of PYTHIA [62], which includes multipartonic interaction (MPI). MPI is crucial to explain the underlying events, multiplicity distributions and charmonia production [124–126]. Also, this version includes color reconnection which mimics the flow-like effects in *pp* collisions. It is note worthy that PYTHIA8 does not have inbuilt thermalization. However, as discussed in Ref. [110], the color reconnection (CR) mechanism along with the multipartonic interactions (MPI) in PYTHIA8 produces features those arise from thermalization of a system such as radial flow and mass dependent rise of mean transverse momentum. In the pQCD-based PYTHIA model, a single string connecting two partons follows the movement of the partonic endpoints and this movement gives a common boost to the string fragments, which become the final state hadrons. CR along with MPI enables two partons from independent hard scatterings to reconnect and increase the transverse boost. This microscopic treatment of final state particle production is quite similar to a macroscopic picture via hydrodynamical description of high-energy collisions. Thus, it is apparent to conclude that PYTHIA8 model with MPI and CR, has the ability to mimic the features of thermalization, which is confirmed in the flow-like phenomena in small collision systems [110]. This represents a consistent picture because enhanced MPI leads to thermalization.

We have generated around 250 million *pp* collision events at $\sqrt{s}$ = 13 TeV with Monash 2013 Tune (Tune:14) [127]. We have implemented the inelastic, non-diffractive component of the total cross-section for all soft QCD processes using the switch SoftQCD:all=on and we use MPI based scheme of color reconnection (ColorReconnection:mode(0)). In our analysis, the minimum bias events are those events where no selection on charged-particle multiplicity and spherocity (defined later) is applied. For the generated events, all the hadrons are allowed to decay except the ones used in our study (HadronLevel:Decay = on). Here the event selection criteria is such that only those events were chosen which have at-least 5 tracks (charged particles). The classes based on charged particle multiplicities

(N_{ch}) have been chosen in the acceptance of V0 detector with pseudorapidity range of V0A ($2.8 < \eta < 5.1$) and V0C ($-3.7 < \eta < -1.7$) [128] to match with experimental conditions in ALICE at the LHC. The events generated using these cuts are divided in ten multiplicity (V0M) classes, each class containing 10% of total events, which is tabulated in Table 4.3.

Table 4.3: V0M multiplicity classes and the charged particle multiplicities in each multiplicity class [65].

V0M class	I	II	III	IV	V	VI	VII	VIII	IX	X
N_{ch}	50-140	42-49	36-41	31-35	27-30	23-26	19-22	15-18	10-14	0-9

Transverse spherocity is defined for an unit vector $\hat{n}(n_T, 0)$ which minimizes the following quantity [129, 130]:

$$S_0 = \frac{\pi^2}{4}\left(\frac{\Sigma_i\ |\vec{p}_{T_i} \times \hat{n}|}{\Sigma_i\ p_{T_i}}\right)^2. \tag{4.51}$$

The events whether they are isotropic or jetty in transverse plane are coupled to the extreme limits of spherocity, which varies from 0 to 1. In the spherocity distribution, the events limiting towards unity are isotropic events while towards zero are jetty ones. The isotropic events are the consequence of soft processes while the jetty events are of hard pQCD processes. Schematic pictures of jetty and isotropic events are shown in chapter 3. The spherocity distribution is selected in the pseudorapidity range of $|\eta| < 0.8$ to match the experimental conditions of ALICE at the LHC and all events have minimum constraint of 5 charged particles with $p_{\rm T}> 0.15$ GeV/c [43]. For minimum bias events (0-100% V0M class), we consider the jetty events are those having $0 \leq S_0 < 0.29$ with lowest 20 percent of total events and the isotropic events are those having $0.64 < S_0 \leq 1$ with highest 20 percent of the total events. As shown in our previous work [47], spherocity distribution also depends on event multiplicity. Thus, we have considered different spherocity ranges for jetty and isotropic events in different multiplicity classes, which are shown in Table 4.4.

With the detailed formalism and analysis methodology, we now move to discuss the results in the next subsection.

Table 4.4: Spherocity ranges for jetty and isotropic events for different multiplicity classes [65].

V0M Classes	S_0 **range**	
	Jetty events	**Isotropic events**
0 – 9	0 – 0.20	0.56 – 1
10 – 14	0– 0.22	0.58– 1
15 – 18	0– 0.24	0.60– 1
19 – 22	0– 0.26	0.62– 1
23 – 26	0– 0.28	0.64– 1
27 – 30	0– 0.30	0.66– 1
31 – 35	0– 0.32	0.66– 1
36 – 41	0– 0.34	0.68– 1
42 – 49	0– 0.38	0.70– 1
50 – 140	0– 0.42	0.74– 1

4.3.3 Results and Discussion

In a hydrodynamically expanding scenario, the produced fireball in ultra-relativistic hadronic and nuclear collisions, expands and cools down, resulting in a temperature profile as a function of space-time. The spacetime evolution of hadronic and heavy-ion collisions at the LHC energies could be thought of following such an expansion governed by relativistic hydrodynamics. Different identified particles decouple from different evolution stages of the fireball because of the different interaction cross sections of the hadrons of different masses. Therefore, the freeze-out temperature in hadronic and heavy-ion collisions should be species dependent.

Table 4.5: The extracted Tsallis parameters (T, q) for identified particles in different multiplicity and spherocity classes [65].

Particles			**V0M classes**									
			I	**II**	**III**	**IV**	**V**	**VI**	**VII**	**VIII**	**IX**	**X**
$\pi^+ + \pi^-$	T (GeV)	S_0-int	0.136 ± 0.005	0.133 ± 0.005	0.129 ± 0.005	0.126 ± 0.004	0.122 ± 0.004	0.119 ± 0.004	0.116 ± 0.004	0.113 ± 0.003	0.112 ± 0.003	0.113 ± 0.003
		Jetty	0.092 ± 0.004	0.094 ± 0.004	0.096 ± 0.004	0.096 ± 0.004	0.097 ± 0.004	0.099 ± 0.001	0.100 ± 0.004	0.101 ± 0.004	0.106 ± 0.004	0.112 ± 0.004
		Iso	0.167 ± 0.007	0.166 ± 0.006	0.161 ± 0.006	0.156 ± 0.005	0.153 ± 0.005	0.149 ± 0.004	0.144 ± 0.004	0.141 ± 0.004	0.137 ± 0.003	0.136 ± 0.003
	q	S_0-int	1.153 ± 0.001	1.151 ± 0.003	1.150 ± 0.003	1.150 ± 0.003	1.150 ± 0.003	1.150 ± 0.003	1.150 ± 0.003	1.151 ± 0.003	1.151 ± 0.003	1.150 ± 0.003
		Jetty	1.220 ± 0.004	1.121 ± 0.004	1.1206 ± 0.004	1.202 ± 0.004	1.197 ± 0.004	1.193 ± 0.003	1.189 ± 0.003	1.186 ± 0.003	1.181 ± 0.003	1.174 ± 0.003
		Iso	1.121 ± 0.004	1.113 ± 0.003	1.112 ± 0.003	1.110 ± 0.003	1.107 ± 0.003	1.104 ± 0.003	1.101 ± 0.003	1.097 ± 0.003	1.093 ± 0.003	1.084 ± 0.003
$\mathbf{K^+ + K^-}$	T (GeV)	S_0-int	0.140 ± 0.009	0.132 ± 0.008	0.125 ± 0.008	0.116 ± 0.007	0.108 ± 0.007	0.102 ± 0.007	0.093 ± 0.006	0.088 ± 0.006	0.085 ± 0.006	0.086 ± 0.006
		Jetty	0.054 ± 0.010	0.058 ± 0.009	0.060 ± 0.009	0.0062 ± 0.009	0.061 ± 0.009	0.062 ± 0.008	0.063 ± 0.008	0.067 ± 0.008	0.075 ± 0.008	0.087 ± 0.007
		Iso	0.181 ± 0.009	0.177 ± 0.009	0.170 ± 0.008	0.160 ± 0.007	0.157 ± 0.007	0.150 ± 0.007	0.136 ± 0.006	0.129 ± 0.006	0.125 ± 0.006	0.124 ± 0.005
	q	S_0-int	1.155 ± 0.005	1.155 ± 0.005	1.156 ± 0.004	1.159 ± 0.004	1.161 ± 0.004	1.162 ± 0.004	1.166 ± 0.004	1.167 ± 0.004	1.169 ± 0.004	1.167 ± 0.004
		Jetty	1.244 ± 0.007	1.234 ± 0.007	1.229 ± 0.009	1.223 ± 0.006	1.220 ± 0.006	1.217 ± 0.006	1.213 ± 0.006	1.208 ± 0.005	1.201 ± 0.005	1.192 ± 0.005
		Iso	1.121 ± 0.004	1.114 ± 0.004	1.113 ± 0.004	1.113 ± 0.004	1.108 ± 0.004	1.106 ± 0.004	1.110 ± 0.004	1.107 ± 0.004	1.102 ± 0.004	1.092 ± 0.004
$\mathbf{p + \overline{p}}$	T (GeV)	S_0-int	0.156 ± 0.014	0.139 ± 0.014	0.117 ± 0.013	0.103 ± 0.013	0.083 ± 0.012	0.069 ± 0.012	0.055 ± 0.011	0.038 ± 0.010	0.031 ± 0.012	0.030 ± 0.010
		Jetty	0.021 ± 0.002	0.031 ± 0.002	0.025 ± 0.003	0.030 ± 0.004	0.026 ± 0.002	0.026 ± 0.002	0.028 ± 0.002	0.024 ± 0.005	0.031 ± 0.007	0.045 ± 0.010
		Iso	0.223 ± 0.014	0.207 ± 0.013	0.189 ± 0.013	0.173 ± 0.012	0.159 ± 0.012	0.135 ± 0.011	0.123 ± 0.010	0.110 ± 0.009	0.094 ± 0.009	0.099 ± 0.009
	q	S_0-int	1.132 ± 0.006	1.134 ± 0.006	1.141 ± 0.006	1.144 ± 0.006	1.151 ± 0.006	1.155 ± 0.006	1.159 ± 0.005	1.166 ± 0.005	1.170 ± 0.006	1.170 ± 0.005
		Jetty	1.235 ± 0.002	1.221 ± 0.003	1.218 ± 0.003	1.210 ± 0.003	1.208 ± 0.002	1.205 ± 0.002	1.200 ± 0.002	1.199 ± 0.002	1.194 ± 0.004	1.186 ± 0.005
		Iso	1.089 ± 0.006	1.087 ± 0.005	1.090 ± 0.005	1.090 ± 0.005	1.090 ± 0.005	1.097 ± 0.005	1.096 ± 0.005	1.096 ± 0.005	1.098 ± 0.005	1.084 ± 0.005
$\mathbf{K^{*0} + \overline{K^{*0}}}$	T (GeV)	S_0-int	0.163 ± 0.015	0.143 ± 0.015	0.125 ± 0.014	0.106 ± 0.013	0.092 ± 0.013	0.075 ± 0.012	0.058 ± 0.012	0.040 ± 0.012	0.030 ± 0.004	0.025 ± 0.002
		Jetty	0.087 ± 0.017	0.081 ± 0.015	0.070 ± 0.016	0.057 ± 0.015	0.050 ± 0.015	0.041 ± 0.011	0.031 ± 0.011	0.023 ± 0.003	0.019 ± 0.002	0.019 ± 0.002
		Iso	0.183 ± 0.016	0.165 ± 0.015	0.147 ± 0.014	0.125 ± 0.014	0.114 ± 0.014	0.095 ± 0.013	0.075 ± 0.013	0.062 ± 0.012	0.048 ± 0.012	0.027 ± 0.010
	q	S_0-int	1.144 ± 0.007	1.148 ± 0.007	1.153 ± 0.007	1.160 ± 0.006	1.163 ± 0.006	1.168 ± 0.006	1.175 ± 0.006	1.182 ± 0.006	1.188 ± 0.002	1.192 ± 0.002
		Jetty	1.189 ± 0.009	1.185 ± 0.008	1.187 ± 0.008	1.191 ± 0.008	1.192 ± 0.008	1.194 ± 0.006	1.198 ± 0.006	1.202 ± 0.003	1.205 ± 0.002	1.209 ± 0.00
		Iso	1.134 ± 0.007	1.137 ± 0.007	1.140 ± 0.007	1.148 ± 0.007	1.148 ± 0.007	1.154 ± 0.007	1.161 ± 0.007	1.163 ± 0.007	1.166 ± 0.007	1.175 ± 0.006
$\mathbf{\Lambda^0 + \overline{\Lambda^0}}$	T (GeV)	S_0-int	0.167 ± 0.020	0.143 ± 0.019	0.115 ± 0.019	0.091 ± 0.019	0.072 ± 0.017	0.049 ± 0.016	0.029 ± 0.004	0.021 ± 0.002	0.017 ± 0.001	0.016 ± 0.001
		Jetty	0.053 ± 0.026	0.040 ± 0.002	0.026 ± 0.005	0.027 ± 0.003	0.020 ± 0.002	0.017 ± 0.001	0.017 ± 0.001	0.015 ± 0.001	0.014 ± 0.001	0.016 ± 0.001
		Iso	0.196 ± 0.021	0.167 ± 0.020	0.152 ± 0.020	0.107 ± 0.021	0.097 ± 0.020	0.059 ± 0.019	0.047 ± 0.007	0.041± 0.003	0.036 ± 0.002	0.030 ± 0.002
	q	S_0-int	1.136±0.008	1.139 ±0.008	1.147 ±0.008	1.154 ± 0.008	1.159 ± 0.008	1.167 ±0.007	1.174 ± 0.002	1.176 ± 0.002	1.179 ±0.002	1.180 ±0.002
		Jetty	1.195 ± 0.013	1.194 ± 0.003	1.197 ±0.003	1.192 ± 0.003	1.192 ± 0.002	1.191 ± 0.002	1.189 ± 0.002	1.190 ± 0.002	1.192 ± 0.002	1.193 ± 0.002
		Iso	1.122 ± 0.008	1.128 ± 0.008	1.129 ± 0.008	1.145 ± 0.009	1.144 ± 0.009	1.160 ± 0.009	1.159 ± 0.004	1.157 ± 0.002	1.157 ± 0.002	1.155 ± 0.002

This means hadrons with smaller cross sections will escape the system earlier than hadrons with larger interaction cross sections. Hence, each hadron species will measure different freeze-out temperature of the system analogous to the cosmological scenario, where different particles go out of equilibrium at different times during the evolution of the universe. In this work, we have considered such a scenario and have evaluated various quantities which are analogous to the thermodynamic quantities such as the heat capacity, scaled heat capacity, CSBM and c_s^2 at different decoupling points of final state particles from the produced fireball. However, it is to be noted that this work uses simulated data from PYTHIA8 which lack thermalisation in true sense but mimics its features as explained in section 4.3.2.

In such a scenario, let's now proceed to calculate the heat capacity (defined by Eq. 4.45), heat capacity scaled by number density of hadrons ($< N >$ in GeV^3 obtained by integrating Eq. 4.40 over three momentum) and scaled with T^3 as a function of charged-particle multiplicity and transverse spherocity for pp collisions at $\sqrt{s}$=13 TeV generated using PYTHIA8. The temperature parameter, T and non-extensive parameter, q for different event multiplicity and spherocity classes are extracted by fitting Tsallis distribution function to $p_{\rm T}$ spectra of identified particles, which are tabulated in Table 4.5. It is to be noted that the thermalization represents soft physics, therefore, in the present context, the low $p_{\rm T}$ sector of high multiplicity events (to ensure multiple interactions) will have a greater possibility to achieve thermalization. The parameter extracted from the inverse slope of the $p_{\rm T}$ distributions provided by Tsallis distribution may be realistically treated as the temperature for large multiplicity classes. Thus for example from Table 4.5, the isotropic temperature of Λ^0 particles, T $\approx$ 0.196 GeV obtained for the range $\rm N_{ch}$ = (50-140) with mean value, $\langle \rm N_{ch} \rangle$ = 95 may be sensibly considered as the temperature of the system. However, the value of T $\approx$ 0.03 GeV retrieved from the inverse slope of the $p_{\rm T}$ distribution for the range $\rm N_{ch}$ = (0-9) (with mean value,$\langle \rm N_{ch} \rangle$ = 4.5) can not be treated as a realistic value of the temperature of the system. Because in the latter case ($\langle \mathrm{N_{ch}} \rangle = 4.5$), a sufficient number of interactions may not take place to achieve thermalization as opposed to the former case ($\langle \mathrm{N_{ch}} \rangle = 95$). However, for a systematic study as a function of event multiplicity, we have taken all the multiplicity classes.

The p_{T}-spectra and the reduced-χ^2 for different event types and multiplicity classes are shown explicitly in Ref.[46]. Using the same formalism, we estimate the conformal symmetry breaking measure and squared speed of sound, defined by Eq. 4.46 and 4.47 respectively, for different particles as a function of event multiplicity and spherocity. As the inputs to these equations, the values of T and q are extracted after fitting the p_{T}-spectra from simulated events using Tsallis distribution given by Eq. 4.40. It is evident from Ref. [46] that different particles have different T and q values. Thus, we consider differential freeze-out scenario. Higher mass particles decouple from the system early in time indicating a higher Tsallis temperature parameter. These particles are expected to carry more initial non-equilibrium effects. The q-value for BG distribution of an equilibrated system is unity and the observation of $q > 1$ in high-energy hadronic collisions is an indication of the created system being away from equilibrium. In the present study, we take light flavor identified particles like pions ($\pi^+ + \pi^-$), kaons ($\mathrm{K}^+ + \mathrm{K}^-$), protons ($p + \overline{p}$), which have higher abundances in the system and heavier strange/multi-strange particles like K^{*0} ($\mathrm{K}^{*0} + \overline{\mathrm{K}^{*0}}$), and $\Lambda^0(\Lambda^0 + \overline{\Lambda^0})$, which have relatively smaller production rates .

4.3.3.1 Event shape and multiplicity dependence of heat capacity (C_V)

Heat capacity of a system is the amount of heat energy required to raise the temperature of the system by one unit. It can be measured experimentally by measuring the energy supplied to the system and resultant change in temperature. It gives the measure of how change in temperature changes the entropy of a system ($\Delta S = \int (C_V/T)\ dT$). The change in entropy is a good observable for studying the phase transition. In the context of heavy-ion collisions, it can be connected to the rapidity (y) distribution ($dN/dy \approx dS/dy$). The heat capacity acts as a bridging observable for experimental measurement and theoretical models, where change in entropy can be estimated. The heat capacity represents the ease of randomization for a particular phase of the matter in opposition to strength of correlation. The scaled value, $C_V/\langle N\rangle$ remains constant with temperature for an ideal gas, since the increase of temperature has no effect on change in interaction strength and its range. The heat capacity will change with some macroscopic conditions if that condition causes changes in the strength of correlation and then ease of randomization. So heat capacity is a good observable to understand how correlation and randomization compete over one another. Thus the study of variation of heat capacity with multiplicity in pp collisions gives opportunities to have a better understanding of how the ease of randomization and the strength of correlation change with number of constituents in a QCD system.

As different event shapes have got different underlying physical mechanisms, it is worth making a comprehensive study of some of the important thermodynamic observables as a function of event topology through particle spectra in pp collisions using PYTHIA8. Left panel of Fig. 4.28 shows the C_V of pions, kaons and protons obtained from Eq. 4.45 using PYTHIA8 simulated data as a function of charged-particle multiplicity for different spherocity classes. The lighter mass particles have higher heat capacity, which can be understood from the fact that the production cross-section decreases as a function of particle mass. It is also observed that the trend of C_V for isotropic and spherocity integrated events are similar and they tend to increase as a function of charged-particle multiplicity. At low multiplicity classes, the trend of C_V remain almost similar for different spherocity classes. However, the C_V for jetty events are always less than the isotropic and spherocity integrated events for high multiplicity classes. This behavior goes inline with our general expectation for the following reasons. It is expected that for the isotropic events, the number of produced particles would be higher com-

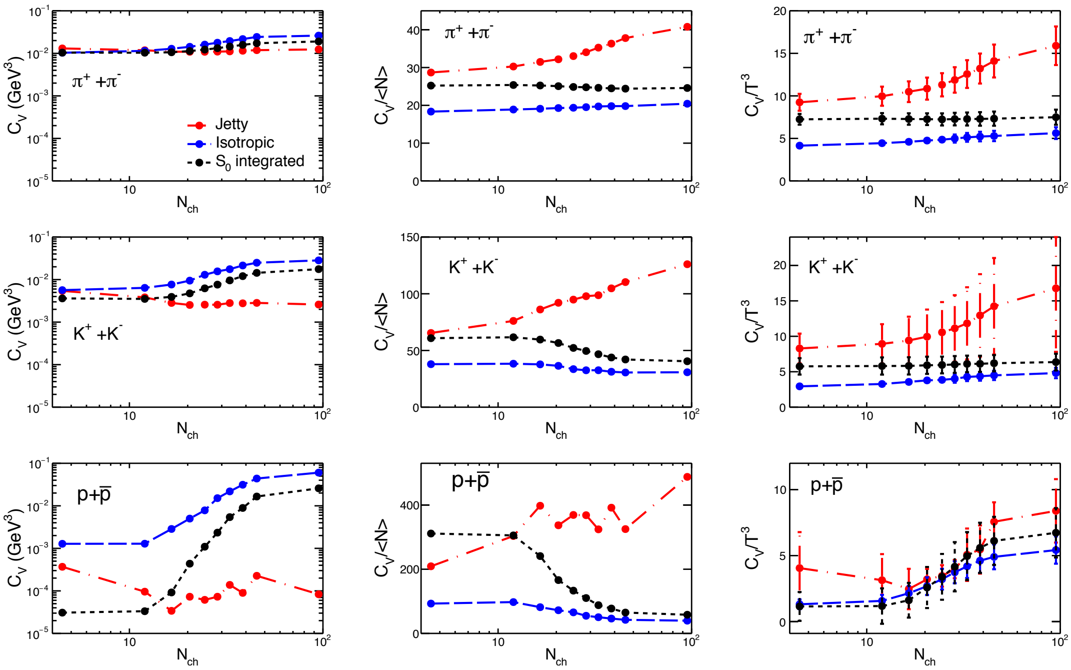

Figure 4.28: (Color Online) Heat Capacity (left), heat capacity scaled by average number of particles (middle) and heat capacity scaled by T^3 of the system (right) obtained using Eq. 4.45 as a function of average charged-particle multiplicity for different event shapes for identified light flavor particles [65].

pared to that of the jetty events. Thus one would need higher energy to increase one unit of temperature in isotropic events compared to that of jetty ones. As heat capacity is a measure of the amount of energy/heat required to increase one unit of temperature of the system, the isotropic events should have higher heat capacity compared to the jetty ones. As the spherocity integrated events are the average of both isotropic and jetty events, the heat capacity remains in between of the isotropic and jetty events. As, the number of particles seems to play important role in heat capacity, it is worthwhile to look at heat capacity scaled with average number of the corresponding particles under study, which is shown in the middle panel of Fig. 4.28. In this case, we observe completely opposite behavior of heat capacity for isotropic and jetty events. This confirms that the number of particles in a system plays a crucial role for the heat capacity. This behavior is supported by the results of final state multiplicity driving the particle production at the LHC energies [131, 132]. However, protons behave differently at low multiplicity classes. The right panel of Fig. 4.28 shows heat capacity scaled with T^3, which makes the quantity dimensionless. The C_V/T^3 increases as a function of charged-particle multiplicity for both isotropic and jetty events but the values for pions and kaons are lower for isotropic compared to jetty events. This suggests that the freeze-out temperature and average number of particles play significant role in the values of heat capacity. However, for protons the C_V/T^3 values seem consistent with each other for different spherocity classes within uncertainties.

Let us now focus on the results from strange particles as it has major significance due to the recent finding of strangeness enhancement in small collision systems like *pp* and p-Pb collisions [12]. Figure 4.29 shows C_V (left), $C_V/<N>$ (middle) and C_V/T^3 (right) of strange particles such as kaons, K^{*0} and Λ^0 obtained from Eq. 4.45 as a function of charged-particle multiplicity for different spherocity classes. We have chosen these particles for our study due to the fact that kaons are the lightest strange mesons, Λ^0 particles are lightest strange baryons and K^{*0} are the strange resonances which go through significant rescattering processes in hadronic phase of the heavy-ion collisions [132, 133]. The behaviors of heat capacity for strange particles are similar to that observed for pions and protons. However, when they are scaled with average number of particles, they show very different behavior compared to pions. The behavior of K^{*0} and Λ^0 are similar to that of protons. It is well known that, for a system with finite flow would follow a mass dependent particle production and the thermodynamic observables would be mass dependent. Keeping this in mind, one can expect the similar behaviors of scaled heat capacity with number of particles or temperature for particles with similar masses. As protons, K^{*0} and Λ^0 have similar masses the behavior of scaled heat capacity seems to be similar for high multiplicity *pp* collisions. As seen in the right panel of Fig. 4.29, the values of

C_V/T^3 for K^{*0} and Λ^0 in different spherocity classes seem to be consistent with each other within uncertainties.

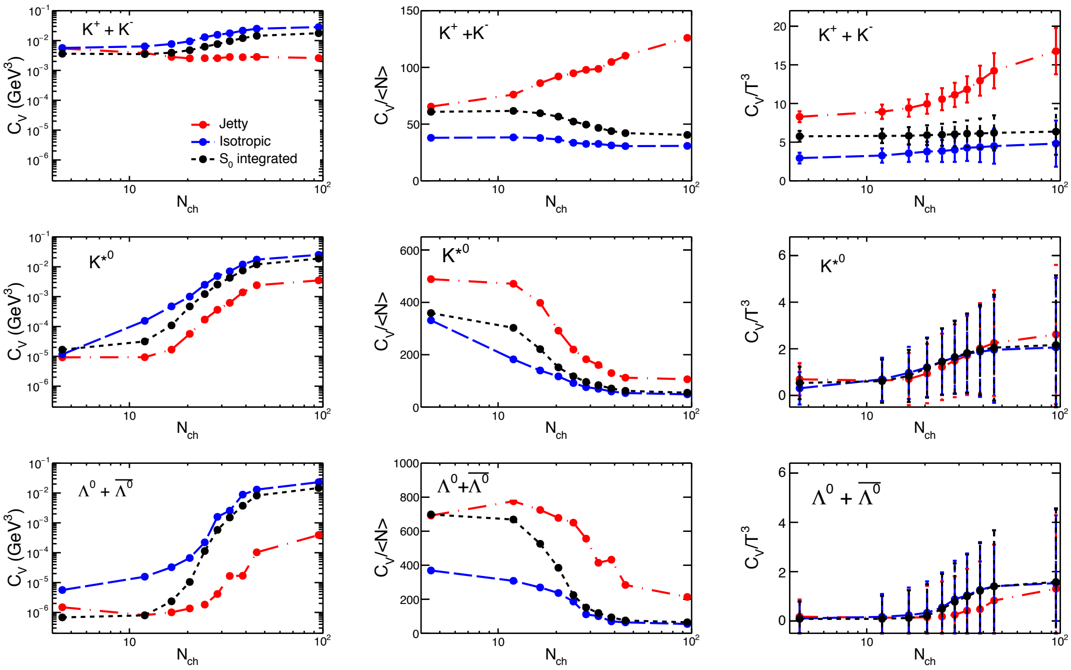

Figure 4.29: (Color Online) Heat Capacity (left), heat capacity scaled by average number of particles (middle) and heat capacity scaled by T^3 of the system (right) obtained using Eq. 4.45 as a function of average charged-particle multiplicity for different event shapes for identified strange particles [65].

The $(\epsilon + p)$, enthalpy density acts as inertia for change in velocity for a fluid cell in thermal equilibrium. For completeness, we have also studied C_V scaled by enthalpy $(\epsilon + p)$, which acts as a proxy to heat capacity i.e, C_V per unit mass. The specific heat for different spherocity classes as a function of multiplicity for identified stable (left panel) and strange particles (right panel) are shown in Fig 4.30. The specific heat seems to have opposite trend to that of heat capacity for all the particles. Also, there is no significant differences of specific heat for different particles as a function of multiplicity and spherocity. It is to be noted here that the behavior of heavier hadrons like proton, K^{*0} and Λ^0 are quite similar except for jetty events in case of proton. These hadrons seem to have S_0 and isotropic events overlap beyond $N_{ch} \simeq$ (20-30). This is expected as heavier hadrons have relatively smaller abundances.

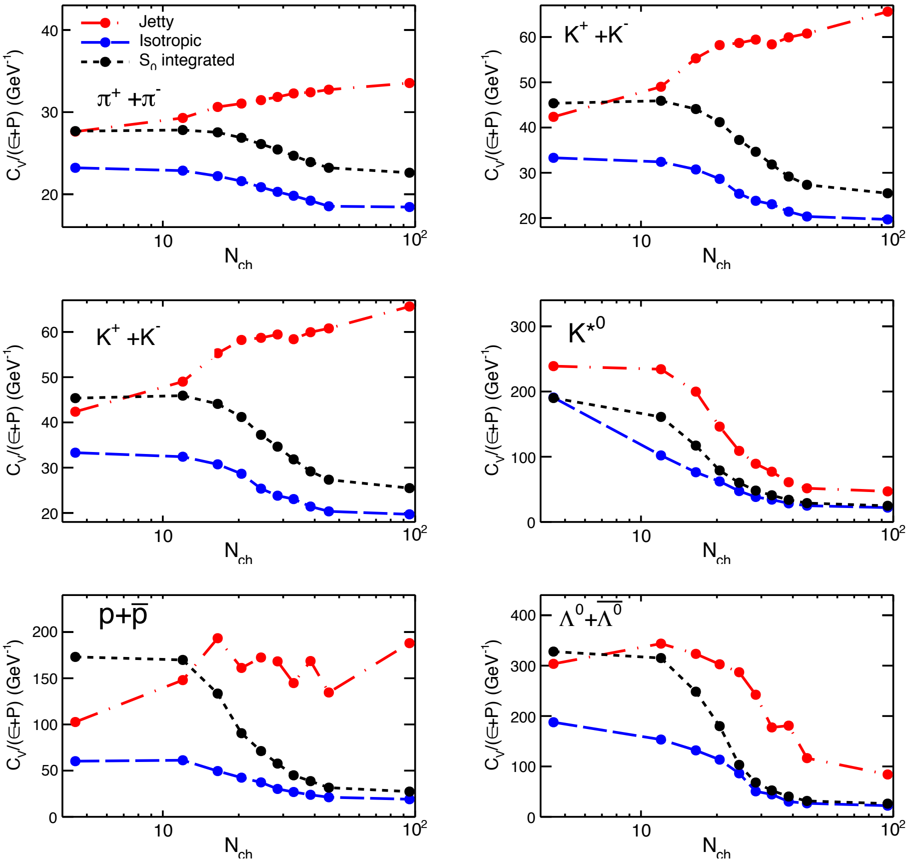

Figure 4.30: (Color Online) Heat capacity scaled by inertial mass of respective light flavor (left) and strange (right) particles as a function of event multiplicity and spherocity [65].

4.3.3.2 Event shape and multiplicity dependence of CSBM, speed of sound

Speed of sound in a system reveals about the strength of interactions of the constituents of a medium. A comparison with the standard massless ideal gas value would give a hint about the system dynamics. The effective mass of the constituents can change in the presence of interaction, which changes the speed of sound in a medium. The measure of deviation from masslessness of the constituents is captured by CSBM (how particle mass and temperature contributes to CSBM for non-interacting (ideal gas) system is discussed in Ref. [64, 115]. For massless particles, $c_s^2 = 1/3$. However for massive particles, it is less than this value. This is because, massive particles do not contribute to the pressure as much as they contribute to the energy of a system. It is expected that the variation of these quantities with event multiplicity will capture the change in effective interaction among the constituents with increase in number of constituents. It becomes important to study these quantities as a function of event topology, as topology is a consequence of the underlying particle production mechanism.

Therefore, we have also studied the conformal symmetry breaking measure (CSBM) and squared speed of sound (c_s^2) as a function of multiplicity and spherocity for identified particles in *pp* collisions, which can be obtained using equations Eq. 4.46, 4.47. Figure 4.31 shows CSBM ($\frac{\epsilon-3P}{T^4}$) of identified stable (left panel) and strange (right panel) particles using T and q obtained from PYTHIA8 as a function of charged-particle multiplicity for different spherocity classes. It is observed that the CSBM increases with increase of mass. For spherocity integrated events, the trace anomaly remains almost flat as a function of multiplicity for pions and kaons while it increases for heavier mass particles like protons, K^{*0} and Λ^0 particles. For pions and kaons the CSBM is higher for jetty events compared to isotropic events throughout all the charged-particle multiplicity classes. However, for other heavier particles CSBM seems to be similar within uncertainties for different spherocity classes in high multiplicity *pp* collisions.

Figure 4.32 shows the squared speed of sound, c_s^2 of identified stable (left panel) and strange (right panel) particles using T and q obtained from PYTHIA8 as a function of charged-particle multiplicity and spherocity. The c_s^2 seems to be mass dependent and decreases with increase in particle mass. Contrary to the other observables, the trend of c_s^2 for different spherocity classes as a function of

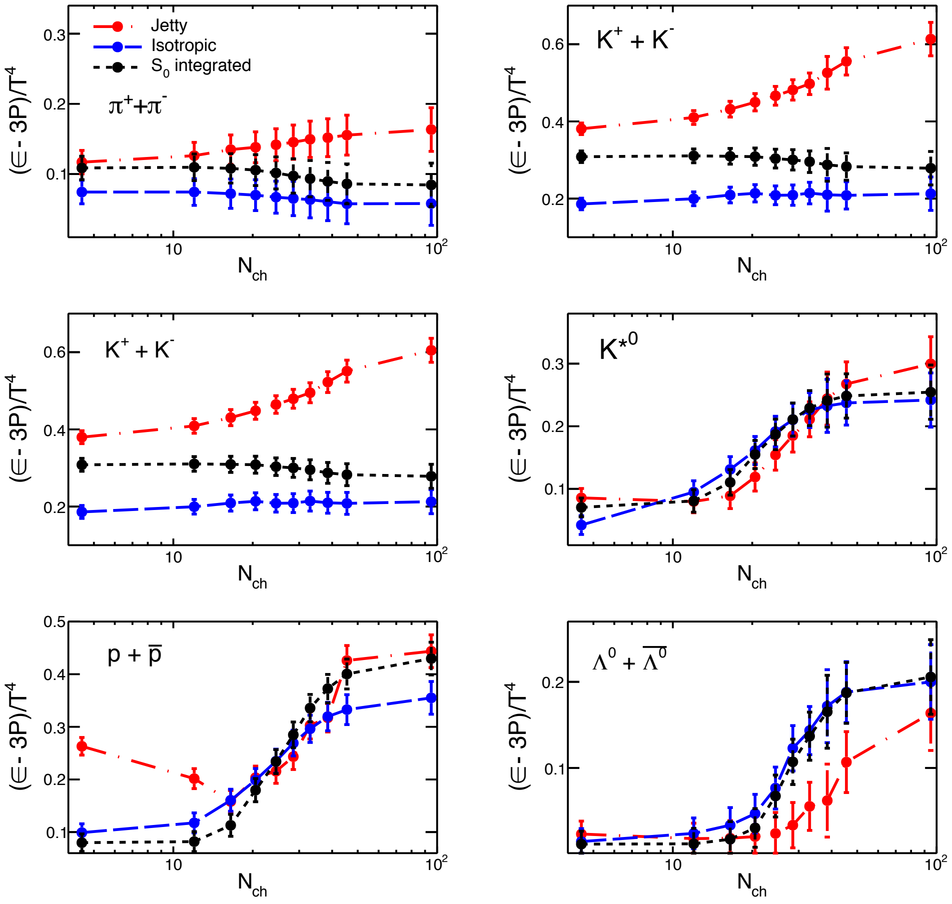

Figure 4.31: (Color Online) CSBM (trace anomaly) for identified light (left) and strange (right) hadrons as a function of event multiplicity and spherocity [65].

multiplicity for all the particles are similar and seems to approach the Stefan-Boltzmann limit of 1/3, asymptotically. This behavior is consistent with our earlier work [64].

For all the above discussed thermodynamic observables, a common feature appears, which is the threshold in final state event multiplicity. The system behavior changes for the value of final state event multiplicity more than $N_{ch} \simeq (10-20)$. This is a confirmatory observation as a threshold final state event multiplicity in high-multiplicity *pp* collisions. This goes inline with many such earlier observations of a threshold in final state event multiplicity after which MPI shows

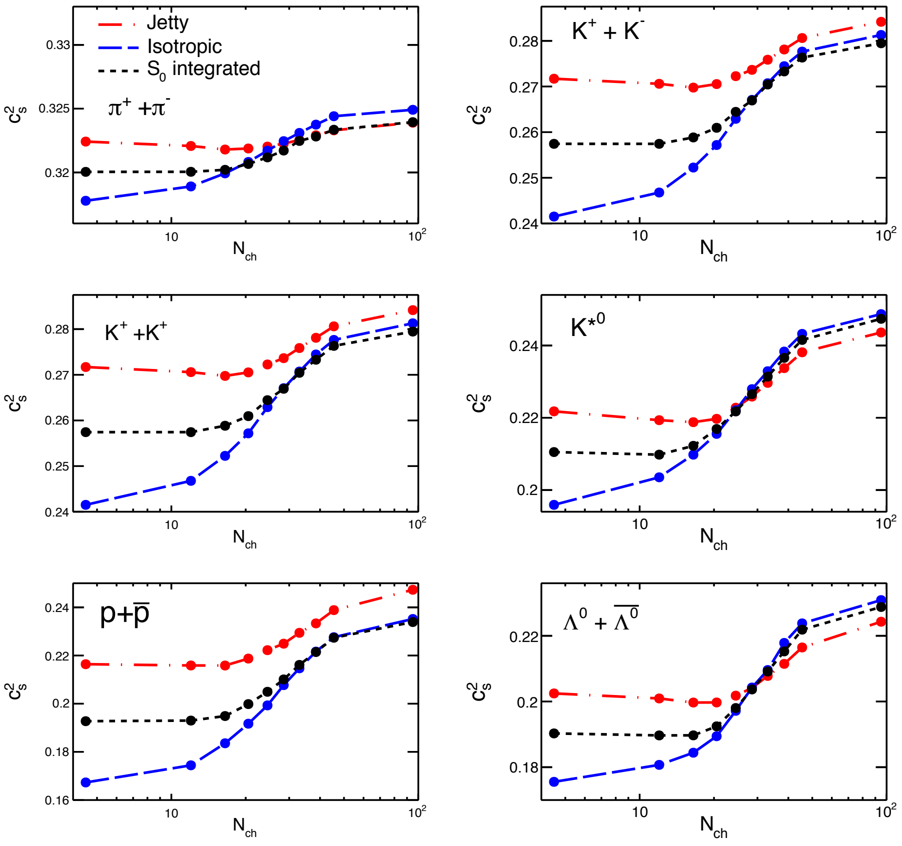

Figure 4.32: (Color Online) Squared speed of sound for identified light (left) and strange (right) hadrons as a function of event multiplicity and spherocity [65].

substantial activity and explains charmonia production [124], thermodynamic limit of all the statistical ensembles showing similar freeze-out properties [134] and the saturation of non-extensive thermodynamical parameters [135]. Further it should be noted here, that as an emerging area of final state multiplicity driving the multiparticle production processes in hadronic and nuclear collisions at the LHC energies, although systematic study taking the final state multiplicity becomes evident, so far the thermodynamics of the system is concerned, the physical interpretation of observables for smaller number density should be taken with caution. We believe, the present work along with many others in the direction of event topology dependent studies at the LHC energies are a way forward in understanding the heavy-ion-like features in high-multiplicity *pp* collisions and a possible formation of QGP-droplets [136, 137]. These aspects should have an experimental exploration, once the corresponding data become available. This study, thus paves a way to understand the high-multiplicity *pp* collisions at the LHC energies.

With the above findings, we finally summarize all the important results in the next section.

4.4 Summary

Section 4.1: In this work, we have investigated predictions of the Glauber model for the initial condition for *pp* collisions, which considers an anisotropic and inhomogeneous proton density profile. The results have been contrasted with experimental data. This model for the density profile is inspired by the structure function obtained from deep inelastic scattering. Instead of distributing the positions of valence quarks randomly by keeping the center of mass intact, we have taken random orientations generated by random rotation around three spatial axes, where the center of three quarks form a plane and connecting gluon tubes always remain fixed in length. This prevents the overlap of two valence quarks in space and possible placement of a quark out of the proton radius, where these two can happen for the first kind of randomization with only the center of mass being fixed [18], and the condition that may bring extra complications in the randomization process for not allowing it, generating "spooky" correlations. However, the present approach, apart from avoiding such complications, will give better handle for future investigations.

With all these considerations, we have studied multiplicity distribution, to obtain the impact parameter to multiplicity relation, multiplicity dependence of initial eccentricity, and azimuthal flow harmonics (v_2). It is found that this model can well reproduce multiplicity distribution produced in *pp* events at ALICE, with the free parameter $f = 0.85$. With properly constraining our model with experimental data and calibrating the range of b with the multiplicity percentile, we have used the estimated $\langle N_{\text{part}} \rangle$ to obtain a nuclear modificationlike factor (R_{HL}) for pp collisions. It is found that the defined factor < 1 for $p_T < 1$ GeV, and beyond this, the factor > 1. Moreover, it tends to reduce at very high p_T, and for $p_T > 1$ GeV, the value of the factor is higher for higher multiplicities. We have also studied R_{HL} for identified particles for pp collisions at $\sqrt{s} = 7$ TeV and found that the trend for R_{HL} is similar to that observed in the p-Pb system but with an increased value. This behavior at higher p_T may be due to noncollective flow effects, which needs further investigation.

The nonavailability of results from experiments which shows the variation of eccentricity and v_2 with multiplicity at $\sqrt{s} = 7$ TeV prevents us from comparing our estimation with experimental data at $\sqrt{s} = 7$ TeV. However, we have compared our result of v_2 with that of pp collisions at $\sqrt{s} = 13$ TeV, as it is observed that the collision energy dependence of v_2 is weak. We found that the result of v_2 obtained from the present approach is in agreement with the result obtained in IP-Glasma model in lower multiplicity region. Also, it is found that the values of v_2 obtained from present model for $N_{\text{ch}} \gtrsim 8$ are very close to that of the experimental data for $\sqrt{s} = 13$ TeV.

The elliptic flow, v_2 measured through the anisotropic momentum distribution of the produced particle is generated by the hydrodynamic pressure gradient resulted from the spatial anisotropy of the system formed initially. Therefore, v_2 can be used to characterize the evolving medium, and to do that, any momentum dependence resulting from other sources has to be subtracted out. The initial conditions required to solve the hydrodynamic equations are quantities that depend on the spatial coordinate but are momentum independent. Therefore, the initial condition obtained in the present study will be relevant for studying the evolving matter formed in pp collisions. The momentum dependent initial condition obtained in the IP-Glasma model (e.g. the work reported in Ref. [138]) can also be useful to study hydrodynamic evolution when the momentum dependence is integrated out.

Section 4.2: We have used Tsallis Boltzmann distribution function to exact temperature (T) and non-extensive parameter (q) in order to calculate specific heat capacity, conformal symmetry breaking measure, speed of sound as a function of multiplicity, system size and collisions energies. The main findings of the work based on the analysis of experimental data from *pp* collision at LHC energies may be summarized as follows:

- We have analyzed how a system produced in *pp* collision at relativistic energies evolves into a collective medium as the the number of produced particles and collision energy increases. For the purpose of this analysis, the thermodynamic quantities like C_V, c_s and CSBM have been chosen for reasons explained in the text. We observe that C_V achieves a plateau for $\langle dN_{\rm ch}/d\eta\rangle > (4-6)$. We also note that $C_V/\langle n_i\rangle$ for pionic and kaonic matter have similar values.

- We have also investigated how conformal symmetry breaking/trace anomaly varies with the degrees of freedom in an environment of QCD many body system. Similar to C_V, a saturation in CSBM with $\langle dN_{\rm ch}/d\eta\rangle$ and $\sqrt{s} \geq 2$ TeV is also observed.

- The importance of high-multiplicity ($\langle dN_{\rm ch}/d\eta\rangle > (4-6)$) for medium formation in small systems is further endorsed by the observation of similar kind of saturating behavior of the thermodynamic quantities considered here with collision energies. This suggests that at collision energies, $\sqrt{s} \geq$ 2 TeV, the sea quarks and gluons within the proton are large enough to produce QCD medium.

- Comparisons of the results extracted from ALICE data with the results obtained from PYTHIA8 simulation have been carried out. It is observed that PYTHIA8 (devoid of medium) explains scaled C_V for heavy particles approximately but it cannot explain the trend of lighter hadrons. This may be a sign that lower mass particles originate from a thermalized medium.

- The deviation in the value of q from unity in TB statistics may indicate the presence of long-range correlations as well as the finiteness of the system. However, it is observed that finite size effect alone cannot account for the appearance of $q \neq 1$ value. This may suggest that the presence of effects other than finiteness *e.g.*, correlations, in QCD system play important role for giving rise to non-extensivity.

Section 4.3: In this work, we have made an attempt to study event topology and event multiplicity dependence of some of the important thermodynamics variables in pp collisions at $\sqrt{s} = 13$ TeV in view of the heavy-ion-like features observed in high-multiplicity events. In the absence of transverse spherocity analysis in experimental data, we have used pQCD inspired PYTHIA8 event generator to simulate pp collisions at $\sqrt{s} = 13$ TeV. As the production dynamics of hard QCD and soft processes contribute differently to the event structures, we have used transverse spherocity as an event topology analysis tool to separate jetty and isotropic events, and then study some of the important thermodynamic observables. It is quite evident from the above observations that the results for spherocity integrated events fall in between of isotropic and jetty events. This suggests that the spherocity plays a significant role of separating events based on their geometrical shapes. This also indicates that studying all the events without looking at the geometrical shape of the events might not contain the entire information about the possible flow-like medium and/or jets. Also, one can notice from all the results that there is a threshold number of charged particles after which the behavior of the observables changes significantly in isotropic, jetty and spherocity integrated events. This threshold is found to be $\mathrm{N_{ch}} \simeq$ (10-20), and becomes an important and confirmatory finding over earlier such observations [124, 139]. In general, in a many particle system the lighter particles predominantly contribute to its thermodynamic properties. In the present context, pions and kaons are lighter as compared to other hadrons considered. Hence these particles govern the thermodynamic behavior of the system with their higher abundances. The variations of thermodynamical quantities considered in present work with $\mathrm{N_{ch}}$ for lighter hadrons like pions and kaons show a plateau which starts at a low value of $\mathrm{N_{ch}}$. We find that a similar plateau-like behavior is also achieved for heavier hadrons, like proton, K^{*0} and Λ^0 for $\langle \mathrm{N_{ch}} \rangle > 40$, indicating a scenario where a thermal bath has been formed with all these hadrons in equilibrium. As heavier hadron are relatively less abundant, it is expected to form a thermal bath for higher $\mathrm{N_{ch}}$ than the lighter hadrons like pions and kaons. We believe such a study based on pQCD inspired PYTHIA8 event generator using event topology and multiplicity becomes important in exploring the production dynamics of high-multiplicity *pp* collisions.

It should be noted here that in PYTHIA8, a partonic medium is not explicitly invoked. Rather, MPI with color reconnection has been successful in describing the collectivity observed in *pp* collisions at the LHC energies. The present observation of a threshold in the particle multiplicity indicating a dynamical behavior in particle production and the thermodynamics of the produced system is a consequence of MPI with color reconnection.

Bibliography

[1] S. A. Bass, M. Gyulassy, H. Stoecker and W. Greiner, J. Phys. G **25**, R1 (1999).

[2] Y. Aoki, G. Endrodi, Z. Fodor, S. D. Katz and K. K. Szabo, Nature **443**, 675 (2006).

[3] M. Krzewicki (ALICE Collaboration), J. Phys. G **38**, 124047 (2011).

[4] K. Aamodt *et al.* (ALICE Collaboration), Phys. Rev. Lett. **106**, 032301 (2011).

[5] T. Hirano, P. Huovinen and Y. Nara, Phys. Rev. C **84**, 011901 (2011).

[6] I. Arsene *et al.* (BRAHMS Collaboration), Nucl. Phys. A **757**, 1 (2005).

[7] B. B. Back *et al.*, Nucl. Phys. A **757**, 28 (2005).

[8] J. Adams *et al.* (STAR Collaboration), Nucl. Phys. A **757**, 102 (2005).

[9] E. V. Shuryak, Nucl. Phys. A **750**, 64 (2005).

[10] M. Gyulassy and L. McLerran, Nucl. Phys. A **750**, 30 (2005).

[11] B. Muller and J. L. Nagle, Ann. Rev. Nucl. Part. Sci. **56**, 93 (2006).

[12] J. Adam *et al.* (ALICE Collaboration), Nature Phys. **13**, 535 (2017).

[13] B. Alver *et al.* (PHOBOS Collaboration), Phys. Rev. C **83**, 024913 (2011).

[14] V. Khachatryan *et al.* (CMS Collaboration), JHEP **1009**, 091 (2010).

[15] V. Khachatryan *et al.* (CMS Collaboration), Phys. Lett. B **765**, 193 (2017).

[16] M. L. Miller, K. Reygers, S. J. Sanders and P. Steinberg, Ann. Rev. Nucl. Part. Sci. **57**, 205 (2007).

[17] J. Adam *et al.* (ALICE Collaboration), Phys. Rev. C **91**, 064905 (2015).

[18] P. Kubiczek and S. D. Glazek, Lith. J. Phys. **55**, 155 (2015).

[19] R. J. Glauber, Phys. Rev. **100**, 242 (1955).

[20] R. J. Glauber, Nucl. Phys. A **774**, 3 (2006).

[21] A. Shor and R. S. Longacre, Phys. Lett. B **218**, 100 (1989).

[22] B. Schenke, P. Tribedy and R. Venugopalan, Phys. Rev. Lett. **108**, 252301 (2012).

[23] C. W. De Jager, H. De Vries and C. De Vries, Atom. Data Nucl. Data Tabl. **14**, 479 (1974); Atom. Data Nucl. Data Tabl. **16**, 580 (1975) [Erratum].

[24] H. De Vries, C. W. De Jager and C. De Vries, Atom. Data Nucl. Data Tabl. **36**, 495 (1987).

[25] R. J. Glauber and G. Matthiae, Nucl. Phys. B **21**, 135 (1970).

[26] X. N. Wang and M. Gyulassy, Phys. Rev. D **44**, 3501 (1991).

[27] B. Alver, M. Baker, C. Loizides and P. Steinberg, arXiv:0805.4411 [nucl-ex].

[28] C. Loizides, J. Nagle and P. Steinberg, SoftwareX **1-2**, 13 (2015).

[29] W. Broniowski, M. Rybczynski and P. Bozek, Comput. Phys. Commun. **180**, 69 (2009).

[30] M. Rybczynski, G. Stefanek, W. Broniowski and P. Bozek, Comput. Phys. Commun. **185**, 1759 (2014).

[31] C. Loizides, Phys. Rev. C **94**, 024914 (2016).

[32] R. Baier, P. Romatschke and U. A. Wiedemann, Phys. Rev. C **73**, 064903 (2006).

[33] B. Alver *et al.* (PHOBOS Collaboration), Phys. Rev. C **81**, 034915 (2010).

[34] T. Isobe (PHENIX Collaboration), nucl-ex/0605016.

[35] M. Mace, V.V. Skokov, P. Tribedy, R. Venugopalan, Phys. Rev. Lett. **121**, 052301 (2018).

[36] M. A. Braun, J. Dias de Deus, A. S. Hirsch, C. Pajares, R. P. Scharenberg and B. K. Srivastava, Phys. Rept. **599**, 1 (2015).

[37] L. D. Landau, Izv. Akad. Nauk. SSSR **17**, 51 (1953).

[38] S. Belenkij and L. D. Landau, Usp. Fiz. Nauk. **56**, 309 (1955).

[39] S. Belenkij and L. D. Landau, Nuovo Cimento Suppl. **3**, 15 (1956),

[40] D. ter Haar (Ed.), Collected papers of L.D. Landau, Gordon & Breach, New York, 1965, p. 665.

[41] L. Van Hove, Phys. Lett. **118B**, 138 (1982).

[42] R. P. Scharenberg, B. K. Srivastava and C. Pajares, Phys. Rev. D **100**, 114040 (2019).

[43] S. Acharya *et al.* (ALICE Collaboration), Eur. Phys. J. C **79**, 857 (2019).

[44] S. Acharya (ALICE Collaboration), PoS HardProbes **2018**, 153 (2019).

[45] A. Ortiz [ALICE, ATLAS, CMS and LHCb Collaborations], PoS LHCP **2019**, 091 (2019).

[46] S. Tripathy, A. Bisht, R. Sahoo, A. Khuntia and M. P. Salvan, Adv. High Energy Phys. **2021**, 8822524 (2021).

[47] A. Khuntia, S. Tripathy, A. Bisht and R. Sahoo, J. Phys. G **48**, 035102 (2021)

[48] R. Rath, A. Khuntia, S. Tripathy and R. Sahoo, MDPI Physics **2**, 679(2020).

[49] G. Wilk and Z. Wlodarczyk, Phys. Rev. Lett. **84**, 2770 (2000).

[50] C. Tsallis, J. Stat. Phys. **52**, 479 (1988).

[51] C. Tsallis, Braz. J. Phys. **29**, 1 (1999).

[52] D. Thakur, S. Tripathy, P. Garg, R. Sahoo and J. Cleymans, Adv. High Energy Phys. **2016**, 4149352 (2016).

[53] P. Sett and P. Shukla, Int. J. Mod. Phys. E **24**, 1550046 (2015).

[54] T. Bhattacharyya, J. Cleymans, A. Khuntia, P. Pareek and R. Sahoo, Eur. Phys. J. A **52**, 30 (2016).

[55] H. Zheng and L. Zhu, Adv. High Energy Phys. **2015**, 180491 (2015).

[56] Z. Tang, Y. Xu, L. Ruan, G. van Buren, F. Wang and Z. Xu, Phys. Rev. C **79**, 051901 (2009).

[57] B. De, Eur. Phys. J. A **50**, 138 (2014).

[58] S. Tripathy, S. K. Tiwari, M. Younus and R. Sahoo, Eur. Phys. J. A **54**, 38 (2018).

[59] S. Tripathy, T. Bhattacharyya, P. Garg, P. Kumar, R. Sahoo and J. Cleymans, Eur. Phys. J. A **52**, 289 (2016).

[60] S. Tripathy, A. Khuntia, S. K. Tiwari and R. Sahoo, Eur. Phys. J. A **53**, 99 (2017).

[61] J. Cleymans and D. Worku, J. Phys. G **39**, 025006 (2012).

[62] Pythia8 online manual:(https://pythia.org/manuals/pythia8245/Welcome.html).

[63] S. Deb, G. Sarwar, D. Thakur, P. Subramani, R. Sahoo and J. e. Alam, Phys. Rev. D **101**, 014004 (2020).

[64] S. Deb, G. Sarwar, R. Sahoo and J. e. Alam, Eur. Phys. J. A **57**, 195 (2021).

[65] S. Deb, S. Tripathy, G. Sarwar, R. Sahoo and J. e. Alam, Eur. Phys. J. A **56**, 252 (2020).

[66] D. d'Enterria, G. K. Eyyubova, V. L. Korotkikh, I. P. Lokhtin, S. V. Petrushanko, L. I. Sarycheva and A. M. Snigirev, Eur. Phys. J. C **66**, 173 (2010).

[67] J. D. Bjorken, S. J. Brodsky and A. Scharff Goldhaber, Phys. Lett. B **726**, 344 (2013).

[68] S. D. Glazek, Few Body Syst. **52**, 367 (2012).

[69] B. L. Combridge, J. Kripfganz and J. Ranft, Phys. Lett. **70B**, 234 (1977).

[70] H. J. Drescher, A. Dumitru, C. Gombeaud and J. Y. Ollitrault, Phys. Rev. C **76**, 024905 (2007).

[71] S. D. Glazek and P. Kubiczek, Few Body Syst. **57**, 425 (2016).

[72] S. Chatrchyan *et al.* (CMS Collaboration), Phys. Lett. B **722**, 5 (2013).

[73] X. N. Wang and M. Gyulassy, Phys. Rev. Lett. **86**, 3496 (2001).

[74] D. Kharzeev and M. Nardi, Phys. Lett. B **507**, 121 (2001).

[75] G. J. Alner *et al.* (UA5 Collaboration), Phys. Lett. **160B**, 199 (1985).

[76] K. Aamodt *et al.* (ALICE Collaboration), Eur. Phys. J. C **68**, 345 (2010).

[77] B. Abelev *et al.* (ALICE Collaboration), Phys. Rev. C **88**, 044909 (2013).

[78] S. Acharya *et al.* (ALICE Collaboration), Phys. Rev. C **99**, 024906 (2019).

[79] G. Bencedi (ALICE Collaboration), arXiv:1609.05665 [nucl-ex].

[80] V. Khachatryan *et al.* (CMS Collaboration), JHEP **1704**, 039 (2017).

[81] A. Adare *et al.* (PHENIX Collaboration), Phys. Rev. C **88**, 024906 (2013).

[82] V. Khachatryan *et al.* (CMS Collaboration), Phys. Rev. Lett. **115**, 012301 (2015).

[83] M. Arneodo, Phys. Rept. **240**, 301 (1994).

[84] S. A. Voloshin, A. M. Poskanzer and R. Snellings, Landolt-Bornstein **23**, 293 (2010).

[85] K. Gajdošov́(ALICE Collaboration), Nucl. Phys. A **982**, 487 (2019).

[86] G. Aad *et al.* (ATLAS Collaboration), Phys. Rev. Lett. **116**, 172301 (2016).

[87] P. Bozek, Eur. Phys. J. C **71**, 1530 (2011).

[88] A. Bzdak, B. Schenke, P. Tribedy and R. Venugopalan, Phys. Rev. C **87**, 064906 (2013).

[89] M. Mukherjee, S. Basu, A. Chatterjee, S. Chatterjee, S. P. Adhya, S. Thakur and T. K. Nayak, Phys. Lett. B **784**, 1 (2018).

[90] S. Borsanyi et al., JHEP **1011**, 077 (2010).

[91] S. Borsanyi et al., J. Phys: Conf. Series **316**, 012020 (2011).

[92] D. Thakur (ALICE Collaboration), PoS HardProbes 2018, **164** (2019).

[93] D. Adamová et al. (ALICE Collaboration), Phys. Lett. B **776**, 91 (2018).

[94] B. Abelev *et al.* (ALICE Collaboration), Physics Letters B **727** 371 (2013).

[95] J. Adams et al. Nature Physics **13**, 535 (2017).

[96] S. Basu, S. Chatterjee, R. Chatterjee, T. K. Nayak and B. K. Nandi, Phys. Rev. C **94**, 044901 (2016).

[97] X. M. Li, S. Y. Hu, J. Feng, S. P. Li, B. H. Sa and D. M. Zhou, Int. J. Mod. Phys. E **16**, 1906 (2007).

[98] Reif, F., Fundamentals of Statistical and Thermal Physics, Mcgraw-Hill International Editions, Singapore, 1985.

[99] E. W. Kolb and M. S. Turner, The Early Universe, Addison-Wesley Publishing Co., Singapore, 1989.

[100] J. Cleymans, AIP Conf. Proc. **1625**, 31 (2015)

[101] C. Tsallis, J. Statist. Phys. **52**, 479 (1988).

[102] C. Tsallis, Eur. Phys. J. A **40**, 257 (2009).

[103] C. Tsallis, Introduction to Nonextensive Statistical Mechanics (Springer, 2009).

[104] G. Wilk, and Z. Włodarczyk, Phys. Rev. Lett. **84**, 2770 (2000) .

[105] G. Wilk, and Z. Włodarczyk, Phys. Rev. C **79**, 054903 (2009).

[106] G. Wilk, and Z. Włodarczyk, Chaos Solitons Fractals **13**, 581 (2001).

[107] J. Cleymans and D. Worku, Eur. Phys. J. A **48**, 160 (2012).

[108] S. K. Tiwari, S. Tripathy, R. Sahoo and N. Kakati, Eur. Phys. J. C **78**, 938 (2018).

[109] T. Sjostrand, S. Mrenna and P. Z. Skands, JHEP **0605**, 026 (2006).

[110] A. Ortiz Velasquez, P. Christiansen, E. Cuautle Flores, I. Maldonado Cervantes and G. Paić, Phys. Rev. Lett. **111**, 042001 (2013).

[111] R. Corke and T. Sjostrand, JHEP **1103**, 032 (2011).

[112] G. Aad *et al.* (ATLAS Collaboration), New J. Phys. **13**, 053033 (2011).

[113] B. C. Li, Z. Zhang, J. H. Kang, G. X. Zhang and F. H. Liu, Adv. High Energy Phys. **2015**, 741816 (2015).

[114] A. Khuntia, H. Sharma, S. Kumar Tiwari, R. Sahoo and J. Cleymans, Eur. Phys. J. A **55**, 3 (2019).

[115] G. Sarwar, S. Chatterjee and J. Alam, J. Phys. G **44**, 055101 (2017).

[116] L. Marques, J. Cleymans and A. Deppman, Phys. Rev. D **91**, 054025 (2015).

[117] J. Cleymans, EPJ Web Conf. **70**, 00009 (2014).

[118] A. Bhattacharyya, R. Ray, S. Samanta and S. Sur, Phys. Rev. C **91**, 041901 (2015).

[119] K. Aamodt *et al.* (ALICE Collaboration), Phys. Lett. B **696**, 328 (2011).

[120] B. B. Abelev *et al.* (ALICE Collaboration), Phys. Lett. B **739**, 139 (2014).

[121] J. Adam *et al.* (ALICE Collaboration), Eur. Phys. J. C **76**, 245 (2016).

[122] K. Saraswat, P. Shukla and V. Singh, J. Phys. Comm. **2**, 035003 (2018).

[123] A. Alkin, Ukr. J. Phys. **62**, 743 (2017).

[124] D. Thakur, S. De, R. Sahoo and S. Dansana, Phys. Rev. D **97**, 094002 (2018).

[125] S. Deb, D. Thakur, S. De and R. Sahoo, Eur. Phys. J. A **56**, 134 (2020).

[126] A. Khatun, D. Thakur, S. Deb and R. Sahoo, J. Phys. G **47**, 055110 (2020).

[127] P. Skands, S. Carrazza and J. Rojo, Eur. Phys. J. C **74**, 3024 (2014).

[128] B. B. Abelev *et al.* (ALICE Collaboration), Int. J. Mod. Phys. A **29**, 1430044 (2014).

[129] A. Banfi, G. P. Salam and G. Zanderighi, JHEP **1006**, 038 (2010).

[130] E. Cuautle, R. Jimenez, I. Maldonado, A. Ortiz, G. Paic and E. Perez, arXiv:1404.2372 [hep-ph].

[131] S. Tripathy (ALICE Collaboration), Springer Proc. Phys. **261**, 683 (2021).

[132] S. Tripathy (ALICE Collaboration), Nucl. Phys. A **982**, 180 (2019).

[133] D. Sahu, S. Tripathy, G. S. Pradhan and R. Sahoo, Phys. Rev. C **101**, 014902 (2020).

[134] N. Sharma, J. Cleymans, B. Hippolyte and M. Paradza, Phys. Rev. C **99**, 044914 (2019).

[135] R. Rath, A. Khuntia, R. Sahoo and J. Cleymans, J. Phys. G **47**, 055111 (2020).

[136] R. Sahoo, Springer Proc. Phys. **248**, 357 (2020).

[137] R. Sahoo, AAPPS Bull. **29**, 16 (2019).

[138] B. Schenke, C. Shen and P. Tribedy, Phys. Lett. B **803**, 135322 (2020)

[139] R. Campanini and G. Ferri, Phys. Lett. B **703**, 237 (2011).

Chapter 5

Summary

"Learn from yesterday, live for today, hope for tomorrow. The important thing is not to stop questioning."

- Albert Einstein

The research works discussed in this PhD thesis have been carried out at the Indian Institute of Technology (IIT) Indore, India, within the ALICE collaboration at the LHC, CERN, Geneva under the financial supports from ALICE Project No. SR/MF/PS-01/2014-IITI(G) of Department of Science & Technology, Government of India.. This PhD project explores the *pp* collision via experimental data analysis and phenomenological studies to understand the hadronic collision at ultra-relativistic energies.

In this thesis, the first measurements of $\mathrm{K}^{*}(892)^{\pm}$ resonance production at midrapidity in *pp* collisions at $\sqrt{s}$ =13 TeV with ALICE at the LHC as a function of transverse spherocity and charged-particle multiplicity are reported. Variation on $\mathrm{K}^{*}(892)^{\pm}$ production because of different transverse spherocity quantiles is also presented. From the transverse momentum spectra results, we observe $\mathrm{K}^{*\pm}$ are mainly produced in isotropic events in the measured p_{T} interval, but for $p_{\mathrm{T}} >$ 3.5 GeV/c in-jet production increases. It is observed that with the increase in $S_{0}^{p_{\mathrm{T}}=1}$ quantiles, spherocity dependence of $\mathrm{K}^{*\pm}$ production seems to less prominent. To understand the dynamics of particles with different quark content, mass, etc., we have calculated the particle ratio of $K^{*\pm}$ with long-lived stable hadrons, an important observation from these results is that the isotropic/integrated ratio is higher and stays flat, while the jetty/integrated rises with p_{T}, implying an increasing relative contribution of hard processes with increasing p_{T}. These results can shed light on tuning the Monte Carlo (MC) models and helps to explore the QGP-like conditions in high-multiplicity pp collisions.

The production dynamics of heavy-flavored hadrons (governed by hard-QCD processes) and light-flavored hadrons (governed by soft-QCD processes) are different in nature. In contrast with light-flavored hadrons, we have extensively studied transverse spherocity and final-state multiplicity dependence of heavy-flavored hadrons production in pp collisions at $\sqrt{s}$ = 13 TeV using the pQCD inspired PYTHIA8 model. As the recent observations in high-multiplicity pp collisions show heavy-ion-like features, the possible formation of QGP-droplets in such small systems cannot be neglected. The novel observation from heavy-flavored results hints at different production dynamics of open charm compared to charmonia. MPIs with color reconnection mechanism play a significant role in such behaviors in PYTHIA8. And the study of heavy-flavored hadrons p_{T} -spectra is one of the mail tools to disentangle collective effects from trivial correlations.

In high-energy heavy-ion collisions, the interpretation of results relies on the use of a model based on initial matter distribution resulting from the overlap of the two colliding nuclei at a given impact parameter (b). Indeed, for estimating quantities such as the number of binary nucleon-nucleon collisions, N_{coll}(b) used to derive the nuclear modification factor (R_{AA}) from the ratio of AA over pp spectra, the elliptic flow parameters (v_2) normalized by the eccentricity (ϵ_2(b)) of the overlap region, the average surface area, A(b) etc., knowing the nuclear overlap function (T_{AA}(b)) is important. And this overlap function depends on a realistic model of the collision geometry. One such model is the Glauber model for heavy-ion collisions, based on the assumption that the proton is a point particle.

Motivated by the fact that at ultra-relativistic energies, this assumption might not be true, we have formulated a Glauber-like model for *pp* collisions employing spherically symmetric distribution densities for three effective quarks from their respective centers and cylindrically symmetric densities for the gluonic flux tubes about the lines joining two adjacent quarks. In order to check the compatibility of the model, we have compared the charged particle multiplicity distribution obtained from the present work with the ALICE experiment for *pp* collisions at 7 TeV. And our model seems to describe the experimental results very well with a 5% - 10% discrepancy. Having information about N_{coll}(b) from our model, we have estimated nuclear modification-like factor in *pp* collisions considering N_{coll} -scaled high and low multiplicity events. We have also calculated ϵ_2(b) using the current approach. By considering a linear scaling of v_2 with ϵ_2(b), we have obtained v_2 as a function of multiplicity and our results with the available experimental results. We found a very good comparison within the error bars.

With the aim of ascertaining the possibility of the formation of a thermalized medium in *pp* collisions, we have used Tsallis parameters obtained from the fitting of experimental ALICE data in pp collisions at center-of-mass energy $(\sqrt{s}) = 7$ TeV, to calculate the marker of thermalization like heat capacity (C_V), conformal symmetry breaking measure (CSBM) and speed of sound (c_s) of the identified charged particles, with the quantities like multiplicity, system size, and collision energy. We found a threshold in charged particle multiplicity beyond which C_V, CSBM, and c_s^2 attain a plateau. We observe that such threshold in multiplicity also appears in the study of these quantities for $\sqrt{s} \geq 2$ TeV. We further observed that the nature of variation of these thermodynamical quantities is similar to that found in heavy-ion collisions at the chemical-freeze-out surface. This observation shows that there may be a hint for the formation of a medium similar to that of heavy-ion collisions. We have also contrasted the obtained results with PYTHIA8 (assume no QGP formation), and it is found that PYTHIA8 is inadequate to explain the features reflected in these quantities, thereby indicating the possibility of thermalization in such small systems.

In view of the production dynamics dependence of event topology, we have used a thermodynamically consistent form of Tsallis non-extensive statistical distribution function, which nicely describes the $p_{\rm T}$-spectra in LHC pp collisions to calculate the specific heat, CSBM, and speed of sound for small collision systems like pp as a function of transverse spherocity and final-state multiplicity using PYTHIA8 event generator. We have observed that the results for spherocity integrated events fall between isotropic and jetty events. This observation suggests that spherocity plays a significant role in separating events based on their geometrical shapes. Further, this also indicates that studying all the events without looking at the geometrical shape of the events might not contain complete information about the possible flow-like medium and/or jets.

The discovery of pp collisions showing QGP-like behavior at the LHC, for example, strangeness enhancement, collective-like phenomena, etc., has generated considerable interest in the scientific community. These developments have significant consequences on the results obtained from heavy-ion collisions, as pp collisions have been used as a benchmark for heavy-ion collisions to understand a possible medium formation. These open up entirely new directions for theoretical and experimental studies of characterizing QGP-like properties and understanding the origin of such observations in small collisions systems. This thesis work attempts to provide directions toward studying a thermalized medium formation in small systems by providing tools/techniques/methods both phenomenological and experimental.